8-3-2021 10:30 AM

The Physical Properties of Volcanic and Impact Melt

Gavin Douglas Tolometti, *The University of Western Ontario*

Supervisor: Neish, Catherine D., *The University of Western Ontario*
Co-Supervisor: Osinski, Gordon R., *The University of Western Ontario*
A thesis submitted in partial fulfillment of the requirements for the Doctor of Philosophy degree in Geology

Abstract

The emplacement mechanisms of lunar impact melt flows, that form from hypervelocity impact events, have been a subject of debate in the lunar science community, because of their unique physical properties that separate them from other geologic features. Understanding how lunar impact melt flows were emplaced on the surface of the Moon will not only grant us new information about the flow dynamics of impact melt but provide insight into the production and distribution of impact melt and how it built and modified the surfaces of planetary surfaces.

Lunar impact melt flows exhibit surface roughness textures and morphologies that are analogous to terrestrial lava flows. For this reason, we seek to quantify the surface roughness of terrestrial lava flows using synthetic aperture radar (SAR) at two localities, Craters of the Moon National Monument and Preserve, Idaho and the 2014-2015 Holuhraun lava flow-field. We focus on using SAR data in this study for two reasons, (1) improve our understanding on how radar surface roughness can be connected to the emplacement mechanisms of volcanic and impact melt, and (2) to highlight the techniques capabilities and limitations for differentiating different lava flow types and lava facies. Impact melt has contrasting intrinsic properties and geologic origins to lava flows, so we include the analysis of a physical property of impact melts that influences melt behaviour. To complement our radar surface roughness analysis, we seek to constrain the temperature of the Mistastin Lake impact structure impact melt deposits by analyzing the crystallographic orientations and microstructures of zircon grains and zirconia crystals encased in melt-bearing impactites. We demonstrate in this work that without entirely understanding the capabilities and limitations of using SAR for lava flow differentiation, we will struggle to interpret the eruption dynamics and history of volcanic landforms on terrestrial bodies, which in turn limits what we can learn about impact melt emplacement. Furthermore, we

discover that high temperature and pressure conditions can be constrained from an impact environment that was once superheated, which has strong implications for discovering high P-T shock indicators in other terrestrial impact structures and also in lunar impactites. In addition, our work has strong applications towards addressing high priority science goals established by research groups such as the Lunar Exploration Analysis Group.

Lay Summary

During impact events on a planetary surface, an immense amount of energy is released, shocking, melting, and vapourizing surrounding rocks and minerals. The rocks and minerals that melt produce material known as impact melt, which is observed in and around impact craters on rocky bodies throughout our Solar System. On the Moon, we observe some of these impact melts as lava-like flows moving downslope within and outside of impact craters. These lava-like features are known as lunar impact melt flows. Understanding how they were emplaced on the lunar surface is regarded as an important topic to study in planetary science since the production and distribution of impact melt can provide insight into how impact cratering processes have altered the surfaces of planetary bodies during the early age of our Solar System. In this work, we focus on studying the surface roughness of terrestrial lava flows using radar data and estimating the formation temperatures of terrestrial impact melt deposits. We included two studies on terrestrial lava flows and impact melt deposits because each of these geologic features offer a different piece of information about melt emplacement (how it was placed on the surface). The surface roughness of a lava flow is connected to how it was placed on the surface during a volcanic eruption. If we can understand how different lava flows were emplaced on Earth using radar and other remote sensing techniques, then we can gain new insights into the emplacement of lunar impact melt flows with similar surface roughness characteristics. The temperatures of volcanic and impact melt strongly influence their flow behaviour on a surface. Due to impact melt temperatures being significantly higher upon formation as compared to lava flows (>1700°C vs 1200°C), we must understand the range of temperatures impact melts can have when they form during impact events. We demonstrate in this work how we can study and

infer the emplacement of terrestrial lava flows using radar data, and how we can provide a much clearer picture of the temperature conditions of impact melt deposits. Moreover, we also stress the importance of terrestrial analogue research, and how our work can contribute to high priority lunar science and exploration goals established by NASA and other space agencies.

Co-Authorship

Chapter 2: The first author, Gavin Tolometti, conducted field work, and the radar remote sensing analysis, microscopic and geochemical analysis portion of this research, and wrote the manuscript for publication. Dr. Catherine Neish (supervisor) provided access to radar data, funding for field work and microscopic analysis, and provided edits for the manuscript. Dr. Gordon Osinski (supervisor) provided funding for geochemical analysis and edits for the manuscript. Dr. Scott Hughes and Dr. Shannon Kobs Nawotniak offered expertise in terrestrial volcanology whilst in the field and provided edits for the manuscript.

Tolometti, G. D., Neish, C. D., Osinski, G. R., Hughes, S. S., & Nawotniak, S. K. (2020). Interpretations of lava flow properties from radar remote sensing data. *Planetary and Space Science*, 104991.

Chapter 3: The first author, Gavin Tolometti, conducted radar remote sensing analysis prior to and after field work at the Holuhraun lava flow-field in central Iceland in 2019. He took field observations, analyzed LiDAR data, and is in the process of preparing this chapter for publication. Dr. Catherine Neish provided funding for field work, access to software for processing and analyzing the radar and LiDAR data. Dr. Christopher Hamilton (collaborate and co-author) provided expertise on terrestrial volcanology and the eruption history of Holuhraun and will provide edits for the manuscript. Dr. Gordon Osinski provided expertise on terrestrial volcanism and will provide edits for the manuscript. Dr Antero Kukko (collaborator and co-author) operated a kinematic LiDAR system in the field to acquire high-resolution LiDAR topography data that Gavin Tolometti used for his research. Dr Antero Kukko will also provide edits for the manuscript. Joana Voigt (PhD Candidate, supervised by Dr. Christopher Hamilton,

collaborator, co-author) also provided expertise on terrestrial volcanology and the eruption history of Holuhraun. She granted access to ArcGIS shapefile data for radar analysis and will be providing edits for the manuscript.

Tolometti, G. D., Neish, C. D., Hamilton, C. W., Osinski, G. R., Kukko, A., Voigt, J, G, R. (not submitted). Differentiation of the Holuhraun Lava Flows Through Quantitative Analysis of Radar and LiDAR Remote Sensing.

Chapter 4: The first author, Gavin Tolometti, conducted optical microscopy, petrographic and geochemical analysis on impact melt samples from the Mistastin Lake impact structure at the University of Western Ontario. He worked with Dr. Timmons Erickson (collaborator and co-author) to run electron-backscatter diffraction analysis on zircon grains and zirconia crystals at the Scanning Electron Microscopy laboratory at the NASA Johnson Space Center in Houston, Texas. Gavin Tolometti wrote the manuscript and addressed edits and comments from co-authors. Dr. Timmons Erickson offered expertise on the analytical technique and taught Gavin Tolometti how to interpret the data. Dr. Timmons Erickson also provided edits for the manuscript. Dr. Gordon Osinski provided funding for Gavin Tolometti to travel to the Johnson Space Center to work with Dr. Timmons Erickson and gave Gavin Tolometti access to Mistastin impact melt samples that were collected during field deployments from 2009-11. Funding included preparing the samples for electron backscatter diffraction at the University of Western Ontario. Dr. Gordon Osinski also provided edits for the manuscript. Dr. Cyirl Cayron (collaborator and co-author) processed the electron backscatter diffraction data using a Python-based software ARPGE designed by himself. Dr. Cyril Cayron also provided edits for the

manuscript. Dr. Catherine Neish provided funding support for Gavin Tolometti to travel to the Johnson Space Center and provided edits for the manuscript.

Tolometti, G. D., Erickson, T. M., Osinski, G. R., Cayron, C., Neish, C. D. (under review). Hot Rocks: Constraining the Thermal Conditions of Impact Melt Deposits Using Zircon and Zirconia Polymorphs. Earth and Planetary Science Letters.

Acknowledgements

Ever since I started my studies in Canada, I was nervous and unsure if I had the potential to pursue a PhD in planetary science. I will not lie saying I had my doubts coming in because it was an entirely new world for me. Completely different to my undergraduate experience. However, the support and motivation given to me by Drs. Catherine Neish and Gordon Osinski is what helped me realize that planetary science is the career I want to pursue. They helped me find the opportunities I needed to develop my leadership and independent research skills, put me in positions where I would lead a field deployment to central Iceland, be part of a field team simulating the in-situ analysis procedure of a Mars rover, put trust in myself to carry out electron micro-probe analysis without supervision, and to represent Western Space as an ambassador while visiting other research institutions. These opportunities are only a few examples of why Drs. Catherine Neish and Gordon Osinski gave me the confidence, drive, and determination to complete my PhD, expand my knowledge in the field of planetary science, and become a new contributing member of the science communication community.

I would like to reach out and extend a huge thanks to Western Space administrator officer Courtney Swinden and Educational Outreach and Communications Specialist Dr. Parshati Patel. Courtney and Parshati saw my enthusiasm for wanting to get involved in outreach and science communication and gave me the chance to become more involved with Western Space. On top of getting to travel to schools across London Ontario and co-organize public events, Courtney and Parshati put their trust in me to represent Western Space as an ambassador at space industry conferences and international space challenges, such as the NASA Space Apps Challenge 2019. I want to acknowledge the assistance of Department of Earth Science technical staff Stephen

Wood and Marc Beauchamp. If it were not for Stephen Wood and Marc Beauchamp, I would not have been able to conduct a majority of my laboratory analysis.

I would also like to acknowledge the University of Western Ontario. The support provided by the institution through internal grants and access to resources, especially during the COVID-19 lockdown, helped ensure the completion of my PhD. The members of staff who have worked tirelessly during the pandemic gave me, and every graduate student the ability to move forward with our graduate studies. I want to formally thank those staff members for their sacrifice during the pandemic and the countless hours they spent making sure we could continue our studies and stay safe in our community.

I would like to thank a few members who assisted me, and my work reported in Chapters 2, 3, and 4.

Chapter 2: Field work was conducted with support from FINESSE (Field Investigations to Enable Solar System Science and Exploration), Jennifer L. Heldmann, PI, funded by the NASA Solar System Exploration Research Virtual Institute (SSERVI), and the National Park Service personnel at Craters of the Moon National Monument and Preserve (Permit #CRMO-2014-SCI-0004). We would also like to thank Ms. Rachel Maj, Mr. Kevin Fan, and Dr. Raymond Francis for their assistance in the field. Thanks also to Dr. Alex Selkhe for providing input on an earlier version of this manuscript. Special thanks to the Canadian Space Agency's Flights and Fieldwork for the Advancement of Science and Technology program for funding this research, and to the Leverhulme Trust Committee (Account No. IND11814) for providing Gavin Tolometti with a scholarship to support his studies. Petrographic and geochemical analysis could not have been possible without the help from technical staff at Western University (Marc Beauchamp, Stephen Wood, and Dr. Charlie Wu).

Chapter 3: This research was funded and supported by the Canadian Space Agency Flights and Fieldwork for the Advancement of Science and Technology (FAST) program. During the field deployment at Holuhraun, work was conducted with support from P. Whelley, K. Young, J. Richardson, and the NASA Goddard Instrument Field Team (GIFT). Thanks to them for their collaboration and assistance in field work logistics. Thanks also to E. Schaefer and C. Rodriguez for assistance in the field and LiDAR site selections.

Chapter 4: This work was supported by funding to GRO from the Natural Sciences and Engineering Research Council of Canada Discovery Grant and Northern Research Supplement programs and the Canadian Space Agency Flights and Fieldwork for the Advancement of Science and Technology program. Support for this research was provided in part by NASA's Planetary Science Research Program.

My supervisors, the university, collaborators and co-authors, and department of earth science staff are not the only figures I want to acknowledge. If it were not for my friends and family who supported me moving to Canada for my postgraduate studies, I would have had an entirely different experience. My parents and siblings showed their support with their numerous questions about what my PhD studies were about and whether I will go to space to conduct research. I would always give the same answer for the first question and never have a clear answer for the second. A special person I would like to thank for providing me the energy and passion to keep moving forward is my girlfriend, Ashley Nickerson. She has always been able to provide advice and support when stress and writers block became very common near the end of my PhD. She has always helped me by letting me talk about my work with her, give emotional support during days where coding scripts would not work, or image analysis commands would keep crashing mid-triangulation. She has always been there when I had a mountain of work to

complete for my thesis. Ashley Nickerson gave me the push to show me what I am capable of, and it let me realize what I could accomplish, not only for her and for the planetary science community, but for myself.

Thank you to everyone.

Landmark Acknowledgement

I acknowledge that the University of Western Ontario is located on the traditional lands of the Anishinaabek, Haudenosaunee, Lūnaapéewak and Attawandaron peoples, on lands connected with the London Township and Sombra Treaties of 1796 and the Dish with One Spoon Covenant Wampum. This land will always be the home to these Indigenous Nations, and we should continue to acknowledge how they are connected to it.

Table of Contents

List of Tables

List of Figures

Chapter 1:

Chapter 2:

Chapter 3:

Chapter 4:

Chapter 5:

List of Appendices

List of Abbreviations and Symbols

AIRSAR – Air Synthetic Aperture Radar

Ano – Anorthoclase

Ap – Apatite

ARPGE – Automatic Reconstruction of Parent Grains from EBSD data

BSE – Backscatter Electron

COTM – Craters of the Moon

CPR – Circular Polarization Ratio

Cpx – Clinopyroxene

Cs – RMS Slope

Cserr – RMS Slope Standard Deviation

dB – Decibels

d – Depth

DEM – Digital Elevation Model

DLP – Degree of Linear Polarization

DTM – Digital Terrain Model

ε' – Real dielectric constant

ε'' – Imaginary dielectric constant

EBSD – Electron Backscatter Diffraction

EDS – Energy Dispersive Spectroscopy

EMPA – Electron Micro-Probe Analysis

FoV – Field of View

FRIGN – Former Reidite in Granular Neoblastic

FSE – Forescatter Electron

GRD – Ground Range Detected

H – Hurst Exponent

Herr – Hurst Exponent Standard Deviation

HiRISE – High Resolution Imaging Science Experiment

GIFT – Goddard Instrument Field Team

IPF – Inverse Pole Figure

ISIS3 – Integrated System for Imagers and Spectrometers

ISRO – Indian Space Research Organization

JSC – Johnson Space Center

LiDAR – Light Detection and Ranging

LRO – Lunar Reconnaissance Orbiter

LRO NAC – Lunar Reconnaissance Orbiter Narrow-Angle Camera

LRO WAC – Lunar Reconnaissance Orbiter Wide-Angle Camera

MGS – Mars Global Surveyor

MOC – Mars Orbiting Camera

MRF – Miniature-Radio Frequency

MRO – Mars Reconnaissance Orbiter

n – Number of sample points

NAIP – National Agriculture Imagery Program

NGA – National Geospatial Intelligence Agency

NSF – National Science Foundation

OC – Opposite-sense Polarization

Ol – Olivine

Op – Opaque's

ρ – Density

Pa – Pascals

Pl – Plagioclase

PPL – Plane-Polarized Light

RMS – Root Mean Square

s - Seconds

SAR – Synthetic Aperture Radar

SC – Same-sense Polarization

SEM – Scanning Electron Microscopy

σ^0 – Backscatter Coefficient

SNAP – SeNtinel Application Program

std – Standard Deviation

tanδ – tangent of the substrate

TAS – Total Akali Silica

μm – Micron

UAS – Unmanned Aerial System

UAVSAR – Uninhabited Aerial Vehicle Synthetic Aperture Radar

ν^2 – Allan variance

W – Stokes Matrix

WDS – Wavelength-Dispersive Spectroscopy

xi – Point along topographic profile

XPL – Cross-Polarized Light

XRF – X-Ray Fluorescence

zi – Topographic profile

ϕ – Incidence angle

Δx – Interval step

Δx_0 – Reference scale

λ – Wavelength

Chapter 1: Introduction and Background

1.1 Research Motivation

The motivation of this research originated from seeking to understand the emplacement of the roughest material on lunar surface, impact melt flows. An impact melt flow is a flow-like structure with lobate marginal features that form when molten impact-generated melt flows downslope under the influence of gravity. Lunar impact melt flows (impact melt flows on the Moon) have been discovered in and around numerous lunar impact craters (Howard and Wilshire, 1975; Hawke and Head, 1977; Neish et al., 2014) and their emplacement mechanisms and physical properties have been a topic of debate in the planetary science community (e.g., Lev et al., in press; Denevi et al., 2012; Stopar et al., 2014; Neish et al., 2017, 2021). Impact melt is a product of impact cratering processes, produced from the decompression of highly shocked target rocks. Its occurrence and physical properties are significant for understanding how impact melting would have built and modified the structure and composition of early crustal material of planetary bodies (Dence, 1971; Marchi et al., 2014; Osinski et al., 2018) and effected the development and evolution of Earth's early atmosphere (Day and Moynier, 2014; Marchi et al., 2016).

Studying the emplacement mechanisms of lunar impact melt has been conducted by other workers using available remote sensing data sets (e.g., Bray et al., 2010; Carter et al., 2012; Neish et al., 2014, 2017; Stopar et al., 2014). A limitation to using only remote sensing data, is that our interpretations are constrained to the spatial resolution, wavelength, and availability of the data. Due to these limitations, we strive to find terrestrial examples for comparative studies.

However, finding examples of impact melt flows to study in detail on Earth is challenging because active erosional (e.g., fluvial, aeolian, and glacial) and tectonic processes (e.g., subduction of oceanic plates and collision of continental plates) have removed surface evidence of impact melt flows. We are able to conduct field work at terrestrial impact structures and perform detailed laboratory analysis on the chemistry, mineralogy, and P-T conditions of impact melt deposit samples (e.g., melt deposits at the Mistastin Lake impact structure, northern Labrador, Canada), but we are not able to study flow morphology, which is necessary to understand emplacement mechanisms. With our inability to directly study fresh lunar impact melt flows, we instead have elected to study terrestrial lava flows that share analogous surface features. Neish et al., (2017) showed that the decimetre-scale roughness of lunar impact melt flows is, to a certain degree, analogous to the surface roughness properties of transitional terrestrial lava flows (e.g., rubbly pāhoehoe) (Figure 1.1).

Surface roughness is a physical property that represents the horizontal topography of a surface and its variation along a profile. The surface roughness of a lava flow is connected to the emplacement mechanisms of an eruption event (Rowland and Walker, 1990; Keszthelyi and Self, 1998; Polacci et al., 1999; Guilbaud et al., 2005; Thordarson and Larsen, 2007; Harris et al., 2017; Hamilton, 2019), providing a window into the volcanic activity that has occurred on planetary bodies. Based on this line of thinking, if we can understand what emplacement mechanisms are responsible for the development of specific lava flow surface roughness, we can infer how impact melt flows with analogous surface features were emplaced on planetary surfaces. To address this, we organized this thesis around two topics. The first topic involves the use of radar remote sensing data sets and ground-truth field measurements to analyze and quantify the surface roughness of terrestrial lava flows from two field sites; Craters of the Moon

National Monument and Preserve, Idaho, and the 2014-2015 Holuhraun lava flow-field, Iceland. The second topic involves investigating the physical property of impact melt that would play a vital role in the emplacement of melt flows, temperature. We focus on constraining the temperature of impact melt because impact melt is considered to be superheated (exceeding rock liquidus) when produced during hypervelocity impact events, which is different to the sub-liquidus eruption temperatures of basaltic lava flows (~1050°C – ~1200°C). Temperature is a physical property that strongly influences the rheology and emplacement of lava flows (Keszthelyi and Denlinger, 1996; Kilburn, 2000; Robert et al., 2014; Kolzenburg et al., 2017). From this reasoning, it would also have a significant effect on the rheology of impact melt and therefore its emplacement.

In this chapter, we cover why the analysis of lava flow surface roughness and constraining the temperature of impact melt is important for understanding impact melt emplacement, and how terrestrial analogues provide a natural laboratory for studying impact melt flows and lava flows on planetary bodies.

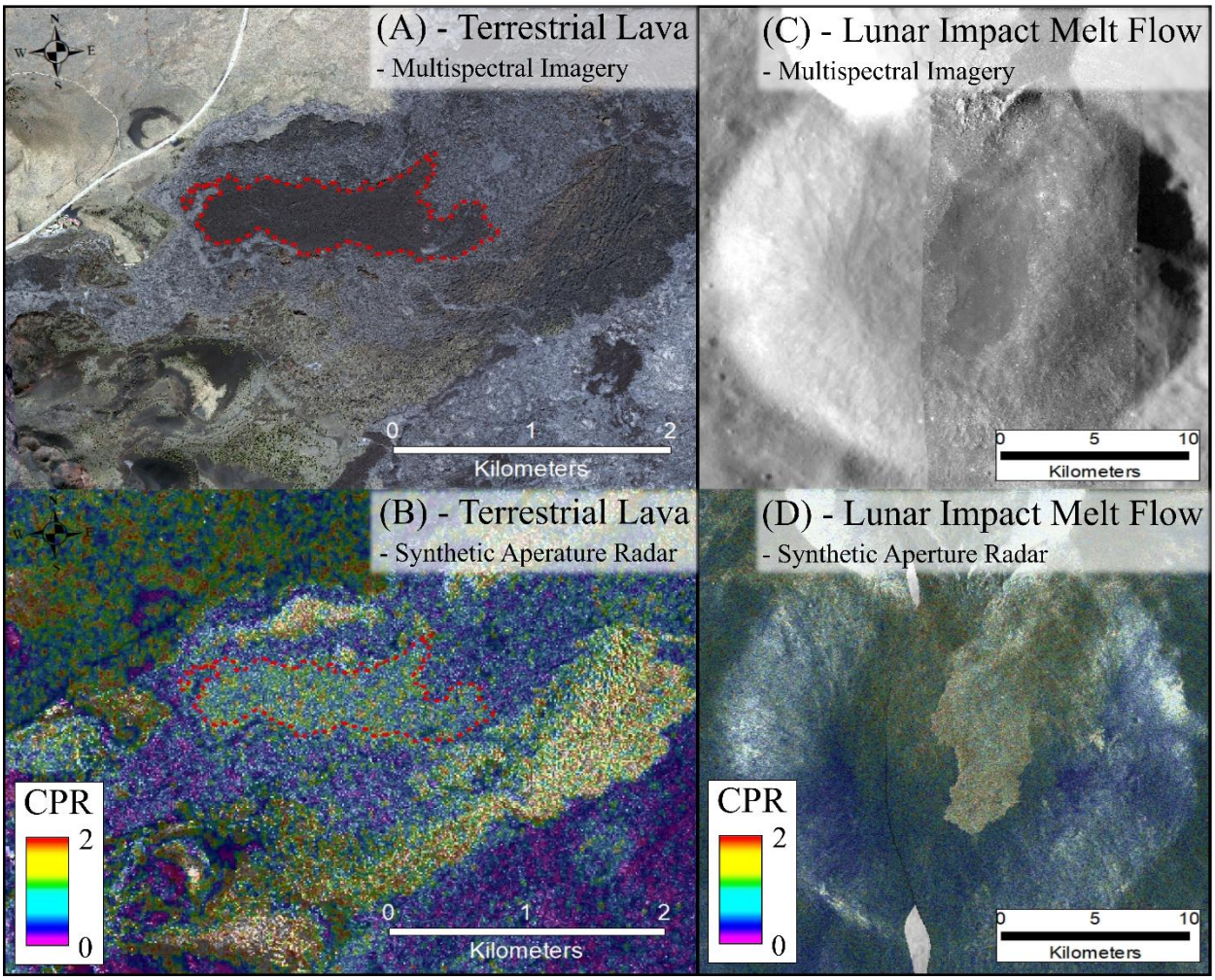

Figure 1.1. Comparison of terrestrial lava flows to lunar impact melt flows through analysis of surface roughness using multispectral imagery and synthetic aperture radar (SAR). The terrestrial lava flow example is a rubbly pāhoehoe flow (dashed red outlines) located at Craters of the Moon National Monument and Preserve lava field in Idaho, USA. The lunar impact melt flow example is from the south rim of Korolev Z crater on the lunar far side. The rubbly pāhoehoe and Korolev Z impact melt flow return similar circular polarization ratio (CPR) data, which indicates that both flows exhibit similar surface roughness textures. (A) Multispectral imagery acquired from the National Agricultural Imagery Program (NAIP) (1 m/pixel). (B) Quad-polarimetric AIRSAR data (λ = 24 cm, 5 m/pixel) showing circular polarization ratio (CPR) data overlying

radar backscatter data. The higher the CPR value, the greater the roughness of the surface (CPR <0.5 = smooth, CPR 0.5-1 = rough). (C) An image strip acquired using the Lunar Reconnaissance Orbiter (LRO) Narrow-Angle Camera (NAC) (0.5 m/pixel) overlying LRO Wide-Angle Camera (WAC) global morphology mosaic data (100 m/pixel). (D) CPR data overlaid on radar backscatter data derived from monostatic Miniature Radio-Frequency SAR data (λ = 12.6 cm, 7.5 m/pixel).

1.2 Lava Flow Roughness Spectrum

Our planet hosts a diverse array of lava flow types that formed under different emplacement mechanisms, which were, in part, influenced by changes in their physical properties (e.g., viscosity, temperature, and crystallinity) and flow dynamics (discharge rate, velocity, etc.). Changes in these physical properties during volcanic eruptions produces a variety of lava flow surface roughness and sub-type morphologies (MacDonald, 1953; Griffiths, 2000; Kilburn, 2000; Harris et al., 2017; Hamilton, 2019). When we think about lava flows, our thoughts turn to the two most commonly documented and extensively studied in volcanology, pāhoehoe and ʻaʻā. Pāhoehoe and ʻaʻā lava flows are perfect examples of how surface roughness and morphology can inform us about emplacement mechanisms. The smooth, glassy surface of a pāhoehoe lava flow is a result of a stable coherent crust providing insulation for a relatively high temperature fluid core (1050 °C – 1200 °C) with a low viscosity (Kilburn, 2000). Typically, pāhoehoe lava is dominant during eruptions with low effusion rates and on terrains with flat-lying topography. In these conditions, flow velocities are moderately low allowing the lava to spread laterally as thin (decimetre thick) sheet-like units instead of as channelized flows with levees. Pāhoehoe flows are not individual flow units, but a complex system of hundreds to tens

of thousands of intermingling tongues and toes that form when fluid lava leaks through localized weaknesses in the chilled, insulating crust along the flow margins (Solana et al., 2004). Inflation of pāhoehoe lava is common since the crust retards the movement of the fluid core a lot more efficiently than ʻaʻā, leading to increased thicknesses in the flow units and the development of inflation plateaus and other volcanic structures such as lava-rise pits. This gives the pāhoehoe surface an undulating or hummocky appearance (Swanson, 1973).

The formation of ʻaʻā lava is a different story. The sub-rounded, sharp, jagged surface of ʻaʻā derives from the continuous disruption of its surface due to a variety of factors, including high flow velocity, high viscosity induced by a greater cooling of the lavas fluid core when exposed on the surface, and high shear stress (Peterson and Tilling, 1980). Aʻā lava flows form channels with levees comprising clinkers and rafted material that fall off the surface of the flow and material that brecciates off the margin of the channel. Aʻā lava is situated on the other end of the spectrum with pāhoehoe and can form when a pāhoehoe lava surpasses the rheological threshold (Peterson and Tilling, 1980; Sehlke et al., 2014).

In addition to pāhoehoe and ʻaʻā, another type of lava, with flow behaviour similar to ʻaʻā is block lava. Block lava is an unusual type of lava flow, with a surface roughness that comprises decimetre- to metre-sized smooth-faced, polyhedral blocks (MacDonald, 1953). Block lava typically exhibits compositions from basaltic andesite to dacite, with high silica (>55 wt.%) content (Ulrich, 1987; Kilburn, 2000; Harris et al., 2017). However, there are some studies reporting that lunar basaltic lava domes and flows with radar returns indicative of blocky surfaces are interpreted to have formed due to a combination of change in composition, effusion rate, and/or cooling effects (Campbell et al., 2009a). A major difference between block and ʻaʻā is that block lavas are more viscous owing to their greater silica content and the lower effusion

rates of andesitic-rhyolitic eruptions. The fluid core of a block lava is stronger and more viscous that the core of an ʻaʻā flow as the surface of the lava breaks apart before a significant amount of cooling has occurred to develop a cohesive crust. Instead of gradually flowing across a surface block lavas move via a creep motion where a layer along the base of the flow is moving but the surface breaks apart (Kilburn, 2000). This motion is similar to how glaciers flow and deform when receding and growing (MacDonald, 1953). There are instances where an ʻaʻā lava can transition to a block lava when the interior of the flow becomes too crystalline to allow the flow to move.

A fourth classification of lava flows that exists outside of the pāhoehoe-ʻaʻā -block spectrum are known as transitional lava flow types (Harris et al., 2017; Hamilton, 2019). In the literature, transitional lava flows are either described as sub-types of pāhoehoe and ʻaʻā lava flows (Duraiswami et al., 2014), or variants exhibiting different volcanic structures (Harris et al., 2017; Hamilton, 2019). Transitional lava flow types form due to changes in eruption dynamics during a volcanic event, local emplacement mechanisms of flow units, crust stability, and/or drastic variations in topography (Figure 1.2). Several types of transitional lava flows have been documented in the literature (e.g., Keszthelyi et al., 2004; Duraiswami et al., 2014; Harris et al., 2017; Hamilton, 2019). However, for simplicity in this thesis, we only cover the transitional lava flows reported in Chapters 2 and 3. The transitional lava flows that have been studied in detail during this thesis are platy, slabby, and rubbly. Platy lavas (Keszthelyi et al., 2004; Hamilton, 2019) comprise metre-sized segments of crust that have been rafted and separated by upwellings of lava, exposed through fractures. Plates can form from either the drainage of a lava pond causing the crust to break, or from the increase pressurization of a molten lava core in an inflating sheet pāhoehoe or plateau (Hamilton, 2019). The continued disruption of a platy lava

can lead to a slabby lava. The plates become inclined relative to the lava flow surface and break apart into smaller sections or slabs (Figure 1.2) when they collide and abrade against each other. If a slabby surface experiences continued disruption or an undisturbed cohesive crust becomes extensively fragmented, equant sized fragments of the lava flow crust form, creating a rubbly texture on the surface (Figure 1.2). Rubbly lavas are commonly associated with ʻaʻā, but have been observed at some localities (e.g., Craters of the Moon National Monument and Preserve, USA and the Deccan Traps, India) to be associated with pāhoehoe lava flow types.

With clear differences in eruption dynamics and emplacement processes responsible for the development of these lava flow types, it is important that we understand how to best utilize remote sensing data sets to identify and differentiate them.

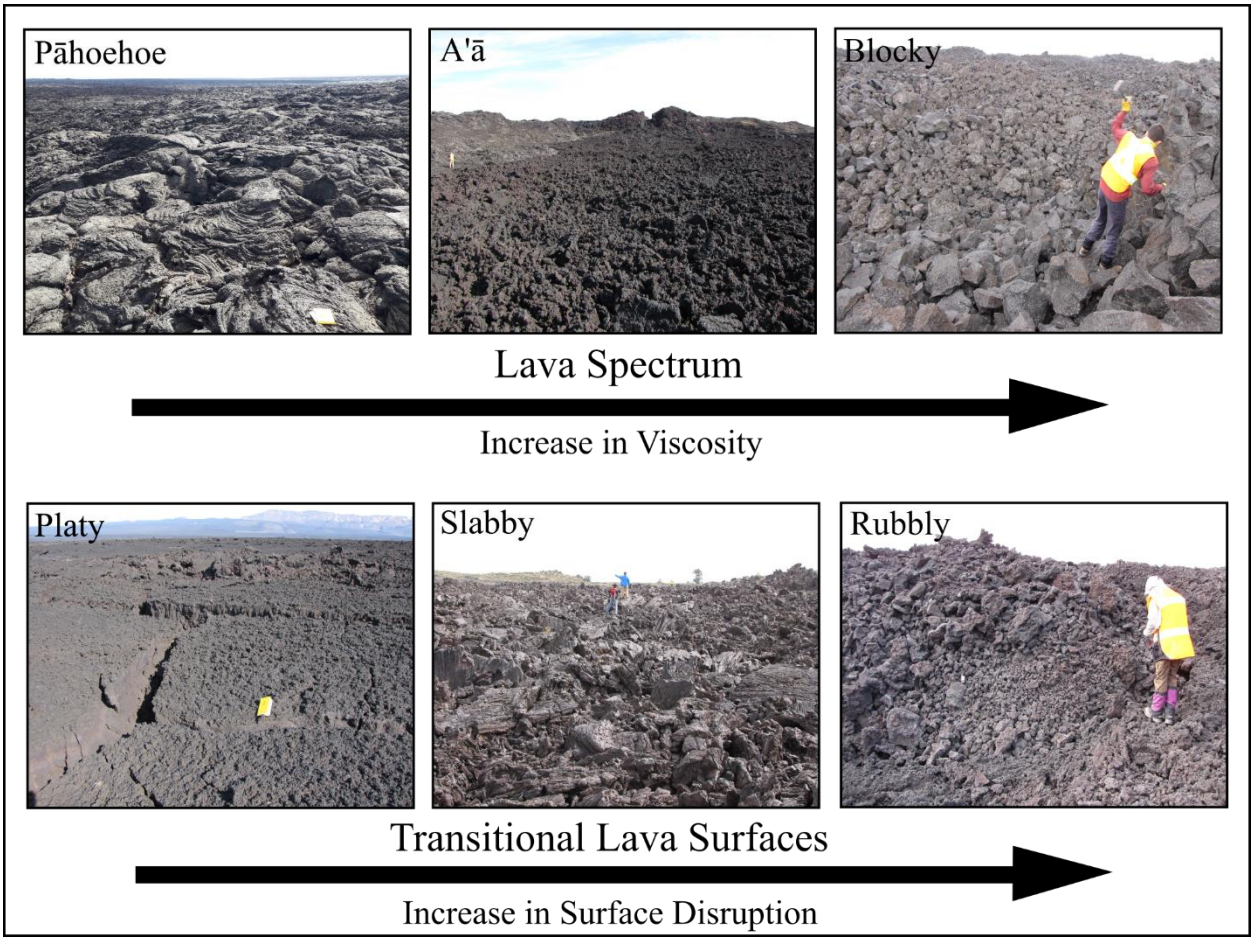

Figure 1.2. Diagrams showing the pāhoehoe-ʻaʻā -block lava spectrum and examples of transitional lava flow types with increasing degrees of surface disruption. The differences on the origin of these lava flow types and surface morphologies reflects changes in lava rheology and eruption dynamics. The pāhoehoe-ʻaʻā -block lava spectrum is controlled by changes in lava flow physical properties and flow dynamics, while the transitional lava surfaces are controlled by the extent of surface disruption.

1.3 Analysis of Lava Flow Surface Roughness

Remote sensing analysis of lava flow surface roughness in terrestrial and planetary science is primarily conducted using synthetic aperture radar (SAR) (Campbell and Shepard, 1996; Shepard et al., 2001; Campbell, 2012; Neish et al., 2017; Dumont et al., 2018; Tolometti et al., 2020). SAR is a radar remote sensing technique that constructs 2-D images of landforms using backscattered radio signals (Campbell 2002; Lee and Pottier, 2009) (Figure 1.3). Investigations of lava flow surface roughness using SAR has primarily focused on monitoring the evolution of volcanic eruptions (Dumont et al., 2018), understanding the influence surface roughness has on radar scattering mechanisms and properties (Campbell and Shepard, 1996; Campbell, 2012), and understanding the distribution of lava flows on rocky bodies such as the Moon (e.g., Campbell et al., 2009b; Lawrence et al., 2013; Morgan et al., 2016), Mars (e.g., Harmon et al., 1999, 2012), and Venus (e.g., Campbell et al., 1999; Carter et al., 2006). Unlike higher frequency remote sensing techniques (e.g., visible-near infrared (λ = 400 nm – 1100 nm) and UV (10 nm – 400 nm)), SAR is capable of penetrating through cm- to m-thick layers of regolith and dust (Campbell, 2002; Neish and Carter, 2014). The ability to penetrate through regolith and dust makes SAR an advantageous remote sensing technique to analyze the surface roughness and morphology of lava flows that are buried on planetary surfaces.

Terrestrial studies conducted by numerous workers (e.g., Campbell and Shepard, 1996; Shepard et al., 2001; Campbell, 2002, 2012; Neish et al., 2017; Tolometti et al., 2020) show that large, individual smooth (e.g., pāhoehoe), rough (e.g., ‘a‘ā), and very rough (e.g., block) lava flows can be differentiated from one another in radar remote sensing data. However, lava flow-fields exhibit more complexity and often include intermediate transitional lava flow types such

as rubbly, slabby, and platy (Griffiths, 2000; Coppola et al., 2019; Hamilton, 2019). Few studies have sought to determine whether all of these lava flow types can be differentiated from one another. This is important since volcanic landforms on other rocky bodies may exhibit more types of lava than the traditional pāhoehoe and ʻaʻā (Keszthelyi et al., 2004; Campbell et al., 2009a; Rodriguez Sanchez-Vahamonde and Neish, 2021).

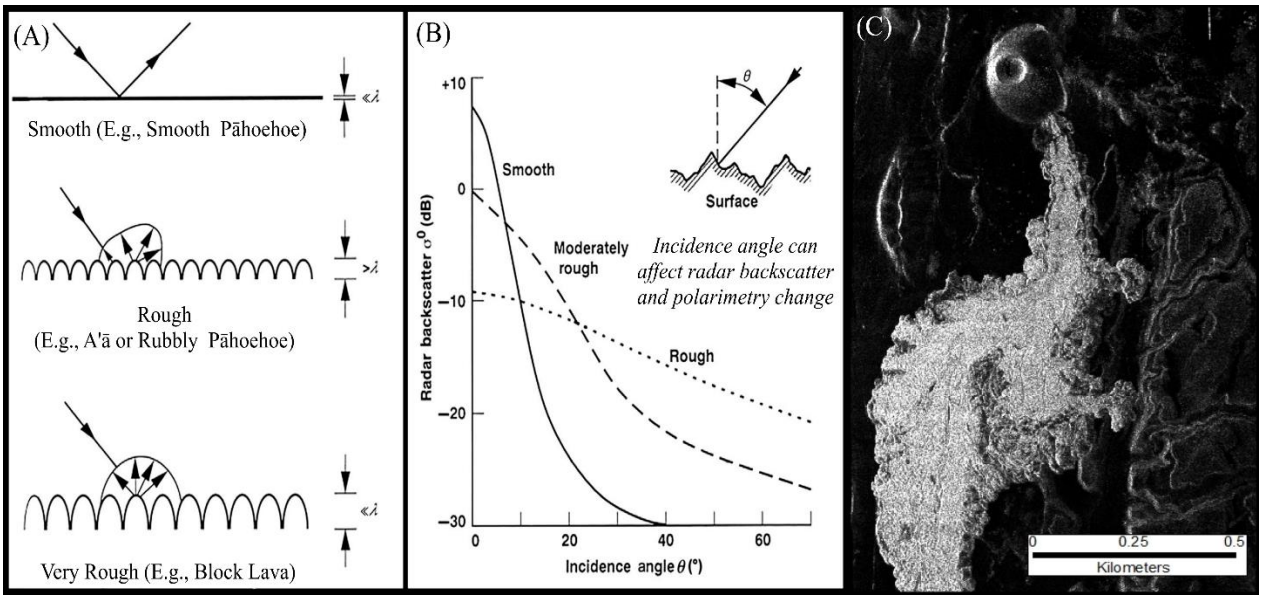

Figure 1.3. Analysis of lava flow surface roughness using SAR total backscatter data. (A) The amount of radar backscattering corresponds to the surface roughness of a lava flow. The rougher the surface at the size of the radar wavelength, the greater the backscatter intensity. (B) The incidence angle of an emitted radio signal affects the radar backscatter returned from a surface. (C) Example of a 2-D SAR total backscatter data; the SP Crater flow located in Arizona, USA. Figure adapted from Farr (1993).

1.4 Temperatures of Impact Melt

1.4.1 Impact Cratering Processes

The production of impact melt is a ubiquitous process that occurs during hypervelocity impact events on planetary bodies (Grieve et al., 1977; Melosh, 1989). To understand the formation of impact melt, we need to first grasp the concept on how an impact crater forms on a planetary body.

The formation of an impact crater is categorized into three stages. Each stage is described as a separate event but the transition between each is continuous and occurs along a time scale from seconds to minutes (Grieve et al., 1977; Melosh, 1989). The point of impact between the projectile (e.g., comet or meteorite) and the target rocks (rocks on the surface and in the sub-surface of a planetary body) is the beginning of the first stage of the impact cratering process, known as the contact and compression stage. The projectile transfers its kinetic energy into the target rocks as a shock wave, which then propagates through the surrounding target rocks and back into the projectile (Melosh, 2012). The shock wave passing through the target rocks is partitioned into kinetic energy, which puts the target rocks into motion and initiates the formation of a crater structure. Later, the kinetic energy converts to internal energy, which leads to shock metamorphism. The shock waves that pass back through the projectile reflect off the top and are reflected back into the target rocks as rarefaction/release waves. The contact and compression stage lasts for only a few seconds, and transitions to the second stage; the excavation stage. The passage of the rarefaction wave through the target rocks, in conjunction with the initial shock wave, produces a cratering flow-field (Dence, 1968; Grieve and Cintala, 1981; Melosh, 1989), which results in the ejection of material in the upper and outer regions of

the crater and downward displacement of material in the lower and central regions of the crater (Stoffler et al., 1975; Grieve et al., 1977) (Figure 1.4A-B). The excavation and displacement of target rock material leads to the opening of a bowl-shaped structure known as the transient cavity. When the cratering-flow field is no longer able to excavate or displace material within and outside the transient cavity (i.e., energy is insufficient) the transient cavity experiences instability. It is at this point that the final stage, known as the modification stage, begins (Figure 1.4C). The modification stage involves the formation of the final crater (Figure 1.4D) (Melosh, 1989). The size and morphology of the final crater is dependent on the gravitational acceleration of the planetary body (Cintala and Grieve, 1998), the cohesive strength of the target rocks (Osinski et al., 2008; Kenkmann et al., 2012), and the existence of pre-existing topography (Eppler et al., 1983; Gulick et al., 2008; Öhman et al., 2010).

Four types of craters can form from impact cratering events (dependent on the size of impactor, impact velocity, and gravity). Small (<2 km on Earth), simple craters (Dence, 1965) retain the bowl-shape of the transient cavity and experience minimal instability of the crater walls. Fresh simple craters have raised and over-turned rims, which are overlain by ejecta deposits. The base of a simple crater is partially filled with deposits of impactites (rocks formed or modified by hypervelocity impacts), specifically impact breccia, with an approximate 1:5 depth/diameter ratio, making the final crater significantly shallower than the original transient cavity (Kenkmann et al., 2012). The impact breccia deposits can contain melt-free, melt-poor, and/or melt-bearing impactites. The extent of modification a simple crater will experience is dependent on the strength of the target material (Osinski et al., 2008; Kenkmann et al., 2012). The more competent the target rocks, the less modification the crater will experience. Larger craters (>4 km) are termed complex (Dence, 1965). These craters exhibit features not observed in

simple craters, including uplifted central peaks, terraced crater walls, and a down-faulted flat floor. The intricacy of complex craters is dependent on the gravitational acceleration of the planetary bodies (e.g., >2 – 4 km diameter craters on Earth will transition from simple to complex structures, while 15-20 km diameter craters on the Moon). The third type of impact crater is termed a peak-ring crater (Morgan et al., 2000). The nomenclature relates to a circular ring of rugged uplifted shocked basement material surrounded by allochthonous and parautochthonous impact melt and impact breccia deposits. These deposits infill a shallow crater floor. Due to erosion, identifying peak-ring impact structures on Earth is challenging. A fourth category of impact structures, known as multi-ring impact basins (Grieve et al., 1981; Grieve and Cintala, 1992; Kring et al., 2016), have been identified on the Moon (Orientale), Mercury (Caloris), Jupiter's moons Ganymede (Anubis) and Callisto (Valhalla), and Saturn's moon Dione (Evander). On Earth, three impact structures are cited as multi-ring basins: Vredefort, Sudbury, and Chicxulub.

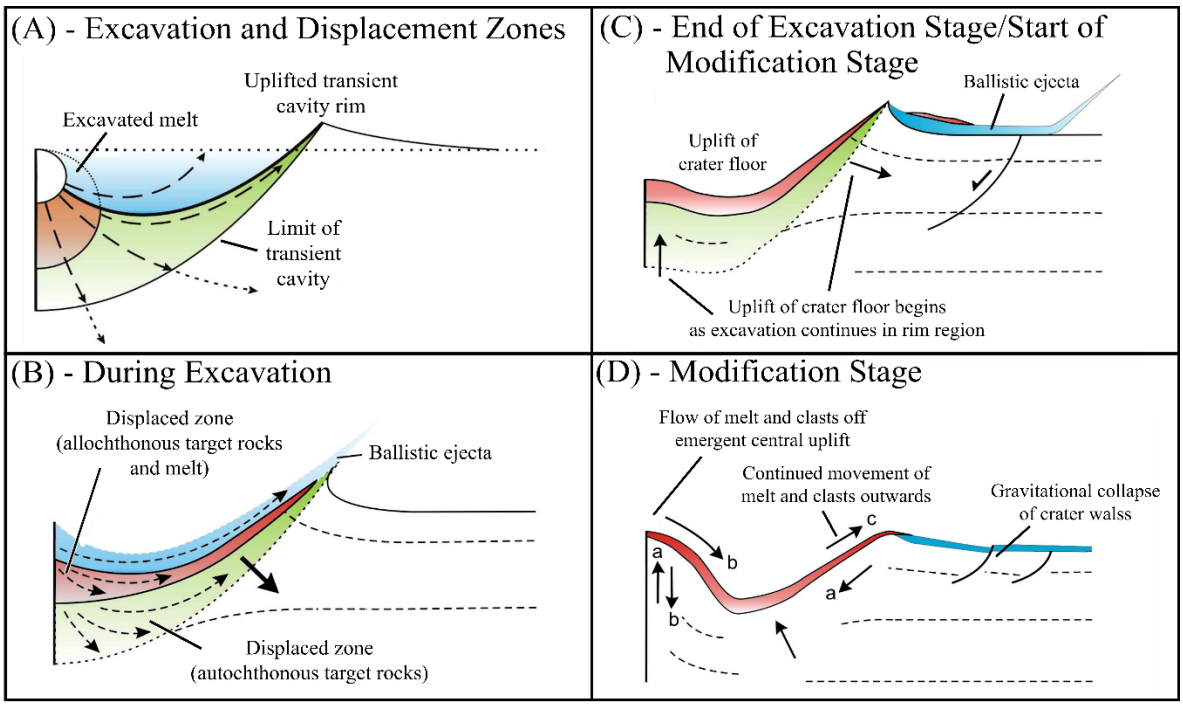

Figure 1.4. Excavation and modification stages of complex crater formation (modified from Osinski et al., (2011)). (A) During the excavation stage, the propagation of the shock and refraction waves create flow-field pathways that excavate material upwards and outwards. (B) Excavated material is ejected over the crater rim and deposited as ballistic ejecta. (C) At the end of the excavation stage and start of the modification stage, the rebound of the crater floor creates an emergent central uplift. Ejecta material continues to move over the crater rim. (D) Melt and clastic material flows off the emergent central uplift and, in some cases, over the crater rim.

1.4.1.1 Impact Melting

Impact melting is a type of shock metamorphism that occurs when rocks are subjected to extremely high pressures (>60 GPa – 100 GPa) and then decompressed by the passing rarefaction wave. The extent to which impact melt occurs is dependent on the peak pressure of

the impact event (Grieve et al., 1977) and the compressibility of the target rocks and their constituent minerals (Osinski et al., 2012). The mass, momentum, and energy of the shock waves are conserved when they pass through the target rocks, and the physical state of each mineral is defined by the Hugoniot equation (Melosh, 1989). The passage of the shock wave causes the minerals to immediately experience changes in terms of volume and shock pressure. This sudden change causes the internal energy of the target materials to increase, and pressure-volume work is applied to the target materials. When the rarefaction wave passes through the target rocks after the passage of the shock wave, decompression initiates, via a release adiabat (Osinski et al., 2012). Not all of the pressure-work applied to the target rocks is recoverable, and the unrecovered work converts to waste heat. It is this waste heat that induces impact melting in target rock material. Greater peak shock pressures will result in greater abundances of impact melt.

Impact melt is described as superheated, which, unlike endogenic melt, far exceeds the liquidus of crustal rocks (>2000 °C) (O'Keefe and Ahrens, 1975, 1977; Pierazzo et al., 1997; Osinski et al., 2018). These superheated temperatures give the melt a very low viscosity, theoretically allowing it to flow with minimal strain and stress resistance. Unlike lava flows, impact melt collects 'cold' clastic material that is in rapid motion in the transient cavity during the excavation stage and early parts of the modification stage. The entrainment of clasts causes rapid cooling of the impact melt, reducing the temperature down to sub-liquidus temperatures, similar to the eruption temperatures of basaltic lava flows (~1200 °C) (Onorato et al., 1978). Initially, this would imply that little to no impact melt would escape over the crater rim. However, a planetary radar study by Neish et al., (2014) reported that small lunar craters with diameters ≤20 km have the longest crater exterior impact melt flows in relative to their size.

Products of impact melting have been documented in different impact structures on Earth. Impact melt products, or deposits, have been found within and around impact structures (Figure 1.5), sometimes hundreds of metres to thousands of kilometres from the point of impact. These impact melt deposits have been described as micron-sized droplets or particles of quenched, glassy material in clastic impact breccias, injections of melt into dyke-like systems cross-cutting the crater floor or central peak structure, tens of metres to kilometre thick impact melt sheets or isolated bodies, or as discrete glassy particles known as tektites (millimetres to centimetres in size) distributed regionally to globally. The concept on whether some impact melt deposits preserved in terrestrial impact structures were emplaced as a flow (similar to melt flows observed on the Moon and Mars) has been discussed by Osinski (2004) and Mader and Osinski (2018). Their work using petrographic analysis of impactites provided evidence that coalescent impact melt did flow during the formation of the Ries (Germany) and Mistastin impact structures (Newfoundland/Labrador, Canada). However, no fresh (uneroded or modified surfaces) impact melt flows have been documented on Earth. Impact melt deposits range from crystalline rocks to aphanitic, glassy rocks with macron and micron scale textures analogous to volcanic rocks. On the Moon, impact melt deposits are observed as thin veneers covering crater rims, melt ponds and melt flows (similar to terrestrial lava ponds and lakes) (Howard and Wilshire, 1975; Hawke and Head, 1977; Cintala and Grieve, 1998; Carter et al., 2012; Neish et al., 2014), and multiple generation impact melt-bearing breccias that were sampled during the Apollo missions (e.g., Simonds, 1975; Onorato et al., 1976; Spudis and Ryder, 1981).

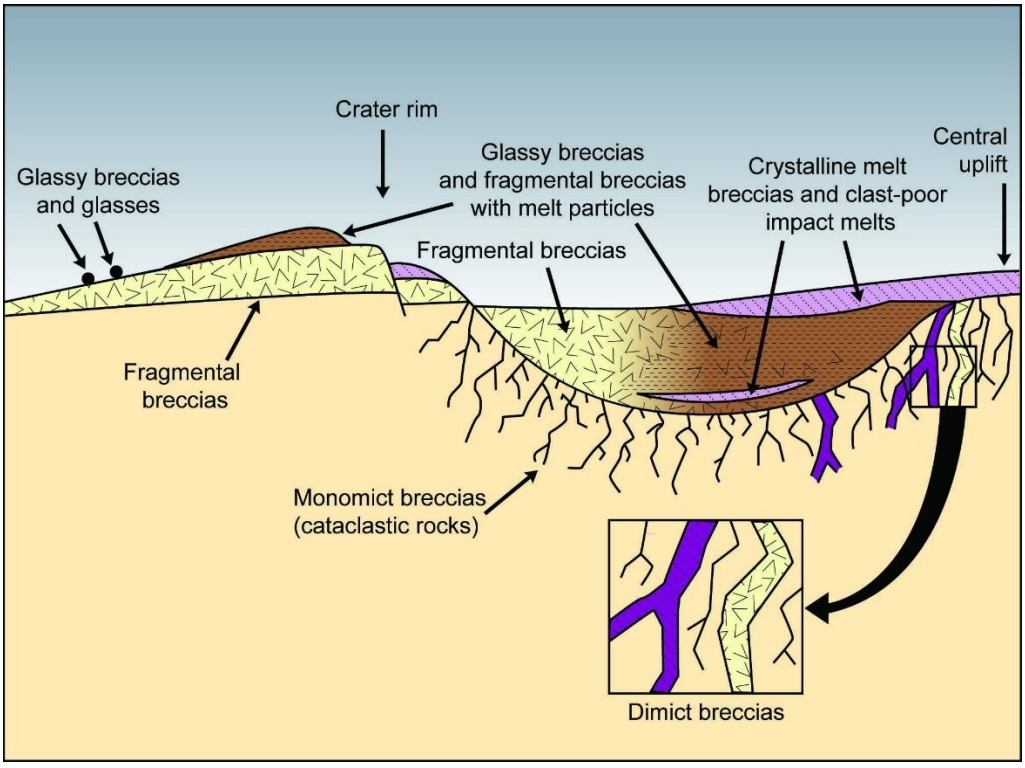

Figure 1.5. Different types of impact melt deposits found within and around a complex impact structure. The cross-section of the impact structure shows the locations of injected melt dykes, thick melt sheets, breccias and lenses, glassy breccias within the structure and over the rim, and glassy particles that have been ejected over the rim. Image credit: LPI (Christine Jilly).

1.4.2 Constraining the Temperature of Impact Melt

Due to active erosional processes, sediment deposition, vegetation cover, and plate tectonics, identifying fresh terrestrial impact melt flows and comparing their surface roughness to lunar impact melt flows is impossible. This is the reason why we turn to studying the surface roughness of terrestrial lava flows. Analyzing the surface roughness of terrestrial lava flows can grant us insight into melt emplacement mechanisms, but the intrinsic properties (temperature and

composition) and formation process of impact melt is significantly different compared to lava (Table 1.1). For this reason, we investigate the temperature conditions impact melt to complement our lava flow surface roughness analysis study.

The temperature of impact melt is still a much-debated topic, because, unlike lava flows, we are unable to observe the formation and cooling of impact melt in the field. The importance of constrain impact melt temperature arose in planetary science when scientists began to accept the vital role impact cratering played in the accretionary evolution of planetesimals and the modification of crustal material on Earth and the Moon during putative episodes of high impact flux (Ryder, 2002). By constraining impact melt temperature, we can acquire new information on the thermal conditions of impact cratering processes on Earth and across the solar system.

In past work, impact melt temperatures have been estimated from petrographic studies of diagnostic shock metamorphic features (Dence, 1971; Simonds, 1975), mineral end-member compositions and isotope chemistry (Hart and Davis, 1978; Lindsley and Andersen, 1983; Cherniak et al., 2007; Marion and Sylvester, 2010), computational and numerical models (Jaeger, 1968; Onorato et al., 1976, 1978; Asimow and Ghiorso, 1998), and geothermobarometers (e.g., Zr and Hf in rutile) (Hart and Davis, 1978; Kyte and Bohor, 1995; Cherniak et al., 2007). These techniques reported peak temperatures between 1700 °C – 2000 °C. It was not until a recent study by Timms et al., (2017b) where a more refined superheated impact melt temperature threshold was reported. Their work provided evidence for the highest rock formation temperature on Earth (>2370 °C), estimated from microstructure and crystallographic analysis of two zircon grains. These grains exhibit coronae of baddeleyite (monoclinic zirconia) found within a black impact glass sample from the Mistastin Lake impact structure, located in Newfoundland/Labrador, Canada. Their two temperature data values are based off the

crystallographic orientations of a monoclinic-zirconia that transformed from a parent cubic-zirconia, a zirconia polymorph that is only stable, at ambient pressures, in melt with temperatures >2370 °C (Cayron et al., 2010; Timms et al., 2017a). Their results exceed the temperature values reported by workers who utilized traditional geothermobarometers and numerical models, providing a more refined picture on the superheated nature of impact melt. For this reason, in this work we implement this methodology to find more data points confirming superheated temperatures in impact melt deposits.

Table 1.1. Physical properties of lava flows compared to impact melt flows.

Physical Property	Lava Flow	Impact Melt
Geologic Origin	Subaerial-subglacial volcanic eruptions	Decompression of shocked target rocks during hypervelocity impacts
Temperature	Sub-liquidis (700 °C – 1200 °C)	Can Superheated (1700 °C – >2370 °C)[1]
Composition	Determined from the chemistry of magmatic source and magmatic processes (e.g., fractional crystallization and crustal contamination)	Reflects the chemistry of wholescale melting of the target rocks
Clast Content	Rare occurrence	Clast abundance can vary from clast-poor (<5%) to clast-rich (>15%)

[1] Not all impact melt will be superheated. The superheated temperatures are dependent on the energy released during the impact event and the target rock materials

1.5 Applications of Terrestrial Analogues

A large focus of this thesis is demonstrating the importance of terrestrial analogue research, by studying the limitations that exist when implementing remote sensing data to infer melt emplacement mechanisms. Planetary analogue research played an important role during the Apollo mission era when NASA trained astronauts at various sites on Earth that share similarities

in landform surface morphology and terrain to the Moon (e.g., volcanic vents and lava flow-fields in Iceland, and Meteor/Barringer Crater in Arizona). Since then, the increased use of planetary analogue studies (e.g., Friedman Lentz et al., 1999; Keszthelyi et al., 2004; Léveillé and Datta, 2010; Hughes et al., 2015, 2019; Martinez-Frias et al., 2017), including the simulation of robotic platforms operating on Mars (Caudill et al., 2019; Osinski et al., 2019) has become a prime focus in planetary science. If we are to understand the emplacement of impact melt flows by studying the surface roughness of terrestrial lava flows and constraining the temperature of impact melt, we need to include sites that are analogous to planetary bodies.

In this thesis, we incorporate three field sites: two for the lava flow surface roughness portion of the study and one for the impact melt temperature portion of the study. For the surface roughness portion, we studied lava flows at Craters of the Moon (COTM) National Monument and Preserve in Idaho, USA, and lava flow types and lava facies at the 2014-2015 Holuhraun lava flow-field in Iceland. These two field sites were selected because they have extensive SAR coverage at decimetre- (L-band, $\lambda = 24$ cm) and centimetre-wavelengths (C-band, $\lambda = 5.6$ cm), and exhibit a diverse array of lava flow surface roughness's and morphologies. Previous studies have compared the volcano-tectonic setting and landforms of COTM to volcanic features on the Moon, Mars, and Venus (Greeley and Schultz, 1977; Hughes et al., 2019), and for Holuhraun, flood basalts on Mars and Jupiter's moon Io (Keszthelyi et al., 2004, 2006; Whelley et al., 2018; Rodriguez Sanchez-Vahamonde and Neish, 2021). For the impact melt temperature portion, we studied melt-bearing impactites from the Mistastin Lake impact structure located in Newfoundland/Labrador, Canada. Mistastin is regarded as an ideal analogue site for studying lunar impact cratering processes and impact melt formation since it hosts some of the most well-preserved impact melt deposits on Earth and it formed in a target rock suite comprising sodic-

anorthosite and granodiorite; rock types that are similar in composition to the anorthositic lunar crust. We also selected Mistastin because it is the impact structure where the hottest rock formation temperatures were previously discovered by Timms et al., 2017b.

1.6 Goals and Objectives

The motivation and aim of this thesis are to determine whether we can gain a better understanding of the emplacement mechanisms of lunar impact melts. We achieve this by analyzing the surface roughness of terrestrial lava flows with analogous surface roughness and morphologies, and by constraining the temperature of impact melt deposits using zircon and zirconia crystallographic orientation data. To address the aim of this thesis, we focus on the goals and objectives listed below.

1.6.1 Thesis Goals

1. To determine if SAR is a sufficient remote sensing technique for inferring the surface roughness, and in turn, emplacement mechanisms of terrestrial lava flows.
2. To determine if the temperature of Mistastin melt-bearing impactites can provide insight into the emplacement of lunar impact melt flows.

1.6.2 Thesis Objectives

a. Use qualitative and quantitative radar analysis to determine if lava flow types and facies can be differentiated to improve our interpretations of remote sensing analysis of lava flow-fields on planetary bodies.

b. Ground-truth SAR data with field measurements to understand the limitations of SAR analysis and interpretations.

c. Analyze the crystallography and microstructures of zircon and zirconia grains in Mistastin Lake impactite samples to search for evidence of impact melt superheated temperatures.

1.6.3 Thesis Outline

The work completed in this thesis has applications beyond seeking to understand the emplacement of lunar impact melt flows. Analyzing terrestrial lava flow surface roughness using SAR data and field observations is applicable to inferring how lava flows and lava flow-fields were erupted onto the surface of planetary bodies such as Mars and Venus. Constraining the temperature of impact melt can greatly improve our understanding of impact cratering processes on all rocky bodies, not just limited to Earth and the Moon. The research conducted in this thesis is separated into four chapters after this section. Chapters 2 and 3 cover the SAR and ground-truthing analysis of lava flows at COTM (Chapter 2) and the Holuhraun lava flow-field (Chapter 3). Chapter 4 reports the results of our crystallographic orientation analysis of zircon and zirconia crystals that was used to constrain the temperature of impact melt deposits at the Mistastin Lake impact structure. In the final chapter (Chapter 5), we discuss the capabilities and limitations of using SAR analysis to differentiate lava flow types and lava facies, and how our impact melt temperature results could be applied to understanding lunar impact melt flow emplacement.

References

Asimow, P.D., and Ghiorso, M.S., 1998, Algorithmic modifications extending MELTS to calculate subsolidus phase relations: American Mineralogist, v. 83, p. 1127–1132.

Bonnefoy, L.E., Hamilton, C.W., Scheidt, S.P., Duhamel, S., Höskuldsson, Jónsdottir, I., Thordarson, T., and Münzer, U., 2019, Landscape evolution associated with the 2014–2015 Holuhraun eruption in Iceland: Journal of Volcanology and Geothermal Research, v. 387, p. 106652, doi:10.1016/j.jvolgeores.2019.07.019.

Bray, V.J. et al., 2010, New insight into lunar impact melt mobility from the LRO camera: Geophysical Research Letters, v. 37, p. 1–5, doi:10.1029/2010GL044666.

Campbell, B.A., 2012, High circular polarization ratios in radar scattering from geologic targets: Journal of Geophysical Research, v. 117, doi:10.1029/2012JE004061.

Campbell, B.A., 2002, Radar Remote Sensing of Planetary Surfaces: Cambridge University Press.

Campbell, B.A., Campbell, D.B., and DeVries, C.H., 1999, Surface processes in the Venus highlands: Results from analysis of Magellan and Arecibo data: Journal of Geophysical Research E: Planets, v. 104, p. 1897–1916, doi:10.1029/1998JE900022.

Campbell, B.A., Hawke, B.R., and Campbell, D.B., 2009a, Surface morphology of domes in the Marius Hills and Mons Rümker regions of the Moon from Earth-based radar data: Journal of Geophysical Research, v. 114, p. 1–10, doi:10.1029/2008JE003253.

Campbell, B.A., Hawke, B.R., Carter, L.M., and Ghent, R.R., 2009b, Rugged lava flows on the Moon revealed by Earth-based radar: Geophyiscal Research Letters, v. 36, p. 1–5,

doi:10.1029/2009GL041087.

Campbell, B.A., and Shepard, M.K., 1996, Lava flow surface roughness and depolarized radar scattering: Journal of Geophysical Research, v. 101, p. 18,941-18,951.

Carter, L.M., Campbell, D.B., and Campbell, B.A., 2006, Volcanic deposits in shield fields and highland regions on Venus : Surface properties from radar polarimetry: Journal of Geophysical Research, v. 111, doi:10.1029/2005JE002519.

Carter, L.M., Neish, C.D., Bussey, D.B.J., Spudis, P.D., Patterson, G.W., Cahill, J.T., and Raney, R.K., 2012, Initial observations of lunar impact melts and ejecta flows with the Mini-RF radar: Journal of Geophysical Research, v. 117, p. 1–13, doi:10.1029/2011JE003911.

Caudill, C.M. et al., 2019, Field and laboratory validation of remote rover operations Science Team findings: The CanMars Mars Sample Return analogue mission: Planetary and Space Science, v. 176, doi:10.1016/j.pss.2019.06.006.

Cayron, C., Douillard, T., Sibil, A., Fantozzi, G., and Sao-Jao, S., 2010, Reconstruction of the cubic and tetragonal parent grains from electron backscatter diffraction maps of monoclinic zirconia: Journal of the American Ceramic Society, v. 93, p. 2541–2544, doi:10.1111/j.1551-2916.2010.03894.x.

Cherniak, D.J., Manchester, J., and Watson, E.B., 2007, Zr and Hf diffusion in rutile: v. 261, p. 267–279, doi:10.1016/j.epsl.2007.06.027.

Cintala, M.J., and Grieve, R.A.., 1998, Scaling impact melting and crater dimensions: Implications for the lunar cratering record: Meteoritics & Planetary Science, v. 33, p. 889–912, doi:10.15713/ins.mmj.3.

Coppola, D., Barsotti, S., Cigolini, C., Laiolo, M., Pfeffer, M.A., and Ripepe, M., 2019, Monitoring the time-averaged discharge rates, volumes and emplacement style of large lava flows by using mirova system: The case of the 2014-2015 eruption at Holuhraun (Iceland): Annals of Geophysics, v. 62, doi:10.4401/ag-7749.

Day, J.M.D., and Moynier, F., 2014, Evaporative fractionation of volatile stable isotopes and their bearing on the origin of the Moon: Philosophical Transactions of the Royal Society A: Mathematical, Physical and Engineering Sciences, v. 372, doi:10.1098/rsta.2013.0259.

Dence, M.R., 1971, Impact Melts: Journal of Geophysical Research, v. 76, p. 5552–5565.

Dence, M.R., 1968, Shock zoning at Canadian craters: petrography and structural implications, *in* French, B.M. and Short, N.M. eds., In Shock Metamorphism of Natural Materials, Baltimore, MD, Mono Book Corp, p. 169–184.

Dence, M.R., 1965, The Extraterrestrial Origin of Canadian Craters: Annals of the New York Academy of Sciences, v. 123, p. 941–969, doi:10.1111/j.1749-6632.1965.tb20411.x.

Denevi, B.W. et al., 2012, Physical constraints on impact melt properties from Lunar Reconnaissance Orbiter Camera images: Icarus, v. 219, p. 665–675, doi:10.1016/j.icarus.2012.03.020.

Dumont, S. et al., 2018, Integration of SAR Data Into Monitoring of the 2014 – 2015 Holuhraun Eruption , Iceland : Contribution of the Icelandic Volcanoes Supersite and the FutureVolc Projects: Frontiers in Earth Science, v. 6, doi:10.3389/feart.2018.00231.

Duraiswami, R.A., Gadpallu, P., Shaikh, T.N., and Cardin, N., 2014, Pahoehoe-a'a transitions in the lava flow fields of the western Deccan Traps, India-implications for emplacement

dynamics, flood basalt architecture and volcanic stratigraphy: Journal of Asian Earth Sciences, v. 84, p. 146–166, doi:10.1016/j.jseaes.2013.08.025.

Eppler, D.T., Ehrlich, R., Nummedal, D., and Schultz, P.H., 1983, Sources of shape variation in lunar impact craters: Fourier shape analysis: Bulletin of the Geological Society of America, v. 94, p. 274–291, doi:10.1130/0016-7606(1983)94<274:SOSVIL>2.0.CO;2.

Farr, T. G., 1993. Radar interactions with geologic surfaces. In: Guide to Magellan Image Interpretation, JPL Publication, 93-24, 148.

Friedman Lentz, R.C., Taylor, G.J., and Treiman, A.H., 1999, Formation of a martian pyroxenite: A comparative study of the nakhlite meteorites and Theo's Flow: Meteoritics and Planetary Science, v. 34, p. 919–932, doi:10.1111/j.1945-5100.1999.tb01410.x.

Greeley, R., 1982, The Snake River Plain, Idaho: Representative of a new category of volcanism: Jounral of Geophysical Research, v. 87, p. 2705–2712.

Greeley, R., and Schultz, P.H., 1977, Possible planetary analogs to Snake River plain basalt features., *in* Volcanism of the Eastern Snake River Plain, Idaho: A Comparative Planetary Geology Guidebook, p. 233–251.

Grieve, R.A.F., and Cintala, M.J., 1981, A method for estimating the initial impact conditions of terrestrial cratering events, exemplified by its application to Brent crater, Ontario: Proc. Lunar Planet. Sci. Conf., v. 12, p. 1607–1621, http://marefateadyan.nashriyat.ir/node/150.

Grieve, R.A.F., and Cintala, M.J., 1992, An analysis of differential impact melt-crater scaling and implications for the terrestrial impact record: Meteoritics, v. 27, p. 526–538, doi:10.1111/j.1945-5100.1992.tb01074.x.

Grieve, R.A.F., Dence, M.R., and Robertson, P.B., 1977, Cratering processes: As interpreted from the occurrence of impact melts, *in* In Impact and Explosion Cratering: Planetary and terrestrial implications, p. 791–814.

Grieve, R.A.F., Robertson, P.B., and Dence, M.R., 1981, Constraints on the formation of ring impact structures, based on terrestrial data: Multi-ring Basins, Proceedings of the Lunar and Planetary Science Conference, v. 12, p. 37–57.

Griffiths, R.W., 2000, The Dynamics of Lava Flows: Annual Review of Fluid Mechanics, v. 32, p. 477–518, doi:10.1146/annurev.fluid.32.1.477.

Gudmundsson, M.T. et al., 2016, Gradual caldera collapse at Bárdarbunga volcano, Iceland, regulated by lateral magma outflow: Science, v. 353, p. aaf8988, doi:10.1126/science.aaf8988.sciencemag.org.

Gulick, S.P.S. et al., 2008, Importance of pre-impact crustal structure for the asymmetry of the Chicxulub impact crater: Nature Geoscience, v. 1, p. 131–135, doi:10.1038/ngeo103.

Hamilton, C.W., 2019, “Fill and Spill” Lava Flow Emplacement: Implications for Understanding Planetary Flood Basalt Eruptions. NASA Technical Memorandum: Marshall Space Flight Center Faculty Fellowship Program, p. 47-56.

Harmon, J.K., Arvidson, R.E., Guinness, E.A., Campbell, B.A., and Slade, M.A., 1999, Mars mapping with delay-Doppler radar: Journal of Geophysical Research-Planets, v. 104, p. 14065–14089, doi:Doi 10.1029/1998je900042.

Harmon, J.K., Nolan, M.C., Husmann, D.I., and Campbell, B. a., 2012, Arecibo radar imagery of Mars: The major volcanic provinces: Icarus, v. 220, p. 990–1030,

doi:10.1016/j.icarus.2012.06.030.

Harris, A.J.L., Rowland, S.K., Villeneuve, N., and Thordarson, T., 2017, Pāhoehoe, ʻaʻā, and block lava: an illustrated history of the nomenclature: Bulletin of Volcanology, v. 79, doi:10.1007/s00445-016-1075-7.

Hart, S.R., and Davis, K.E., 1978, Nickel Partitioning between Olivine and Silicate Melt: Earth and Planetary Science Letters, v. 40, p. 203–219, doi:https://doi.org/10.1016/0012-821X(78)90091-2.

Hawke, B.R., and Head, J.W., 1977, Impact Melt in Lunar Cratr Interiors: In Lunar and Planetary Science Conference, v. 8.

Hjartardóttir, Á.R., Einarsson, P., Gudmundsson, M.T., and Högnadóttir, T., 2016, Fracture movements and graben subsidence during the 2014 Bárdarbunga dike intrusion in Iceland: Journal of Volcanology and Geothermal Research, v. 310, p. 242–252, doi:10.1016/j.jvolgeores.2015.12.002.

Howard, K.A., and Wilshire, H.G., 1975, Flows of impact melt at lunar craters: U. S. Geological Survey, Journal of Research, v. 3, p. 237–251.

Hughes, S.S. et al., 2019, Basaltic Terrains in Idaho and Hawai'i as Planetary Analogs for Mars Geology and Astrobiology: Astrobiology, v. 19, p. 260–283, doi:10.1089/ast.2018.1847.

Hughes, S.S., Kobs Nawotniak, S.E., Sears, D.W.G., Garry, W.B., Haberle, C.W., Bleacher, J.E., Lim, D.S.S., and Heldmann, J.L., 2015, King's Bowl, Idaho – A Volcanic Analog For Fissure Eruptions, Pit Craters And Dike Injection Along Rima Hyginus, Moon, And Cyane Fossae, Mars: In Lunar and Planetary Science Conference, v. 46, p. 2846.

Hughes, S.S., Smith, R.P., Hackett, W.R., and Anderson, S.R., 1999, Mafic Volcanism and Environmental Geology of the Eastern Snake River Plain, Idaho: Guidebook to the Geology of Eastern Idaho, p. 143–168.

Hughes, S.S., Wetmore, P.H., and Casper, J.L., 2002, Evolution of Quaternary Tholeiitic Basalt Eruptive Centers on the Eastern Snake River Plain , Idaho: Idaho Geological Survey Bulletin, v. 30, p. 1–23.

Jaeger, J.C., 1968, Cooling and solidification of igneous rocks in basalts, *in* Hess, H.H. and Poldervaart, A. eds., The Poldervaart Treatise on Rocks of Basaltic Composition, New York, John Wiley, p. 503–533.

Kenkmann, T., Collins, G.S., and Wünnemann, K., 2012, The modification stage of crater formation, *in* Impact Cratering: Processes and Products, p. 60–75.

Keszthelyi, L., and Denlinger, R., 1996, The initial cooling of pahoehoe flow lobes: Bulletin of Volcanology, v. 58, p. 5–18.

Keszthelyi, L., Self, S., and Thordarson, T., 2006, Flood lavas on Earth, Io and Mars: Journal of the Geological Society, v. 163, p. 253–264, doi:10.1144/0016-764904-503.

Keszthelyi, L., Thordarson, T., McEwen, A., Haack, H., Guilbaud, M.N., Self, S., and Rossi, M.J., 2004, Icelandic analogs to Martian flood lavas: Geochemistry, Geophysics, Geosystems, v. 5, p. 1–32, doi:10.1029/2004GC000758.

Kilburn, C.R.J., 2000, Lava Flows and Flow Fields, *in* Encyclopedia of Volcanoes, p. 291–305.

Kolzenburg, S., Giordano, D., Thordarson, T., Höskuldsson, A., and Dingwell, D.B., 2017, The rheological evolution of the 2014/2015 eruption at Holuhraun, central Iceland: Bulletin of

Volcanology, v. 79, doi:10.1007/s00445-017-1128-6.

Kring, D.A., Kramer, G.Y., Collins, G.S., Potter, R.W.K., and Chandnani, M., 2016, Peak-ring structure and kinematics from a multi-disciplinary study of the Schrödinger impact basin: Nature Communications, v. 7, p. 13161.

Kyte, F.T., and Bohor, B.F., 1995, Nickel-rich magnesiowiistite in Cretaceous/Tertiary boundary spherules crystallized from ultramafic, refractory silicate liquids: Geochimica et Cosmochimica Acta, v. 59, p. 4967–4974, doi:10.1016/0016-7037(95)00343-6.

Lawrence, S.J. et al., 2013, LRO observations of morphology and surface roughness of volcanic cones and lobate lava flows in the Marius Hills: Journal of Geophysical Research E: Planets, v. 118, p. 615–634, doi:10.1002/jgre.20060.

Lee, J.-S., and Pottier, 2009, Polarimetric Radar Imaging: from basics to applications (B. J. Thompson, Ed.): New York, CRC Press Taylor & Francis Group, http://www.ghbook.ir/index.php?name=فرهنگ و رسانه های نوین&option=com_dbook&task=readonline&book_id=13650&page=73&chkhashk=ED9C9491B4&Itemid=218&lang=fa&tmpl=component.

Leeman, W.P., 1982, Evolved and hybrid lavas from the Snake River Plain, *in* Bonnichsen, B. and Breckenridge, R.M. eds., Cenozoic Geology of Idaho, Idaho Bureau of Mines and Geology, Bulletin 26, p. 193–202.

Leeman, W.P., Vitaliano, C.J., and Prinz, M., 1976, Evolved Lavas from the Snake River Plain: Contributions to Mineralogy and Petrology, v. 56, p. 35–60.

Lev, E., Hamilton, C.W., Voigt, J.R.C., Stadermann, A.C., Zhan, Y., and Neish, C.D.

Emplacement conditions of lunar impact melt flows: Icarus,.

Léveillé, R.J., and Datta, S., 2010, Lava tubes and basaltic caves as astrobiological targets on Earth and Mars: A review: Planetary and Space Science, v. 58, p. 592–598, doi:10.1016/j.pss.2009.06.004.

Lindsley, D.H., and Andersen, D.J., 1983, A Two-Pyroxene Thermometer: Journal of Geophysical Research, v. 88, p. 887–906.

MacDonald, G.A., 1953, Pahoehoe, Aa, and Blocky Lava: American Journal of Science, v. 251, p. 169–191, https://gsa.confex.com/gsa/2007AM/finalprogram/abstract_130670.htm.

Marchi, S., Black, B.A., Elkins-Tanton, L.T., and Bottke, W.F., 2016, Massive impact-induced release of carbon and sulfur gases in the early Earth's atmosphere: Earth and Planetary Science Letters, v. 449, p. 96–104, doi:10.1016/j.epsl.2016.05.032.

Marchi, S., Bottke, W.F., Bierhaus, M., Wuennemann, K., Morbidelli, A., and Kring, D.A., 2014, Widespread mixing and burial of Earth's Hadean crust by asteroid impacts: Nature, v. 511, p. 578–582, doi:10.1038/nature13539.

Marion, C.L., and Sylvester, P.J., 2010, Composition and heterogeneity of anorthositic impact melt at Mistastin Lake crater, Labrador: Planetary and Space Science, v. 58, p. 552–573, doi:10.1016/j.pss.2009.09.018.

Martinez-Frias, J., Mederos, E.M., and Lunar, R., 2017, The scientific ad educational significance of geoparks as planetary analogues: the example of Lanzarote and Chinijo Islands UNESCO Global Geopark: IUGS Episodes, v. 40, p. 343–347.

Melosh, H.J., 1989, Impact Cratering: A Geologic Process: Oxford University Press (Oxford

Monographs on Geology and Geophysics, No. 11), 253 p.

Melosh, H.J., 2012, The contact and compression stage of impact cratering, *in* Impact Cratering: Processes and Products, p. 32–42.

Morgan, G.A., Campbell, B.A., Campbell, D.B., and Hawke, B.R., 2016, Investigating the stratigraphy of Mare Imbrium flow emplacement with Earth-based radar: Journal of Geophysical Research, v. 121, p. 1498–1513, doi:10.1002/2016JE005041.Received.

Morgan, J. V., Warner, M.R., Collins, G.S., Melosh, H.J., and Christeson, G.L., 2000, Peak-ring formation in large impact craters: Geophysical constraints from Chicxulub: Earth and Planetary Science Letters, v. 183, p. 347–354, doi:10.1016/S0012-821X(00)00307-1.

Neish, C.D. et al., 2017, Terrestrial analogues for lunar impact melt flows: Icarus, v. 281, p. 73–89, doi:10.1016/j.icarus.2016.08.008.

Neish, C.D., Cannon, K.M., Tornabene, L.L., Flemming, R.L., Zanetti, M., and Pilles, E., 2021, Spectral properties of lunar impact melt deposits from Moon Mineralogy Mapper (M3) data: Icarus, v. 361, p. 114392, doi:10.1016/j.icarus.2021.114392.

Neish, C.D., and Carter, L.M., 2014, Planetary Radar, *in* Encyclopedia of the Solar System, p. 1133–1159.

Neish, C.D., Madden, J., Carter, L.M., Hawke, B.R., Giguere, T., Bray, V.J., Osinski, G.R., and Cahill, J.T.S., 2014, Global distribution of lunar impact melt flows: Icarus, v. 239, p. 105–117, doi:10.1016/j.icarus.2014.05.049.

O'Keefe, J.D., and Ahrens, 1977, Impact-induced energy partitioning, melting, and vapourization on terrestrial planets: Proc. Lunar Planet. Sci. Conf., v. 8, p. 3357–3374.

O’Keefe, J.D., and Ahrens, T.J., 1975, Shock effects from a large impact on the moon: Proc. Lunar Planet. Sci. Conf., v. 6, p. 2831–2844.

Öhman, T., Aittola, M., Korteniemi, J., Kostama, V.P., and Raitala, J., 2010, Polygonal impact craters in the solar system: Observations and implications, in Large Meteorite Impacts and Planetary Evolution IV: Geological Society of America Special Paper, v. 465, p. 51–65, doi:10.1130/2010.2465(04).

Onorato, P.I.K., Uhlmann, D.R., and Simonds, C.H., 1976, Heat flow in impact melts: Apollo 17 Station 6 Boulder and some applications to other breccias and xenolith laden melts: Proceedings of the Lunar Science Conference, v. 7, p. 2449–2467, http://www.ghbook.ir/index.php?name=فرهنگ و رسانه های نوین&option=com_dbook&task=readonline&book_id=13650&page=73&chkhashk=ED9C9491B4&Itemid=218&lang=fa&tmpl=component.

Onorato, P.I.K., Uhlmann, D.R., and Simonds, C.H., 1978, The Thermal History of the Manicouagan Impact Melt Sheet , Quebec: Journal of Geophysical Research, v. 83, p. 2789–2798, doi:https://doi.org/10.1029/JB083iB06p02789.

Osinski, G.R. et al., 2019, The CanMars Mars Sample Return analogue mission: Planetary and Space Science, v. 166, p. 110–130, doi:10.1016/j.pss.2018.07.011.

Osinski, G.R., Grieve, R.A.F., Bleacher, J.E., Neish, C.D., Pilles, E.A., and Tornabene, L.L., 2018, Igneous rocks formed by hypervelocity impact: Journal of Volcanology and Geothermal Research, v. 353, p. 25–54, doi:10.1016/j.jvolgeores.2018.01.015.

Osinski, G.R., Grieve, R.A.., Collins, G., Marion, C., and Sylvester, P., 2008, The Effect of Target Lithology on the Products of Impact Melting: Meteoritics & Planetary Science, v.

43, p. 1939–1954, http://adsabs.harvard.edu/abs/2007bget.conf...93O.

Osinski, G.R., Grieve, R.A.F., Marion, C.L., and Chanou, A., 2012, Impact Melting, *in* Osinski, G.R. and Pierazzo, E. eds., Impact Cratering: Processes and Products, Wiley-Blackwell, p. 125–145, doi:10.1002/9781118447307.ch9.

Peterson, D.W., and Tilling, R.I., 1980, Transition of Basaltic Lava From Pahoehoe to Aa, Kilauea Volcano, Hawaii: Field Observations and Key Factors: Jounral of Volcanology and Geothermal Researc, v. 7, p. 271–293.

Pierazzo, E., Vickery, A.M., and Melosh, H.J., 1997, A Re-evaluation of Impact Melt Production: Icarus, v. 127, p. 408–423.

Putirka, K.D., Kuntz, M. a., Unruh, D.M., and Vaid, N., 2009, Magma evolution and ascent at the craters of the moon and neighboring volcanic fields, Southern Idaho, USA: Implications for the evolution of polygenetic and monogenetic volcanic fields: Journal of Petrology, v. 50, p. 1639–1665, doi:10.1093/petrology/egp045.

Robert, B., Harris, A., Gurioli, L., Médard, E., Sehlke, A., and Whittington, A., 2014, Textural and rheological evolution of basalt flowing down a lava channel: Bulletin of Volcanology, v. 76, p. 1–21, doi:10.1007/s00445-014-0824-8.

Rodriguez Sanchez-Vahamonde, C., and Neish, C., 2021, The Surface Texture of Martian Lava Flows as Inferred from Their Decimeter- and Meter-scale Roughness: The Planetary Science Journal, v. 2, doi:https://doi.org/10.3847/PSJ/abbfac.

Ryder, G., 2002, Mass flux in the ancient Earth-Moon system and benign implications for the origin of life on Earth: Journal of Geophysical Research E: Planets, v. 107,

doi:10.1029/2001je001583.

Sehlke, A., Whittington, A., Robert, B., Harris, A., Gurioli, L., Médard, E., and Sehlke, A., 2014, Pahoehoe to áá transition of Hawaiian lavas: An experimental study: Bulletin of Volcanology, v. 76, doi:10.1007/s00445-014-0876-9.

Shepard, M.K., Campbell, B.A., Bulmer, M.H., Farr, T.G., Gaddis, L.R., and Plaut, J.J., 2001, The roughness of natural terrain: A planetary and remote sensing perspective: Journal of Geophysical Research E: Planets, v. 106, p. 32777–32795, doi:10.1029/2000JE001429.

Sigmundsson, F. et al., 2015, Segmented lateral dyke growth in a rifting event at Bárðarbunga volcanic system, Iceland: Nature, v. 517, p. 191–195, doi:10.1038/nature14111.

Simonds, C.H., 1975, Thermal regimes in impact melts and the petrology of the Apollo 17 Station 6 boulder, *in* 6th Lunar and Planetary Science Conference, p. 641–672.

Solana, M.C., Kilburn, C.R.J., Rodriguez Badiola, E., and Aparicio, A., 2004, Fast emplacement of extensive pahoehoe flow-fields: The case of the 1736 flows from Monta??a de las Nueces, Lanzarote: Journal of Volcanology and Geothermal Research, v. 132, p. 189–207, doi:10.1016/S0377-0273(03)00345-7.

Spudis, P.D., and Ryder, G., 1981, Apollo 17 impact melts and their relation to the Serenitatis basin, *in* In Multi-ring basins: Formation and evolution, p. 133–148.

Stoffler, D., Gault, D.E., Wedekind, J., and Polkowski, G., 1975, Experimental Hypervelocity Impact Into Quartz Sand: Distribution and Shock Metamorphism of Ejecta: Journal of Geophysical Research, v. 80, p. 4062–4077.

Stopar, J.D., Hawke, B.R., Robinson, M.S., Denevi, B.W., Giguere, T.A., and Koeber, S.D.,

2014, Occurrence and mechanisms of impact melt emplacement at small lunar craters: Icarus, v. 243, p. 337–357, http://dx.doi.org/10.1016/j.icarus.2014.08.011.

Swanson, D.A., 1973, Pahoehoe flows from the 1969-1971 mauna ulu eruption, kilauea volcano, Hawaii: Geological Society of America Bulletin, v. 84, p. 615–626, doi:10.1130/0016-7606(1973)84<615:PFFTMU>2.0.CO;2.

Thordarson, T., and Larsen, G., 2007, Volcanism in Iceland in historical time: Volcano types, eruption styles and eruptive history: Journal of Geodynamics, v. 43, p. 118–152, doi:10.1016/j.jog.2006.09.005.

Timms, N.E., Erickson, T.M., Pearce, M.A., Cavosie, A.J., Schmieder, M., Tohver, E., Reddy, S.M., Zanetti, M.R., Nemchin, A.A., and Wittman, A., 2017a, A pressure-temperature phase diagram for zircon at extreme conditions: Earth-Science Reviews, v. 165, p. 185–202, doi:10.1016/j.earscirev.2016.12.008.

Timms, N.E., Erickson, T.M., Zanetti, M.R., Pearce, M.A., Cayron, C., Cavosie, A.J., Reddy, S.M., Wittmann, A., and Carpenter, P.K., 2017b, Cubic zirconia in >2370◦C impact melt records Earth's hottest crust: Earth and Planetary Science Letters, v. 477, p. 52–58, doi:10.1016/j.epsl.2017.08.012.

Tolometti, G.D., Neish, C.D., Osinski, G.R., Hughes, S.S., and Nawotniak, S.E.K., 2020, Interpretations of lava flow properties from radar remote sensing data: Planetary and Space Science, v. 190, p. 104991, doi:https://doi.org/10.1016/j.pss.2020.104991.

Ulrich, G.E., 1987, SP Mountain cinder cone and lava flow , northern Arizona: Centennial Field Guide, v. 2, p. 385–388.

Whelley, P. et al., 2018, Analogs of Ice and Fire: Conducting Fieldwork in the Icelandic Highlands to Inform Volcanic Interpretations on Mars and Instrument Development for Europa, *in* American Geophysical Union, Fall Meeting,.

Chapter 2: Interpretations of Lava Flow Properties from Radar Remote Sensing Data[1]

2.1 Introduction

The lava properties and emplacement processes of volcanic features on Earth and other planetary bodies are often inferred from their surface roughness (Griffiths and Fink, 1992; Crisp and Baloga, 1994; Keszthelyi et al., 2004; Guilbaud et al., 2005; Khan et al., 2007; Campbell et al., 2009; Harmon et al., 2012; Lawrence et al., 2013; Neish et al., 2017). The scale of surface roughness can vary on a single lava flow and reflect multiple factors that may have influenced it during an eruption (MacDonald, 1953; Gregg and Fink, 1995, 1996, Sehlke et al., 2014). Thus, understanding the formation of surface roughness features at different scales can help justify interpretations about lava properties and emplacement processes.

For example, centimetre scale roughness (e.g., crescent ripples and folds) is produced when the lava encounters small topographic obstacles and when a (plastic) crust of a few mm thickness is deformed during cooling. Smooth pāhoehoe surfaces typically form from lavas with low silica content and low viscosity, erupted at temperatures near the liquidus of basalt (1200°C) (Tilley and Thompson, 1970). Changes in roughness at the decimetre scale (e.g., clinker ʻaʻā fragments) require extensive disruption of the lava flow crust. In contrast to smooth pāhoehoe, rough ʻaʻā forms when lava is ruptured due to increasing viscosity or rate of shear as the lava cools and degasses (Peterson and Tilling, 1980; Sehlke et al., 2014). Highly siliceous blocky lava flows (>55 wt% SiO_2) disrupt their surfaces due to creep fracturing, which typically form decimetre to metre-sized polyhedral blocks with smooth faces (MacDonald, 1953). However,

[1] Tolometti G. D., Neish C. D., Osinski G. R., Hughes S. S., Nawotniak S. E., 2020. Interpretations of Lava Flow Properties from Radar Remote Sensing Data. *Planetary and Space Science*, 190. 104991.

viscous rupturing and creep fracturing are not the only mechanisms to produce rough flows. Rough lava can also form through the mechanical fracturing of a solidified pāhoehoe crust, producing a class of lava flows known as transitional lava flows (Keszthelyi *et al.*, 2004; Guilbaud *et al.*, 2005). These flows often exhibit "rubbly" or "slabby" textures, with pāhoehoe crust fragments ranging from tens of centimetres to metres in size (Keszthelyi et al., 2004; Guilbaud et al., 2005; Hamilton et al., 2013; Robert et al., 2014; Neish et al., 2017). Transitional pāhoehoe lava flows studied in Iceland (Keszthelyi et al., 2000, 2004; Guilbaud et al., 2005), Idaho (Neish et al., 2017), Hawaii (Peterson and Tilling, 1980), and India (Duraiswami et al., 2014) exhibit surfaces with metre-sized slabs of pāhoehoe crust, fractured by lava flow inflation (Keszthelyi et al., 2004). Rubbly pāhoehoe textures can form in sequence after slabby pāhoehoe if the crust is extensively fragmented. In some cases where lava flows have been degraded and/or buried, rubbly pāhoehoe has been falsely interpreted as ʻaʻā (Bondre et al., 2004; Duraiswami et al., 2008a). Their similarities in brecciated surfaces and roughness scale can make them almost indistinguishable when eroded. Table 2.1 summarizes the surface roughness and morphologies of lava flows documented in the field on Earth.

When field observations are not available, radar data can provide important information about lava surface roughness at different scales. This is especially relevant for other planetary bodies where ground truth is limited or non-existent. Radar data has been used to distinguish and quantify the surface roughness of lava flows on planetary surfaces to interpret their lava properties and emplacement processes. For example, Earth-based radar data has been used to map and analyse the distribution of lava flows on the lunar surface. Morgan et al. (2016) and other workers (Campbell et al., 2007, 2009a) used Arecibo P-band (70-cm) radar to penetrate through the lunar regolith and map the lava flow boundaries in lunar mare using same-sense

circularly polarized radar data. In Figure 2.1, circular polarization ratios (CPR) calculated from returned Arecibo P-band radar data show the variations in meter-scale lava flow surface roughness in the Imbrium Mare. Lava flows with moderate-high CPR (~0.5) indicate rough surfaces while lava flows with low CPR (< 0.5) indicate smooth surfaces. These values can be compared to radar data of terrestrial lava flows, to aid in the interpretation of the properties of lunar lava flows. Thus, understanding the surface morphology and roughness of terrestrial lava flows with similar CPR values can improve our inferences on the volcanic surface features on planetary surfaces, and refine the interpretations made using remote sensing methods.

Depending on the remote sensing method used, the surface roughness values can vary, which will ultimately influence interpretations about lava properties and emplacement processes. On Earth, we can quantify surface roughness using a suite of in-situ, airborne, and satellite remote sensing instruments. For example, remote sensing methods such as LiDAR have been used to distinguish and quantify surface roughness of lava flows at different resolutions and scales (Glenn et al., 2006; Glaze and Baloga, 2007; Rosenburg et al., 2011; Whelley et al., 2014, 2017). However, for studying other planetary surfaces, radar is the only remote sensing technique capable of quantifying roughness at the decimetre scale. Decimetre scale surface features are too small to observe with presently available visible imagery; the highest resolution cameras provide data at 0.5-1 m resolution (Chin et al., 2007; McEwen et al., 2007). Thus, in order to infer the decimetre scale surface roughness of lava flows on other planetary bodies (Campbell et al., 2009, 2010; Carter et al., 2012; Harmon et al., 2012; Neish et al., 2014, 2017), we need to use radar datasets.

Table 2.1. Descriptions and surface roughness scale of lava flow morphologies on Earth are summarized from measurements of crustal material on their surfaces and notes taken in the field. [a]Kuntz *et al.* (2007), [b]Guilbaud *et al.* (2005) and Duraiswami *et al.* (2008), [c]Keszthelyi *et al.* (2000), [d]Sehlke *et al.* (2014). For more field descriptions and detailed discussions on the lava flows surface morphologies refer to Kilburn (2000) and Harris *et al.* (2017).

Lava Flow Morphology	Description	Surface Roughness Scale
Smooth Pāhoehoe	A smooth lava flow with a thin, glassy crust that may collapse due to inflation or strength instability; cm-scale ropey textures form on the surface while the flow is in motion.	Lava flow appears smooth at km- and m-scales. Small features such as ropey and spiney textures make the lava appear rougher at cm- and mm-scales.
Hummocky Pāhoehoe	Undulating pāhoehoe lava comprising lava toes, small lobes, and tumuli. The surface morphology resembles a bulbous shape where lava has risen by a few m to tens of m and connected by steep troughs. Lava is also referred as a 'bulbous' pāhoehoe flow.[a]	Lava flow appears smooth at km-scales. Hummocks make the lava flow relatively rough at m-scales while the pāhoehoe textures described above make it rough at cm-scales.
Rubbly Pāhoehoe	A lava flow with a preserved flow base and brecciated pāhoehoe crust.[b]. The surface becomes fractured and brecciated due to disruption from syn- or post-emplacement processes. Common in flow fields with linear volcanic vent systems.[c]	Lava flow appears roughest at m and dm-scales.
Slabby Pāhoehoe	Metre to kilometre-sized slabs of pāhoehoe crust, which were fractured, tilted, and carried by an advancing or draining underlying lava.	Rough at m- and km-scales and smooth at cm-scales (notwithstanding ropey and spiney textures described above).
ʻAʻā	Lava flow with a rough clinkered surface formed by the development of a yield strength and increase in viscosity.[d] Interior becomes viscously torn as it advances further from its source.	Similar to rubbly pāhoehoe surfaces.
Blocky to High Relief ʻaʻā (Block-ʻaʻā)	Rough and jagged with occasional vesicular (>70%) froth, and weakly conchoidal fractures.	Conchoidal fractures and rough jagged surface appear rough at m- to dm-scale.
Blocky	Lava flows covered with a broken carapace of decimetre to metre-sized fragments with smooth faces and dihedral angles.	Lava is rough at dm- and m-scales. Block surfaces smooth at cm-scales.

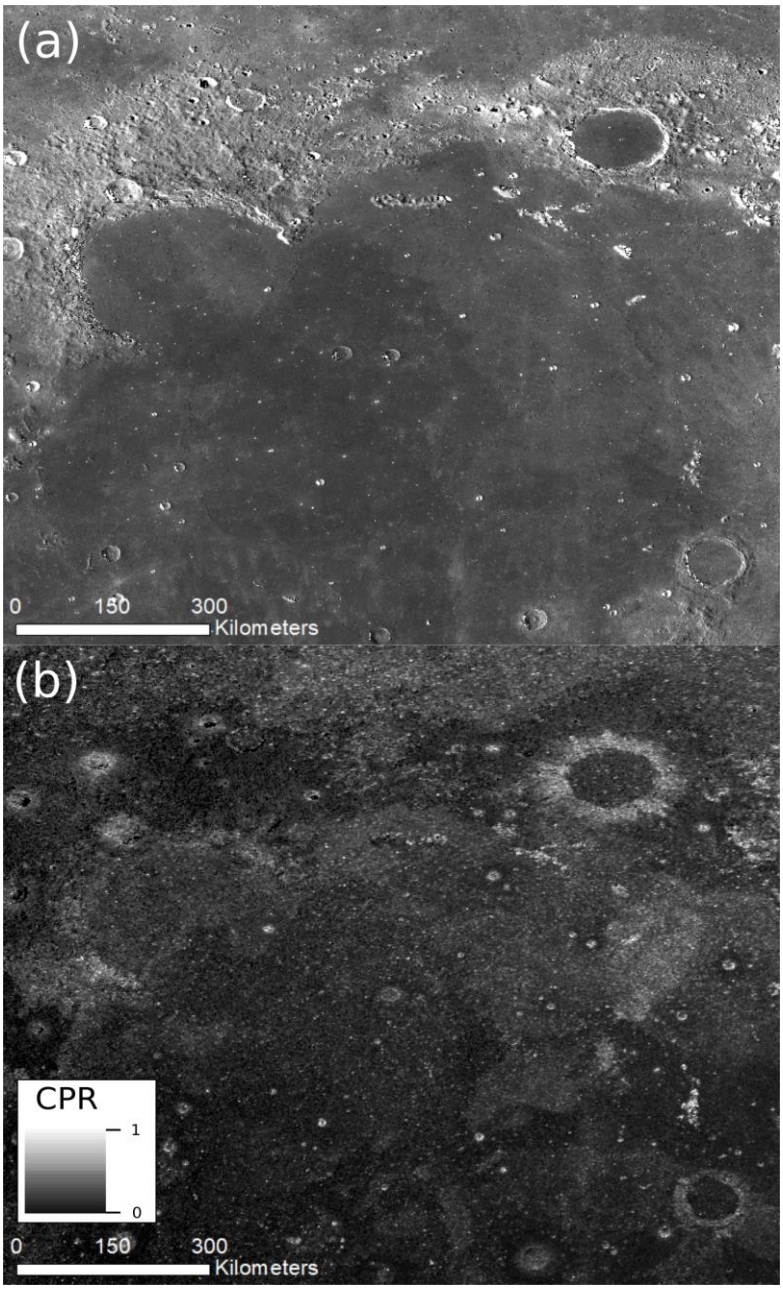

Figure 2.1. Imbrium Mare lava flows revealed using Earth-based radar: (a) Lunar Reconnaissance Orbiter Wide-Angle Camera mosaic (100m/pixel) of the Imbrium Mare. (b) Arecibo P-Band radar data (70 cm wavelength, 200 m/pixel) of the same region. The lava flows in the mare have large variation in their CPR values, which suggests a range of surface textures. Flows with high CPR are rough, while those with low CPR are smooth.

Generalized relationships between surface roughness, composition, petrographic textures, and crystallinity in lava fields have been discussed for flows located in areas such as Iceland (Keszthelyi et al., 2000, 2004; Guilbaud et al., 2005), Hawaii (Peterson and Tilling, 1980; Cashman et al., 1999; Robert et al., 2014; Sehlke et al., 2014), and Guatemala (Soldati et al., 2016). These studies suggest that increasing micro-crystallinity and decreasing temperature with distance from the vent cause increases in viscosity and yield strength, which result in increased surface roughness at the centimeter-metre scale. On the other hand, transitional lava flow surface roughness formed by syn- or post emplacement processes such as changes in effusion rates, pāhoehoe crust inflation, and topographic variability, can produce similar surface roughness for very different reasons. This may lead to misinterpretations about the style of volcanism in regions where there is little or non-existent ground truth and where we must rely on remote sensing data such as radar.

Our chosen field site, Craters of the Moon (COTM) National Monument and Preserve in Idaho, is a 1650 km^2 polygenetic lava field with cinder and spatter cones, non-eruptive fissures, lava tubes, and basaltic lava flows of varying compositions emplaced from 15–2 ka (Leeman et al., 1976; Greeley and King, 1977; Kuntz et al., 1982, 1992; Kuntz, 1989; Hughes et al., 2002) (Figure 2.2). The lava flows display blocky, block-‘a‘ā, ‘a‘ā, and rubbly, slabby, hummocky and smooth pāhoehoe morphologies (Kuntz, 1989; Kuntz et al., 2007). The compositions of the individual lava flows vary with respect to SiO_2, MgO, FeO, TiO_2, P_2O_5, and Th (e.g. SiO_2 ranges from 45 wt% to 65 wt%) (Reid, 1995; Hughes et al., 1999; Putirka et al., 2009) with blocky and block-‘a‘ā lava flows exhibiting SiO_2 content >55 wt% (Stout et al., 1994). Research conducted by previous workers has proposed that fractional crystallization (Leeman et al., 1976; Hughes et al., 2002), country rock assimilation (Leeman, 1982; Kuntz et al., 1986), and/or evolved magma

reservoirs (Kuntz et al., 1982; Kuntz et al., 1986) are responsible for the different compositions. Hughes et al. (2016) described some of the northernmost lava flows as chemically evolved latites (aka trachydacite) based on MgO and TiO_2 contents and suggested that their compositions reflect hybridized crystallization due to crustal contamination, magma mixing, and long-term fractionation in crustal magma reservoirs. Extensive work on the geochemistry of the lava flows at COTM has provided a general understanding of their magmatic origin and processes, but to date, little work has focused on the diversity of their surface morphologies and roughness.

In this work, we investigate the surface roughness of lava flows in the northernmost part of COTM, to further our understanding of how surface roughness properties correlate to the petrography and geochemistry of a lava flow, and whether these are distinguishable using radar remote sensing data. We then use this information to discuss what interpretations can be made if we are restricted to using radar data to infer the lava properties and emplacement styles of lava flows on other planetary bodies.

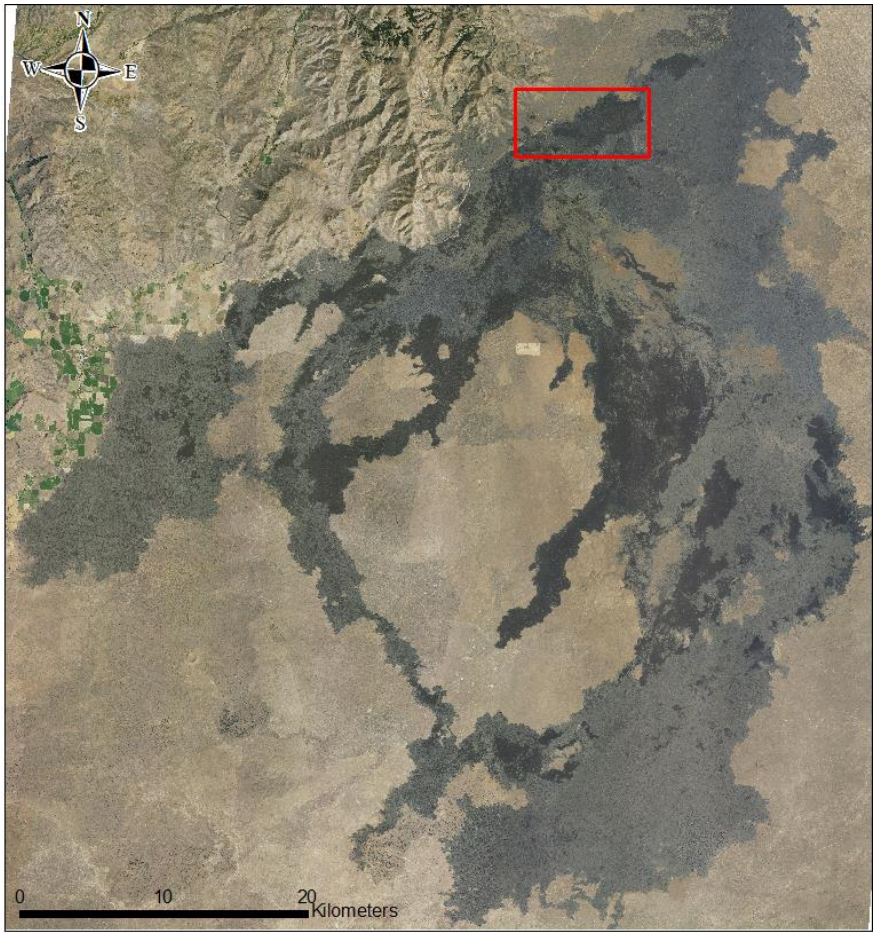

Figure 2.2. Overview of COTM. National Agriculture Imagery Program (NAIP) data of COTM acquired in 2015. The red box outlines the field area for this study. Field site coordinates: 43.2058° N, 113.5002° W (see Figure 2.3).

2.2 Methods

2.2.1 Field sampling

Field work was conducted in August 2016 and 2017 at COTM. A total of twenty-six samples were collected from six lava flows: Big Craters (Rubbly pāhoehoe), Blue Dragon (Smooth pāhoehoe), Devils Orchard (Blocky), Highway (Block-ʻaʻā), North Crater (Hummocky

pāhoehoe), and Serrate flow (Blocky) (Figure 2.3). Due to accessibility (many of the lava flows were difficult to traverse on foot), the majority of the sampling was conducted 10 m to ~100 m from the lava flow margins; a small number of samples were collected closer to the flow center where the terrain allowed for easier access. As many samples as possible were collected in each studied lava flow. This was done to look for any variations in the petrographic and geochemical data. For the petrography and geochemistry of the samples to best represent the interior of the lava flow, sampling was restricted to >5 cm below the lava crust. This is important because the geochemistry and petrography of the lava flow crust only represents the rapid cooling of the lava on the surface and not the interior that remained molten for a longer period. Comparing the geochemistry and petrography of the crust to the remote sensing data would not provide insight into how the lava properties of the lava flow influenced its surface morphology and roughness.

2.2.2 Petrographic and geochemical analyses

Polished thin section slides were prepared from all twenty-six samples. Mineral mode (%), crystallinity (%), volcanic glass (%), vesicularity (%), and mineral size (mm-cm) were estimated for each sample by point counting on a 1000-point grid in each of the polished thin sections. Backscattered electron (BSE) images were used to study the microlites in the volcanic glass, as well as to record petrographic textures that were not observable with optical microscopy. Microlite compositions were determined by electron probe micro-analysis (EPMA) (15 kV, 20 nA, 5 µm spot size, standards: Albite – Si, Al, and Na; Rutile – Ti; Fayalite – Fe; SanCarlos – Mg; Rhodonite – Mn; Anorthite – Ca; Orthoclase – K, Celesite – Sr; Barite – Ba) using the JEOL JXA-8530F field-emission electron microprobe at the University of Western Ontario.

All samples were prepared for X-ray fluorescence (XRF) analysis to obtain bulk geochemical data. Samples were prepared by removing surface weathering using a rock saw and then powdered using a steel rock crusher and agate mill. During the powdering stage, the rock crusher and agate mill were cleaned between each sample using ethanol to mitigate contamination. The powdered samples were heated in a Katanax K2 Prime Fusion Machine with lithium metaborate to create fused glass discs, which were analyzed using the XRF PANalytical PW-2400 model at the University of Western Ontario to obtain major element geochemical data (SiO_2, TiO_2, Al_2O_3, Fe_2O_3, MnO, MgO, CaO, Na_2O, K_2O, and P_2O_5).

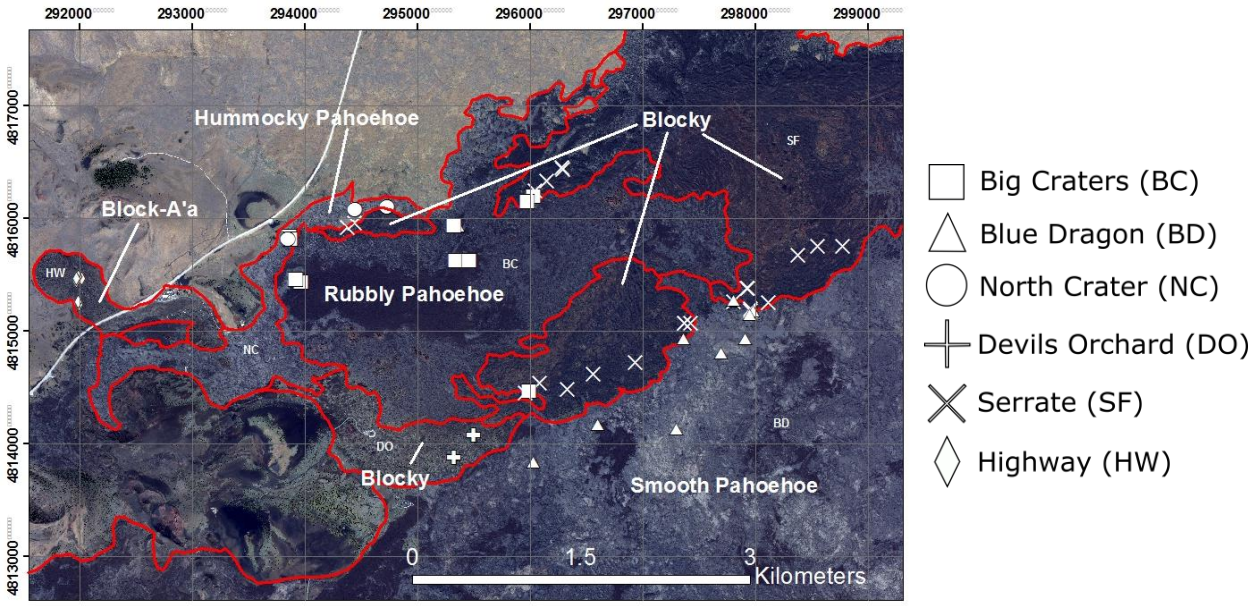

Figure 2.3. Field site at COTM. Symbols mark the locations of the 26 samples studied in this work. Red lines mark the lava flow margins from the Kuntz et al. (1989, 2007) geological map of COTM. The image was taken from NAIP data acquired in 2015. Labels of the lava flows provide a generalized surface roughness description (some flows show localized changes in surface roughness).

2.2.3 Surface roughness determination using radar datasets

To differentiate the surface roughness of lava flows remotely, we used previously processed Airborne Synthetic Aperture Radar (AIRSAR) L-Band (24 cm wavelength, 10 m/pixel resolution) datasets (Evans et al., 1986; Khan et al., 2007), which are sensitive to surface roughness at the decimetre scale (Carter et al., 2011; Neish and Carter, 2014). A low-flying aircraft collected the AIRSAR L-Band data in March 2003. We utilized CPR maps described in Neish et al. (2017) to quantify the surface roughness of the lava flows. A CPR value represents the ratio between the returned radar signal with the same circular polarization as transmitted (SC) to the returned signal with the opposite circular polarization (OC). Smooth surfaces produce single bounce backscatter, which flips the polarization of the radar signal returning more data in the opposite polarization. Rougher surfaces produce multiple-bounce backscatter returning an approximately equal number of OC and SC returns. Thus, low CPR (<0.5) indicates smooth surfaces, while moderate to high CPR (0.5-1) indicates rough surfaces. CPR values can exceed unity (>1) when double-bounce radar backscattering occurs on surfaces with natural corner reflectors, rock edges, and cracks (Campbell, 2012). Pāhoehoe flows typically have low (<0.5) CPR, ʻaʻā and transitional lava flows typically have moderate to high (0.5-<1.0) CPR, and blocky flows typically have CPR greater than one (Neish et al., 2017).

Radar signals also have the ability to penetrate the surface and scatter off subsurface interfaces and materials such as voids or clasts (Carter et al., 2011; Neish and Carter, 2014). To determine if the radar scattering was produced by surface scattering or subsurface interfaces, the degree of linear polarization (DLP) was also calculated. The DLP provides subsurface scattering information, which tells us about material and/or lithological boundaries beneath the surface. When the circular polarized radar signal penetrates the surface it changes to an elliptical signal,

adding a linear component and therefore increasing the DLP. For example, a lithological contact is dominated by a quasi-specular subsurface scattering that returns high DLP, while buried boulders are dominated by diffuse subsurface scattering that returns moderate-high DLP (Carter et al., 2004, 2006, 2011). A combination of CPR and DLP is useful to understand the structure of the surface and subsurface of planetary surfaces. For example, low CP and high DLP indicates a smooth surface with a subsurface interface, while high CPR and low DLP indicates a rough surface with no subsurface interfaces (Neish and Carter, 2014).

The AIRSAR data has been made available in compressed Stokes matrix format, so we used the Stokes matrix (W) to calculate the DLP (Equation 2.1) (Campbell, 2002).

$$DLP = |W_{12}|/W_{11} \quad \text{Equation 2.1}$$

To compare the radar data to the geochemical and petrographic results, we extracted mean CPR and DLP values from areas of the lava flows where samples were collected. To ensure the extracted mean CPR and DLP values are representative of the general surface roughness of the region, the resultant shape files covered multiple sample locations (not individual points). In addition, they did not include areas where vegetation and volcanic ash deposits were present. We then used the zonal statistics tool in ArcGIS to measure mean CPR and DLP and standard deviation for each representative area.

2.3 Results

The six studied lava flows at COTM and their surface morphologies and roughness are shown in Figure 2.4. The descriptions of each lava flow are based on field observations; while

lava flow morphologies vary somewhat across the flow, we are specifically interested in the dominant characteristics that are associated with the samples we collected. Blue Dragon is a smooth pāhoehoe lava flow with localized areas of inflated pāhoehoe crust and collapsed lava tube ceilings (Figure 2.4a). The lava flow name derives from its unique blue, titanium magnetite-rich crust (Faye and Miller, 1973). Devils Orchard (Figure 2.4b) and Serrate flows (Figure 2.4c) are blocky latite lavas (Kuntz, 1989; Kuntz et al., 2007), composed of decimetre to metre-sized polyhedral blocks with smooth faces and dihedral angles. North Crater is a hummocky pāhoehoe lava flow with a faint blue colour similar to Blue Dragon (Figure 2.4d). Big Craters is a transitional lava flow with a rubbly pāhoehoe surface (Figure 2.4e). The rubbly surface is comprised of centimetre to decimetre-sized fragments of pāhoehoe crust, with no evidence of viscous disruption. Highway Flow, a latite, is described by Kuntz et al. (1988, 2007) as a blocky-ʻaʻā morphology, which is consistent with our field observations describing the surface as very jagged, sharp, and vesicular with conchoidal fracture features (Figure 2.4f).

2.3.1 Geochemical analysis

We categorized the lithology of each lava flow using the standard TAS volcanic classification ($Na_2O + K_2O$ vs. SiO_2) scheme (Figure 2.5). This shows that each lava flow falls into one of two major categories with a few outliers: (1) basalt, trachybasalt, and basaltic trachyandesite, and (2) trachyandesite, and trachyte/trachydacite. The basalt and trachybasalt categories include the majority of the smooth, hummocky, and rubbly pāhoehoe samples, although a few rubbly pāhoehoe samples plot as basaltic trachyandesite. Blocky and block-ʻaʻā lava flows have higher SiO_2 (>55 wt%) and alkali contents (7–10 wt%), classifying the lava flows as trachyandesite and trachyte/trachydacite. A few blocky samples plot as basaltic

trachyandesite; these samples are randomly located in Devils Orchard and Serrate flows. Blocky and block-ʻaʻā flows are evolved, with relatively high SiO_2 (55–65 wt%), Na_2O (3.7–5.1 wt%) and K_2O (4.0–4.9 wt%) contents, and low TiO_2 (0.6–1.5 wt%), Fe_2O_3 (8.0–15.5 wt%), CaO (2.8–4.9 wt%), and MgO (0.2–1.3 wt%) (Figure 2.6). Primitive smooth, hummocky, and rubbly pāhoehoe flows are low in SiO_2 (48–52 wt%), Na_2O (2.75–4.3 wt%) and K_2O (1.9–2.3 wt%), and high in TiO_2 (2.5–3.05 wt%), Fe_2O_3 (15–17.7 wt%), CaO (6.3–7.2 wt%), and MgO (2.3–4.2 wt%) (Figure 2.6). Despite having an evolved composition, the blocky Devils Orchard and Serrate flows yielded a few samples that plot as a third group, between the primitive and evolved lava flows. We focus on SiO_2 in this study because it influences silicate melt properties (e.g., increased polymerization of the silicate network), which in turn influences the lava viscosity affecting the surface roughness (Lejeune and Richet, 1995; Campbell et al., 2009).

Figure 2.4. Studied lava flows at COTM: (a) Blue Dragon smooth pāhoehoe lava flow in the southern region of the field site. (b) Blocky Devils Orchard lava flow; image was taken at the lip of the lava flow close to the flow margin between Serrate and Devils Orchard. (c) Blocky Serrate lava flow; image was taken close to the Serrate-Devils Orchard lava flow margin. (d) Hummocky pāhoehoe North Crater lava flow with the distinctive blue colouring on its surface. (e) Big Craters lava flow with a rubbly pāhoehoe surface. Notice the chaotic distribution of the fragments and clasts of the lava flow. (f) The block-ʻaʻā latite Highway flow.

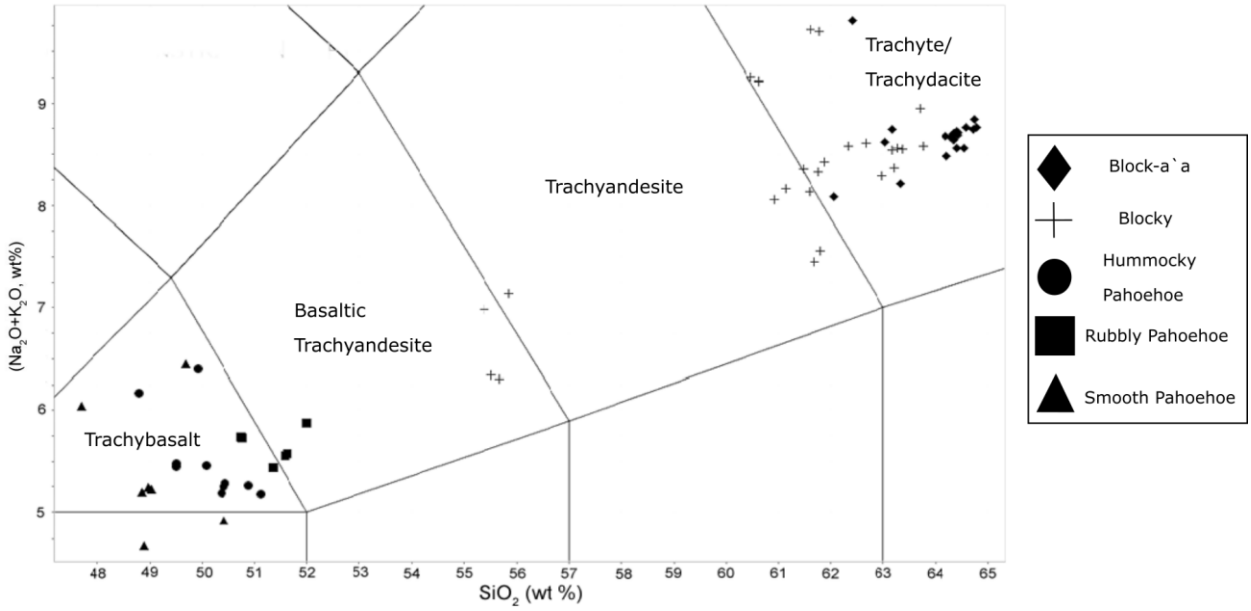

Figure 2.5. Volcanic TAS diagram comparing COTM lava flows using alkali (Na_2O+K_2O) and silica (SiO_2) compositions. COTM lavas show a range of volcanic types from basalt to trachyte/trachydacite.

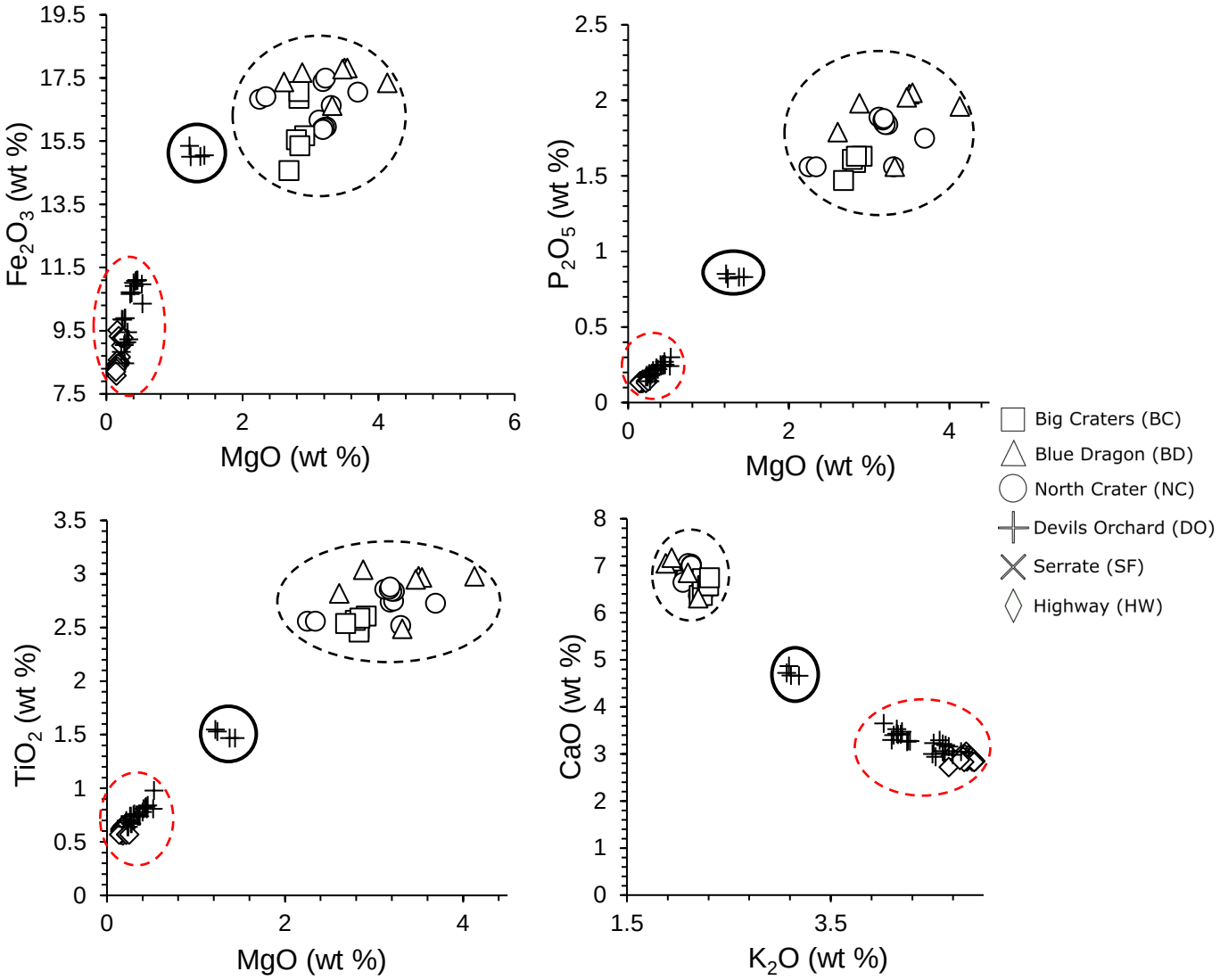

Figure 2.6. Major element XRF data from COTM. Oxides of Mg, Fe, P, Ti, K and Ca plotted to show the similarities and diversity between composition and surface roughness. The surface roughness described in the field are clustered as two separate groups, with a few data points from the blocky lava flows (Devils Orchard and Serrate) plotted in an intermediate zone. Black dashed outlines highlight the primitive lava compositions, red dash outlines highlight the more evolved lava compositions, and the solid black circle highlights samples with intermediate compositions. Legend above applies to all of the graphs.

2.3.2 Petrographic analysis

The primitive lava flows exhibit similar mineralogical and petrographic properties, with elongate and partially tabular plagioclase crystals (0.1–0.2 mm, 32–55 vol%) and fine-grained anhedral to subhedral fayalite and augite crystals (0.05–0.1 mm, 4–15 vol%) (Figure 2.7a-b). The crystals are all encased within a quenched, black, opaque glass matrix. The lava flows all contain large vesicles, some reaching diameters >1 cm, with most within the range of 0.1–0.5 cm. Larger vesicles with diameters >5 cm were observed in the field (summarized in Table 2.2).

Plagioclase crystals in the hummocky and rubbly pāhoehoe flows become oriented sub-parallel to the local flow direction further from the volcanic vent (Figure 2.7c). Along with the orientation, the average plagioclase crystal size slightly decreases from 0.2 mm to 0.1–0.05 mm. The amount of black, opaque glass matrix also decreases with distance from the lava flow source. Crystallinity increases from ~40% at the vents to 60% at a down-flow distance of 1.6 km (Table 2.2). Distinct orientation of plagioclase crystals is not observed in most smooth pāhoehoe samples, but the plagioclase crystals are 0.5–1 mm larger than the crystals in hummocky and rubbly pāhoehoe. When plagioclase orientation is present however, it is not well defined. The orientation of plagioclase crystals and change in crystallinity shows a transition from hypocrystalline to trachytic textures with distance from vent. The smooth pāhoehoe lava flow does not show changes in petrographic texture. The lava flow maintained a hypocrystalline texture, except close to the flow margins where cooling was slightly faster and produced a more glass-rich texture. The textural changes observed in rubbly pāhoehoe flow was not associated with a change in surface roughness, unlike the hummocky pāhoehoe, though both flows were geochemically and petrographically similar (Figures 2.6 and 2.7b-c).

Table 2.2. Mineral modes, textures, and vesicularity of thin section samples from COTM lava flows. The table summarizes the texture and mineralogy in the lava flow samples. Opaque's (Op) comprises ülvospinel and magnetite crystals. Mineral abbreviations: Olivine (Ol), clinopyroxene (Cpx), apatite (Ap), plagioclase (Pl), and anorthoclase (Ano). The dashes mean absent data.

Sample No.	Lava Flow	Coordinates	Surface Roughness	Textures	Pl (%)	Ol (%)	Cpx (%)	Op (%)	Ano (%)	Ap (%)	Glass (%)	Crystallinity (%)	Vesicles (%)
COTM16009	Big Craters	43°28'0.76" N, 113°32'53.37" W	Rubbly Pāhoehoe	Hypocrystalline-Trachytic	30	10	5	2	-	Trace	52	47	30
COTM16011	Big Craters	43°27'48.48" N, 113°32'48.61" W	Rubbly Pāhoehoe	Hypocrystalline-Trachytic	40	5	3	2	-	Trace	50	50	30
COTM16012	Big Craters	43°27'49.35" N, 113°32'50.87" W	Rubbly Pāhoehoe	Hypocrystalline	40	10	5	7	-	Trace	38	62	50
COTM16031	Big Craters	43°28'4.65" N, 113°32'30.96" W	Rubbly Pāhoehoe	Hypocrystalline	50	2	1	2	-	-	45	55	50
COTM16034	Big Craters	43°27'56.02" N, 113°31'42.78" W	Rubbly Pāhoehoe	Trachytic	55	5	5	3	-	2	30	70	40
COTM16035	Big Craters	43°28'15.33" N, 113°31'17.86" W	Rubbly Pāhoehoe	Trachytic	50	3	2	2	1	Trace	42	58	55
COTM16036	Big Craters	43°28'13.62" N, 113°31'20.39" W	Hummocky Pāhoehoe	Trachytic	40	5	2	2	-	1	50	50	20
COTM16001	Blue Dragon	43°27'46.74" N, 113°29'57.68" W	Smooth Pāhoehoe	Hypocrystalline	50	3	1	4	1	1	40	60	40
COTM16007	Blue Dragon	43°27'35.52" N, 113°30'16.86" W	Smooth Pāhoehoe	Hypocrystalline	32	3	1	3	-	1	60	40	20
COTM16016	Blue Dragon	43°27'43.12" N, 113°29'51.00" W	Smooth Pāhoehoe	Hypocrystalline	45	10	3	4	1	-	37	63	35
COTM16020	Blue Dragon	43°27'50.46" N, 113°29'52.47" W	Hummocky Pāhoehoe	Hypocrystalline	40	5	5	4	-	Trace	46	54	40
COTM16027	Blue Dragon	43°27'19.31" N, 113°31'17.54" W	Hummocky Pāhoehoe	Hypocrystalline	39	5	3	3	-	Trace	50	50	30
COTM16033	Blue Dragon	43°28'6.01" N, 113°31'47.31" W	Hummocky Pāhoehoe	Hypocrystalline	45	3	3	3	-	2	44	56	30

COTM16002	Devils Orchard	43°27'46.79" N, 113°29'57.65" W	Rubbly	Aphanitic	50	4	2	2	2	-	40	60	50
COTM16004	Devils Orchard	43°27'40.17" N, 113°30'16.74" W	Blocky	Trachytic	50	3	2	3	1	-	41	59	50
COTM16006	Devils Orchard	43°27'40.10" N, 113°30'17.01" W	Blocky	Trachytic	50	3	3	4	-	-	40	60	25
COTM16022	Devils Orchard	43°27'29.03" N, 113°31'2.50" W	Blocky	Trachytic	55	3	3	2	-	Trace	37	63	45
COTM16026	Devils Orchard	43°27'21.58" N, 113°31'13.40" W	Blocky	Trachytic	50	10	5	6	1	-	28	72	45
COTM16028	Devils Orchard	43°27'18.65" N, 113°31'18.71" W	Blocky	Trachytic	50	10	3	2	-	-	35	65	40
COTM16029	Devils Orchard	43°27'6.28" N, 113°31'38.87" W	Blocky	Trachytic	50	3	2	1	2	-	42	58	50
HF16001	Highway Flow	43°27'48.01" N, 113°34'16.90" W	Blocky – ʻaʻā	Holohyaline	-	-	-	-	-	-	100	0	80
HF16002	Highway Flow	43°27'48.06" N, 113°34'16.89" W	Blocky – ʻaʻā	Holohyaline	2	-	-	-	-	-	98	2	>80
HF16003	Highway Flow	43°27'47.82" N, 113°34'17.26" W	Blocky – ʻaʻā	Holocrystalline	55	3	5	1	2	2	32	68	50
HF16004	Highway Flow	43°27'47.75" N, 113°34'17.33" W	Blocky – ʻaʻā	Vitrophyric - Holohyaline	-	-	-	-	-	-	95	5	65
COTM16010	North Crater	43°28'0.91" N, 113°32'54.46" W	Smooth Pāhoehoe	Hypocrystalline	50	5	5	3	-	-	37	63	20
COTM16013	Serrate Flow	43°27'44.79" N, 113°29'50.85" W	Blocky	Trachytic	50	3	3	2	2	Trace	40	60	45
COTM16014	Serrate Flow	43°27'44.37" N, 113°29'50.72" W	Blocky	Trachytic	50	3	1	4	2	-	40	60	50
COTM16017	Serrate Flow	43°27'47.83" N, 113°29'43.84" W	Blocky	Trachytic	50	3	1	3	1	-	42	58	80
COTM16018	Serrate Flow	43°27'50.73" N, 113°29'52.48" W	Blocky	Trachytic	50	10	3	5	-	-	32	68	60
COTM16019	Serrate Flow	43°27'50.68" N, 113°29'52.00" W	Blocky	Trachytic	50	10	5	4	-	-	31	69	20

The chemically evolved blocky lava flows exhibit more crystal orientation than the less evolved lava flows and have a finer grained (<50 μm to 1 mm) groundmass. Plagioclase crystals are slightly more acicular than tabular. Subhedral to anhedral fayalite and augite crystals ranging in size from 0.05–1 mm are encased in a deep brown volcanic glass matrix. Also, within the glass matrix are vesicles with an average diameter of 0.5 mm with some larger vesicles >1 cm in diameter.

Crystallinity in the evolved lava flows is greater than the primitive lava flows (60–70% vs 40–60%). Close to the volcanic vent, the blocky flows exhibit aphanitic textures (Figure 2.7d) that transition to micro-trachytic textures. The glass content remains unchanged during this transition, remaining between 35–40%. Progressing further from the vent the texture becomes more trachytic, with slightly coarser (increasing from <50 μm–1 mm to 0.5 mm–1.5 mm) and more oriented plagioclase crystals.

The Highway block-`a`ā lava flow, although classed as evolved lava, exhibits different petrographic properties. The vesicularity ranges from ~30% to >80% in localized patches in the field. The surface has a holohyaline texture, with very fine-grained crystals that are not observable under optical microscopy, is very vesicular (Figure 2.7e), and comprises a deep orange glass matrix. The interior of the flow, however, is porphyritic (Figure 2.7f).

A closer investigation of the black opaque and deep brown glass matrix using BSE imagery revealed an array of quench textures. In the black glass, skeletal fayalite nucleated around the margins of the elongate and partially tabular plagioclase crystals (Figure 2.8a). Augite crystals grew around the tips of the plagioclase, creating a feathered texture. In the deep brown glass, the quenched textures are not as well defined. Skeletal fayalite and feathered augite are not

as abundant, and most of the matrix is composed of single quenched glass matrix with no microlites (Figure 2.8b).

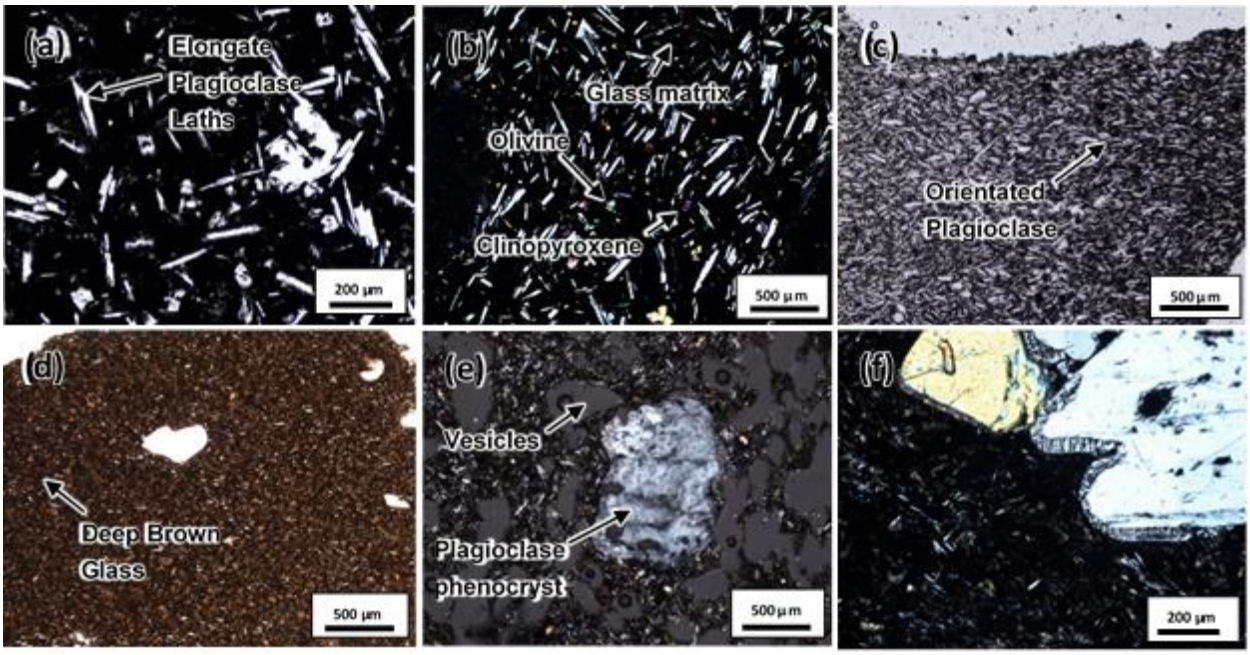

Figure 2.7. Petrographic images from COTM lava flows. (a) Elongate plagioclase laths encased in volcanic glass from Blue Dragon flow. (b) Black opaque glass matrix encasing elongate plagioclase, subhedral clinopyroxene, and fine-grained olivine crystals from Big Craters (c) Elongate plagioclase crystals are orientated sub-parallel to the lava flow direction. Sample is from Big Craters flow. (d) Deep brown glass matrix in an aphanitic texture. Sample is from Devils Orchard flow. (e) Plagioclase phenocryst with partially consumed crystal margins. Sample is from Highway flow. (f) Porphyritic texture with olivine and plagioclase phenocrysts with no zonation patterns. Sample is from Highway flow.

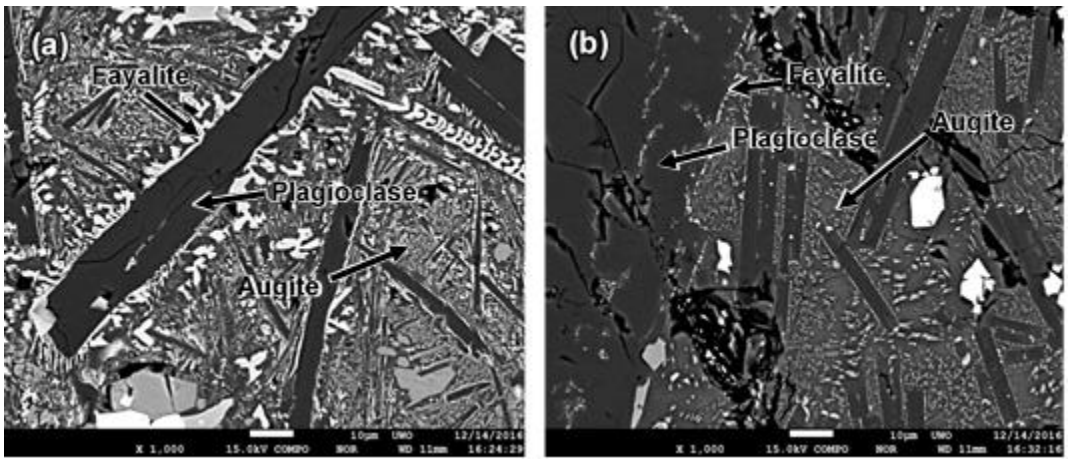

Figure 2.8. Images of quenched volcanic textures as observed using BSE analysis; skeletal fayalite and feather-like augite. Augite crystallized on the margins of the elongate tabular plagioclase crystals. The textures in the left image (a) are from lava flows with smooth and rubbly pāhoehoe samples (primitive), and the right image (b) are from blocky lava flows (evolved).

2.3.3 Radar properties

Ten polygons were traced on the AIRSAR L-band dataset over areas where samples were collected. These were used to calculate the mean CPR, which is representative of the surface roughness of the associated lava flow (Table 2.3). The size of all the polygons are not uniform because they were traced to fit clustered samples, and avoid vegetation, degraded lava surfaces and volcanic ash deposits. A low pass filter was applied to the AIRSAR L-Band dataset to reduce the speckle noise in the image, which scales as $1/N^{1/2}$, where N is the number of looks in each pixel. The low pass filter averaged the CPR over a 3x3 pixel area, increasing the number of looks per pixel from 9 to 81 (hence reducing the speckle noise from 33% to 11%). The zonal

statistics tool in ArcGIS was applied after filtering to calculate the mean CPR for each region of interest (Table 2.3). The smooth pāhoehoe surface returned values of 0.34 ± 0.11, consistent with single bounce backscattering (quasi-specular). The blocky surfaces returned values between 0.91–1.14 ± 0.19–0.2, consistent with double bounce backscattering (Neish and Carter, 2014). The block-`a`ā lava flow returned a value of 0.69 ± 0.25, almost identical to the rubbly pāhoehoe flow, 0.73 ± 0.24, and is consistent with multiple bounce backscattering (diffuse). The "Humm_Blocky" polygon is not its own lava flow but the rubbly and smooth pāhoehoe flows overlying a blocky flow (Figure 2.9). The polygon's mean CPR value (0.65 ± 0.34) is less than the block-`a`ā and rubbly pāhoehoe but greater than the hummocky pāhoehoe surface from North Crater (0.48 ± 0.19) and Big Craters (0.56 ± 0.21). The large standard deviation calculated from the Humm_Blocky polygon is likely due to the presence of two different surface roughness textures in this region (Section 4.2, Figure 2.11).

In addition to surface scattering, radar has the capability to penetrate through the surface to any underlying clasts, voids, or interfaces (e.g., lithological contacts). The penetration depth (d) of a radar signal is dependent on the illumination wavelength (λ), the loss tangent of the substrate ($\tan\delta$), and its real dielectric constant (ε') (Equation 2.2).

$$d = \lambda / (2\pi\sqrt{(\varepsilon')}\tan\delta) \qquad \text{Equation 2.2}$$

For example, Neish et al. (2014) calculated the penetration depth of a 19 cm radar signal into lunar impact melt flows (estimated 2.5 g/cm^3 density) to be within a range of 20–500 cm (calculated using dielectric constant values from Ulaby et al. (1988)). Basaltic lava flows exhibit densities of 3-3.3 g/cm^3. Using real ($\varepsilon' = 1.96^{\rho(3\text{-}3.3)}$) and imaginary ($\varepsilon''$) dielectric constant

values from volcanic rocks within this density range ($\varepsilon'' = 0.11–0.18$ from Ulaby et al. (1988)) we calculated the loss tangent ($\tan\delta = \varepsilon''/\varepsilon'$). With these values, we calculated a penetration depth for the 24 cm L-band radar from 60–100 cm. Since the penetration depth is less than a metre, we would not expect much subsurface scattering in the AIRSAR data within the COTM field site.

In order to determine if the radar returns were the result of surface or subsurface scattering, we calculated the DLP of the lava flows (Neish and Carter, 2014) using the Stokes Matrix (Section 2.3, Equation 2.1). A lowpass filter was applied to the DLP dataset to reduce speckle noise, and quantified values were calculated using zonal statistics. The lava flows returned low DLP values of 0.18-0.2 ± 0.05-0.06 (Table 2.3), compared to areas in the northern and western part of the field site, which returned DLP values of 0.25 ± 0.06 (Figure 2.10). These regions of higher DLP are covered in ash deposits, where one would expect more subsurface scattering from buried lava flows. Low values of DLP are consistent with subsurface layered materials where the dielectric constant only gradually increases with depth or lithological contacts that are deeper than the penetration depth (Carter et al., 2006). In our study area, the smooth pāhoehoe lava flow has a mean CPR of 0.34 and mean DLP of 0.18. With a low CPR and DLP, this suggests a smooth surface with little subsurface scattering (Carter et al., 2011). The rest of the lava flows exhibit moderate to high CPR and low DLP. This suggests a rough surface with little subsurface scattering.

Table 2.3. The above table contains the CPR mean and standard deviation and DLP mean values of the traced lava flow polygons. The polygons covered areas of the lava flows where samples were collected to allow for comparisons between the remote sensing, geochemical, and petrographic data. Mean CPR values show differences and similarities between the surface roughness descriptions, but DLP remains relatively homogeneous at 0.18–0.20.

Polygon Raster ID	Surface Roughness	Mean CPR	CPR STD	Mean DLP	STD
Block_'a'ā	Block-'a'ā	0.69	0.25	0.2	0.06
Blocky_1	Blocky	1.1	0.35	0.2	0.05
Blocky_2	Blocky	0.91	0.3	0.19	0.05
Blocky_3	Blocky	1.05	0.34	0.2	0.06
Blocky_4	Blocky	1.14	0.32	0.19	0.05
Hummocky_Pāhoehoe_1	Hummocky	0.56	0.21	0.18	0.05
Hummocky_Pāhoehoe_2	Hummocky	0.48	0.19	0.2	0.06
Humm_Blocky	Hummocky over Blocky	0.65	0.34	0.19	0.05
Rubbly_Pāhoehoe	Rubbly	0.73	0.24	0.19	0.05
Smooth_Pāhoehoe	Smooth Pāhoehoe	0.34	0.11	0.18	0.05

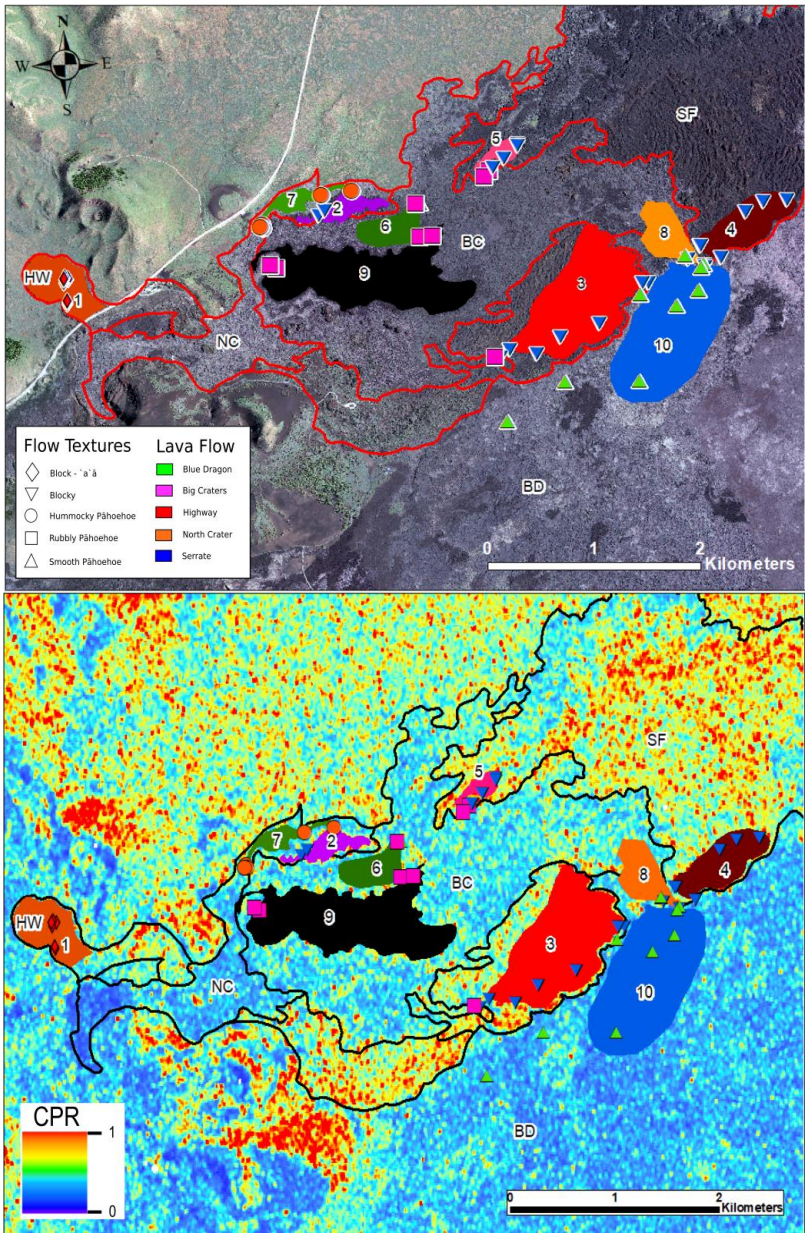

Figure 2.9. The AIRSAR data covering the COTM field site. Locations of lava flow shape files traced in ArcGIS, overlain on a NAIP visual image (top). Sample locations are indicated by white symbols. AIRSAR CPR data (~12 m/pixel) set after a 3x3 lowpass filter has been applied (bottom). The CPR values within each polygon raster were averaged using zonal statistics. Some samples were not incorporated because they are in areas with vegetation and volcanic ash deposits. The symbols are the same as in Figure 2.3.

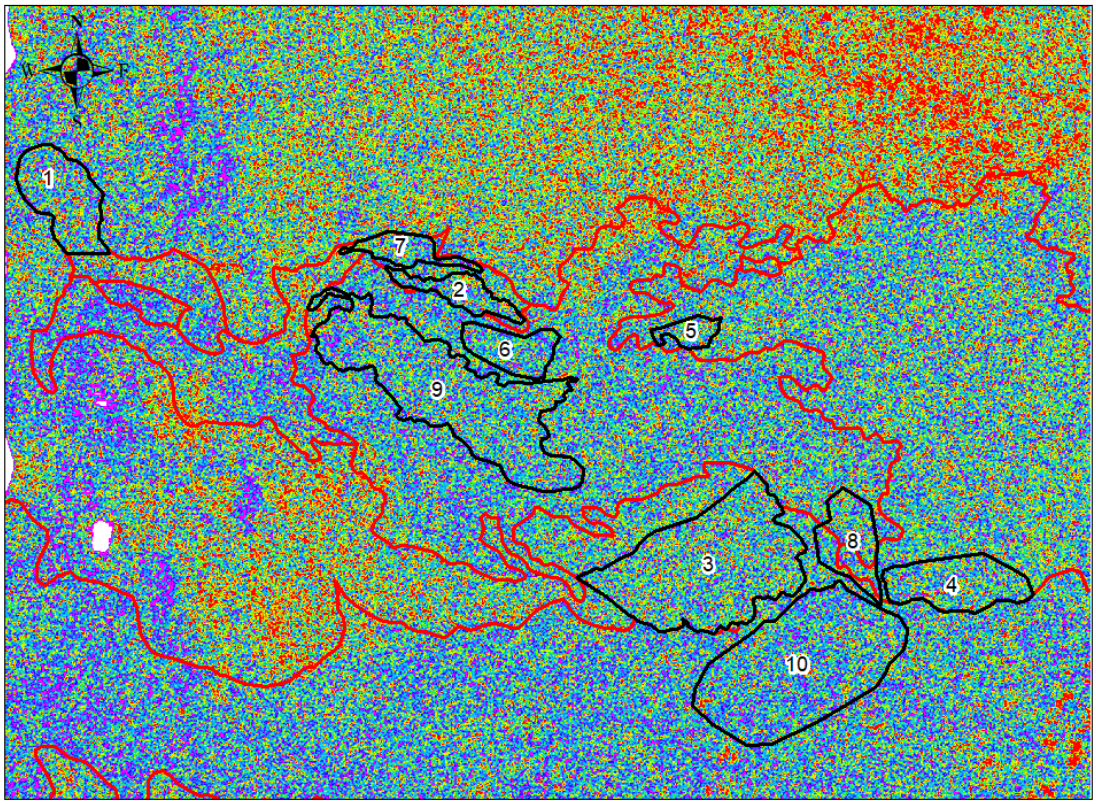

Figure 2.10. DLP pixels calculated from AIRSAR L-band data. The lava flows show low DLP values indicating little backscatter from subsurface interfaces and material. Red-orange areas (≥0.3) represent ash deposits, lapilli, and aeolian sediments. Their greater values are most likely indicating subsurface scattering from older buried lava flows.

2.4 Discussion

Lava flows on Earth and other planetary surfaces can exhibit similar surface morphologies when analysed using remote sensing data (Campbell and Shepard, 1996; Campbell et al., 2010; Harmon et al., 2012; Neish et al., 2017), making it difficult to infer their differing lava properties and emplacement processes. To help address this issue, the overarching goal of this study was to investigate whether there was any correlation between the geochemistry,

petrography, and radar data of a diverse range of lava flows at COTM. This will allow us to understand the extent to which we can predict the lava properties and emplacement processes of a lava flow using only a remotely derived measure of decimetre scale roughness.

2.4.1 Radar statistics compared to surface morphology

Our results show that the blocky lava flows returned CPR values reaching and exceeding unity while the smooth, hummocky, and rubbly pāhoehoe lava flows returned values <0.75. The smooth pāhoehoe surfaces have a CPR of 0.34 ± 0.11, indicative of single bounce backscattering, common for smooth surfaces. The blocky surfaces returned values between 0.91–1.14 (±0.25–0.35), suggestive of double bounce backscattering from natural corner reflectors. The rubbly pāhoehoe surfaces have a CPR of 0.73 ± 0.24, which implies the surface scattered the radar signal in multiple directions (diffuse scattering). The hummocky flow overlying the blocky flows also returned similar CPR values, 0.65 ± 0.34 ("Humm_Blocky" in Figure 2.10). Even though this does not represent an individual flow, it may be difficult to distinguish rough lava flows from smooth lava flows overlying older rougher lava flows in remote sensing data. The block-ʻaʻā flow has a CPR of 0.69 ± 0.25, which is also similar to the rubbly pāhoehoe. The block-ʻaʻā lava flow was anticipated to return a CPR value greater than the rubbly pāhoehoe flow because of its jagged, sharp, vesicular surface, and conchoidal fracture features. However, the surface of the block-ʻaʻā flow must lack the natural corner reflectors required for double bounce backscattering. Thus, when observed with L-band radar (Figure 2.9), the block-ʻaʻā and rubbly pāhoehoe lava flows appear analogous. It would be difficult to distinguish them as different surface morphologies without in situ data. Hawaiian ʻaʻā lava flows also have CPR values similar to rubbly pāhoehoe (Campbell, 2002) complicating the matter further.

In addition, our results show that lava flows exhibiting similar CPR values also have contrasting petrographic textures. The rubbly pāhoehoe transitions from holocrystalline to trachytic textures while the block-ʻaʻā exhibits holohyaline and porphyritic textures. It is not surprising that these two lava flows exhibit different petrographic textures since both formed under different processes. The rubbly pāhoehoe formed via mechanical fracturing of a quenched pāhoehoe crust while the block-ʻaʻā flowed over the surface in a creeping-motion in response to its high SiO_2 and viscosity, and an increase in rate of shear. On the other hand, the rubbly pāhoehoe and hummocky pāhoehoe lava flows are easily distinguishable in the field and in the radar data (Figure 2.9). Their geochemistry and petrography, however, are indistinguishable, both exhibiting similar major elemental content (Figures 2.5 and 2.6, Section 3.1), and hypocrystalline and trachytic textures (Table 2.3, Section 3.2).

Without ground-truth information, our interpretations of the lava flow properties and emplacement processes using radar data are therefore limited. However, the diverse surface roughness and morphology of the studied COTM lava flows provides a wide selection of examples to compare to lava flows in other volcanic regions on Earth and other planetary surfaces, aiding in our understanding of their origin and emplacement.

2.4.2 Radar statistics compared to SiO_2 content

The SiO_2 of the lava flows varies across the northern area of COTM (45–65 wt%). With such a wide variation in SiO_2 content, and with composition being a property that influences surface morphology and roughness, we might expect to observe some correlation between SiO_2 and the CPR values. To test this hypothesis, we plotted SiO_2 versus mean CPR for each lava flow studied (Figure 2.11). Using Pearson's correlation coefficient, we calculated the strength of

the relationship between SiO_2 and CPR. Pearson's correlation coefficient formula determines whether a correlation exists between two variables (Egghe and Rousseau, 1990). A positive correlation will return values ≥0.5–1 while a negative correlation will return values ≤-0.5 – -1. Coefficient values close or equal to zero indicate a weak or non-existent correlation between the variables. A calculated value of 0.63 indicates the CPR and SiO_2 have a positive correlation. However, we observed some exceptions to this correlation. The smooth, hummocky, and rubbly pāhoehoe lava flows showed an increase in CPR as expected, but the SiO_2 did not change. This is because the rubbly pāhoehoe surface forms from mechanical fracturing, rather than viscosity changes related to increasing SiO_2. The block-'a'ā flow also does not follow the upward trend in CPR with SiO_2. Although it is as siliceous as the blocky flows, the block-'a'ā lacks natural corner reflectors on its surface so it is unable to return CPR values above unity. The emplacement of the block-'a'ā flow may be more akin to an 'a'ā flow than a blocky flow and may have not been emplaced under the creep fracturing movement associated with blocky lava eruptions (MacDonald, 1953).

Therefore, although there is a general increase in CPR with silica content, if this correlation was applied to interpret the surface morphology and roughness of lava flows on other planetary surfaces, incorrect interpretations could arise. Highly siliceous lava flows will not always return high CPR values if they lack the natural corner reflectors necessary for double bounce backscattering. They would appear indistinguishable to transitional lava flows such as rubbly pāhoehoe flows or Hawaiian 'a'ā flows (Campbell, 2002). Similarly, lava flows with lower silica content that have been mechanically fractured will show an increase in CPR unrelated to their composition, as we see for the rubbly pāhoehoe at COTM.

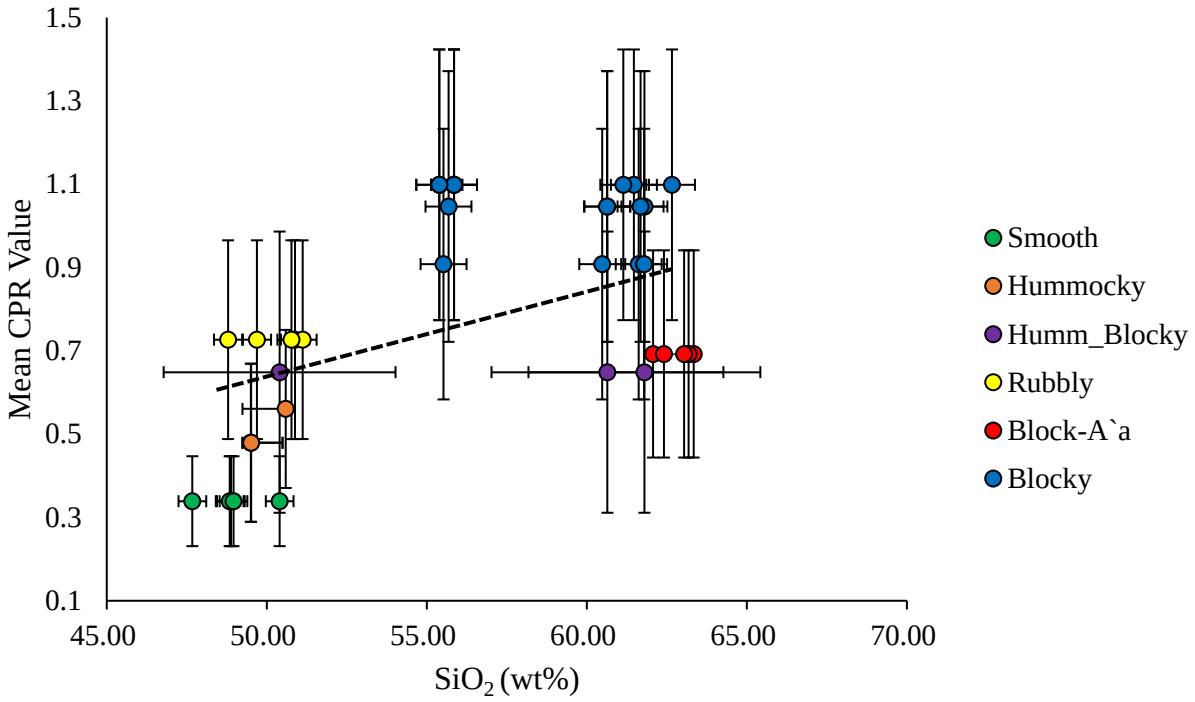

Figure 2.11. Mean CPR vs SiO_2 content for each lava flow studied in this work. The data points represent the different surface roughness descriptions of the lava flows. The dashed outline is the trend line for the data points.

2.4.3 Using radar statistics to reconstruct lava emplacement mechanisms

To infer lava properties and emplacement processes on other planetary surfaces and remote locations on Earth where fieldwork is not possible, we must rely on morphological and surface roughness studies from remote sensing data sets (Campbell, 2012; Campbell et al., 2010, 2009; Carter et al., 2006; Harmon et al., 2012; Morgan et al., 2016; Patterson et al., 2017; Shepard et al., 2001). From our results, we show that radar data cannot always distinguish lava flows with different surface morphologies. The similar mean CPR values from the block-ʻaʻā and rubbly pāhoehoe flow would lead to ambiguous interpretations about their emplacement

conditions and lava properties if one were to rely on radar data alone. The difference in CPR between the siliceous blocky and block-ʻaʻā demonstrates that not all siliceous lava flows exhibit double-bounce backscattering and return CPR values ≥1.0. In some cases, visible imagery might be able to distinguish the lava flows and aid in interpreting the emplacement styles, but only if the resolution is high enough. For example, in high-resolution (1 m/pixel) optical images, the hummocky pāhoehoe flow can be seen covering the blocky flows, providing evidence that it is a younger flow overlying an older, rougher flow. In many instances though, such high-resolution imagery is not publicly available, or its scale is too coarse to highlight centimetre -decimeter scale roughness differences. In planetary science, the highest-resolution optical data available, notably the 0.25 m/pixel HiRISE instrument on the Mars Reconnaissance Orbiter (McEwen et al., 2007) and the 0.5 m/pixel Lunar Reconnaissance Orbiter Camera instrument (Chin et al., 2007) can observe some surface features such as metre-sized pāhoehoe slabs. However, surface features such as clinkered ʻaʻā and rubbly pāhoehoe cannot be observed.

As a result, CPR coupled with high-resolution optical imagery is insufficient to differentiate all lava surfaces at our study site in COTM. Without ground-truth information (field observations, and geochemical and petrographic data), misinterpretations about the lava properties and emplacement processes of the COTM lava flows would have been made. The lava flows may have been presumed to be emplaced under similar conditions, leading to false interpretations about their volcanic eruption history and magmatic origin. However, the use of radar for understanding lava flow emplacement and properties should not be disregarded because of these results. In fact, a general trend of increasing in CPR with increasing SiO_2 is observed. Instead, we suggest that caution needs to be taken when interpreting remote sensing data. For example, a study by Kolzenburg et al. (2018) raises the concern that rheological inferences on

lava flows using remote sensing data may be over exaggerated because inflation after eruption cessation would continue to change the surface morphology and roughness.

Note that the AIRSAR data was at 24 cm wavelength and is only sensitive to surface features of that scale. Smaller radar wavelengths such as C-Band (5.6 cm wavelength) may have revealed different discrepancies between the lava flow surfaces if centimetre scale features were detected. The same would apply if longer radar wavelengths (e.g., P-Band, 70 cm) were used. L-Band data was used in this study because it best discriminated the lava flow surface roughness types at COTM (Zanetti et al., 2018).

In summary, radar remote sensing data provides important information about lava flow emplacement, but still has its limitations and ambiguities, especially when studying lava flows on other planetary surfaces where ground-truth information is not available. Until extensive ground-truth data becomes available for planetary bodies, when interpreting radar data, we should consider multiple lava flow types that can produce a common CPR value. For example, Arecibo P-band CPR data of Imbrium Mare lava flows are similar to CPR values for terrestrial lava flows (Campbell et al., 2007; Morgan et al., 2016). Radar bright mare flows with a CPR of 0.6 match values for terrestrial ‘a‘ā, hummocky, and slabby pāhoehoe at L-Band. These wavelengths differ by more than a factor of two (24 cm vs. 70 cm), so we cannot exactly compare the results. The P-band data will be sensitive to roughness at a slightly larger scale than that of the L-band data. Nonetheless, we use this comparison to illustrate the point that one CPR value cannot be unambiguously distinguish the lava flow properties. With such a wide range of potential surface morphologies, only in-situ measurements can provide clarification regarding their emplacement style. Until future missions return to the Moon to provide ground truth

information about the mare lava flows, more than one type of surface morphology could explain the radar remote sensing data.

2.5 Conclusions

The goal of this work was to establish a relationship between the geochemistry, petrography, and surface morphology/roughness of lava flows to improve predictions on their lava properties and emplacement processes using remote sensing data. Geochemically the lava flows were divisible into two major groups and one intermediate group. Each lava flow exhibited a variety of petrographic textures from hypocrystalline, porphyritic, aphanitic, trachytic, and holohyaline. The COTM lava flows exhibit a range of morphologies including smooth, hummocky, and rubbly pāhoehoe, block-ʻaʻā, and blocky flows. The AIRSAR L-Band data revealed that rubbly pāhoehoe and block-ʻaʻā lava flows exhibit similar mean CPR values, making them appear almost identical. If ground-truth information was not obtained both lava flows could have been interpreted to be the same type of flow, which would have led to ambiguous interpretations about their emplacement and lava properties. Lava flows with different surface morphologies that exhibit similar mean CPR values can impede our interpretations on the lava properties and emplacement processes of lava flows on other planetary bodies, where no such ground truth data is available. We recommend that caution needs to be taken when studying the surface roughness and morphology of lava flows on other planetary bodies such as the Moon. By taking precaution, we can begin to improve our understanding of volcanic surfaces on the Moon, which can be applied to future lander/rover missions with the objective to study lunar volcanism.

References

Bondre, N.R., Duraiswami, R.A., Dole, G., 2004. A brief comparison of lava flows from the Deccan Volcanic Province and the Columbia-Oregon Plateau Flood Basalts : Implications for models of flood basalt emplacement. J. Earth Syst. Sci. 113, 809–817.

Campbell, B.A., 2012. High circular polarization ratios in radar scattering from geologic targets 117, 1–9. https://doi.org/10.1029/2012JE004061

Campbell, B.A., 2002. Radar Remote Sensing of Planetary Surfaces. Cambridge University Press.

Campbell, B.A., Campbell, D.B., Margot, J.-L., Ghent, R.R., Nolan, M., Chandler, J., Carter, L.M., Stacy, N.J., 2007. Focused 70-cm wavelength radar mapping of the Moon. IEEE Trans. Geosci. Remote Sens. 45, 4032–4042.

Campbell, B.A., Carter, L.M., Campbell, D.B., Nolan, M., Chandler, J., Ghent, R.R., Ray Hawke, B., Anderson, R.F., Wells, K., 2010. Earth-based 12.6-cm wavelength radar mapping of the Moon: New views of impact melt distribution and mare physical properties. Icarus 208, 565–573. https://doi.org/10.1016/j.icarus.2010.03.011

Campbell, B.A., Carter, L.M., Hawke, B.R., Campbell, D.B., Ghent, R.R., 2008. Volcanic and impact deposits of the Moon's Aristarchus Plateau: A new view from Earth-based radar images. Geology 36, 135–138. https://doi.org/10.1130/G24310A.1

Campbell, B.A., Hawke, B.R., Campbell, D.B., 2009. Surface morphology of domes in the Marius Hills and Mons Rümker regions of the Moon from Earth-based radar data. J. Geophys. Res. 114, 1–10. https://doi.org/10.1029/2008JE003253

Campbell, B.A., Hawke, B.R., Thompson, T.W., 1997. Long-wavelength Radar Studies of the Lunar Maria. Jounral Geophys. Res. 102, 19,307-19,320.

Campbell, B. a, Shepard, M.K., 1996. Lava flow surface roughness and depolarized radar scattering. J. Geophys. Res. 101, 18,941-18,951.

Campbell, B., Hawke, B., Morgan, G., Carter, L., Campbell, D., Nolan, M., 2014. Improved discrimination of volcanic complexes, tectonic features, and regolith properties in Mare Serenitatis from Earth-based radar mapping. J. Geophys. Res. Planets 119, 313–330. https://doi.org/10.1016/S0733-8619(03)00096-3

Carter, L.M., Campbell, D.B., Campbell, B.A., 2011. Geologic studies of planetary surfaces using radar polarimetric imaging. Proc. IEEE 99, 770–782. https://doi.org/10.1109/JPROC.2010.2099090

Carter, L.M., Campbell, D.B., Campbell, B.A., 2006. Volcanic deposits in shield fields and highland regions on Venus : Surface properties from radar polarimetry. J. Geophys. Res. 111. https://doi.org/10.1029/2005JE002519

Carter, L.M., Campbell, D.B., Campbell, B.A., 2004. Impact crater related surficial deposits on Venus : Multipolarization radar observations with Arecibo. Jounral Geophys. Res. 109. https://doi.org/10.1029/2003JE002227

Carter, L.M., Neish, C.D., Bussey, D.B.J., Spudis, P.D., Patterson, G.W., Cahill, J.T., Raney, R.K., 2012. Initial observations of lunar impact melts and ejecta flows with the Mini-RF radar. J. Geophys. Res. 117, 1–13. https://doi.org/10.1029/2011JE003911

Chin, G., Brylow, S., Foote, M., Garvin, J., Kasper, J., Keller, J., Litvak, M., Mitrofanov, I.,

Paige, D., Raney, K., Robinson, M., Sanin, A., Smith, D., Spence, H., Spudis, P., Stern, S.A., Zuber, M., 2007. Lunar Reconnaissance Orbiter Overview : The Instrument Suite and Mission. Space Sci. Rev. 129, 391–419. https://doi.org/10.1007/s11214-007-9153-y

Crisp, J., Baloga, S., 1994. Influence of crystallization and entrainment of cooler material on the emplacement of basaltic aa lava flows. J. Geophys. Res. 99, 11819–11831.

Duraiswami, R.A., Bondre, N.R., Managave, S., 2008. Morphology of rubbly pahoehoe (simple) fl ows from the Deccan Volcanic Province : Implications for style of emplacement. J. Volcanol. Geotherm. Res. 177, 824–838. https://doi.org/10.1016/j.jvolgeores.2008.01.048

Duraiswami, R.A., Gadpallu, P., Shaikh, T.N., Cardin, N., 2014. Pahoehoe-a'a transitions in the lava flow fields of the western Deccan Traps, India-implications for emplacement dynamics, flood basalt architecture and volcanic stratigraphy. J. Asian Earth Sci. 84, 146–166. https://doi.org/10.1016/j.jseaes.2013.08.025

Egghe, L., Rousseau, R., 1990. Introduction to Informetrics. Quantitative Methods in Library, Documentation and Information Science. Elsevier Science Publishers.

Evans, D.L., Farr, T.G., Ford, J.P., Thompson, T.W., Werner, C.L., 1986. Multipolarization Radar Images for Geologic Mapping and Vegetation Discrimination. IEEE Trans. Geosci. Remote Sens. GE-24, 246–257. https://doi.org/10.1109/TGRS.1986.289644

Faye, G., Miller, R., 1973. " Blue Dragon " Basalt from Graters of the Moon National Monument , ldaho : Origin of Color. Am. Mineral. 58, 1048–1051.

Glaze, L.S., Baloga, S.M., 2007. Topographic variability on Mars: Implications for lava flow modeling. J. Geophys. Res. E Planets 112, 1–9. https://doi.org/10.1029/2006JE002879

Glenn, N.F., Streutker, D.R., Chadwick, D.J., Thackray, G.D., Dorsch, S.J., 2006. Analysis of LiDAR-derived topographic information for characterizing and differentiating landslide morphology and activity. Geomorphology 73, 131–148. https://doi.org/10.1016/j.geomorph.2005.07.006

Greeley, R., King, J.S., 1977. Volcanism of the eastern Snake River Plain, Idaho: A Comparative planetary geology-guidebook. Washington, D.C., NASA CR 154621.

Gregg, T.K.P., Fink, J.H., 1996. Quantification of extraterrestrial lava flow effusion rates through laboratory simulations. J. Geophys. Res. 101, 16891–16900. https://doi.org/10.1029/96JE01254

Gregg, T.K.P., Fink, J.H., 1995. Quantification of submarine lava-flow morphology through analog experiments. Geology 23, 73–76. https://doi.org/10.1130/0091-7613(1995)023<0073

Griffiths, R.W., Fink, J.H., 1992. The morphology of lava flows in planetary environments: Predictions from analog experiments. J. Geophys. Res. 97, 19739. https://doi.org/10.1029/92JB01953

Guilbaud, M.-N., Self, S., Thordarson, T., Blake, S., 2005. Morphology, surface structures, and emplacement of lavas produced by Laki, A.D. 1783 – 1784. GSA Spec. Pap. 396, 81–102. https://doi.org/10.1130/2005.2396(07).

Hamilton, C.W., Glaze, L.S., James, M.R., Baloga, S.M., 2013. Topographic and stochastic influences on pāhoehoe lava lobe emplacement. Bull. Volcanol. 75, 1–16. https://doi.org/10.1007/s00445-013-0756-8

Harmon, J.K., Nolan, M.C., Husmann, D.I., Campbell, B. a., 2012. Arecibo radar imagery of Mars: The major volcanic provinces. Icarus 220, 990–1030. https://doi.org/10.1016/j.icarus.2012.06.030

Hughes, S.S., Kobs-Nawotniak, S.E., Borg, C., Mallonee, H.C., Purcell, S., Neish, C., Garry, W.B., Haberle, C.W., Lim, D.S.S., Heldmann, J.L., Team, the F., 2016. Diverse Eruptions at ~2,200 Years B.P. on the Great Rift, Idaho: Inferences for Magma Dynamics Along Volcanic Rift Zones., in: Conference, L. and P.S. (Ed.), Diverse Eruptions at ~2,200 Years B.P. on the Great Rift, Idaho: Inferences for Magma Dynamics Along Volcanic Rift Zones. 47th Lunar and Planetary Science Conference, pp. 6–7.

Hughes, S.S., Smith, R.P., Hackett, W.R., Anderson, S.R., 1999. Mafic Volcanism and Environmental Geology of the Eastern Snake River Plain, Idaho. Guideb. to Geol. East. Idaho 143–168.

Hughes, S.S., Wetmore, P.H., Casper, J.L., 2002. Evolution of Quaternary Tholeiitic Basalt Eruptive Centers on the Eastern Snake River Plain , Idaho. Idaho Geol. Surv. Bull. 30, 1–23.

Keszthelyi, L., Mcewen, A.S., Thordarson, T., 2000. Terrestrial analogs and thermal models for Martian flood lavas. J. Geophys. Res. E Planets 105, 15,027-15,049. https://doi.org/10.1029/1999je001191

Keszthelyi, L., Thordarson, T., McEwen, A., Haack, H., Guilbaud, M.N., Self, S., Rossi, M.J., 2004. Icelandic analogs to Martian flood lavas. Geochemistry, Geophys. Geosystems 5, 1–32. https://doi.org/10.1029/2004GC000758

Khan, S., Essam, H., Jaime, F., 2007. Mapping exposed and buried lava flows using synthetic

aperture and ground-penetrating radar in craters of the moon lava field. 2007 GSA Denver Annu. Meet. (28–31 Oct. 2007) 72, 123. https://doi.org/10.1190/1.2793298

Kuntz, M.A., 1989. Geology of the Craters of the Moon Lava Field, Idaho, in: Ruebelmann, K.L., Smith, R.P., Downs, W.F., Christiansen, R.L., Hacket, W.R., Morgan, L.M., Leeman, W.P., Wood, S.H., Malde, H.E., Kuntz, M.A. (Eds.), Snake River Plain-Yellowstone Volcanic Province: Jackson, Wyoming to Boise, Idaho. pp. 51–61. https://doi.org/https://doi.org/10.1029/FT305p0051

Kuntz, M.A., Champion, D.E., Lefebvre, R.H., 1988. Geologic map of the Craters of the Moon, Kings Bowl, and Wapi Lava Fields, and the Great Rift Volcanic Rift Zone, south-central Idaho. U.S. Geol. Surv. Misc. Investig. Ser.

Kuntz, M.A., Champion, D.E., Spiker, E.C., Lefebvre, R.H., 2005. Contrasting magma types and steady-state, volume-predictable, basaltic volcanism along the Great Rift, Idaho (USA). Geol. Soc. Am. Bull. 97, 579–594. https://doi.org/10.1130/0016-7606(1986)97<579:CMTASV>2.0.CO;2

Kuntz, M.A., Covington, H.R., Schorr, L.J., 1992. An overview of basaltic volcanism of the eastern Snake River Plain, Idaho, in: Regional Geology of Eastern Idaho and Western Wyoming. Geological Society of America Memoir, 179, pp. 227–267.

Kuntz, M.A., Skipp, B., Champion, D.E., Gans, P.B., Van Sistine, P., Snyders, S.R., 2007. Geological map of Craters of the Moon 30’ x 60’ quadrangle, Idaho. US Geol. Surv. Sci. Investig. Map.

Kuntz, M. a, Champion, D.E., Spiker, E.C., Lefebvrelsd, R.H., Mcbroomes, L. a, 1982. The Great Rift and the Evolution of the Craters of the Moon Lava Field , Idaho. Cenezoic Geol.

Idaho Idaho Bur. Mines Geol. Bull. 26, 423–437.

Kuntz, M.E.L.A., Survey, U.S.G., Champion, D.E., Survey, U.S.G., Park, M., Spiker, E.C., Survey, U.S.G., 1986. basaltic volcanism along the Great Rift , Idaho 579–594.

Lawrence, S.J., Stopar, J.D., Hawke, B.R., Greenhagen, B.T., Cahill, J.T.S., Bandfield, J.L., Jolliff, B.L., Denevi, B.W., Robinson, M.S., Glotch, T.D., Bussey, D.B.J., Spudis, P.D., Giguere, T.A., Garry, W.B., 2013. LRO observations of morphology and surface roughness of volcanic cones and lobate lava flows in the Marius Hills. J. Geophys. Res. E Planets 118, 615–634. https://doi.org/10.1002/jgre.20060

Leeman, W.P., 1982. Evolved and hybrid lavas from the Snake River Plain, in: Bonnichsen, B., Breckenridge, R.M. (Eds.), Cenozoic Geology of Idaho. Idaho Bureau of Mines and Geology, Bulletin 26, pp. 193–202.

Leeman, W.P., Vitaliano, C.J., Prinz, M., 1976. Evolved Lavas from the Snake River Plain. Contrib. to Mineral. Petrol. 56, 35–60.

Lejeune, A.M., Richet, P., 1995. Rheology of crystal-bearing silicate melts: An experimental study a high viscosities. Jounral Geophys. Res. 100, 4215–4229.

MacDonald, G.A., 1953. Pahoehoe, Aa, and Blocky Lava. Am. J. Sci. 251, 169–191.

Mcewen, A.S., Eliason, E.M., Bergstrom, J.W., Bridges, N.T., Hansen, C.J., Delamere, W.A., Grant, J.A., Gulick, V.C., Herkenhoff, K.E., Keszthelyi, L., Kirk, R.L., Mellon, M.T., Squyres, S.W., Thomas, N., Weitz, C.M., 2007. Mars Reconnaissance Orbiter ' s High Resolution Imaging Science Experiment (HiRISE). Jounral Geophys. Res. 112. https://doi.org/10.1029/2005JE002605

Morgan, G.A., Campbell, B.A., Campbell, D.B., Hawke, B.R., 2016. Investigating the stratigraphy of Mare Imbrium flow emplacement with Earth-based radar. J. Geophys. Res. 121, 1498–1513. https://doi.org/10.1002/2016JE005041.Received

Neish, C.D., Carter, L.M., 2014. Planetary Radar, in: Encyclopedia of the Solar System. pp. 1133–1159.

Neish, C.D., Hamilton, C.W., Hughes, S.S., Nawotniak, S.K., Garry, W.B., Skok, J.R., Elphic, R.C., Schaefer, E., Carter, L.M., Bandfield, J.L., Osinski, G.R., Lim, D., Heldmann, J.L., 2017. Terrestrial analogues for lunar impact melt flows. Icarus 281, 73–89. https://doi.org/10.1016/j.icarus.2016.08.008

Neish, C.D., Madden, J., Carter, L.M., Hawke, B.R., Giguere, T., Bray, V.J., Osinski, G.R., Cahill, J.T.S., 2014. Global distribution of lunar impact melt flows. Icarus 239, 105–117. https://doi.org/10.1016/j.icarus.2014.05.049

Patterson, G.W., Stickle, A.M., Turner, F.S., Jensen, J.R., Bussey, D.B.J., Spudis, P., Espiritu, R.C., Schulze, R.C., Yocky, D.A., Wahl, D.E., Zimmerman, M., Cahill, J.T.S., Nolan, M., Carter, L., Neish, C.D., Raney, R.K., Thomson, B.J., Kirk, R., Thompson, T.W., Tise, B.L., Erteza, I.A., Jakowatz, C. V., 2017. Bistatic radar observations of the Moon using Mini-RF on LRO and the Arecibo Observatory. Icarus 283, 2–19. https://doi.org/10.1016/j.icarus.2016.05.017

Peterson, D.W., Tilling, R.I., 1980. Transition of Basaltic Lava From Pahoehoe to AA, Kilauea Volcano, Hawaii: Field Observations and Key Factors. Jounral Volcanol. Geotherm. Researc 7, 271–293.

Putirka, K.D., Kuntz, M. a., Unruh, D.M., Vaid, N., 2009. Magma evolution and ascent at the

craters of the moon and neighboring volcanic fields, Southern Idaho, USA: Implications for the evolution of polygenetic and monogenetic volcanic fields. J. Petrol. 50, 1639–1665. https://doi.org/10.1093/petrology/egp045

Reid, M.R., 1995. Processes of mantle enrichment and magmatic differentiation in the eastern Snake River Plain: Th isotope evidence. Earth Planet. Sci. Lett. 131, 239–254.

Robert, B., Harris, A., Gurioli, L., Médard, E., Sehlke, A., Whittington, A., 2014. Textural and rheological evolution of basalt flowing down a lava channel. Bull. Volcanol. 76, 1–21. https://doi.org/10.1007/s00445-014-0824-8

Rosenburg, M.A., Aharonson, O., Head, J.W., Kreslavsky, M.A., Mazarico, E., Neumann, G.A., Smith, D.E., Torrence, M.H., Zuber, M.T., 2011. Global surface slopes and roughness of the Moon from the Lunar Orbiter Laser Altimeter 116, 1–11. https://doi.org/10.1029/2010JE003716

Sehlke, A., Whittington, A., Robert, B., Harris, A., Gurioli, L., Médard, E., Sehlke, A., 2014. Pahoehoe to áá transition of Hawaiian lavas: An experimental study. Bull. Volcanol. 76. https://doi.org/10.1007/s00445-014-0876-9

Shepard, M.K., Campbell, B.A., Bulmer, M.H., Farr, T.G., Gaddis, L.R., Plaut, J.J., 2001. The roughness of natural terrain: A planetary and remote sensing perspective. J. Geophys. Res. E Planets 106, 32777–32795. https://doi.org/10.1029/2000JE001429

Soldati, A., Sehlke, A., Chigna, G., Whittington, A., 2016. Field and experimental constraints on the rheology of arc basaltic lavas : the January 2014 Eruption of Pacaya (Guatemala). https://doi.org/10.1007/s00445-016-1031-6

Stout, M.Z., Nicholls, J., Kuntz, M. a, 1994. Petrological and mineralogical variations in 2500-2000 yr {B.P. Lava Flows, Crater of the Moon, Idaho}. J. Petrol. 35, 1681–1715.

Tilley, C.E., Thompson, R.N., 1970. MELTING AND CRYSTALL:ZAT10N RELATIONS OF THE SNAKE RIVER BASALTS OF SOUTHERN IDAHO, USA. Earth Planet. Sci. Lett. 8, 79–92.

Ulaby, F.T., Begnal, T., East, J., Dobson, M.C., Garvin, J., Evans, D., 1988. Microwave dielectric spectrum of rocks. Report 23817-1-TU.

Whelley, P.L., Garry, W.B., Hamilton, C.W., Bleacher, J.E., 2017. LiDAR-derived surface roughness signatures of basaltic lava types at the Muliwai a Pele Lava Channel , Mauna Ulu , Hawai ‘ i. Bull. Volcanol. 79. https://doi.org/10.1007/s00445-017-1161-5

Whelley, P.L., Glaze, L.S., Calder, E.S., Harding, D.J., 2014. LiDAR-Derived Surface Roughness Texture Mapping : Application to Mount St . Helens Pumice Plain Deposit Analysis. IEEE Trans. Geosci. Remote Sens. 52, 426–438. https://doi.org/10.1109/TGRS.2013.2241443

Zanetti, M., Neish, C.D., Kukko, A., Choe, B.-H., Osinski, G.R., Tolometti, G.D., Fan, K., Maj, R., 2018. Surface Roughness and Radar Scattering Properties of Volcanic Terrain: Geologic Application of Kinematic Mobile LiDAR Scanning. InlLunar Planet. Sci. Conf. 49.

Chapter 3: Differentiating Lava Facies and Flow Types Using RADAR and LiDAR Remote Sensing Data

3.1 Introduction

Studying large basaltic lava flow-fields is essential for understanding the emplacement mechanisms of flood lavas and flood basalts. This information can provide important insight into how fissure-fed eruptions have modified the surface of Earth and other planetary bodies (Wilson and Head, 1994; Keszthelyi and Self, 1998; Zimbelman, 1998; Self et al., 2005, 2006; Thordarson and Larsen, 2007). An exceptional terrestrial analogue for studying fissure-fed eruptions on planetary bodies is the 2014-2015 Holuhraun lava flow-field located in Iceland, as it exhibits a diverse array of lava flow morphologies and a complex emplacement history (Hamilton, 2015; Kolzenburg et al., 2017, 2018; Pedersen et al., 2017; Bonny et al., 2018; Dirscherl and Rossi, 2018; Bonnefoy et al., 2019). The Holuhraun lava flow-field is made up of lava facies, which are mappable domains that record the collective emplacement history within a particular area (Voigt et al., 2021). Each facies is comprised of multiple lava flow types, each representing a mode of emplacement that occurred at a particular stage of the eruption (e.g., Kilburn, 1981, 2000; Rowland and Walker, 1990; Solana et al., 2004; Thordarson and Larsen, 2007; Harris et al., 2017; Hamilton, 2019; Voigt et al., 2021). When a lava flow-field exhibits multiple-types of lava facies, it implies that there were changes in at least one of the following parameters during the eruption: magma composition, effusion rates, lava transportation processes, and/or emplacement styles. Changes in these parameters can be further deconstructed by studying the emplacement of the lava flow types that make up each lava facies.

To infer the emplacement mechanisms of lava flow-fields in our Solar System, we need to be able to differentiate lava facies in terrestrial lava flow-fields using remote sensing techniques, since we cannot directly study lava flow-fields, flood lavas, or flood basalts on the surface of other planetary bodies. One property of lava flows that is measurable using remote sensing data and is related to emplacement mechanisms is surface roughness (Rowland and Walker, 1990; Griffiths and Fink, 1992; Campbell and Shepard, 1996; Kilburn, 2000; Guilbaud et al., 2005; Duraiswami et al., 2008b, 2014; Harris et al., 2017). Surface roughness is defined as a measure of the variation in topography at scales of up to a few metres (Campbell and Shepard, 1996). The surface roughness of lava flows have been quantified using a variety of field and remote sensing techniques, including 1-D profile measurements (e.g., Campbell and Shepard, 1996; Shepard et al., 2001), synthetic aperture radar (e.g., Campbell and Shepard, 1996; Neish et al., 2017; Tolometti et al., 2020), and high-resolution topography data (e.g., Fan et al., 2018; Morris et al., 2008; Rodriguez Sanchez-vahamonde and Neish, 2021; Voigt et al., in press; Whelley et al., 2017; Zanetti et al., 2018). These techniques allow us to measure and compare surface roughness at various scales and link them to a lava flow's emplacement style (Rowland and Walker, 1990; Hon et al., 1994; Shepard et al., 2001; Tolometti et al., 2020).

Previous work by Voigt et al., (in press) discusses the challenges in differentiating the lava facies within the Holuhraun lava flow-field using high resolution (20 cm/pixel) imagery data. Their work discusses how the dominant presence of transitional lava flow types (e.g., rubbly pāhoehoe, spiny pāhoehoe, and shelly pāhoehoe), within the lava facies makes them difficult to discern using remote sensing data. However, Voigt et al., (in press) only applied aerial imagery and Digital Terrain Models (DTMs) generated from multi-view stereophotogrammetry to analyze the surface roughness of the lava facies. We can make

additional inferences using complimentary data sets, such as radar remote sensing and high-resolution LiDAR data.

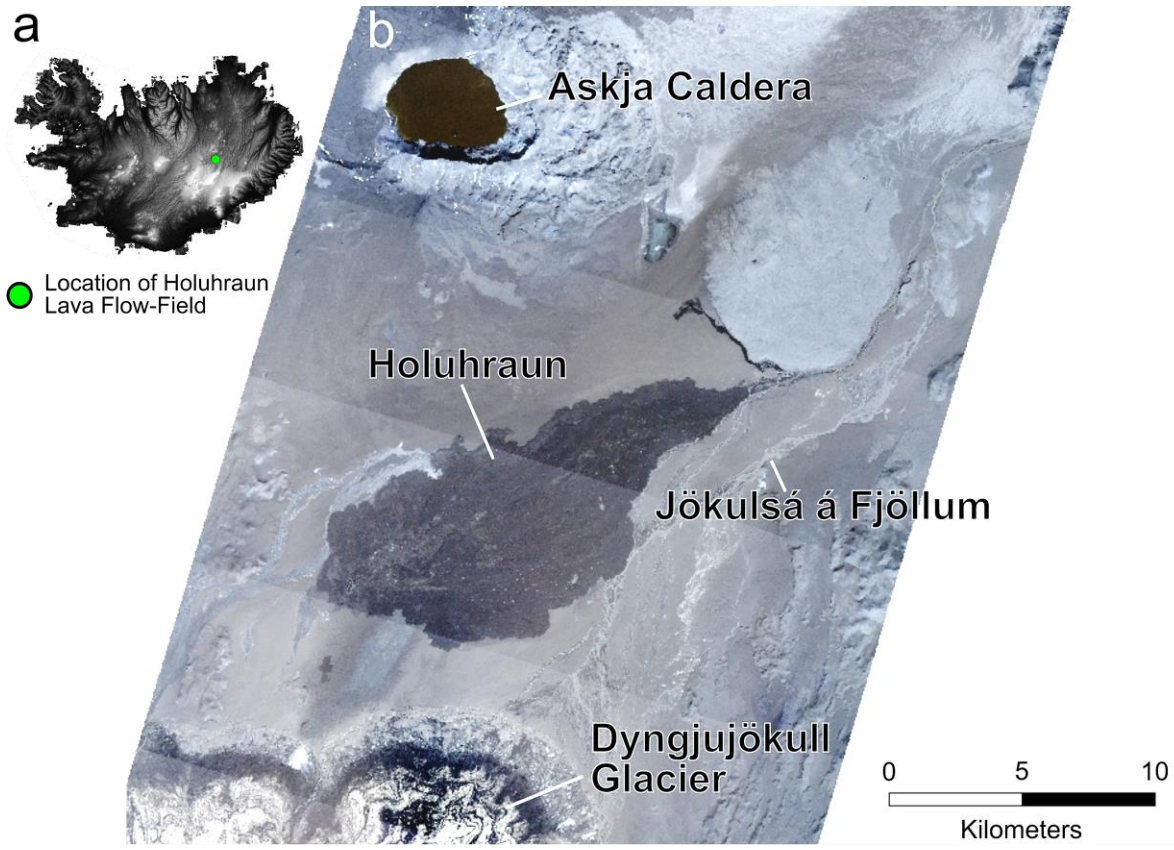

Figure 3.1. Location of the Holuhraun lava flow-field in central Iceland. (a) An ArcticDEM Digital Elevation Model (DEM) hillshade image of Iceland at 1 km/pixel scale shows the location of the lava field (green point). The ArcticDEM data was acquired from the National Geospatial-Intelligence Agency (NGA)-National Science Foundations (NSF) Initiative. (b) Mosaic of six RGB images (3 m/pixel) collected by the PlanetScope satellite constellation Dove CubeSats of the Holuhraun lava flow-field in between the Askja Caldera and the Vatnajökull glacier. The Dover CubeSats are operated by Planet (Planet Team, 2017) and the RGB images were collected on August 21st, 2020.

In this work, we utilize polarimetric radar remote sensing data to determine if the Holuhraun lava facies can be remotely differentiated from one another. Polarimetric radar is an active remote sensing technique that transmits and receives radar signals to acquire information about the physical and electric properties of surfaces (e.g., surface roughness and dielectric constants) (Carter et al., 2011; Neish and Carter, 2014; Neish et al., 2017). Quad-polarized Uninhabited Aerial Vehicle Synthetic Aperture Radar (UAVSAR) L-band (λ = 24 cm) and dual-polarized Sentinel-1 C-band (λ = 5.6 cm) radar data are available for the entire surface of the Holuhraun lava flow-field, providing the opportunity to analyze surface roughness at two different wavelengths. This will allow us to govern if one radar imaging mode is more efficient for differentiating the Holuhraun lava facies than another, helping us to determine which radar instruments should be prioritized for future planetary missions with a focus on planetary volcanism (e.g., Ghail et al., 2012; Hensley et al., 2012; Smrekar et al., 2016). The Holuhraun lava flow-field comprises eight facies (as mapped by Voigt et al., (2021)): rubbly (57.35%), spiny (25.96%), undifferentiated rubbly-spiny (9.59%), shelly (5.58%), pāhoehoe (1.24%), flat-lying knobby (0.58%), vent-proximal edifice (0.19%), and channel interior (0.16%). We focus on determining if polarimetric radar can differentiate the rubbly, spiny, and undifferentiated rubbly-spiny facies, since they are the dominant units (area coverage ~93%) and therefore record most of the lava flow-field emplacement history.

To compliment the radar analysis, we also seek to deconvolve the lava facies by analyzing the surface roughness of their lava flow types. The resolution of the Sentinel-1 and UAVSAR radar data sets are too coarse to discern the lava flow types within the lava facies. To discern them, we use roughness statistics calculated from high-resolution (cm-scale) topography data acquired from a kinematic LiDAR system.

3.1.1 Geologic Setting

The 2014–2015 Holuhraun lava flow-field (Figure 3.1) is situated on a fissure system associated with the Bárðarbunga–Veiðivötn volcanic system in Iceland. The eruption began on the 15th of August in 2014 when minor seismic swarm activity was detected beneath the northeastern flank of the Bárðarbunga volcano (Sigmundsson et al., 2015; Gudmundsson et al., 2016; Hjartardóttir et al., 2016; Bonny et al., 2018; Dirscherl and Rossi, 2018; Bonnefoy et al., 2019; Coppola et al., 2019). The seismic swarm propagated 48 km along a lineament to the northeast and terminated in a floodplain 8 km north of the Dyngjujökull outlet glacier (Bonnefoy et al., 2019) (Figure 3.1). On the 29th of August 2014, a fissure opened and erupted for ~4 hours. Following two days of hiatus, the fissure re-activated, and an effusive basaltic eruption began on the 31st of August 2014 and lasted until the 27th of February 2015. The transportation of lava during the eruption is described to have occurred in three stages: (1) channel-fed transportation, (2) lava ponding, and (3) tube-fed lava transport (Pedersen et al., 2017). By the end of the eruption, a total estimated dense rock equivalent (DRE) volume (assuming mean bulk lava void space of 15 to 20%) of 1.2 ± 0.1 km^3 (Bonny et al., 2018) had erupted onto the floodplain, covering an area of ~83.82 km^2 (Voigt et al., 2021). The Holuhraun eruption is documented as the largest effusive basaltic eruption to have occurred in Iceland since the 1783–1784 Laki eruption and has a bulk composition consistent with an olivine tholeitte (Halldórsson et al., 2018).

3.1.2 Geologic Background: Holuhraun Lava Facies

Here, we summarize the lava facies and their corresponding lava flow types to provide geologic context for this work. We refer to Voigt et al., (2021), for a more detailed and in-depth discussion on the morphology and textures of the facies and their field and remote sensing interpreted emplacement history.

From the three most dominant Holuhraun lava facies, the rubbly facies cover the largest area of the lava flow-field (57.35%). The surface of the rubbly facies exhibits centimetre to metre-scale clasts with shapes ranging from blocky to slabby. The facies margins have steep-sided lobes, while the interior exhibits a rubbly texture with flow-aligned lineation's and ridge-and-trough structures oriented perpendicular to the flow direction. Inside the lava facies, it is composed primarily of rubbly pāhoehoe lava flows with minor amounts of slabby pāhoehoe and ʻaʻā. The spiny facies (25.96%) is situated primarily in the northeastern and northern regions of the lava flow-field. For the most part, the spiny facies have a coherent crust, but exhibit localized areas with a fractured and brecciated surface. In the interior of the flow, the spiny facies have hummocky surfaces with a variety of volcanic structures, including lobes, lava-rise pits, and tumuli (Mattsson and Höskuldsson, 2005; Harris et al., 2017; Hamilton et al., 2020). The spiny facies are composed primarily of spiny pāhoehoe lava flows with minor amounts of slabby pāhoehoe, rubbly pāhoehoe, toothpaste lava, and ʻaʻā. The last facies - the undifferentiated rubbly-spiny - is a combination of the rubbly and spiny facies.

3.2 Methods

3.2.1 Radar Processing

3.2.1.1 UAVSAR Quad-Polarized L-Band Radar

To analyze the surface roughness of the rubbly, spiny, and undifferentiated rubbly-spiny facies, we calculated the circular polarization ratio (CPR) from radar data acquired by the quad-polarized L-band (λ = 24 cm) UAVSAR (Rosen et al., 2006) airbourne platform and VH/VV polarization ratios from dual-polarized C-band (λ = 5.6 cm) radar data from the European Space Agency (ESA) Sentinel-1 satellite (Torres et al., 2012). UAVSAR observations were obtained on May 30th, 2015, on flights 15083 DT 4 and DT 5. CPR is defined as the ratio of the same-sense circular (SC) polarization of the transmitted radar signal to the opposite-sense circular (OC) polarization of the transmitted signal (Neish and Carter, 2014). Smooth surfaces (e.g., lava ponds) typically return a lot of OC backscatter because of their single-bounce, mirror-like reflections (quasi-specular scattering) that flip the polarization of the transmitted signals. This produces low CPR values (<0.5). Rough surfaces (e.g., ‘a‘ā clinker) scatter signals in multiple directions, returning an approximately equal number of SC and OC signals (volume/diffuse scattering). Rough surfaces typically produce CPR values that approach one (0.5–1.0). CPR exceeds unity when signals reflect off rock edges and cracks or natural corner reflectors (e.g., polyhedral blocks with smooth facets). This produces double-bounce backscatter (dihedral scattering), which flips the polarization twice and thus increases the SC backscatter (Campbell, 2012).

The UAVSAR data was downloaded as orthorectified data products from the Jet Propulsion Laboratory (JPL) UAVSAR site (https://uavsar.jpl.nasa.gov). The data represent components of the scattering matrix, present as combinations of vertical (V) and horizontal (H) transmit and receive polarizations, including $S_{hh}S_{hh}$*, $S_{vv}S_{vv}$*, $S_{hv}S_{hv}$*, $S_{hh}S_{hv}$*, $S_{hv}S_{vv}$*, and $S_{hh}S_{vv}$*. To obtain the CPR values for each lava facies, we calculated the compressed Stokes Matrix parameters W_{11}, W_{14} and W_{44} from the scattering matrix (Zebker and Lou, 1990; Campbell, 2002) (Equation 3.1-3.3), and used these to calculate the SC and OC backscatter (Equation 3.4-3.5) values and the CPR (Equation 3.6).

$$W11 = 0.25 * [S_{hh}S_{hh} + S_{vv}S_{vv} + 2*[S_{hv}S_{hv}]] \quad \text{Equation 3.1}$$

$$W14 = -0.5 * [S_{hh}S_{hh} + S_{hv}S_{vv}] \quad \text{Equation 3.2}$$

$$W44 = 0.5 * [S_{hv}S_{hv} - S_{hh}S_{vv}] \quad \text{Equation 3.3}$$

$$SC = W11 + 2*W14 + W44 \quad \text{Equation 3.4}$$

$$OC = W11 – W44 \quad \text{Equation 3.5}$$

$$CPR = SC/OC \quad \text{Equation 3.6}$$

The VH/VV polarization ratios were calculated using the backscatter coefficient (σ^0, dimensionless radar scattering cross-section per unit area (Campbell, 2002)) of two orthogonal polarization states, σ^0_{VH} and σ^0_{VV}, obtained by the Sentinel-1 satellite. To obtain the backscatter coefficients, we processed Level-1 Ground Range Detected (GRD) Sentinel-1 data using the freely available SeNtinel Application Program (SNAP) developed by ESA. The GRD products

consist of multi-looked SAR images that were projected to ground range using the Earth ellipsoid model WGS84. We used radiometric calibration tools to convert the amplitude and phase of the returned radar signals to σ^0_{VH} and σ^0_{VV} (Figure 3.3a-b). Following radiometric calibrations, the σ^0 images in SNAP were converted to readable TIF files for ArcGIS, where they were georeferenced to overlie multispectral imagery of the lava flow-field and the UAVSAR CPR data.

3.2.2 Extracting and Analyzing Radar Data

Following the steps described above to produce CPR and VH/VV ratio images (Figures 3.2 and 3.3c), we reduced the radar speckle noise using a low-pass filter tool in ESRI ArcGIS (version 10.7-10.8). The lowpass filter averaged the pixel values in the CPR and VH/VV data over a 3 × 3 pixel area, increasing the number of looks per pixel from 9 to 81 (Tolometti et al., 2020). After the low-pass filter was applied, we extracted the mean CPR and VH/VV ratios from the lava facies polygons traced by Voigt et al., (2021). These lava facies polygons are freely accessible as a geodatabase on the University of Arizona Campus Repository (Voigt and Hamilton, 2021)).

We excluded all CPR data extracted from the westernmost UAVSAR data set (Flight 15083 D5). This is because the flight observation has an incidence angle >65°, which is approximately 10° greater than the max incidence angle in the easternmost UAVSAR observation (Flight 15083 DT 4), which covers the majority of the lava flow-field. CPR increases with increasing incidence angle (Campbell, 2002; Carter et al., 2004, 2011), and thus these values would not be comparable to the CPR values in the other UAVSAR image (Flight 15083

D4). The Sentinel-1 radar data is not influenced by large differences in incidence angle because of the greater altitude of the orbiter compared to the low-flying UAVSAR airbourne platform. Despite this however, we restricted our analysis to the rubbly, spiny, and undifferentiated rubbly-spiny facies in the main body of the lava flow-field west of the vent to facilitate the comparison between the dual and quad-polarized radar results.

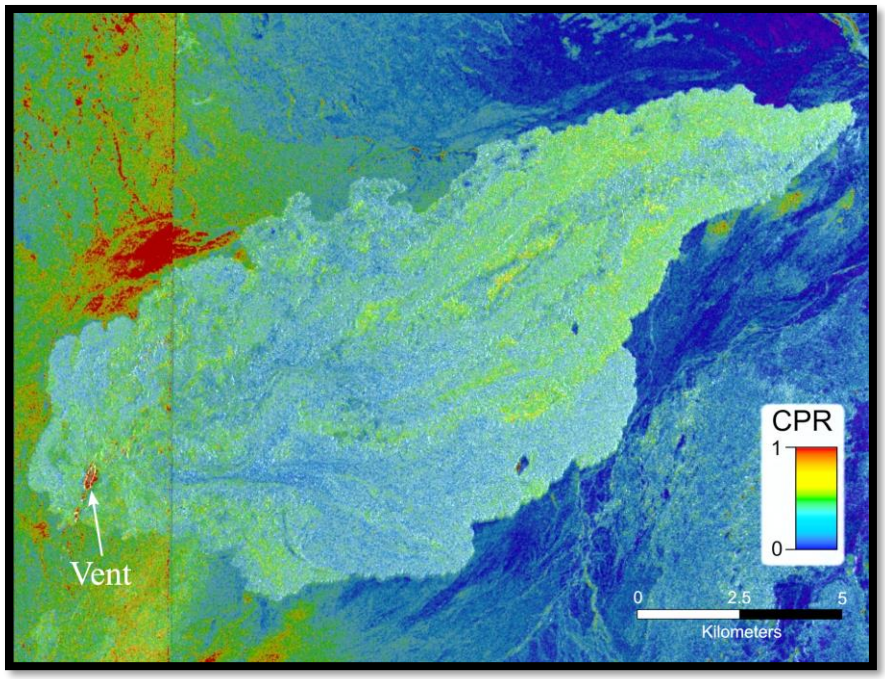

Figure 3.2. A circular polarization ratio (CPR) image (5 m/pixel), overlaid on a total backscatter image, of the Holuhraun lava flow-field calculated from polarimetric radar data acquired by the UAVSAR airbourne platform. The CPR image is a mosaic of two UAVSAR flight swaths collected in May 2015 (ID: PolSAR: Flight 15083 (2015-05-30), DT 4, v1 (right strip: main body of lava flow-field) and PolSAR: Flight 15083 (2015-05-30), DT 5, v1 (left strip: vent of lava flow-field). The speckle noise was reduced in the image by applying a low-pass filter, increasing the number of looks from 9 to 81. Note that the image on the left is east-looking, and the image on the right is west-looking. As a result, the highest incidence angles are near the image seam (N-S oriented line east of the vent).

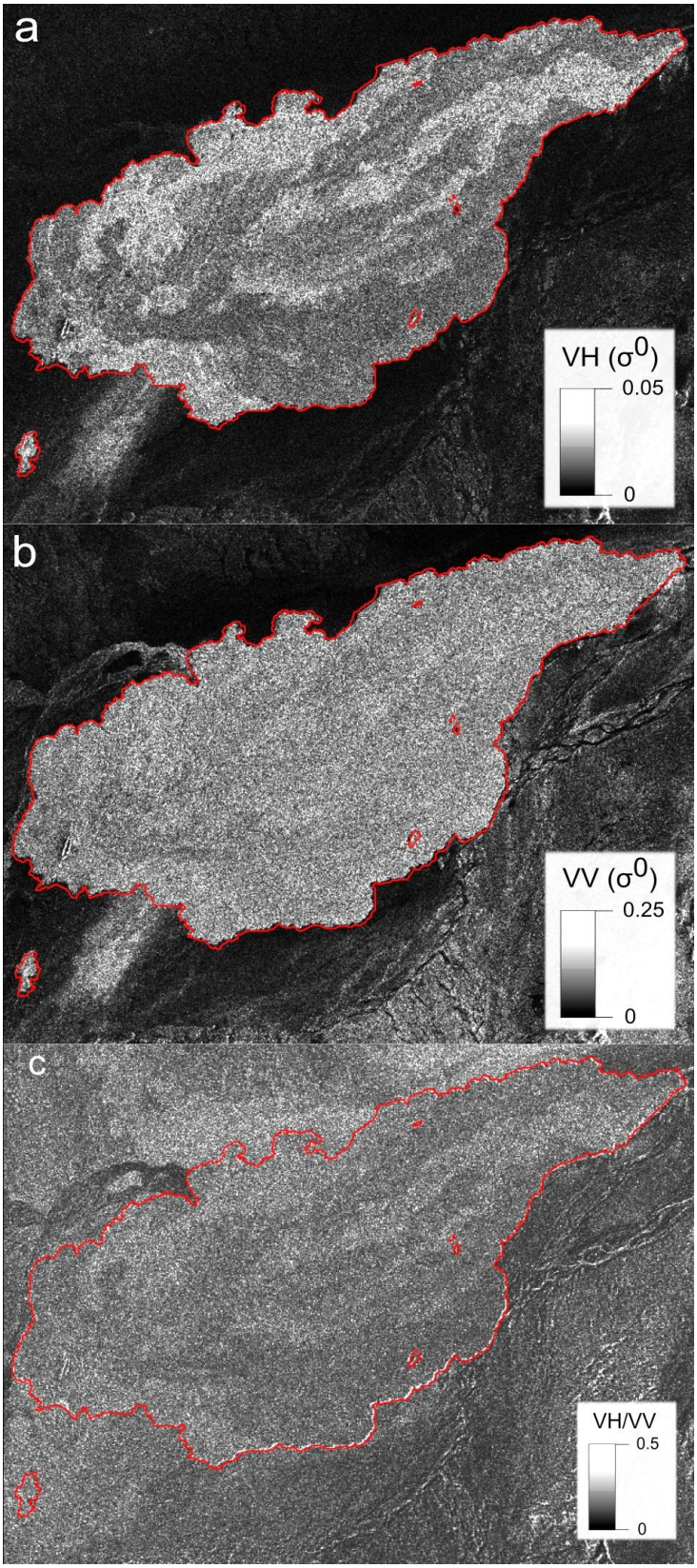
a
VH (σ^0)
0.05
0
b
VV (σ^0)
0.25
0
c
VH/VV
0.5
0

Figure 3.3. Dual-polarization Sentinel-1 C-Band radar image of the Holuhraun lava flow-field. The Sentinel-1 data was acquired on August 6th, 2019 and was processed by the European Space Agency (ID - S1B_IW_GRDH_1SDV_20190806T073250_20190806T073315_017462_020D76_0DA9) on August 31st, 2019 (Copernicus Sentinel data 2015). The data was downloaded as Ground Range Detection products and were calibrated using ESA's SNAP software. Image is set to a WGS84/UTM Zone 28 projection, centered at 65°12'14°N; 17°56'45°W, and has a 10 m/pixel resolution. (a) Image of the σ^0_{VH} polarization data. (b) Image of the σ^0_{VV} polarization data. (c) VH/VV ratio image.

In addition to extracting CPR and VH/VV polarization ratios, we produced two polarimetric radar threshold maps showcasing different radar data ranges. We subdivided the CPR and VH/VV data into five ranges (CPR: 0 – 0.2, 0.2 – 0.4, 0.4 – 0.6, 0.6-0.8, and 0.8 – >1.0 and VH/VV: 0.0 – 0.2, 0.2 – 0.4, 0.4 – 0.6, 0.6 – 0.8, 0.8 – >1.0). Before setting the above thresholds, we reduced any remaining speckle noise in the SAR data by applying an Enhanced Lee filter using the Image Analysis Speckle Function tool in ArcGIS. The Enhanced Lee Filter reduces speckle noise while minimizing the loss of radiometric and textural characteristics in the radar images (Lee and Pottier, 2018). This filter was not used previously when extracting CPR and VH/VV data because we did not need to worry about preserving textural characteristics to get those results. We set the Enhanced Lee Filter size to 9 × 9 looks because it marks the point at which the reduction in speckle noise is no longer beneficial, and if we increased the number of looks beyond it we would begin to lose radiometric and textural characteristics (López-Martínez and Fàbregas, 2008; Lee and Pottier, 2018).

3.2.3 Topography Data

High-resolution 3D topographic LiDAR data was collected using the AKHKA-R4DW kinematic dual-wavelength laser scanning system (Kukko et al., 2020). The kinematic LiDAR system collected dense point clouds from ~50 m × ~50 m areas covering different lava flow type surfaces within the lava facies. Surfaces were scanned by a Riegl VUX-1-HA that illuminates a target with a laser at 1017 kHz pulse frequency and 250 lines/second, measuring the ground range values. The scanner operates at a wavelength of 1550 nm. A second laser scanner, a Riegl miniVUX-1UAV, was used in conjunction with the primary scanner, operating at a wavelength of 905 nm and providing 100 kHz pulse frequency and 100 lines/second. Both laser scanning systems have a 360° Field of View (FoV) to map surrounding areas in cross-track scanning, but there is a 30-degree angle between the scan planes of the two. A Labybug5+ panoramic camera (FLIR systems, Inc., USA) was used to collect imagery synchronously with the other data. A GNSS (Global Navigation Satellite System) receiver and antenna attached to the instrument provided absolute global positioning in the field based on GPS (Global Positioning System) and GLONASS (a space-based Global Navigation Satellite System) constellation satellites aided with a stationary base station for differential processing. Sensor orientation and short-term dynamics are captured with near navigation grade inertial measurement unit, data of which is fused in tightly coupled processing of the trajectory (Waypoint Inertial Explorer, NovAtel Inc., Canada). After raw data calibration and processing using Riegl RiProcess and RiPrecision software modules (RIEGL Laser Measurement Systems GmbH, Austria), the point clouds were converted into digital elevation models (DEM) using ESRI ArcGIS. The maximum resolution set for the DEMs in this work is 5 cm/pixel, equal to the max resolution of some of the stereo-derived

DTMs used by Voigt et al., (in press) to analyze the topographic roughness of the Holuhraun lava facies.

Metre-scale surface roughness measurements of the lava facies were also obtained from ArcticDEM topography data. The ArcticDEM data was acquired from the National Geospatial Intelligence Agency (NGA)-National Science Foundations (NSF) Initiative and constructed from in-track and cross-track high-resolution (0.5 m) stereoimagery acquired from the DigitalGlobe constellation (WorldView-1, WorldView-2, WorldView-3, and GeoEye-1 optical imaging satellites). We downloaded the 2 m/pixel topography data tile that covers the entire Holuhraun lava flow-field from the NGA ArcticDEM Web Map database (https://www.pgc.umn.edu/data/arcticdem/), produced on July 22nd, 2018 (ID: 16_54_2m_reg_dem).

3.2.4 Topographic Roughness Statistics

To extract topographic roughness statistics from the LiDAR and ArcticDEM topography data, we calculated the root-mean-square (RMS) slope and Hurst exponent (*H*), which are parameters recommended by Shepard et al. (2001) for surface roughness characterization. The RMS slope is described as the standard deviation of slopes about a mean along a set profile (Shepard et al., 2001). The *H* value describes the scaling behaviour of a surface, i.e. how roughness changes with changing scale. *H* values can range from 0 to 1. When *H* approaches 0, it indicates that the surface becomes smoother or rougher as the scale increases. If *H* approaches 1, it indicates that surface roughness remains unchanged with an increase in scale. Typically,

natural surfaces fall around $H \approx 0.5$, termed as Brownian behaviour. This is because natural surfaces are complex and are composed of different surface roughness elements with a variety of sizes (Shepard et al., 2001).

To calculate RMS slope, we first needed to calculate the Allan variance (v^2) (Equation 3.7), which samples the topographic profile (z_i) at every interval step (Δx).

$$v^2(\Delta x) = \frac{1}{n}\sum_{i=1}^{n}[z(x_i) - z(x_i + \Delta x)]^2 \quad \text{Equation 3.7}$$

The value n represents the number of sample points in the topographic profile (examples are shown in Figure 3.4), and $z(x_i)$ is the height of the surface at point x_i. Using values from Equation 3.7, we calculated RMS slope using Equation 3.8,

$$RMS_{slope} = \frac{v(\Delta x)}{\Delta x} \quad \text{Equation 3.8}$$

We calculated *H* using Equation 3.9 where Δx_0 is the set reference scale (Figure 3.5). For some surfaces, one *H* value is not enough to describe roughness. Breakpoints can occur when the roughness transitions from one *H* value to another (Figure 3.5, breakpoint at $\Delta x = 0.2$ m for the rubbly pāhoehoe surface), assumed to represent different processes that either produced or modified the surface (Shepard et al., 2001).

$$v(\Delta x) = RMS_{slope}\left(\frac{\Delta x}{\Delta x_0}\right)^H \quad \text{Equation 3.9}$$

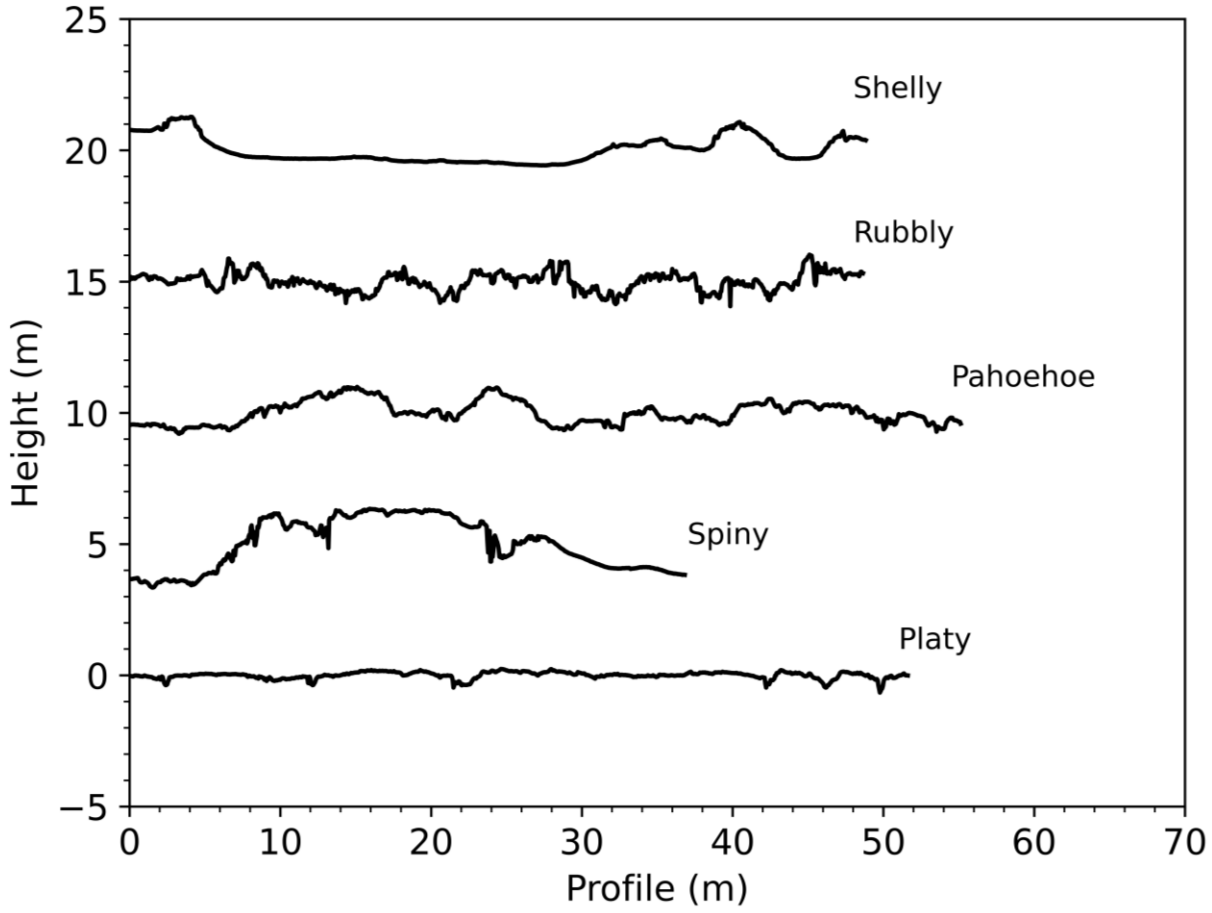

Figure 3.4. Topographic profiles of the four Holuhraun lava flow types and a subset of the spiny pāhoehoe (platy; plate-ridged structures and extension zones with toothpaste-like lava squeeze-ups) extracted from DEMs with a horizontal resolution of 5 cm/pixel. A best-fit line was removed from the profile, to correct for any regional slope. Each profile is offset by 5 m to prevent data overlap. The topographic profiles were extracted from the following LiDAR Data (see Table 3.3): 20190801_1_c (Shelly), 20190803_1_a (Rubbly), 20190805_1_a (Pāhoehoe), 20190803_1_c (Spiny), and 20190729_2_d (Platy).

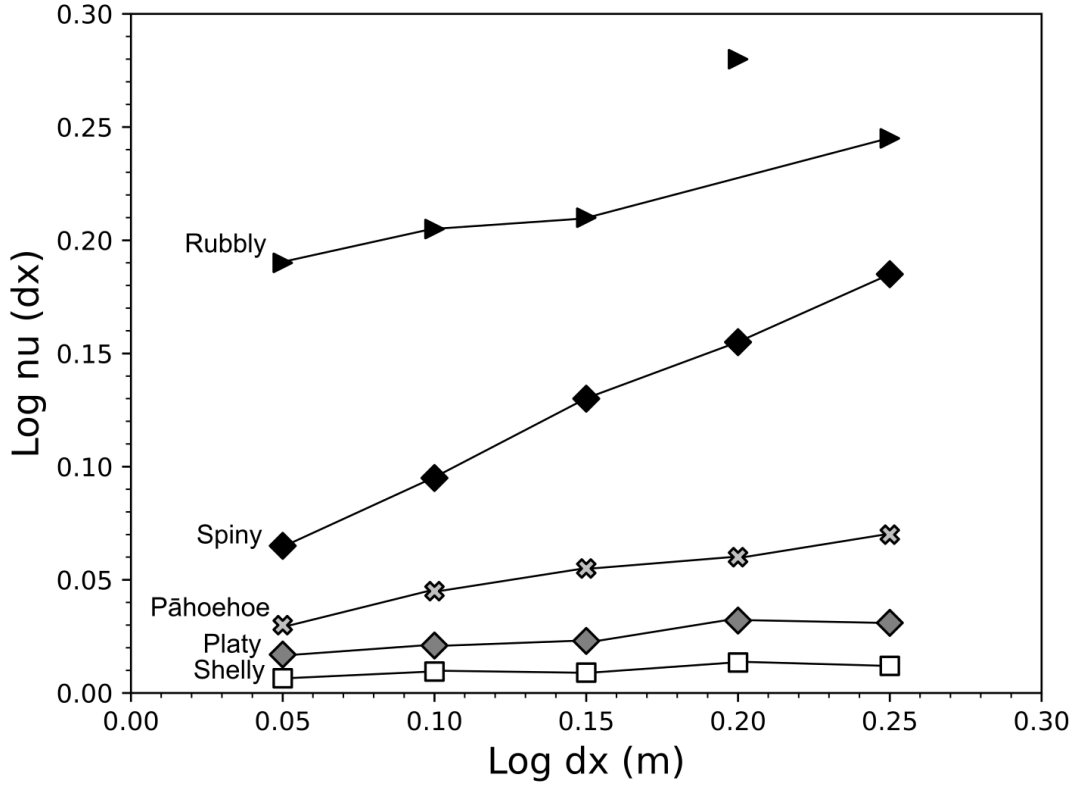

Figure 3.5. Variograms of the lava flow types and a subset variants of the spiny pāhoehoe (platy; plate-ridged structures and extension zones with toothpaste-like lava squeeze-ups) plotted using data from the topographic profiles shown in Figure 3.4. Points are plotted every 5 cm between 5 cm and 25 cm. H is the slope of the line and the RMS slope is related to the *y*-intercept of the variogram.

Three profile lengths were selected for this study to incorporate a range of surface roughness measurements at different scales (centimetre-scale, decimetre-scale, and metre-scale). The first profile length was set at 2.5 m to obtain roughness statistics over a 0.05 m to 0.25 m reference scale with step intervals of 0.05 m. The second profile length was set at 20 m to obtain

roughness statistics over a 0.25 m to 2 m reference scale with step intervals of 0.25 m. The third profile length, which was only applied to the metre-scale ArcticDEM data, was set at 100 m to obtain roughness statistics over a 2 m to 12 m reference scale with step intervals of 2 m. We adhered to the recommendations by Shepard et al., (2001) that the profile length should be approximately 10 times the size of the largest value in the set reference scale. Both the second and third reference scales have been used to study the surface roughness of lava flows and impact melt flows on terrestrial planetary bodies (e.g., Campbell and Shepard, 1996; Shepard et al., 2001; Neish et al., 2017; Rodriguez Sanchez-vahamonde and Neish, 2021).

We extracted the 2.5 m and 20 m profiles along the lava surfaces in the LiDAR DEMs, and the 100 m profiles along the lava facies in the ArcticDEM data in 2-D perpendicular directions (across and along flow). We detrended the profiles by removing the best-fit linear function from the data and calculated the Allan variance. The final step involved extracting the RMS slope and *H* from the resultant variograms. This process was repeated with the starting point on the DEM increasing by one-pixel until we reached the end of the first row of data. We then repeated this for each row until each pixel was assigned an RMS slope and *H* value. We extracted the mean and standard deviation of the RMS slope and *H* from the produced raster's (see Figure 3.10) using the zonal statistics tool in ArcGIS.

3.3 Results

3.3.1 Lava Flow Types: Field Observations

The surface roughness of the lava flow types within the lava facies are described using field observations (Figure 3.6) and the high resolution DEMs derived from the kinematic LiDAR data. Due to accessibility and the cohesive strength of some of the lava flow types crust, we were only able to analyze the lava flow types within two of the dominant lava facies: rubbly and spiny. The undifferentiated rubbly-spiny facies are situated too far from the margins of the lava flow-field to access on foot safely. The lava flow types in this facies can only be documented using aerial imagery, which have been reported by Voigt et al., (2021). In the rubbly facies we were able to analyze a rubbly pāhoehoe lava flow type. In the spiny facies, we were able to analyze spiny pāhoehoe lava flow types, including one morphological subset of a spiny pāhoehoe: a spiny surface with plate-ridged structures and extension zones with toothpaste-like lava squeeze-ups. Although not part of the radar analysis portion of this research, we also collected data from the shelly and pāhoehoe facies situated east and southeast of the volcanic vent.

The rubbly pāhoehoe lava is comprised of rounded to subangular clasts with fractured and vesicular textures. Large, metre-scale boulders are present on the surface near the distal regions of the lava flow-field (at the flow end in the northeast, see Figure 3.1); where the clast size distribution is the most chaotic and heterogenous (Bonnefoy et al., 2019) (Figure 3.6a). Viscously torn lava was identified in conjunction with the rubbly pāhoehoe lava in some locations along the northern and northeastern region of the lava flow-field, resembling the traditional ‘a‘ā clinker texture. However, these textures were not analyzed using the kinematic LiDAR system as it was difficult to acquire ~50 m × ~50 m scans on these surfaces.

The surface of the spiny pāhoehoe lava is rough and irregular at the millimetre to centimetre-scale, with elongate spines oriented parallel to the local flow direction. The spiny facies along the northern and western margins of the lava flow-field exhibit a hummocky surface, containing a network of coalesced spiny pāhoehoe lobes and toes that later inflated (Figure 3.6b). The interior of the spiny facies contains inflation plateaus with a solidified surface and wave-like structures known as lava waves, which have spinose textures with spines oriented perpendicular to the front of the lava waves. In some regions of the inflation plateaus are platy surfaces (Figure 3.6c) bounded by extension fractures with extrusions of toothpaste-like lava and collision ridges composed of disrupted slabs of the once coherent spiny pāhoehoe crust. For simplicity, in the rest of this study we label the platy surface containing spiny pāhoehoe, slabs of spiny crust, and toothpaste lava as platy lava. Within the inflation plateaus, we documented circular and elliptical lava-rise pits that formed via the inflation of the spiny pāhoehoe surface during later stages of the eruption (Figure 3.6d).

The shelly pāhoehoe lava flow type in the shelly facies has a coherent crust similar to the spiny pāhoehoe lava flows (Figure 3.6e). It is only found along the northern and eastern margins of the volcanic vent and inside an E-W oriented channel that fed lava into the central region of the lava flow-field (Pedersen et al., 2017; Bonnefoy et al., 2019; Voigt et al., 2021). Unlike the spiny pāhoehoe lava, excavation of lava and/or gas from the flow interior left behind a thin (<10 cm) shell with empty voids reaching depths 10s of centimetres to a few metres. The fragility of the shelly crust limited the areas where we could acquire LiDAR scans of the surface. We were only able to acquire scans along the eastern margin of the vent where the coherent strength of the crust was durable enough to allow us to traverse and cover ~50 m × ~50 m areas. This area is the

location of a lava pond that drained during the early to mid-stages of the Holuhraun eruption (Pedersen et al., 2017).

The pāhoehoe lava flow type in the pāhoehoe facies has a classic smooth and hummocky coherent crust with ropes, wrinkles, and billows on its surface (Figure 3.6f). Lobate features and toes are stacked into sheet-like structures in the pāhoehoe lava, ranging in size and thickness. Upon closer inspection of the pāhoehoe crust, we note that the surface exhibits millimetre to centimetre-size spines, similar to the spines present on the surface of the spiny pāhoehoe and toothpaste lava in the spiny facies.

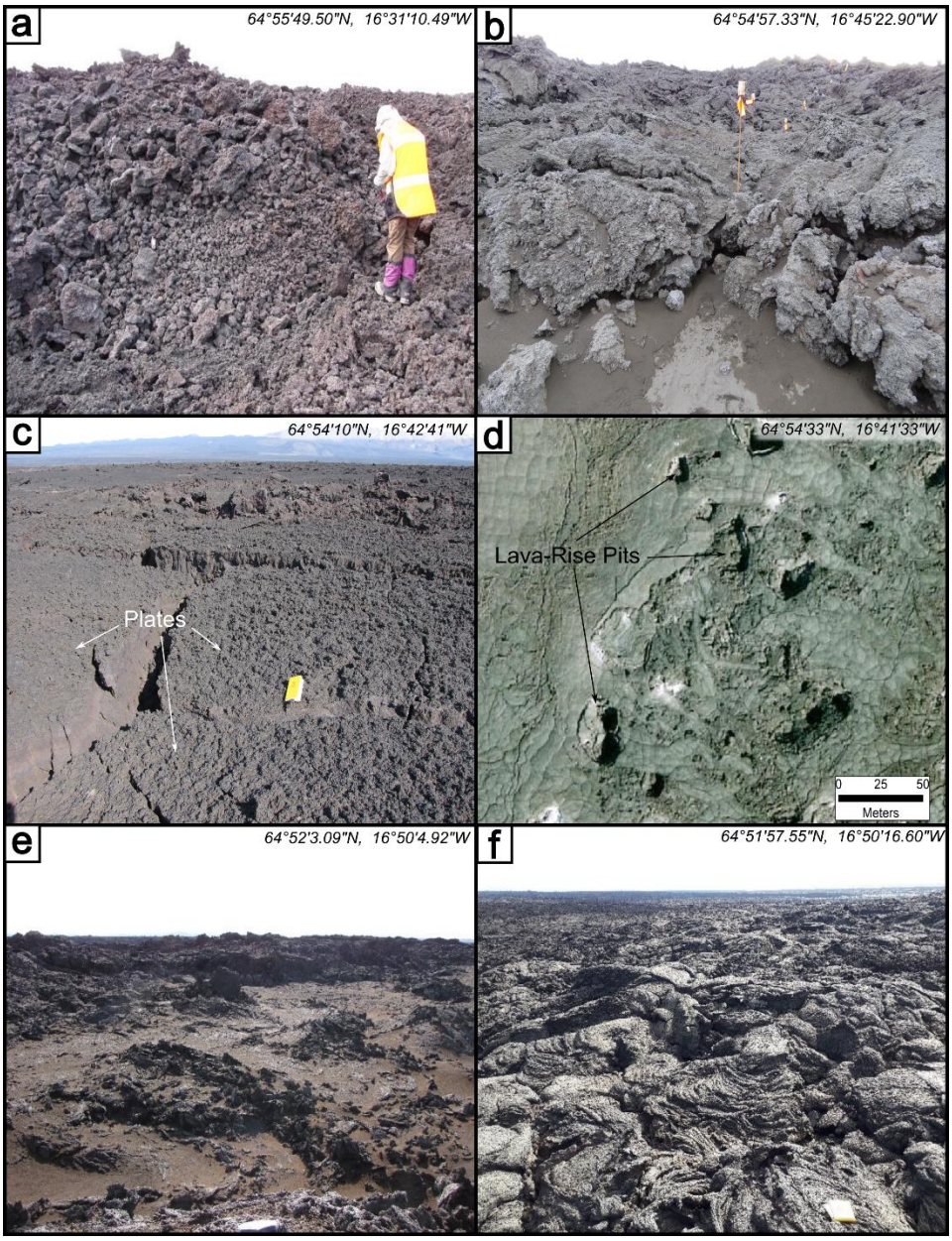

Figure 3.6. The lava flow types and morphological subsets studied at Holuhraun. (a) Rubbly pāhoehoe lava with centimetre to decimetre-scale fragments of a once coherent crust. Some fragments exhibit block-shapes similar to blocky lava surfaces. (b) Spiny pāhoehoe lava along the margins of the lava flow-field. (c) Plate-ridged (i.e., Platy) morphology within the spiny facies. Plates are separated by extrusions of toothpaste lava squeeze-ups and slabby collision ridges. (d) Spiny pāhoehoe lava flow surface with lava-rise pits (no field image was available;

this is a high resolution (15 cm/pixel) aerial image taken by the company Loftmyndir.ehf (https://www.loftmyndir.is/)). (e) Shelly pāhoehoe with a fragile spiny pāhoehoe-like crust near the eastern margin of the vent. (f) Pāhoehoe lava with a hummocky and lobate morphology along the east and south margins of the vent.

3.3.2 Radar Surface Roughness

To determine whether polarimetric radar is capable of differentiating the rubbly, spiny, and undifferentiated rubbly-spiny facies at the Holuhraun lava flow-field, we extracted CPR and VH/VV ratios from UAVSAR and Sentinel-1 radar data using the lava facies polygons traced by Voigt et al., (2021). We obtained the average CPR and VH/VV from each lava facies polygon, except for the polygons proximal to the vent.

The results show that all three facies return moderate CPR values, with the spiny facies returning the lowest mean CPR overall (Figure 3.7a). The spiny facies returned a CPR value of 0.45 ± 0.08, the rubbly facies a CPR value of 0.47 ± 0.1, and the undifferentiated rubbly-spiny facies a CPR value of 0.47 ± 0.09. From the Sentinel-1 data, the rubbly and undifferentiated rubbly-spiny facies also return similar VH/VV ratios, but with greater data overlap than the UAVSAR CPR data (Figure 3.7b). The rubbly facies return a mean VH/VV of 0.21 ± 0.13 while the undifferentiated rubbly-spiny facies return 0.20 ± 0.13. The spiny facies are more distinguishable from the rubbly and undifferentiated rubbly-spiny facies in the dual-polarized radar data, returning a lower mean VH/VV polarization ratio of 0.16 ± 0.09. The spiny facies in the northern and northeastern regions of the lava flow-field have a greater VH/VV ratio compared to the rubbly facies and undifferentiated rubbly-spiny facies (Figure 3.3). The rubbly

facies in the central and southern regions of the lava flow-field show some of the lowest VH/VV results and σ^0_{VH} values (see Figure 3.3).

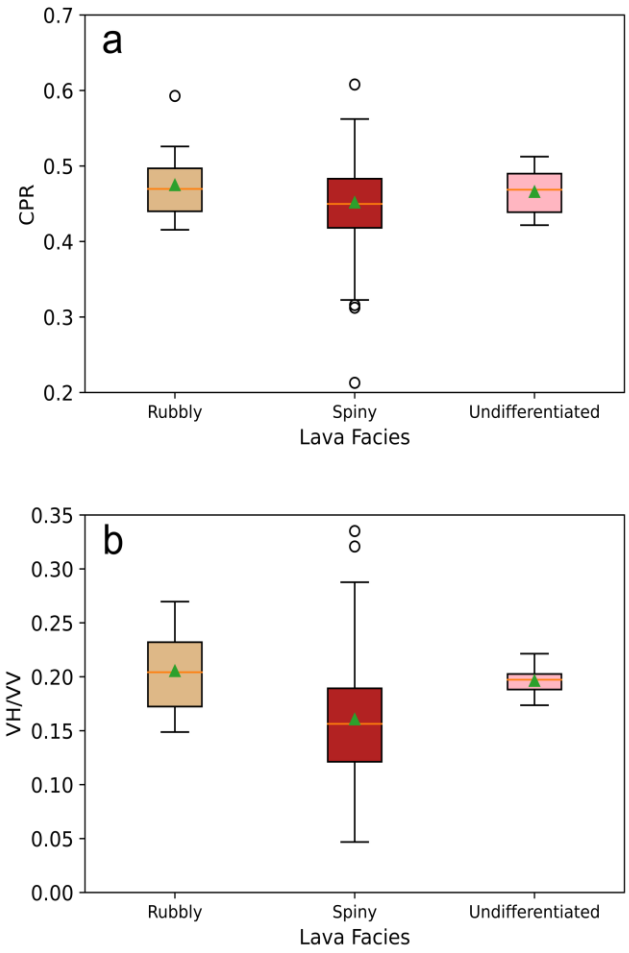

Figure 3.7. Boxplots showing the average mean (green triangle), median (pink line), outliers (white circles), and distribution of the Holuhraun lava facies radar data. (a) CPR values extracted from the rubbly, spiny, and undifferentiated rubbly-spiny facies. The data extracted from the spiny facies polygons is the most diverse, but the means of the three facies show only subtle differences. (b) VH/VV ratios extracted from the rubbly, spiny, and undifferentiated rubbly-spiny facies. Similar to the L-Band CPR, the spiny facies show the greatest variation in mean VH/VV, but unlike the CPR results, the VH/VV of the three facies appear more separable.

From the CPR and VH/VV threshold maps (Figures 3.8 and 3.9) we observe some similarities between the Holuhraun lava facies. In the CPR threshold map (Figure 3.8) we observe a noticeable difference between the rubbly and spiny facies across the lava flow-field. In the northeastern and northwestern region, the rubbly facies appear to have a greater CPR (Figure 3.8b), standing out from the spiny facies that also covers a large extent of these regions (Figure 3.8c). The rubbly facies in the northeastern and northwestern regions comprise small areas with CPR ranging from 0.6 – 0.8, whereas the spiny facies return no CPR greater than 0.6. In the central and southern regions however, the rubbly facies CPR has a lower CPR than the spiny facies (Figure 3.8c). The undifferentiated rubbly-spiny facies are more challenging to discern since it returns CPR similar to the rubbly facies (Figure 3.8d). The VH/VV threshold map (Figure 3.9) shows very similar patterns, with the rubbly and spiny facies showing differences in returned radar data (Figures 3.9b-c). A major difference is that the undifferentiated rubbly-spiny facies are more comparable to the spiny facies than the rubbly facies (see Figures 3.9c-d).

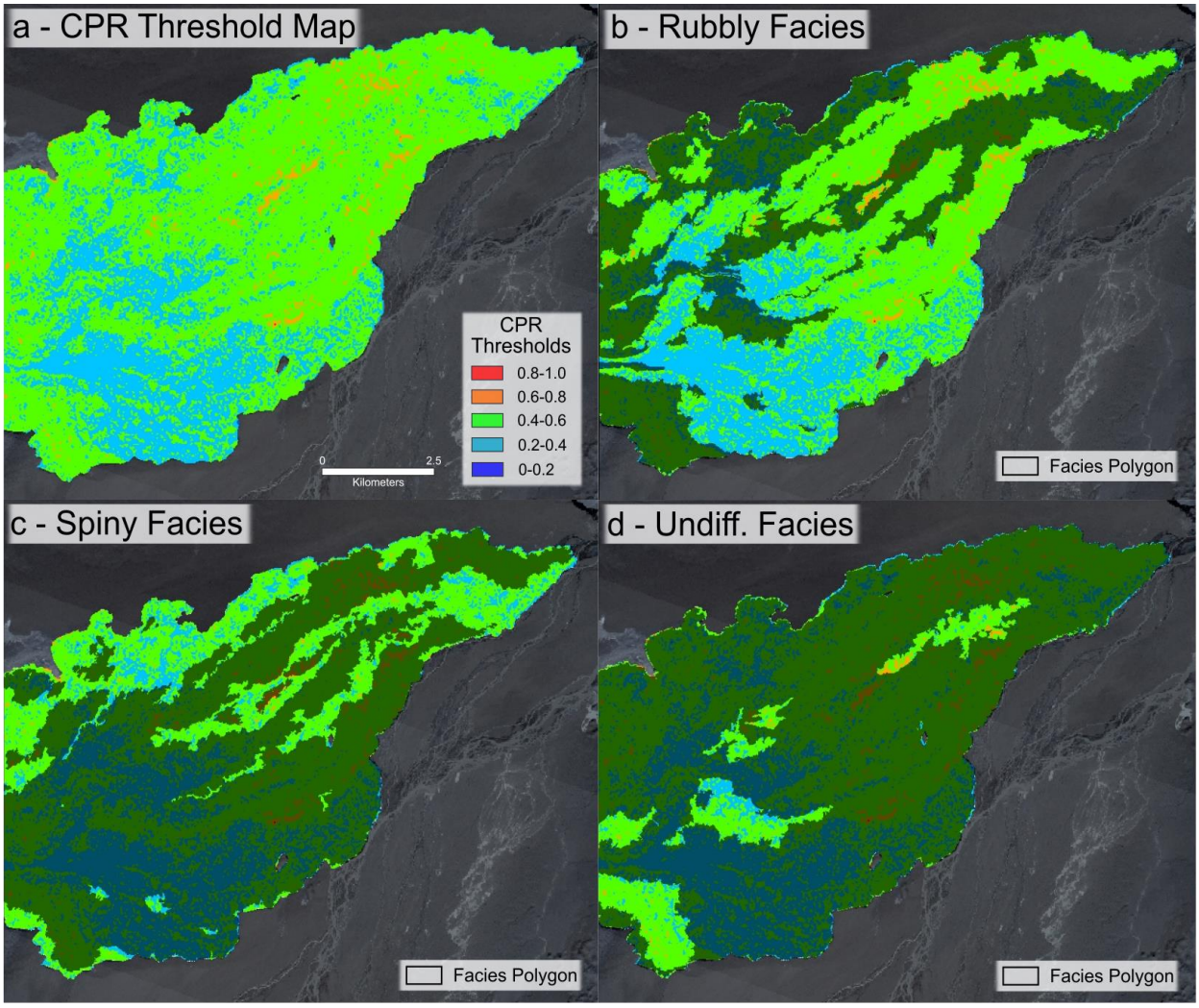

Figure 3.8. A threshold map of the UAVSAR CPR data overlaid with the lava facies polygons available from Voigt and Hamilton, (2021). In images b-d, the described facies are highlighted by graying out the adjacent facies in the lava flow-field (e.g., the spiny and undifferentiated facies are grayed out to highlight the rubbly facies). (a) CPR threshold map of the 2014-2015 Holuhraun lava flow-field produced by applying a 9 × 9 Enhanced Lee filter to the CPR data. Vent region is not included in this image due to the greater incidence angles of the UAVSAR observation. (b) Rubbly facies in the CPR threshold map. (c) Spiny facies in the CPR threshold map. (d) Undifferentiated rubbly-spiny facies in the CPR threshold map.

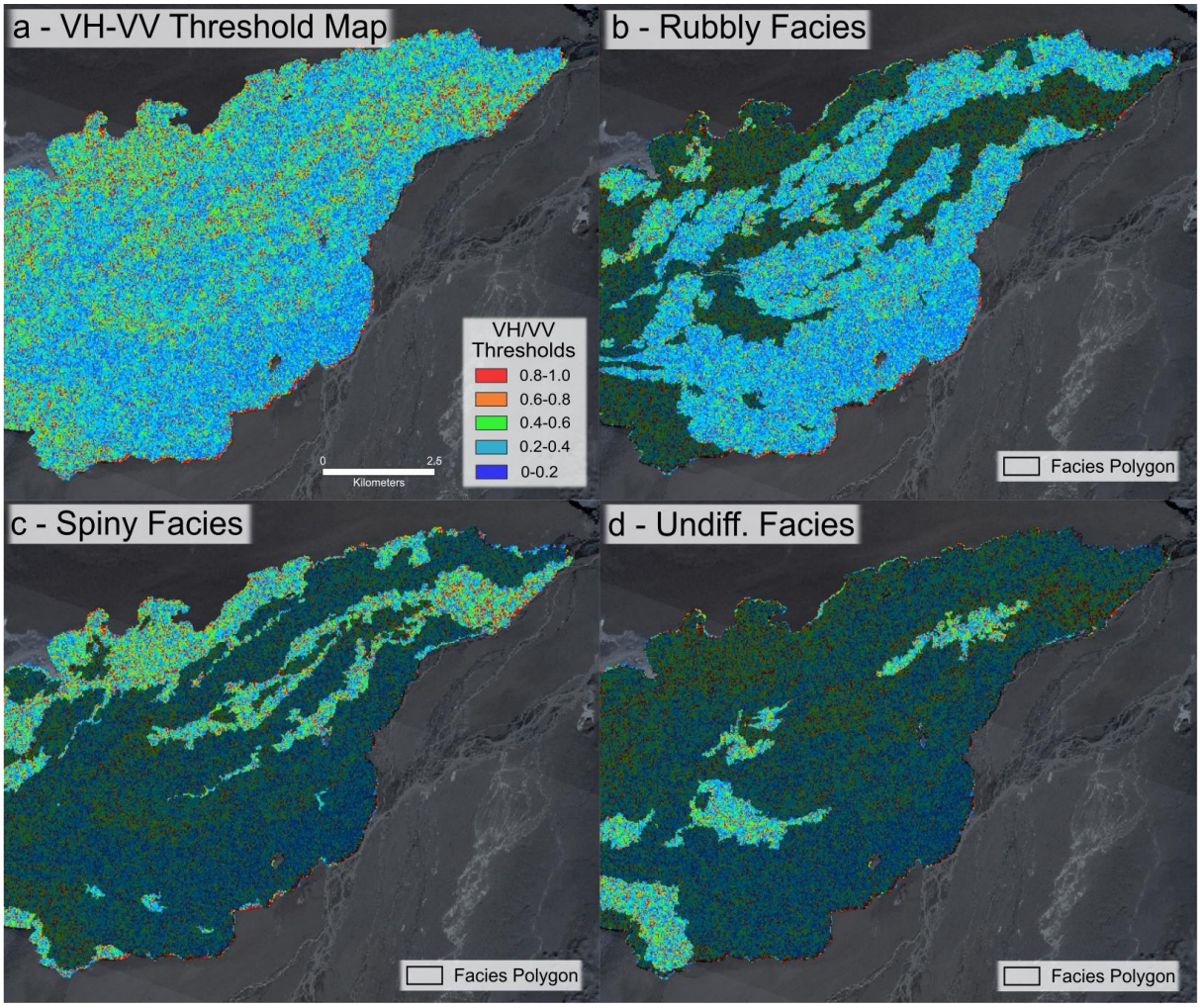

Figure 3.9. A threshold map of VH/VV ratios calculated from Sentinel-1 σ°_{VH} and σ°_{VV} data overlaid with the lava facies polygons available from Voigt and Hamilton, (2021). In images b-d, the described facies highlighted by graying out the adjacent facies in the lava flow-field (e.g., the spiny and undifferentiated facies are grayed out to highlight the rubbly facies). (a) VH/VV threshold map of the 2014-2015 Holuhraun lava flow-field produced by applying a 9 × 9 Enhanced Lee filter to the VH/VV data. Vent region is not included to make the comparison with the UAVASAR CPR threshold map impartial. (b) Rubbly facies in the VH/VV threshold map. (c) Spiny facies in the VH/VV threshold map. (d) Undifferentiated rubbly-spiny facies in the VH/VV threshold map.

To test whether the rubbly, spiny, and undifferentiated rubbly-spiny facies can be differentiated from one another, we applied the One-Way analysis of variance (ANOVA) (Olea, 2008) and Tukey-Kramer test (Benjamini and Braun, 2002) to determine if the means of the radar data are significantly different. One-Way ANOVA is used to determine whether the means of three of more independent groups are significantly different. The test compares the means between each group of data (in this case, the lava facies CPR and VH/VV ratio data) and determines whether we accept the alternative hypothesis; at least two of the groups are statistically significantly different from each other. The One-Way ANOVA test is an omnibus statistic test, so it is not capable of telling us which specific groups are different. Therefore, if the alternative hypothesis is accepted, we need to then determine specifically which of the groups are statistically significantly different. This is why we introduce the Tukey-Kramer test. The Tukey-Kramer is a post hoc test, based on the studentized range distribution (Stoline, 1978), that is required when statistically significant results are identified between groups of data, but we want to determine which groups are actually different.

The One-Way ANOVA test results in Table 3.1 report the P-value (P), F-value (F), and detection probability ($F_{critical}$). To determine whether the lava facies show variance between the data, we require P to be <0.005 and $F_{critical}$ to be less than the F value. Based off the ANOVA test results, we can state that there is a significant difference between the three lava facies in the CPR and VH/VV data. The results of the Tukey-Kramer test are reported in Table 3.2. To determine if the lava facies are statistically significantly different, the absolute mean difference (A. Mean Diff. in Table 3.2) between the lava facies groups needs to be greater than the Q critical value ($Q_{critical}$), which was calculated using the pooled variance across all groups, the q value from the studentized range distribution, and the sample size for a given group (Stoline, 1978; Benjamini

and Braun, 2002). From our results, we observe a significant difference between the spiny facies and the rubbly and undifferentiated rubbly-spiny facies in the CPR data. The rubbly facies and undifferentiated rubbly-spiny facies show no significant difference, which is consistent with their large data overlap as shown in Figure 3.7. According to the Tukey-Kramer test for the VH/VV data, all three facies are significantly different, which is unusual considering their large data error overlaps and the identical means of the rubbly and undifferentiated rubbly-spiny facies (Figure 3.8).

Table 3.1. Summary of the One-Way ANOVA test for the three lava facies L-Band CPR and C-Band VH/VV values. F-stat – calculated F-value, P – P-value, and F-crit – Critical F-value. Information on statistical values available through Olea (2008). Results reported at two confidence levels, $\alpha = 0.05$ and $\alpha = 0.01$.

	α=0.05			α=0.01		
Source	**F stat**	**P**	**F-crit**	**F stat**	**P**	**F-crit**
Lava Facies in CPR Data	5984.57	<0.001	3	5984.57	<0.001	4.61
Lava Facies in VH/VV Data	12599.7	<0.001	3	12599.65	<0.001	4.61

Table 3.2. Summary of the Tukey-Kramer test results. Significance between each lava facies is reported. Yes indicates facies are separable and No indicates facies are not separable. For details on statistical test and results, we refer to Benjamini and Braun, (2002). Results reported at two confidence levels, $\alpha = 0.05$ and $\alpha = 0.01$.

Facie Comparison	A. Mean Diff. (CPR)	Qcritical (CPR)	Significant (CPR)	A. Mean Diff. (VH/VV)	Qcritical (VH/VV)	Significant (VH/VV)
α=0.05						
Rubbly vs Spiny	0.017	0.003	Yes	0.049	0.001	Yes
Spiny vs Undifferentiated	0.019	0.003	Yes	0.042	0.001	Yes
Rubbly vs Undifferentiated	0.002	0.003	No	0.006	0.001	Yes
α=0.01						
Rubbly vs Spiny	0.017	0.029	Yes	0.049	0.001	Yes
Spiny vs Undifferentiated	0.019	0.029	Yes	0.042	0.001	Yes
Rubbly vs Undifferentiated	0.002	0.029	No	0.006	0.001	Yes

[1]*Absolute difference between the group means*

3.3.3 Topographic Surface Roughness

The purpose of acquiring high-resolution LiDAR data from the individual lava flow types and their morphological subsets in the lava facies was to deconvolve the lava facies and study the surface roughness of their corresponding lava flow types. In part, we seek to determine if centimetre-scale roughness that is typically hidden in coarser remote sensing data can be inferred from radar remote sensing data.

We collected a total of 25 LiDAR scans in the field, 16 of which cover surfaces of spiny pāhoehoe lava flow types (13 of the platy lava surface and three of the spiny pāhoehoe lava along the margins of the lava flow-field), three cover the pāhoehoe lava flow type, two cover the

shelly pāhoehoe lava flow type, and four cover the rubbly pāhoehoe lava flow type. We were able to collect more spiny data because these surfaces were easier to access and traverse within the spiny facies. Examples of the lava flow type DEMs and roughness statistic raster's generated from the LiDAR data are presented in Figure 3.10 (a-e). The roughness data collected from the LiDAR scans were calculated at 0.05 – 0.25 m (profile length, 2.5 m and Δx, 0.05 m) and 0.25 – 2 m reference scales (profile length, 20 m and Δx, 0.25 m) (Table 3.3). As a note, we were only able to extract one RMS slope and *H* mean value from the rubbly pāhoehoe surface at the decimetre-scale because 3 of the 4 LiDAR scans had dimensions less than double the profile length (20 m). At the centimetre-scale (0.05 – 0.25 m), the RMS slope of the lava flows returned values from 4.78° to 16.70° and *H* from 0.13 to 0.6, showing us that the lava flow types vary in roughness (Figure 3.11). The three pāhoehoe lava flows from the pāhoehoe facies are relatively rough, returning RMS slope values from 10.29° ± 2.04° to 10.70° ± 1.83° and *H* from 0.38 to 0.49 (Figure 3.11b). The high RMS slope values for the pahoehoe lava flow is possibly a result of the centimetre-scale surface features such as the ropy billows, wrinkles, and sharp spinose textures. The two shelly pāhoehoe lava flow types returned lower RMS slope values compared to the pāhoehoe lava flow types, 5.27° ± 0.95° and 6.35° ± 1.25°, and a *H* of 0.44 (Figure 3.11c).

The rubbly pāhoehoe returned the greatest RMS slope, 16.70° ± 3.67°, owing to the size of the fragments on its disrupted crustal surface, and the lava flow type returned from greatest variation in *H*, 0.29 to 0.6 (Figure 3.11d). The platy lava has the greatest variation in RMS slope values and has the smoothest surface at the centimetre-scale (RMS slope, 4.78° ± 1.05° to 11.56° ± 3.88° and *H*, 0.13 to 0.39) (Figure 3.11e). The three spiny pāhoehoe lava flow types with lobe and toe features (Figure 3.11f) along the western margin of the lava flow-field have RMS slopes ranging from 7.90° ± 1.51° to 11.52° ± 2.86°, and *H* values from 0.2 to 0.36. In general, it is

difficult to discriminate between the lava flow types using the RMS slope and *H* values. However, the rubbly pāhoehoe does stand out as having the highest values of RMS slope and *H* observed in this data set.

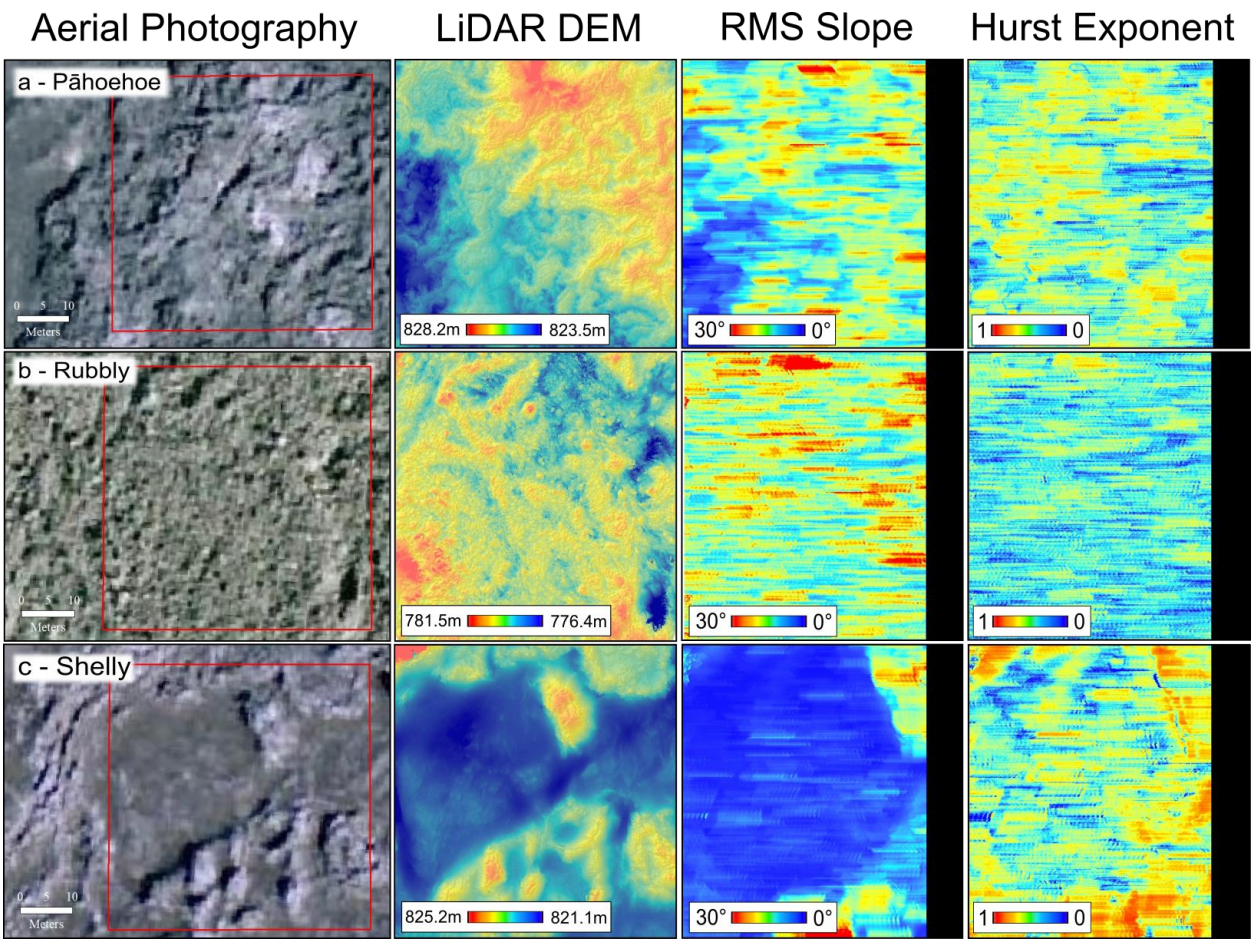

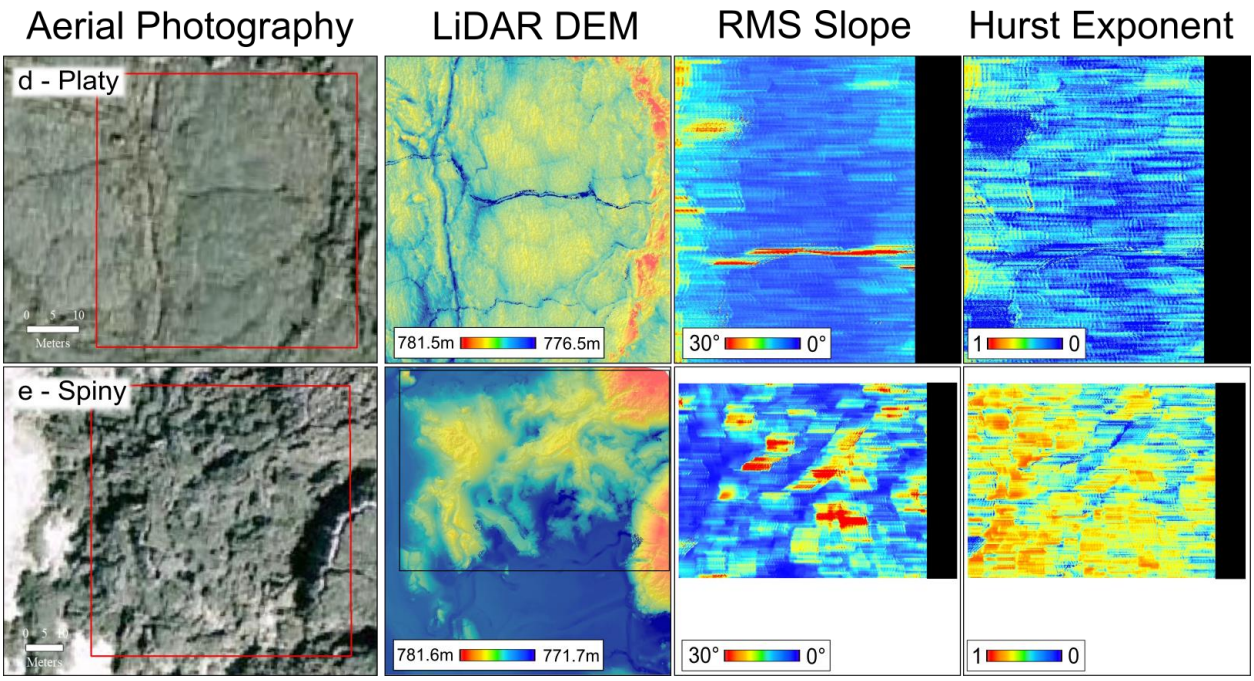

Figure 3.10. Topography and roughness statistic data of an example of each lava flow type and subset lava flow type presented in this study. The first column contains Loftmyndir.ehf aerial photography images of the lava flows, the second column an example of the colourized LiDAR DEMs overlying an elevation hillshade, and the third and fourth columns are the RMS slope and *H* raster's (0.05 m – 0.25 m reference scale, 2.5 m profile) produced from the DEMs. The images represent a (a) pāhoehoe, (b) rubbly, (c) shelly, (d) platy lava, (e) spiny. The resolution of the DEMs are 5 cm/pixel, which allows us to view their centimetre-scale surface roughness, including pāhoehoe ropy textures, lava waves, and spiny toes. The red boxes show the boundaries of the DEMs over the Loftmyndir aerial imagery. The black region in the RMS slope and *H* rasters represent the last 2.5 m of the row; each pixel represents the parameters extracted from one 2.5 m profile, so we cannot obtain values for this region. The black polygon in the spiny LIDAR DEM image is the extent of where the RMS slope and *H* was extracted (surrounding glacial and fluvial sediment was excluded from the roughness calculations).

The second reference scale used for this study was 0.25 – 2 m (Figure 3.12). Compared to the centimetre-scale topographic roughness data, these results returned greater *H* values, up to 0.6, and but only marginally greater RMS slope values, up to 16.9°. The platy lava returned a range of RMS slope values, from 3.5° ± 0.31° to 7.6° ± 0.71°, with most roughness data overlapping the shelly pāhoehoe and pāhoehoe flow types. The spiny pāhoehoe and the rubbly pāhoehoe are the roughest lava flow surfaces at this scale (16.2° ± 1.22° and 16.9° ± 1.14°). However, the rubbly pāhoehoe data point errors do overlap with one of the spiny pāhoehoe flow types along the lava flow-fields western margins (Figure 3.12).

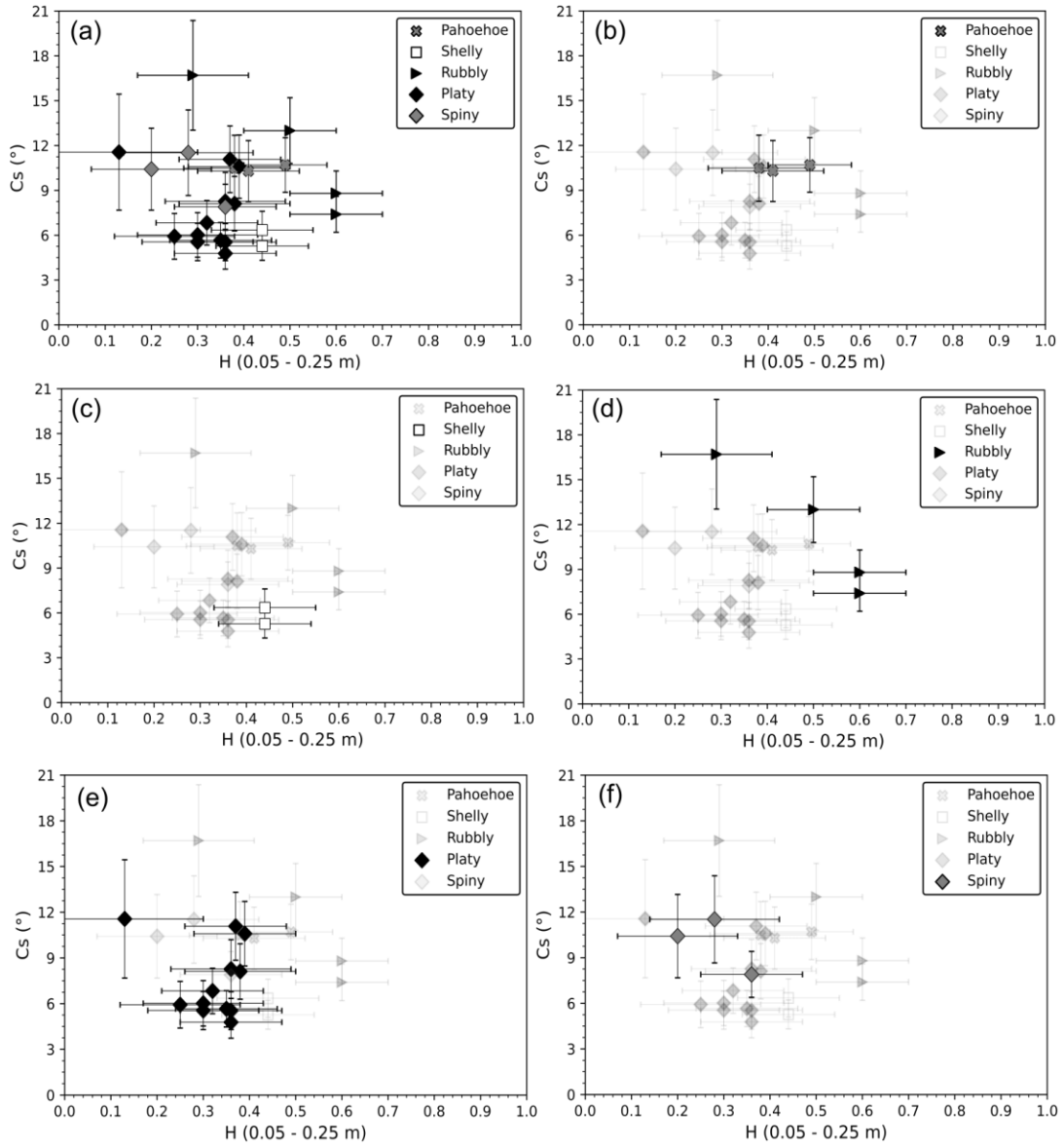

Figure 3.11. Centimetre-scale roughness (Cs – RMS slope) of the studied Holuhraun lava flow types and the platy lava subset of the spiny pāhoehoe lava flow type, derived from LiDAR DEMs with 5 cm/pixel horizontal resolution. Profile length was set to 2.5 m with a step interval of 0.05 m and a reference scale set at 0.05–0.25 m. Graphs a–f show the location and scattering of the lava flow type roughness data: (a) all studied lava flow types, (b) pāhoehoe, (c) shelly pāhoehoe (d) rubbly pāhoehoe, (e) platy lava, and (f) spiny pāhoehoe.

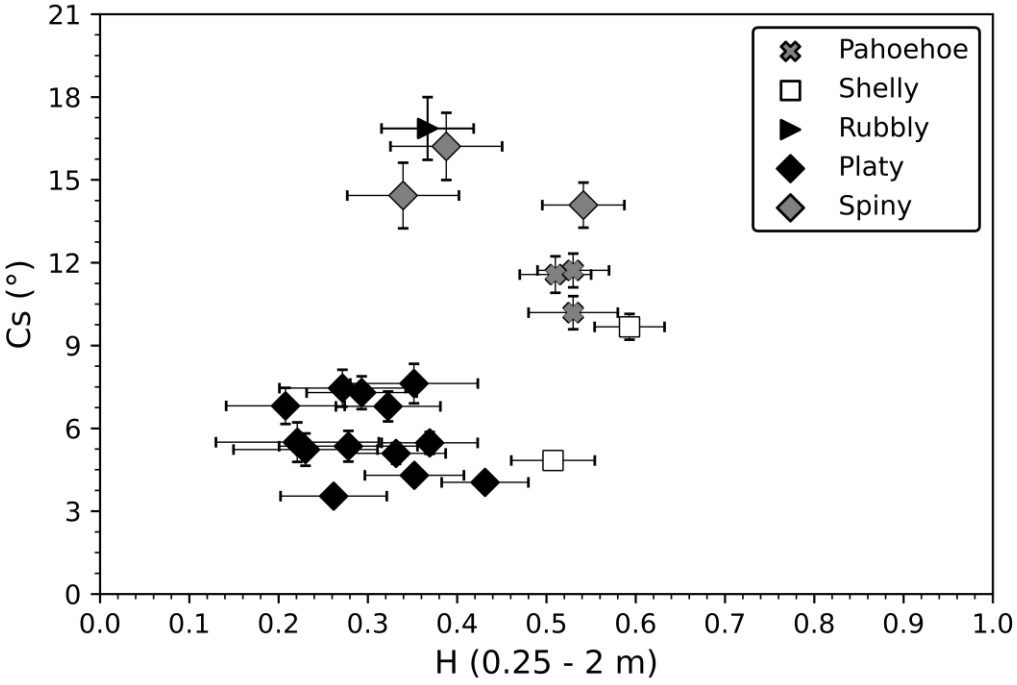

Figure 3.12. Decimetre-scale roughness (Cs – RMS slope) of the studied Holuhraun lava flow types and the platy lava subset of the spiny pāhoehoe lava flow type, derived from LiDAR DEMs with 5 cm/pixel horizontal resolution. Profile length was set to 20 m with a step interval of 25 cm and a reference scale set to 0.25–2 m.

Table 3.3. Summary of RMS slope and *H* data calculated from the LiDAR DEM data sets at 0.05 m – 0.25 m[a] and 0.25 m – 2 m[b] scales. Table includes RMS slope, Hurst Exponent (*H),* RMS slope standard deviation (std), Hurst exponent standard deviation (H_{err}).

LiDAR Dataset	Surface Roughness	Rms slope[a]	Rms slope std[a]	H^a	$H_{err}{}^a$	Rms slope[b]	Rms slope std[b]	H^b	$H_{err}{}^b$
20190805_1_a	Pāhoehoe	10.29	2.04	0.41	0.11	11.60	0.66	0.50	0.04
20190805_1_b	Pāhoehoe	10.48	2.21	0.38	0.11	10.20	0.60	0.50	0.05
20190805_1_c	Pāhoehoe	10.70	1.83	0.49	0.09	11.70	0.61	0.50	0.04
20190803_1_a	Rubbly	16.70	3.67	0.29	0.12	16.90	1.14	0.40	0.05
hotsprings_a_1	Rubbly	7.40	1.20	0.60	0.10	-	-	-	-
hotsprings_a_2	Rubbly	8.80	1.50	0.60	0.10	-	-	-	-
hotsprings_a_3	Rubbly	13.00	2.20	0.50	0.10	-	-	-	-
20190801_1_b	Shelly	5.27	0.95	0.44	0.10	4.84	0.24	0.50	0.05
20190801_1_c	Shelly	6.35	1.25	0.44	0.11	9.68	0.47	0.60	0.04
20190729_2_a	Platy	11.08	2.23	0.37	0.11	6.82	0.66	0.20	0.07
20190729_2_b	Platy	10.59	2.12	0.39	0.11	7.29	0.59	0.30	0.06
20190729_2_c	Platy	4.78	1.05	0.36	0.11	3.55	0.31	0.30	0.06
20190729_2_d	Platy	5.54	1.24	0.36	0.11	4.04	0.26	0.40	0.05
20190729_2_e	Platy	5.66	1.19	0.35	0.11	5.47	0.40	0.40	0.05
20190729_3_a	Platy	6.47	1.87	0.23	0.15	5.50	0.71	0.20	0.09
20190729_3_b	Platy	5.93	1.53	0.25	0.13	5.23	0.58	0.20	0.08
20190802_1_e	Platy	11.56	3.88	0.13	0.17	7.46	0.67	0.30	0.07
20190804_1_a	Platy	6.02	1.49	0.30	0.13	7.62	0.71	0.40	0.07
20190804_1_b	Platy	6.83	1.49	0.32	0.11	5.09	0.38	0.30	0.06
20190804_1_c	Platy	8.11	1.82	0.38	0.12	6.79	0.54	0.30	0.06
20190804_2_a	Platy	5.55	1.25	0.30	0.12	4.30	0.31	0.40	0.06
20190804_3_a	Platy	8.27	1.93	0.36	0.13	5.35	0.56	0.30	0.08
20190802_1_d	Spiny	10.42	2.74	0.20	0.13	14.40	1.19	0.30	0.06
20190803_1_b	Spiny	11.52	2.86	0.28	0.14	16.20	1.22	0.40	0.06
20190803_1_c	Spiny	7.90	1.51	0.36	0.11	14.10	0.82	0.50	0.05

In addition to the LiDAR data, we analyzed the metre-scale roughness of the lava facies using a DEM (2 m/pixel) (Figure 3.13) acquired by the ArcticDEM project (Polar Geospatial Center, 2017). It has greater coverage than the LiDAR data used in this study, and although its resolution is coarser, it is more comparable to DEM data sets produced from stereo-pairs of high-resolution images taken by the Mars Reconnaissance Orbiter (MRO) High Resolution Imaging Science Experiment (HiRISE) camera (McEwen et al., 2007) and the Lunar Reconnaissance Orbiter (LRO) Narrow-Angle Camera (NAC) (Chin et al., 2007). From the ArcticDEM data, we were able to extract RMS slope and *H* values at a scale of 2–12 m (profile length, 100 m and Δx, 2 m) (Table 3.4). This scale has been used by other workers to study the metre-scale roughness of other terrestrial lava flows (Neish et al., 2017) and Martian lava flows (Rodriguez-Sanchez-Vahamonde and Neish, 2021). We set the profile length to 100 m and found that the rubbly, spiny, and undifferentiated rubbly-spiny facies returned RMS slope values lower than the lowest value extracted from the lava flow types at the centimetre-scale (Figure 3.14). However, the *H* values are significantly greater, >0.75, implying surface roughness will be maintained as the scale increases.

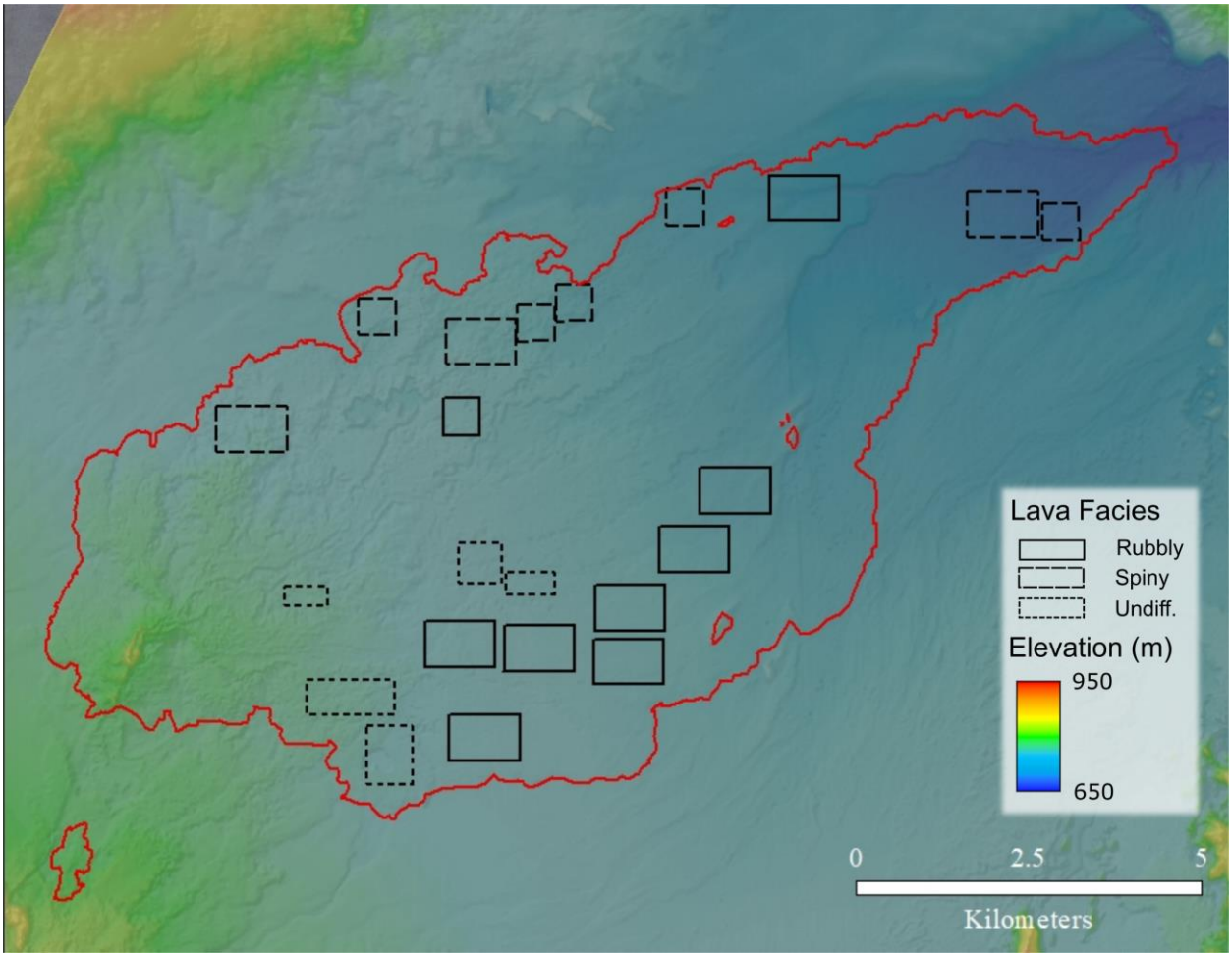

Figure 3.13. ArcticDEM colourized topography data overlaid on a DEM hillshade. The polygons represent the locations of where topography data was extracted for metre-scale roughness statistic calculations. The red shapefile marks the boundaries of the Holuhraun lava flow-field.

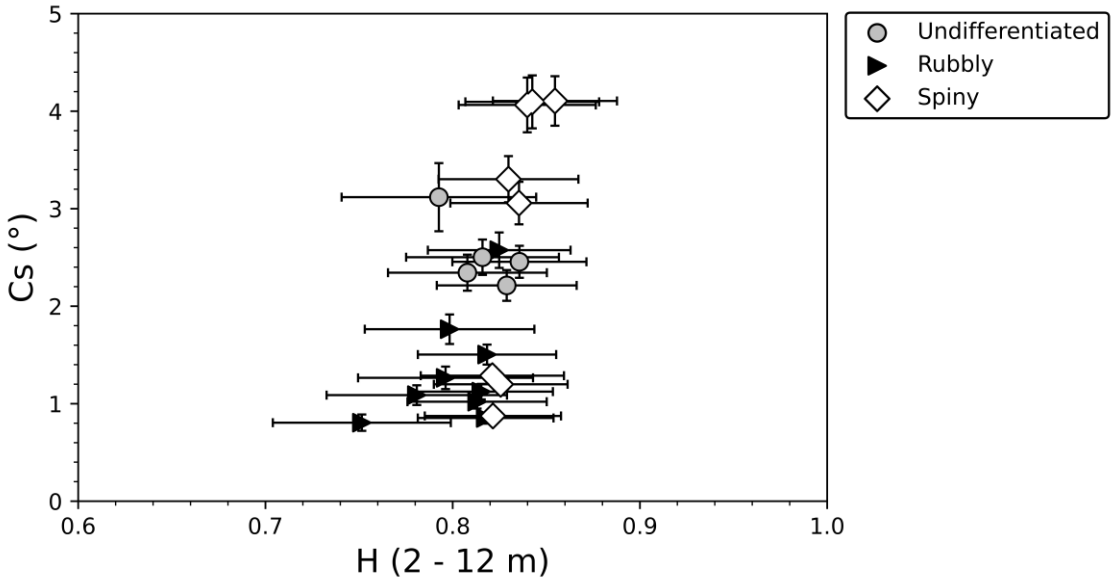

Figure 3.14. Metre-scale roughness (Cs – RMS slope) of the three dominant lava facies in the 2014-2015 Holuhraun lava flow-field. The RMS slope and H were calculated from ArcticDEM data with a spatial resolution of 2m/pixel. All of the lava facies are smooth at the metre-scale, but the rubbly facies are the smoothest (RMS slope <2.6°) out of the three.

Table 3.4. Summary of the RMS slope and *H* data calculated from the ArcticDEM data set (16_54_1_2_2m_v3.0) at 2 m – 12 m. Table includes RMS slope, *H*, RMS slope std, and H_{err}. Data is plotted in Figure 3.14. Note: Undiff – Undifferentiated rubbly-spiny facies.

Lava Facies	Rms slope	Rms slope std	*H*	*H*err
Rubbly	0.81	0.08	0.75	0.05
Rubbly	1.27	0.12	0.8	0.05
Rubbly	1.76	0.15	0.8	0.05
Rubbly	1.02	0.07	0.81	0.04
Rubbly	1.12	0.08	0.82	0.04
Rubbly	1.09	0.1	0.78	0.05
Rubbly	1.5	0.1	0.82	0.04
Rubbly	0.85	0.06	0.82	0.04
Rubbly	2.57	0.18	0.82	0.04
Spiny	4.06	0.28	0.84	0.04
Spiny	3.3	0.24	0.83	0.04
Spiny	4.1	0.27	0.84	0.04
Spiny	4.1	0.25	0.85	0.03
Spiny	3.06	0.22	0.84	0.04
Spiny	1.2	0.08	0.83	0.04
Spiny	0.87	0.06	0.82	0.04
Spiny	1.29	0.09	0.82	0.04
Undiff	2.5	0.18	0.82	0.04
Undiff	2.34	0.18	0.81	0.04
Undiff	2.21	0.16	0.83	0.04
Undiff	2.46	0.16	0.84	0.04
Undiff	3.12	0.35	0.79	0.05

3.4 Discussion

3.4.1 Differentiation of Lava Facies Using Radar

In this work, we seek to determine whether quad-polarized and/or dual-polarized radar data is capable of differentiating the three dominant lava facies in the 2014-2015 Holuhraun lava flow-field. Each of the lava facies records the integrated emplacement history of lava at a specific domain of the lava flow-field. Therefore, the ability to differentiate these lava facies will assist immensely when utilizing radar and other remote sensing data sets to understand the emplacement history and eruption dynamics of flood lavas and flood basalts on other terrestrial bodies (Lancaster et al., 1995; Self et al., 1996; Keszthelyi and Self, 1998; Zimbelman, 1998; Keszthelyi et al., 2006; Thordarson and Larsen, 2007).

Initial observations of the CPR and VH/VV polarization ratios, and the radar threshold maps show that the spiny facies are the only lava facies that can be differentiated from the rubbly facies and undifferentiated rubbly-spiny facies. The distribution of the CPR data within each lava facie is high, but the Tukey-Kramer test results state that the spiny facies are the only facies that are separable from amongst the three. This is in line with our interpretations of the observed lower mean CPR of the spiny facies and the CPR threshold map. The Tukey-Kramer test results for the VH/VV data state that all three lava facies are separable from one another. This is a surprising result because the mean values for the rubbly and undifferentiated rubbly-spiny facies are almost identical, and the distribution of VH/VV values extracted from all three facies overlap immensely (see Figure 3.7). However, we can state that the spiny facies is quantitatively separable from the Sentinel-1 data since it returns a VH/VV mean value that is lower than the

rubbly facies and undifferentiated rubbly-spiny facies, and stands out in the VH/VV imagery data and threshold maps (see Figures 3.7 and 3.9). The challenge in differentiating the undifferentiated rubbly-spiny from the rubbly facies is probably due to their similarities in the types of lava flows present within their domains. In both facies, the rubbly pāhoehoe lava flow type is the most dominant, and therefore, its surface roughness and morphology would most likely be the main contributor to scattering radar signals.

The approach in isolating thresholds in the UAVSAR and Sentinel-1 radar data, to some extent, was effective in revealing differences between the rubbly and spiny facies. In the northwestern and northeastern regions, where the L-Band CPR values are the greatest across the entire lava flow-field east of the vent (Figure 3.8), the rubbly facies show a higher CPR compared to the spiny facies. Compared to Voigt et al., (2021) facies map, the areas where CPR is greatest overlaps with the locations of the rubbly facies, and the lower CPR areas overlap with the spiny facies. However, the decrease in the rubbly facies' CPR from the northwestern and northeastern regions of the lava flow-field to the central and southern regions made it more challenging to differentiate the facies from the spiny facies. For a decrease in CPR to occur, the rubbly facies in the central and southern regions must either exhibit surfaces that are more favourable for quasi-specular reflection (i.e., single-bounce; mirror-like reflection) (Neish and Carter, 2014), which is not consistent with the scattering mechanisms typically associated with rubbly surfaces, or the size of fragments on the surface of the rubbly facies are smaller than the UAVSAR L-band wavelength. Almost the entire central and southern region of the lava flow-field was mapped based off aerial imagery, with ground-truthing impossible due to these rubbly facies only being accessible from the southern margin of the lava flow-field, which is prone to daily flooding from glacial meltwater. Without ground-truth data, it is challenging to say how

similar or different the rubbly facies in the central and southern regions are compared to the northeastern and northwestern regions. In Voigt et al., (2021), they mapped the remains of a lava channels that contain circular to elongate pieces of flat-lying material with surface texture and albedo characteristics that are similar to the shelly facies in the rubbly facies in the central and southern regions. It is possible that these flat-lying materials are contributing to more quasi-specular radar scattering, lowering the overall CPR of the rubbly facies.

VH/VV ratios of the rubbly facies are the lowest compared to the spiny and undifferentiated rubbly-spiny facies, implying that their surfaces are smoother at the centimetre-scale. We only observe marginal differences in VH/VV between the areas where CPR is high and low for the rubbly facies. This implies that at the centimetre-scale, the surface roughness of the rubbly facies is more consistent and shows little to no change from the vent to the end of the lava flow-field in the northeast. If centimetre-scale roughness remains consistent, and decimetre-scale roughness appears to increase moving further from the vent, perhaps the rubbly facies surface comprises more decimetre to metre-sized surface scatterers in the northeastern and northwestern regions. A change in a lava flow's surface roughness is typically connected to the emplacement style and evolution of the lava flow-fields eruption dynamics (e.g., Guilbaud et al., 2005; Harris et al., 2017; Rowland and Walker, 1990; Tolometti et al., 2020). The rubbly facies variable CPR across the lava flow-field is perhaps connected to transitions in lava transportation processes that were occurrent during the Holuhraun eruption.

To understand how changes in lava transportation processes may be connected to the rubbly facies variable surface roughness at the decimetre-scale, we need to review how the emplacement styles of the Holuhraun lava flow-field evolved during the eruption. The central region of the Holuhraun lava flow-field was fed by the formation of a lava pond situated east of

the vent from mid-October to late November 2014 (Pedersen et al., 2017). This ponded lava became the distributing point for the lava field until December 2014 when emplacement styles evolved to a tube-fed lava transport system. The lava escaping the pond flowed over the Holuhraun lava flows that were emplaced during the first months of the eruption and produced new lobes of rubbly pāhoehoe lava along the lava field's southern margin. Lava flows fed by the accumulation of the ponded lava, during what is described as the second stage of emplacement by Pederson et al., (2017), left behind a deflated pond with CPR values that are lower (CPR, 0.3–0.4) than the spiny facies and rubbly facies along the northwestern and northeastern regions. Since the facies in the deflated pond are described as rubbly, spiny, and undifferentiated rubbly-spiny facies (Voigt et al., 2021), we would expect them to have comparable CPR to their counterparts along the western and northeastern regions. It is possible that the increased CPR in the northwestern and northeastern regions is a result of the extensive and continuous disruption of the lava flow crust that occurred when the lava transportation process evolved from a pond fed system to a lava tube-fed system (Pederson et al., 2017; Voigt et al., 2021). As the material on the lava surface was transported for greater distances, more would have brecciated into smaller pieces. For the rubbly facies, surface material would have been transported for a longer period of time since it is the farthest region from the volcanic vent. From field observations in the northeastern region, we noted a greater size distribution of clasts in the brecciated rubbly pāhoehoe crust in the rubbly facies. Large blocks were also present on the surface, with dimensions equivalent and greater than the UAVSAR L-band wavelength (24 cm). These blocks would cause a greater change in radar polarization than smaller sized fragments, and therefore return greater CPR values. To explain the greater CPR, the rubbly facies surfaces in the northeastern and northwestern regions might be blockier than the rubbly facies in the central and

southern regions of the lava flow-field. Without ground-truth information we cannot confirm this hypothesis, but the radar observations do point towards this possibility.

3.4.1.1 Interpreting Without Field Context

It is worth noting that while we sought to determine whether the three dominant Holuhraun lava facies can be differentiated using radar remote sensing data, we required the inclusion of ground-truth data to test our hypotheses and justify our interpretations. If we analyzed the UAVSAR and Sentinel-1 radar data without any field context, we would come to slightly different conclusions. Based off the UAVSAR radar data alone, the undifferentiated rubbly-spiny facies and rubbly facies would be grouped together since their CPR results are indistinguishable. The rubbly facies in the northeastern and northwestern regions and the central and southern regions would be identified as two separate facies under the UAVSAR CPR data but seen as one facies under the dual-polarized C-band radar data. The spiny facies would be identified as its own facies, but we would need to include high resolution imagery to study the morphological and surface textures of the lava facies. All of this would pose problems when attempting to understand the emplacement history of a lava flow-field with no field context (e.g., on other planetary bodies). Despite demonstrating that radar remote sensing data has, to an extent, some capabilities for differentiating lava facies, without the inclusion of at least high-resolution imagery (spatial resolution comparable to the C-band and L-band radar wavelengths, 5 cm to 25 cm), we will be limited in our interpretations. Most of the aerial remote sensing data used by Voigt et al., (2021) to study the surface characteristics of the lava facies and their corresponding lava flow types is on par with high resolution data available for the Moon (LRO

NAC, 0.5-1 m/pixel (Chin et al., 2007)) and Mars (MRO HiRISE, 0.25-0.5 m/pixel (McEwen et al., 2007)). These data sets have proven to be advantageous for identifying and mapping lava facies, and in conjunction with radar data, we can acquire more information about their surface roughness and how they can be partially differentiated from orbit.

3.4.2 LiDAR Roughness of Lava Flows Types

An in-depth analysis of the topographically derived surface roughness of the lava facies individual lava flow types at the centimetre- and decimetre-scale reveal a lack of separability. Particularly at the centimetre-scale, the spiny pāhoehoe and platy lava from the spiny facies, and the shelly pāhoehoe and pāhoehoe lava flow types exhibit similar RMS slope values. The rubbly pāhoehoe lava flow type from the rubbly facies returned the greatest RMS slope (16.7°) and the greatest *H* overall. However, the differences in the roughness statistics between the rubbly pāhoehoe and the other lava flow types is only marginal, and not enough to state that the rubbly pāhoehoe lava flows are distinctive from the other lava flow types in terms of roughness.

At the decimetre-scale, we observe an indistinct difference between the lava flow types, with less overlap in standard deviations and mean RMS slope. The rubbly pāhoehoe and the spiny pāhoehoe are the roughest lava flows analyzed at this scale. The pāhoehoe lavas southeast from the vent exhibit roughness values that do separate them from the rougher rubbly pāhoehoe and spiny pāhoehoe lava flows and the slightly smoother platy lava and shelly pāhoehoe lava. The lava flow types are more challenging to separate using *H* compared to their RMS slope values, due to their data clustering (Figure 3.12). As significant as *H* values are for understanding

the fractal behaviour of a surface, it is evident that RMS slope is more appropriate for differentiating lava flow types.

In general, we find that the high-resolution topographic roughness data is not effective at discriminating the different transitional lava flow types and their morphological subsets at the centimetre-scale but is able to do so more reliably at the decimetre-scale. Field observations and measurements, in conjunction with surface roughness analysis, can provide us with a more complete picture of the structure and appearance of a lava flows surface roughness, the coherency of the lava crust (including the size of fragments on disrupted crusts), and the presence of different types of micro-scale textures (e.g., fractured rubbly clasts vs ʻaʻā clinker).

3.4.3 Remote Sensing Planetary Analogue Analysis

The Holuhraun lava flow-field has been described as a potential analogue site for studying the surface morphology and emplacement styles of large, fissure-fed, lava flow-fields on Mars (Hamilton, 2015; Whelley et al., 2018; Rodriguez-Sanchez-Vahamonde and Neish, 2021; Voigt et al., 2021). The platy lava with plate-ridged morphologies from the spiny facies resembles the morphology of the platy-ridged lava flows imaged by the MRO HiRISE camera and the Mars Global Surveyor (MGS) Mars Orbiting Camera (MOC) (Keszthelyi et al., 2008). Despite their contrasting dimensions (Martian plates are larger than terrestrial plates by a factor of >2), the morphological and surface roughness similarities imply that platy-ridged lava flows on Mars may have formed under similar emplacement styles as the platy lava at Holuhraun (Keszthelyi et al., 2000, 2004, 2006). The occurrence of extensional rift zones implies that the plates were separated from stress applied to the base of the lava crust by a viscous mobile lava

interior. The collision ridges would have formed the same way as the slabby collision boundaries observed in the spiny facies, from plates colliding into one another during the disruption of a coherent lava crust and movement of a still molten lava interior. However, we can only make inferences based off decimetre to metre-scale remote sensing data sets, because quantifiable centimetre-scale topography data and high-resolution radar remote sensing data is currently not available for the surface of Mars.

Harmon et al., (2012) has reported Arecibo S-band (λ = 12.6 cm) radar data of the Martian surface, providing an in-depth investigation into understanding the morphology and distribution of volcanic regions on Mars. However unfortunately, this radar data is not available for detailed analysis, so we have to use qualitative comparisons with terrestrial data based off of radar brightness. Recent work by Rodriguez-Sanchez-Vahamonde and Neish (2021) provided metre-scale roughness values for lava flows on Mars. Their work reported that a majority of lava flows (both radar 'bright' and radar 'dark') are smooth at the metre-scale. Radar 'bright' regions are assumed to be rough at the decimetre-scale, while radar 'dark' regions are assumed to be smooth at the decimetre-scale. Using HiRISE DEM (2 m/pixel) data sets, Rodriguez-Sanchez-Vahamonde and Neish (2021) discovered that lava flows on Mars do not exceed RMS slopes >6.5° and that *H* ranges from 0.45 to 0.9. Figure 3.15 shows the comparison of the metre-scale surface roughness of Martian lava flows and the three dominant Holuhraun lava facies. The lava facies return high *H* >0.75 but extremely low RMS slopes, 0.81° ± 0.08° to 2.57° ± 0.18°. From our results, it appears that the rubbly facies are the most analogous to radar bright Martian lava flows, since they are smooth at the metre-scale and rough at the decimetre-scale with high *H* values (Figure 3.15). Very few surface roughness measurements from the spiny and undifferentiated rubbly-spiny facies overlap with the high *H* and radar-bright Martian lava flows.

Care must be taken in assessing the actual resolution of a metre-scale raster, however. Neish et al., (2017) and Rodriguez-Sanchez-Vahamonde and Neish (2021) report that the effective resolution of a DEM is often lower than the actual reported value. As the resolution decreases, the RMS slope of a surface will in general decrease. Despite this, it is still notable that the Holuhraun rubbly facies have a surface roughness consistent with some Martian lava flows.

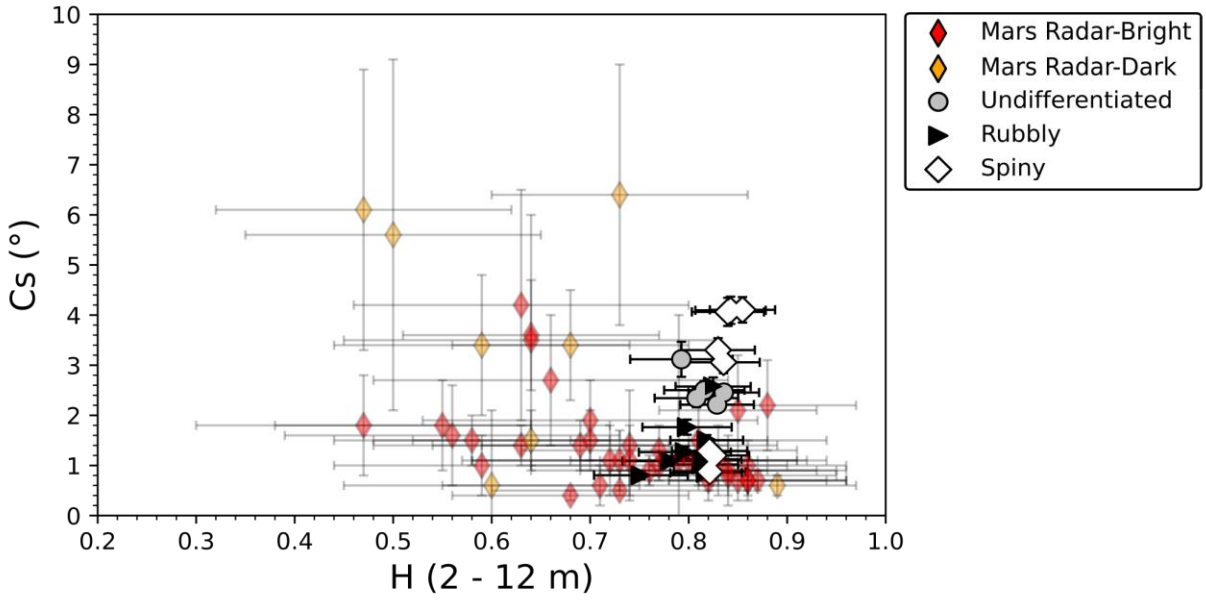

Figure 3.15. Metre-scale roughness plot of the three dominant Holuhraun lava facies (rubbly, spiny, and undifferentiated rubbly-spiny) and Martian lava flow surfaces studied by Rodriguez Sanchez-vahamonde and Neish, (2021). The RMS slope (Cs) and Hurst exponent (*H*) were extracted from ArcticDEM data (2 m/pixel), with a profile length of 100 m, reference scale of 2 m to 12 m, and a step size of 2 m. The transparent orange and red data points represent the surface roughness of radar-dark and radar-bright lava flows on Mars quantified using HiRISE DTMs (2 m/pixel) (Rodriguez Sanchez-vahamonde and Neish, 2021).

3.5 Conclusion

In this work, we sought to determine if the lava facies in the Holuhraun lava flow-field could be differentiated using radar remote sensing data, and if the lava flow types within the facies can be differentiated using high-resolution LiDAR data. We analyzed UAVSAR L-Band CPR data, and Sentinel-1 C-Band VH/VV ratio data. From our results, we discovered that only the spiny facies are separable from the CPR data, and despite conflicting radar observations and extracted mean values, statistically, all three lava facies are separable from the VH/VV data. We note that some of our interpretations seeking to understand changes in the rubbly facies radar roughness across Holuhraun would not have been possible without the inclusion of high-resolution aerial imagery, orbital multispectral imagery, and field context.

When we attempt to deconvolve the lava facies and analyze the topographic roughness of their corresponding lava flow types using high-resolution LiDAR data, we discovered that the rubbly pāhoehoe and spiny pāhoehoe flow types are the roughest at the decimetre-scale. At the centimetre-scale, we observe no clear distinctions between any of the studied lava flow types, in particular the platy lava and the spiny pāhoehoe lava in the spiny facies. Using metre-scale topography data, we observed similarities between radar 'bright' Martian lava flows with H >0.75 and the rubbly facies. We infer that the radar 'bright' lava flows on Mars could therefore exhibit lava flow types similar to those present within the rubbly facies at Holuhraun. To further investigate whether radar remote sensing data can be utilized for identifying and differentiating lava facies on other planetary bodies, new missions need to prioritize the incorporation of a SAR instrument with wavelengths comparable to terrestrial radar systems (e.g., L-band). The proposed NASA Mars Ice Mapper mission (Davis, 2021) for Mars, for example, includes a SAR

instrument that would be capable of measuring the surface roughness of volcanic terrains at wavelengths analogous to the UAVSAR L-band data and other terrestrial SAR platforms (e.g., ALOS PALSAR). If funded, the Mars Ice Mapper mission would gather vital radar backscatter and polarization data that could be used to investigate and interpret the emplacement of lava flow-fields, flood lavas, and flood basalts on Mars.

References

Benjamini, Y., and Braun, H., 2002, John W. Tukey's contributions to multiple comparisons: ETS Research Report Series, v. 2, doi:10.1214/aos/1043351247.

Bonnefoy, L.E., Hamilton, C.W., Scheidt, S.P., Duhamel, S., Höskuldsson, Jónsdottir, I., Thordarson, T., and Münzer, U., 2019, Landscape evolution associated with the 2014–2015 Holuhraun eruption in Iceland: Journal of Volcanology and Geothermal Research, v. 387, p. 106652, doi:10.1016/j.jvolgeores.2019.07.019.

Bonny, E., Thordarson, T., Wright, R., Höskuldsson, A., and Jónsdóttir, I., 2018, The Volume of Lava Erupted During the 2014 to 2015 Eruption at Holuhraun, Iceland: A Comparison Between Satellite- and Ground-Based Measurements: Journal of Geophysical Research: Solid Earth, v. 123, p. 5412–5426, doi:10.1029/2017JB015008.

Campbell, B.A., 2012, High circular polarization ratios in radar scattering from geologic targets: Journal of Geophysical Research, v. 117, doi:10.1029/2012JE004061.

Campbell, B.A., 2002, Radar Remote Sensing of Planetary Surfaces: Cambridge University Press.

Campbell, B.A., and Shepard, M.K., 1996, Lava flow surface roughness and depolarized radar scattering: Journal of Geophysical Research, v. 101, p. 18,941-18,951.

Carter, L.M., Campbell, D.B., and Campbell, B.A., 2011, Geologic studies of planetary surfaces using radar polarimetric imaging: Proceedings of the IEEE, v. 99, p. 770–782, doi:10.1109/JPROC.2010.2099090.

Carter, L.M., Campbell, D.B., and Campbell, B.A., 2004, Impact crater related surficial deposits on Venus : Multipolarization radar observations with Arecibo: Jounral of Geophysical Research, v. 109, doi:10.1029/2003JE002227.

Center, P.G., 2017, Polar Geospatial CenterGuide: Introduction to ArcticDEM: , p. 4, https://www.pgc.umn.edu/guides/arcticdem/introduction-to-arcticdem/ (accessed December 2020).

Chin, G. et al., 2007, Lunar Reconnaissance Orbiter Overview : The Instrument Suite and Mission: Space Science Reviews, v. 129, p. 391–419, doi:10.1007/s11214-007-9153-y.

Coppola, D., Barsotti, S., Cigolini, C., Laiolo, M., Pfeffer, M.A., and Ripepe, M., 2019, Monitoring the time-averaged discharge rates, volumes and emplacement style of large lava flows by using mirova system: The case of the 2014-2015 eruption at holuhraun (Iceland): Annals of Geophysics, v. 62, doi:10.4401/ag-7749.

Davis, R.D., 2021, International Mars Ice Mapper Mission: The First Human Exploration Reconnaissance Mission to Mars, *in* 52nd Lunar and Planetary Science Conference, p. 2614.

Dirscherl, M., and Rossi, C., 2018, Geomorphometric analysis of the 2014–2015 Bárðarbunga

volcanic eruption, Iceland: Remote Sensing of Environment, v. 204, p. 244–259, doi:10.1016/j.rse.2017.10.027.

Duraiswami, R.A., Bondre, N.R., and Managave, S., 2008, Morphology of rubbly pahoehoe (simple) flows from the Deccan Volcanic Province: Implications for style of emplacement: Journal of Volcanology and Geothermal Research, v. 177, p. 822–836, doi:10.1016/j.jvolgeores.2008.01.048.

Duraiswami, R.A., Gadpallu, P., Shaikh, T.N., and Cardin, N., 2014, Pahoehoe-a'a transitions in the lava flow fields of the western Deccan Traps, India-implications for emplacement dynamics, flood basalt architecture and volcanic stratigraphy: Journal of Asian Earth Sciences, v. 84, p. 146–166, doi:10.1016/j.jseaes.2013.08.025.

Fan, K.A., Neish, C.D., Zanetti, M., and Kukko, A., 2018, An Improved Methodology for the 3-Dimensional Characterization of Surface Roughness as Applied to Lava Flows, *in* Lunar and Planetary Science Conference, p. 2526.

Favalli, M., Fornaciai, A., Mazzarini, F., Harris, A., Neri, M., Behncke, B., Pareschi, M.T., Tarquini, S., and Boschi, E., 2010, Evolution of an active lava flow field using a multitemporal LIDAR acquisition: Journal of Geophysical Research: Solid Earth, v. 115, doi:10.1029/2010JB007463.

Ghail, R. et al., 2012, EnVision: taking the pulse of our twin planet: Experimental Astronomy, v. 2–3, p. 337–363.

Griffiths, R.W., and Fink, J.H., 1992, The morphology of lava flows in planetary environments: Predictions from analog experiments: Journal of Geophysical Research, v. 97, p. 19739, doi:10.1029/92JB01953.

Gudmundsson, M.T. et al., 2016, Gradual caldera collapse at Bárdarbunga volcano, Iceland, regulated by lateral magma outflow: Science, v. 353, p. aaf8988, doi:10.1126/science.aaf8988.sciencemag.org.

Guilbaud, M.-N., Self, S., Thordarson, T., and Blake, S., 2005, Morphology, surface structures, and emplacement of lavas produced by Laki, A.D. 1783 – 1784: GSA Special Papers, v. 396, p. 81–102, doi:10.1130/2005.2396(07).

Halldórsson, S.A. et al., 2018, Petrology and geochemistry of the 2014–2015 Holuhraun eruption, central Iceland: compositional and mineralogical characteristics, temporal variability and magma storage: Contributions to Mineralogy and Petrology, v. 173, p. 1–25, doi:10.1007/s00410-018-1487-9.

Hamilton, C.W., 2019, "Fill and Spill" Lava Flow Emplacement: Implications for Understanding Planetary Flood Basalt Eruptions:

Hamilton, C.W. et al., 2020, Lava-Rise Plateaus and Inflation Pits in the McCartys Lava Flow Field, New Mexico: An Analog for Pāhoehoe-Like Lava Flows on Planetary Surfaces: Journal of Geophysical Research: Planets, v. 125, doi:10.1029/2019JE005975.

Hamilton, C.W., 2015, Team gets firsthand look at the new Holuhraun eruption site: Eos, v. 96, doi:doi:10.1029/2015EO041197.

Hamilton, C.W., Glaze, L.S., James, M.R., and Baloga, S.M., 2013, Topographic and stochastic influences on pāhoehoe lava lobe emplacement: Bulletin of Volcanology, v. 75, p. 1–16, doi:10.1007/s00445-013-0756-8.

Harris, A.J.L., Rowland, S.K., Villeneuve, N., and Thordarson, T., 2017, Pāhoehoe, ʻaʻā, and

block lava: an illustrated history of the nomenclature: Bulletin of Volcanology, v. 79, doi:10.1007/s00445-016-1075-7.

Hensley, S., Smrekar, S.E., and Pollard, B., 2012, VERITAS: A Mission Concept for the High Resolution Topographic Mapping and Imaging of Venus, *in* American Geophysical Union, Fall Meeting, p. P33C-1950.

Hjartardóttir, Á.R., Einarsson, P., Gudmundsson, M.T., and Högnadóttir, T., 2016, Fracture movements and graben subsidence during the 2014 Bárdarbunga dike intrusion in Iceland: Journal of Volcanology and Geothermal Research, v. 310, p. 242–252, doi:10.1016/j.jvolgeores.2015.12.002.

Hon, K., Kauahikaua, J., Denlinger, R., and Mackay, K., 1994, Emplacement and inflation of pahoehoe sheet flows: observations and measurements of active lava flows on Kilauea volcano, Hawaii: Geological Society of America Bulletin, v. 106, p. 351–370, doi:10.1130/0016-7606(1994)106<0351:EAIOPS>2.3.CO;2.

Hoskuldsson, A., Jónsdóttir, I., Riishus, M.S., Pedersen, G.B.M., Gudmundsson, M.T., Thordarson, T., and Drouin, V., 2015, Magma discharge and lava flow field growth in the Nornahraun/Bardarbunga eruption Iceland, *in* Geophysical Research Abstracts EGU General Assembly, v. 17.

Keszthelyi, L., Jaeger, W., McEwen, A., Tornabene, L., Beyer, R.A., Dundas, C., and Milazzo, M., 2008, High resolution imaging science experiment (HiRISE) images of volcanic terrains from the first 6 months of the Mars reconnaissance orbiter primary science phase: Journal of Geophysical Research E: Planets, v. 113, p. 1–25, doi:10.1029/2007JE002968.

Keszthelyi, L., McEwen, A.S., and Thordarson, T., 2000, Terrestrial analogs and thermal models

for Martian flood lavas: Journal of Geophysical Research E: Planets, v. 105, p. 15027–15049, doi:10.1029/1999JE001191.

Keszthelyi, L., and Self, S., 1998, Some physical requirements for the emplacement of long basaltic lava flows: Journal of Geophysical Research, v. 103, p. 27447–27464.

Keszthelyi, L., Self, S., and Thordarson, T., 2006, Flood lavas on Earth, Io and Mars: Journal of the Geological Society, v. 163, p. 253–264, doi:10.1144/0016-764904-503.

Keszthelyi, L., Thordarson, T., McEwen, A., Haack, H., Guilbaud, M.N., Self, S., and Rossi, M.J., 2004, Icelandic analogs to Martian flood lavas: Geochemistry, Geophysics, Geosystems, v. 5, p. 1–32, doi:10.1029/2004GC000758.

Kilburn, C.R.J., 2000, Lava Flows and Flow Fields, *in* Encyclopedia of Volcanoes, p. 291–305.

Kilburn, C.R.J., 1981, Pahoehoe and aa lavas: a discussion and continuation of the model of Peterson and Tilling: Journal of Volcanology and Geothermal Research, v. 11, p. 373–382, doi:10.1016/0377-0273(81)90033-0.

Kolzenburg, S., Giordano, D., Thordarson, T., Höskuldsson, A., and Dingwell, D.B., 2017, The rheological evolution of the 2014/2015 eruption at Holuhraun, central Iceland: Bulletin of Volcanology, v. 79, doi:10.1007/s00445-017-1128-6.

Kolzenburg, S., Jaenicke, J., Münzer, U., and Dingwell, D.B., 2018, The effect of inflation on the morphology-derived rheological parameters of lava flows and its implications for interpreting remote sensing data - A case study on the 2014/2015 eruption at Holuhraun, Iceland: Journal of Volcanology and Geothermal Research, v. 357, p. 200–212, doi:10.1016/j.jvolgeores.2018.04.024.

Kukko, A., Kaartinen, H., Osinski, G., and Hyyppä, J., 2020, Modelling Permafrost Terrain Using Kinematic, Dual-Wavelength Laser Scanning: ISPRS Annals of the Photogrammetry, Remote Sensing and Spatial Information Sciences, v. 5, p. 749–756, doi:10.5194/isprs-annals-V-2-2020-749-2020.

Lancaster, M.G., Guest, J.E., and Magee, K.P., 1995, Great Lava Flow Fields on Venus: Icarus, v. 118, p. 69–86, doi:10.1006/icar.1995.1178.

Lee, J.-S., and Pottier, E., 2018, Polarimetric SAR Speckle Filtering, *in* Polarimetric Radar Imaging: From Basics to Applications, p. 143–177, doi:10.1201/9781420054989-5.

López-Martínez, C., and Fàbregas, X., 2008, Model-based polarimetric SAR speckle filter: IEEE Transactions on Geoscience and Remote Sensing, v. 46, p. 3894–3907, doi:10.1109/TGRS.2008.2002029.

Mattsson, H.B., and Höskuldsson, Á., 2005, Eruption reconstruction, formation of flow-lobe tumuli and eruption duration in the 5900 BP Helgafell lava field (Heimaey), south Iceland: Journal of Volcanology and Geothermal Research, v. 147, p. 157–172, doi:10.1016/j.jvolgeores.2005.04.001.

McEwen, A.S. et al., 2007, Mars Reconnaissance Orbiter ’ s High Resolution Imaging Science Experiment (HiRISE): Jounral of Geophysical Research, v. 112, doi:10.1029/2005JE002605.

Morris, A.R., Anderson, F.S., Mouginis-Mark, P.J., Haldemann, A.F.C., Brooks, B.A., and Foster, J., 2008, Roughness of Hawaiian volcanic terrains: Journal of Geophysical Research E: Planets, v. 113, doi:10.1029/2008JE003079.

Neish, C.D. et al., 2017, Terrestrial analogues for lunar impact melt flows: Icarus, v. 281, p. 73–89, doi:10.1016/j.icarus.2016.08.008.

Neish, C.D., and Carter, L.M., 2014, Planetary Radar, *in* Encyclopedia of the Solar System, p. 1133–1159.

Olea, R.A., 2008, Basic Statistical Concepts and Methods for Earth Scientists: U.S. Geological Survey: 191 p.

Pedersen, G.B.M. et al., 2017, Lava field evolution and emplacement dynamics of the 2014–2015 basaltic fissure eruption at Holuhraun, Iceland: Journal of Volcanology and Geothermal Research, v. 340, p. 155–169, doi:10.1016/j.jvolgeores.2017.02.027.

Rodriguez Sanchez-Vahamonde, C., and Neish, C., 2021, The Surface Texture of Martian Lava Flows as Inferred from Their Decimeter- and Meter-scale Roughness: The Planetary Science Journal, v. 2, doi:https://doi.org/10.3847/PSJ/abbfac.

Rosen, P.A., Hensley, S., Wheeler, K., Sadowy, G., Miller, T., Shaffer, S., Muellerschoen, R., Jones, C., Zebker, H., and Madsen, S., 2006, UAVSAR: A new NASA airborne SAR system for science and technology research, *in* IEEE National Radar Conference, IEEE, p. 22–29, doi:10.1109/RADAR.2006.1631770.

Rowland, S.K., and Walker, G.P.L., 1990, Pahoehoe and aa in Hawaii: volumetric flow rate controls the lava structure: Bulletin of Volcanology, v. 52, p. 615–628.

Sanchez-vahamonde, C.R., 2019, Quantification of Surface Roughness of Lava Flows on Mars: The University of Western Ontario.

Self, S., Thordarson, T., Keszthelyi, L., Walker, G.P.L., Hon, K., Murphy, M.T., Long, P., and

Finnemore, S., 1996, A new model for the emplacement of Columbia River basalts as large inflated pahoehoe lava flow fields: Geophyiscal Research Letters, v. 23, p. 2689–2692.

Self, S., Thordarson, T., and Widdowson, M., 2005, Gas Fluxes from Flood Basalt Eruptions: Elements, v. 1, p. 283–287, doi:10.2113/gselements.1.5.283.

Self, S., Widdowson, M., Thordarson, T., and Jay, A.E., 2006, Volatile fluxes during flood basalt eruptions and potential effects on the global environment: A Deccan perspective: Earth and Planetary Science Letters, v. 248, p. 518–532, doi:10.1016/j.epsl.2006.05.041.

Shepard, M.K., Campbell, B.A., Bulmer, M.H., Farr, T.G., Gaddis, L.R., and Plaut, J.J., 2001, The roughness of natural terrain: A planetary and remote sensing perspective: Journal of Geophysical Research E: Planets, v. 106, p. 32777–32795, doi:10.1029/2000JE001429.

Sigmundsson, F. et al., 2015, Segmented lateral dyke growth in a rifting event at Bárðarbunga volcanic system, Iceland: Nature, v. 517, p. 191–195, doi:10.1038/nature14111.

Smrekar, S.E., Dyar, M.D., Hensley, S., Helbert, J., and Team, V.S., 2016, VERITAS (Venus Emissivity, Radio Science, InSAR, Topography And Spectroscopy): A Proposed Discovery Mission, *in* AAS/DPS Meeting Abstract# 48, p. 216– 07.

Solana, M.C., Kilburn, C.R.J., Rodriguez Badiola, E., and Aparicio, A., 2004, Fast emplacement of extensive pahoehoe flow-fields: The case of the 1736 flows from Monta??a de las Nueces, Lanzarote: Journal of Volcanology and Geothermal Research, v. 132, p. 189–207, doi:10.1016/S0377-0273(03)00345-7.

Stoline, M.R., 1978, Tables of the studentized augmented range and applications to problems of multiple comparison: Journal of the American Statistical Association, v. 73, p. 656–660,

doi:10.1080/01621459.1978.10480073.

Thordarson, T., and Larsen, G., 2007, Volcanism in Iceland in historical time: Volcano types, eruption styles and eruptive history: Journal of Geodynamics, v. 43, p. 118–152, doi:10.1016/j.jog.2006.09.005.

Tolometti, G.D., Neish, C.D., Osinski, G.R., Hughes, S.S., and Nawotniak, S.E.K., 2020, Interpretations of lava flow properties from radar remote sensing data: Planetary and Space Science, v. 190, p. 104991, doi:https://doi.org/10.1016/j.pss.2020.104991.

Torres, R. et al., 2012, GMES Sentinel-1 mission: Remote Sensing of Environment, v. 120, p. 9–24, doi:10.1016/j.rse.2011.05.028.

Voigt, J.R.C., and Hamilton, C.W., 2021, Facies map for the 2014–2015 Holuhraun eruption in Iceland: University of Arizona, Department of Planetary Sciences, Lunar and Planetary Laboratory,.

Voigt, J.R.C., Hamilton, C.W., Scheidt, S.P., Münzer, U., Höskuldsson, Á., Jónsdottir, I., and Thordarson, T., 2021, Geomorphological Characterization of the 2014–2015 Holuhraun Lava Flow-Field in Iceland: Journal of Volcanology and Geothermal Research, doi:https://doi.org/10.1016/ j.jvolgeores.2021.107278.

Voigt, J.R.C., Hamilton, C.W., Steinbrügge, G., and Scheidt, S. P., in press, Surface Roughness Characterization of the 2014-2015 Holuhraun Lava Flow-Field in Iceland: Implications for Facies Mapping and Remote Sensing: Journal of Volcanology and Geothermal Research.

Whelley, P. et al., 2018, Analogs of Ice and Fire: Conducting Fieldwork in the Icelandic Highlands to Inform Volcanic Interpretations on Mars and Instrument Development for

Europa, *in* American Geophysical Union, Fall Meeting,.

Whelley, P.L., Garry, W.B., Hamilton, C.W., and Bleacher, J.E., 2017, LiDAR-derived surface roughness signatures of basaltic lava types at the Muliwai a Pele Lava Channel , Mauna Ulu , Hawai ‘ i: Bulletin of Volcanology, v. 79, doi:10.1007/s00445-017-1161-5.

Wilson, L., and Head, J.W., 1994, Mars: Review and Analysis and of Volcanic Eruption To Theory Relationships Landforms: Reviews of Geophysics, v. 32, p. 221–263.

Zanetti, M., Neish, C.D., Kukko, A., Choe, B.-H., Osinski, G.R., Tolometti, G.D., Fan, K., and Maj, R., 2018, Surface Roughness and Radar Scattering Properties of Volcanic Terrain: Geologic Application of Kinematic Mobile LiDAR Scanning, *in* In Lunar and Planetary Science Conference, v. 49.

Zebker, H.A., and Lou, Y., 1990, Phase Calibration of Imaging Radar Polarimeter Stokes Matrices: IEEE Transactions on Geoscience and Remote Sensing, v. 28, p. 246–252.

Zimbelman, J.R., 1998, Emplacement of long lava flows on planetary surfaces: J. Geophys. Res., v. 103, p. 27503–27516, doi:10.1029/98jb01123.

Chapter 4: Hot Rocks: Constraining the Thermal Conditions of Impact Melt Deposits Using Zircon and Zirconia Polymorphs[2]

4.1 Introduction

Impact cratering is a widespread geologic process throughout the Solar System and has played a critical role in the accretion of planetary bodies (e.g., Melosh, 1989; Osinski and Pierazzo, 2012). A common product of all impact cratering events is impact melt, which forms upon decompression of rocks subjected to high shock pressures (>60–100 GPa; e.g., Dence, 1971; Melosh, 1989). Unlike decompression and flux melting that occurs in planetary interiors, impact melting is (1) instantaneous, (2) follows different thermodynamic laws and relations (i.e., abide by the eutectic compositions and partial melting of protolithic lithologies), and (3) the composition is controlled by the wholescale melting of the target rocks as opposed to the minerals with the lowest solidus temperatures (Grieve et al., 1977; Melosh, 1989; Osinski et al., 2018). Evidence for the melting of refractory minerals that require temperatures >1400–1800° C (such as rutile and zircon; El Goresy, 1965, 1968; Dressler et al., 1987), led to the hypothesis that impact melts were superheated. In this context, superheated means that the minerals have achieved temperatures well above their liquidus. At these temperatures, impact melt would behave as a Newtonian fluid, exhibiting a viscosity that remains constant until sufficient cooling has commenced and is no longer a Newtonian fluid (Chhabra, 2010). The temperature of impact melt is therefore a key physical property for understanding the formation and emplacement of impact melt deposits (e.g., Lev et al., in press; Osinski et al., 2011). It also can provide critical

[2]Tolometti G. D., Erickson T. M., Osinski G. R., Cayron C., Neish C. D. *under review*. Hot Rocks: Constraining the Thermal Conditions of Impact Melt Deposits Using Zircon and Zirconia Polymorphs. *Earth and Planetary Science Letters*. Ref. No: EPSL-D-21-00707.

information about how impact cratering modified and devolatilized the crustal material of the early Earth and Moon (Kring and Cohen, 2002; Gomes et al., 2005; Marchi et al., 2014).

Estimating rock formation temperatures requires preservation of geothermometers, such as compositional endmembers in mineral systems (Hart and Davis, 1978; Lindsley and Andersen, 1983; Sack and Ghiorso, 1991; Cherniak et al., 2007). However, conventional geothermometers are not suitable for estimating the superheated temperatures of impact melt as none are known to exceed 1800°C and these geothermometers only work in thermodynamically equilibrated rocks. Rather, impact melt temperatures can only be constrained by examining the crystallographic orientation relationships of accessory minerals that can partially withstand hypervelocity impact conditions (e.g., Cavosie et al., 2016; Timms et al., 2017a; Erickson et al., 2019). Two minerals used in impact cratering studies to constrain both impact melt temperatures and impact cratering pressures are zirconia (ZrO_2) and zircon ($ZrSiO_4$). Superheated temperatures can be constrained by examining zirconia crystals (El Goresy, 1965; Kaiser et al., 2008; Timms et al., 2017a), which are a dissociation product of zircon at temperatures above 1673 °C. Zircon is a durable accessory mineral that can record both temperature (to an extent) and pressure conditions (Kusaba et al., 1985; Wittmann et al., 2006; Morozova, 2015; Cavosie et al., 2016).

Previous work by Timms et al. (2017b) discovered evidence of two zircon grains with coronae of baddeleyite (monoclinic zirconia) crystals that had back transformed from cubic zirconia in a single impact glass sample from the Mistastin Lake impact structure, Newfoundland/Labrador, Canada. Evidence for the cubic zirconia polymorph transformation implies superheated temperatures >2370°C (cf. Kaiser et al. 2008); this is the highest recorded formation temperature for any crustal rock on Earth. In addition, a recent study by White et al.

(2020) discovered a ~250 μm, subhedral baddeleyite grain with similar systematic orientations indicative of cubic zirconia in the coarse-grained lunar troctolite. The baddeleyite grain analyzed by White et al. (2020) is purported to have been entrained in a superheated melt generated from a basin-forming impact event, suggesting hypervelocity impacts on the Moon, and potentially other rocky planetary bodies, produce superheated impact melts far in excess of the liquidus. If superheating is common during impact cratering processes, then we would expect to find evidence for high temperature melt conditions in all melt-bearing impactites distributed across impact structures.

In this work, we analyzed zircon grains and zirconia crystals from a diverse suite of impactites from the Mistastin Lake impact structure (Figure 4.1). The impactites selected for this study include a sample of the same type of impact glass studied by Timms et al. (2017b), in addition to a clast-poor vesicular impact melt rock, a clast-rich impact melt rock, and a glass-bearing impact breccia (Figures. 4.1C-F). Each of the analyzed samples were selected to represent a different unit within the Mistastin impact structures impactite stratigraphy as described from field observations and petrographic analysis (Grieve, 1975; Mader and Osinski, 2018).

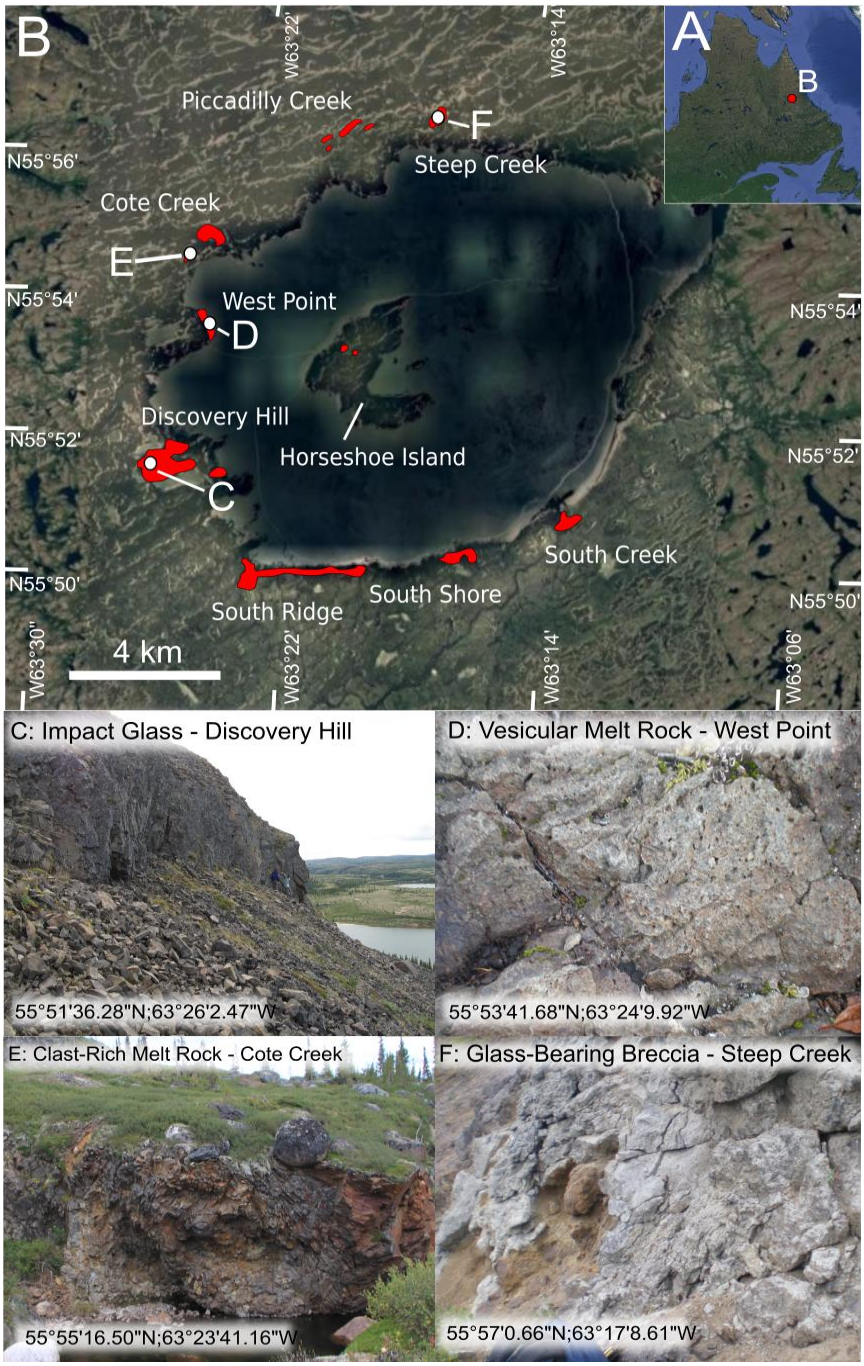

Figure 4.1. (A) Location of the Mistastin Lake impact structure in Labrador, Canada (55.8833° N; 63.3333°W). (B) Google Earth image (Landsat/Copernicus Maxar Technologies) of Mistastin showing the locations of the impactite samples. Red polygons represent impact deposits mapped by Currie (1971), Grieve (1975), and Marion and Sylvester (2010). Locations of the impactites studied here are Discovery Hill (C), West Point (D), Cote Creek (E) and Steep Creek (F).

4.1.1 Geologic Setting

Mistastin is a 28-km diameter, 37.83 ± 0.05 Ma (Sylvester et al., 2013) complex impact structure formed in a target of Na-anorthosite, granodiorite, and quartz monzonite (Grieve, 1975, 2006; Marion and Sylvester, 2010). The impact structure is situated within the northeastern region of the Mesoproterozoic Mistastin Batholith, made primarily of anorthositic and granitic rocks with minor amounts of gabbroic rocks. Within the center of the impact structure is a near circular lake, occupying the inner 16 km diameter of the crater (Figure 4.1B). Two islands, Horseshoe Island and Bullseye Island, are located near the center of Mistastin Lake. These islands are interpreted to be the remnants of a central uplift (Marion and Sylvester, 2010), which has since been eroded by glacial processes. The majority of the impact melt deposits are found along the western margin of the lake, with a few small outcrops also present on Horseshoe Island and along the south and southeastern shoreline (Figure 4.1B).

The impactite deposits around the structure have varying proportions of impact melt. Grieve (1975) and Mader and Osinski (2018) describe these impactites in a structured impactite stratigraphy (generalized example in Figure 4.2), from the base upwards: unshocked target → fractured and shocked target rocks → monomict impact breccias → polymict impact breccias → impact melt rocks (increase in grain size and decrease in clast abundance from bottom to top) (Figures. 4.2A-D). The lowermost melt-bearing impactites are allochthonous glass-bearing impact breccias (Figures. 4.1F and 4.2D), which overlie melt-free monomict and polymict lithic clastic breccias. Moving up the stratigraphy, the glass-bearing breccia transitions to clast-rich impact melt (Figures. 4.1E and 4.2C). The contact zone between these two impactites is 1–3 m thick, with sinuous and amoeboid shaped lenses of the two impactites intermingling with each other (Mader and Osinski, 2018). Further up the impactite stratigraphy, the clast-rich impact melt

unit transitions to a fine to medium-grained clast-poor impact melt rock. At this transition, the abundance of clasts decreases from >15% to <10% and, at the West Point locality the melt rock is vesicular.

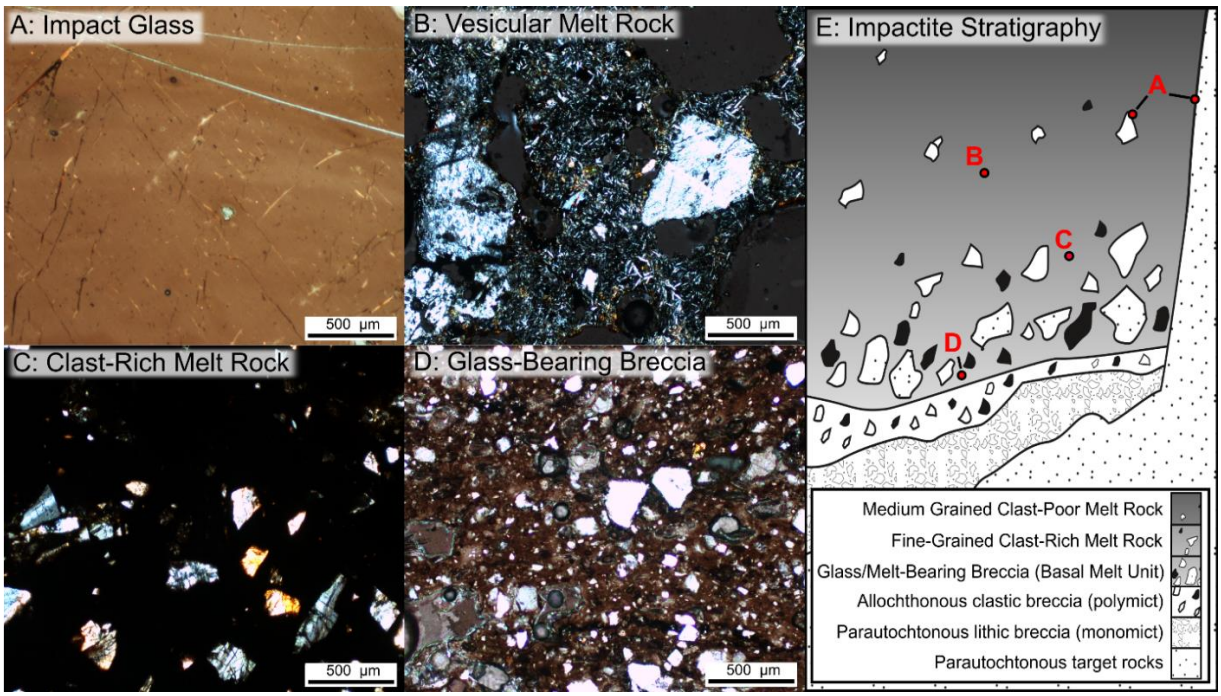

Figure 4.2. Petrographic images of the four impactite samples and their spatial relation in the impactite stratigraphy described by Grieve (1975) and Mader and Osinski (2018). (A) Plane-polarized light (PPL) image of the deep brown hyaline impact glass. (B) Vesicular clast-poor melt rock showing a matrix comprising elongate plagioclase crystals. Clasts of quartz and plagioclase with undulous extinction, annealed boundaries, toasting textures (quartz clasts only) are evenly distributed throughout the entire sample. (C) Aphanitic to fine-grained clast-rich melt rock containing clasts of clinopyroxene, quartz, and plagioclase. Extinction twinning is still visible in the plagioclase under cross-polarized light (XPL). (D) PPL image of the deep brown glass matrix in the glass-bearing breccia. Clasts of quartz and plagioclase in the glass matrix are

<100 µm and range from sub-rounded to angular in shape. (E) Generalized impactite stratigraphy of Mistastin with annotations marking the inferred origin of the impactite samples. Note the impact glass has two potential locations, along the contact with the crater wall and as a quenched melt rind surrounding a large clast. The impact glass was not collected in-situ so its exact stratigraphic position at the Discovery Hill melt deposit at Mistastin is unknown. Image modified from Osinski et al., (2008).

4.2 Methods

One polished thin section was prepared from the glass-bearing impact breccia, clast-rich melt rock and clast-poor melt rock, and four polished thin sections were prepared from the impact glass sample to identify zircon grains entrained within their glass and crystalline matrices. We were only able to analyze one thin section from the glass-bearing impact breccia, clast-rich melt rock, and clast-poor melt rock because due to cost and time restraints using the analytical techniques in this study. Optical microscopy was used to study the microtextures and mineralogy of the glass/melt matrices of the four impactite samples at the University of Western Ontario's Earth and Planetary Materials Analysis (EPMA) Laboratory. From the polished thin sections, a total of 69 zircon grains were identified using electron micro-probe analysis (EMPA) on a JEOL JXA-8530F field emission electron microprobe at the EPMA laboratory. A summary of how many grains were found in each impactite sample and their size dimensions are reported in Table 4.1. A backscattered electron (BSE) image was obtained for each zircon grain to help characterize the grain morphology, shock metamorphic features, and to identify, if present, evidence of zircon dissociation. In addition to collecting images of the zircon grains,

wavelength-dispersive spectroscopy spot analysis was used to analyze the glass and crystalline matrix composition of the impactite samples to determine if they were homogenous. After EMPA, the polished thin sections were prepared for electron backscatter diffraction (EBSD) analysis. Each thin section was further polished using colloidal silica dispersion in NaOH for three hours on a Buehler Vibromet II polisher to ensure a polish of 50 nm was achieved. Finally, a 5 Å-thick carbon-coat was applied to each polished thin section to mitigate electron charging on the surface during EBSD analysis.

Crystallographic orientation maps of the zircon grains were obtained using a JEOL 7600F field emission Scanning Electron Microscopy (SEM) instrument in the E-beam analytical suite of the Astromaterials Research and Exploration Science division at the Johnson Space Center, Houston, TX, USA. The operation conditions were optimized in the SEM for EBSD analysis, including a stage tilt of 70° relative to the incident angle of the electron beam, an acceleration voltage of 20 kV, a beam current of 10 nA, and a 50 – 250 nm step size (Erickson et al., 2021). The microstructures of the zircon grains were analyzed using forescatter electron (FSE) imaging and EBSD mapping. Electron backscatter diffraction patterns were collected using an Oxford Instruments Symmetry detector. The phase and orientations of individual EBSD patterns from the 69 grains were indexed using match units based on the 1 atm unit cell of Hazen & Finger (1979) for zircon, the unit cell of Howard et al. (1988) for baddeleyite, and 0.69 GPa unit cell of Farnan et al. (2003) for reidite. The EBSD data was processed using Oxford's Channel5 program suite; phase and orientation maps were produced using Tango and pole figures were produced using Mambo. To confirm if any of the zircon grains with coronas of baddeleyite have preserved the cubic to monoclinic zirconia transformation, we reconstructed their EBSD orientation data using the Python based ARPGE phase reconstruction software (Cayron, 2007).

4.3 Results

4.3.1 Impactite Petrography

Each of the impactite samples represent a different position within the Mistastin impactite stratigraphy (Figure 4.2). Here we describe the petrographic textures and shock metamorphic features in the four different impactite samples. The impact glass sample has a deep brown to black hyaline matrix (Figure 4.2A). The glass contains clasts of extensively fractured and toasted quartz and fractured plagioclase, all exhibiting undulous extinction under cross-polarized light. At the macro-scale (hand specimen) the impact glass matrix appears homogenous. However, we discovered using EMPA that the matrix is locally heterogenous with flow textures comprising the hyaline glass and schlieren. The hyaline glass has a Na-anorthosite composition and the schlieren, compared to the hyaline glass, is depleted in SiO_2, Al_2O_3, and Na_2O, but enriched in MgO and FeO (See Appendix A.1, Table A1.1 and Figure A1.22). No zircon grains were found within the schlieren, only in the hyaline glass.

The clast-poor vesicular melt rock has a fine to medium-grained crystalline matrix comprising elongate plagioclase crystals (Figure 4.2B). Clasts of quartz and plagioclase exhibit low to no shock metamorphic features and the vesicles in the melt have an average size of 1 cm. The clast-rich melt rock is an aphanitic to fine-grained melt matrix with 15% abundance of clasts. Mineral clasts of clinopyroxene, quartz and plagioclase exhibit extensive fracturing (Figure 4.2C), and undulous extinction under cross-polarized light. The glass-bearing impact breccia has a glass and clastic matrix with the glass matrix exhibiting a deep brown colour under plane polarized light (Figure 4.2D). The clast abundance is >25 %, with the glass matrix

containing numerous sub-rounded to angular fragments of quartz and plagioclase, most exhibiting undulous extinction and irregular fractures.

Table 4.1. A summary of the number of zircon grains identified in the four impactite samples and their size dimensions (min to max measured).

Table 4.1. Number of Zircon Grains

Sample ID	Impactite	No. of Zircon Grains	Zircon Grain Width/Length Dimensions	
CM09-05	Impact Glass	45	3 – 40 μm	8 – 130 μm
MM11-023A	Vesicular Clast-Poor Melt Rock	4	10 – 40 μm	20 – 75 μm
MM10-010	Clast-Rich Melt Rock	4	10 – 55 μm	15 – 90 μm
MM09-033 A2	Glass-Bearing Breccia	16	10 – 25 μm	15 – 40 μm

4.3.2 Microstructure and Crystallographic Analysis

4.3.2.1 Glass-Bearing Impactites

4.3.2.1.1 Impact Glass

Here we describe the morphology and microstructures of the zircon grain and zirconia crystal discovered in the impact glass sample. We identified a total of 45 zircon grains in the impact glass sample, 17 of which have vermicular coronas of baddeleyite crystals. The width/length dimensions of the zircon grains range from 3 – 40 μm/8 – 130 μm (Table 4.1) and

the zirconia crystals width/length dimensions range from <0.5 – 3 μm/<1 – 10 μm. From the 45 zircon grains, 22 display no diagnostic features indicative of ZrO_2-SiO_2 dissociation or shock metamorphism. Instead, they exhibit irregular fractures and anhedral crystal shapes (Figure 4.3A). Shock twinning is observed in one zircon grain showing {112} twin lamellae, oriented sub-vertical along the grain (Figure 4.3B). The grain also exhibits crystal-plastic microstructural deformation, and cumulative plastic strain ranging up to 23°. From the 17 zircon grains with vermicular coronae of baddeleyite (Figure 4.3C), seven exhibit systematic orientations indicating a transformation of cubic to monoclinic zirconia, potentially by a two-stage process via tetragonal zirconia (Cayron et al., 2010). Their zircon cores show no shock metamorphic features, only low angle boundaries (misorientations <10 °) (see Texture Component Maps in Figure 4.3A-C). One of the zircon grains with a vermicular corona of baddeleyite exhibits granular textures with small <1 μm grains of zirconia infilling inclusions within voids in the granular core (Figure 4.3D). EBSD analysis of the zircon neoblasts in the granular core reveal clear 90° misorientations that align with the $<110>_{zircon}$ direction (see Appendix A.1, Figure A2.11). These misorientations are hallmarks for the previous existence of the high pressure polymorph reidite, making this granular core a former reidite granular core (e.g., Former Reidite In Granular Neoblasts (FRIGN) (Cavosie et al., 2018b)). In addition, the FRIGN zircon grain records ~65° disorientation relationships about the $<110>_{zircon}$ with alignments of both {110} and {112} between two domains with similar oriented neoblasts (see Appendix A.1, Figure A1.11). These microstructural hallmarks are indicative of {112} twinning, suggesting that in addition to reidite, some of the granules nucleated from deformation twins.

Five of the 45 zircon grains have completely dissociated to zirconia (Figure 4.3E) and no evidence of preserved silica polymorphs were discovered using EMPA. We also analyzed the

crystallographic orientations of the five fully dissociated grains to determine if cubic → monoclinic zirconia transformation occurred. Our results show that none of the fully dissociated grains exhibit the orientation relationships indicative of a cubic zirconia parent grain. However, due to the size of the fully dissociated grains it is challenging to determine if the margins of these grains are idiomorphic to the original zircon or whether they are a 2D slice of a corona of baddeleyite that was cut during polished thin section preparations.

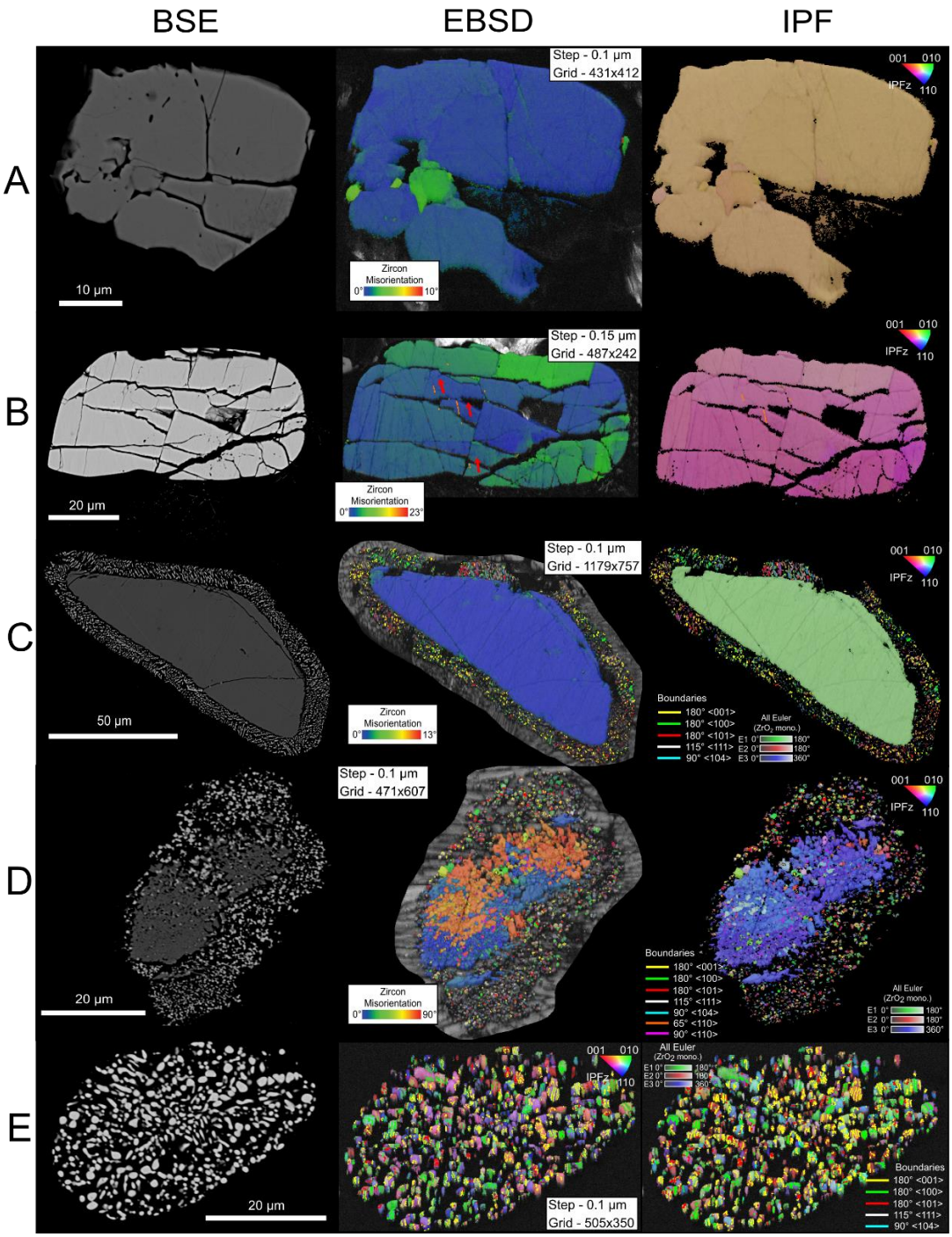

Figure 4.3. Overview of the zircon grain textures identified in the impact glass sample. Left column shows backscatter electron images of the grains, the center column shows EBSD zircon texture component maps, and the right column shows the inverse pole figure (IPF) orientations of each zircon grain and detected zirconia crystals acquired from EBSD analysis. Zircon

orientations are assigned the IPF colour scheme and zirconia crystals are assigned Euler plots. (A) Anhedral zircon grain with irregular fractures cross-cutting the center. (B) Zircon grain with evidence of shock twinning ({112} twin lamellae); visible sub-vertical planar fractures cross-cutting the grain (red arrows pointing to subvertical planar fractures cross-cutting grain). (C) Zircon grain with a ~5 μm thick vermicular corona of baddeleyite crystals. (D) A granular zircon grain surrounded by a vermicular corona of baddeleyite with thickness ranging from 2 μm – 10 μm. Zirconia crystals are also found as inclusions within individual granules, in addition to small voids filled with the surrounding silicate glass. (E) Fully dissociated zircon grain with elongate and globular zirconia. No crystalline silica phases were detected in the EMPA and EBSD data.

One of the most interesting zircon grains in our sample is Zircon CM09_05A-02. Shown in Figure 4, it is one of the seven zircon grains with vermicular coronas of baddeleyite that exhibit systematic orientation relations indicative of cubic to monoclinic zirconia transformation. The zircon core shows minor disorientations less than 7° (Figure 4.4B). The core is elongate, up to ~30 μm long and 5 – 10 μm wide and is surrounded by a 1 – 8 μm thick corona of baddeleyite crystals ranging in size from <0.5 μm – 2 μm wide and up to 5 μm long. The baddeleyite crystals exhibit two distinct morphologies: elongate and sub-rounded, which may either represent different growth habits of baddeleyite crystals or 2D (i.e., basal and prismatic) slices of the same crystal morphology. Using the ARPGE Python-based program, we reconstructed the clusters of baddeleyite crystals to cubic zirconia using the measured EBSD orientation data and theoretical orientation relationships of cubic to tetragonal to monoclinic zirconia transformations reported by Cayron et al. (2010). The misorientations between the baddeleyite crystals were analyzed in detail because they exhibit 90°, 115°, and 180° disorientation (minimum misorientation) angles

that are consistent with cubic-monoclinic transformation twinning (Timms et al., 2017b) (Figure 4.4D). The pole figures of the baddeleyite crystals (see $<100>_{mono}$ i, ii and iii in Figure 4.4E) and reconstructed cubic zirconia crystals (see $<100>_{cubic}$ i, ii and iii in Figure 4.4E) show three distinct clusters. These clusters are composed of twelve unique crystallographic orientation variants that form ~20° cross-shaped patterns on pole figures <100>. Each cluster is spatially distinct, and orthogonal with a ~90° disorientation. This is consistent with the phase transformation from a cubic zirconia parent crystal (Cayron et al., 2010; Timms et al., 2017a,b). Out of the seven zircon grains with vermicular coronas of baddeleyite, four returned positive results confirming cubic → monoclinic zirconia. The other three grains returned results that imply tetragonal zirconia was the dominant high temperature phase (>1673 °C – <2370 °C).

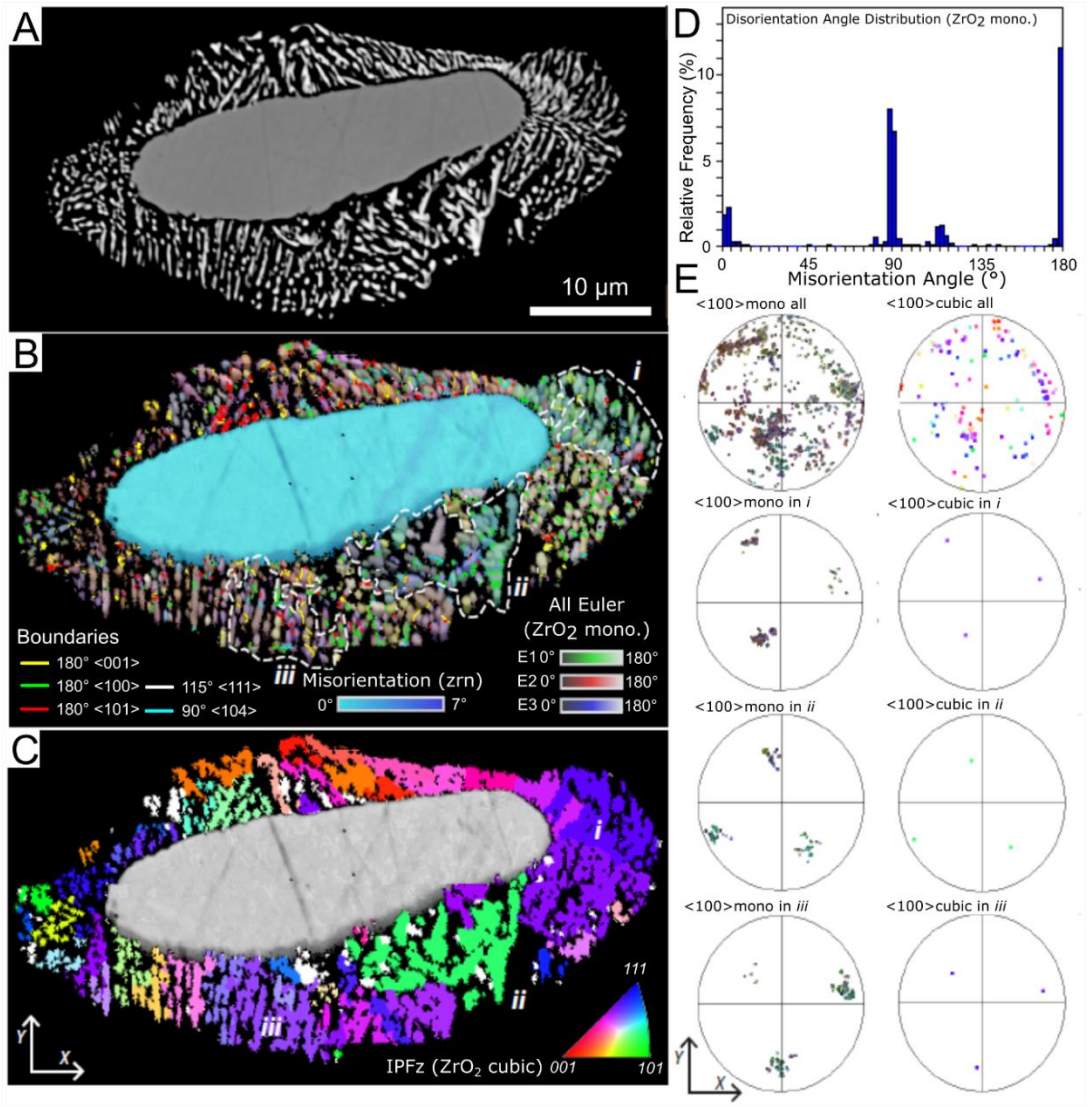

Figure 4.4. Phase reconstruction of one of four zircon grains (CM09_05A-2) with crystallographic evidence of cubic zirconia within the corona of zirconia. (A) BSE image and (B) EBSD orientation map of the zircon grain. (C) Inverse pole figure (IPF) reconstruction of cubic zirconia within the corona using theoretical cubic → monoclinic transformations (Cayron et al. 2010). (D) Histogram of the disorientation angle distribution in the baddeleyite crystals; systematic 90°, 115°, and 180° disorientations are consistent with a cubic parent. (E) Pole figures with <100> baddeleyite and reconstructed <100> cubic zirconia orientations from three baddeleyite domains in the corona.

4.3.2.1.2 Glass-Bearing Breccia

In the glass-bearing breccia sample, we identified 16 zircon grains, two of which are polymineralic inclusions in a quartz clast while the rest are in contact with the melt matrix. The zircon grains in this sample have sizes ranging from 10 μm – 80 μm (Table 4.1). The majority of the grains are anhedral with minor brittle deformation and preserve low angle disorientations (misorientations, 0° – 20°) (e.g., Figure 4.5A-B). Four of the 16 zircon grains exhibit granular zircon textures, three of which also contain domains of reidite (example of reidite, Figure 4.5C, and example of fully granular grain, Figure 4.5D). This is the first discovery of reidite at Mistastin.

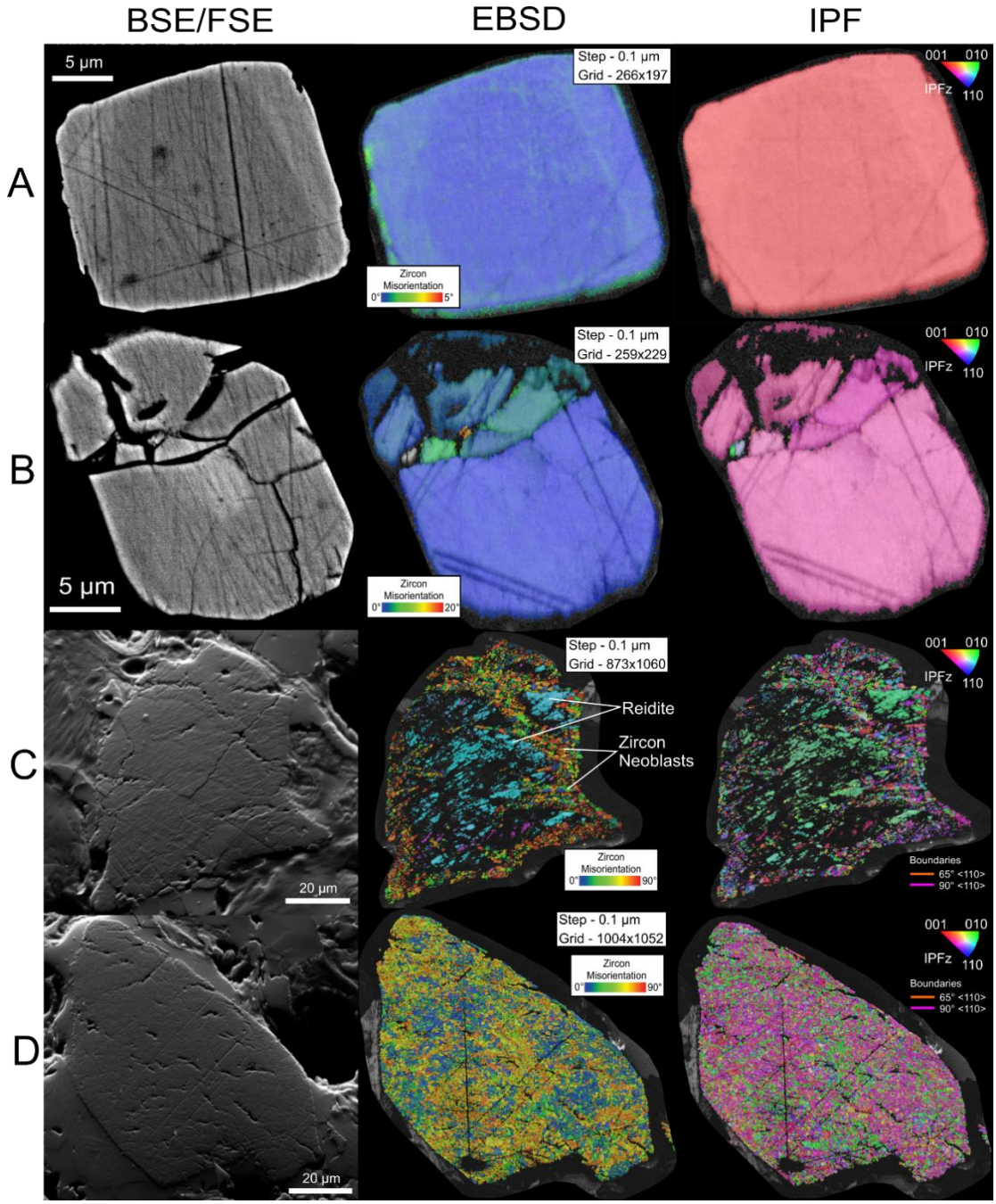

Figure 4.5. Overview of the zircon grain textures identified in the glass-bearing impact breccia sample. Left column shows backscatter electron (BSE) or forescatter electron (FSE) images of the grains, the center column shows EBSD zircon texture component maps, and the right column shows the inverse pole figure (IPF) orientations of the zircon grain acquired from EBSD analysis. (A) Zircon grain with smoothed margins showing no evidence of fracturing or

diagnostic shock metamorphic features. Linear markings shown in the phase and EBSD orientation maps are scratches created from thin section polishing. (B) Subhedral zircon grain with cross-cutting irregular fractures. (C) A granular zircon grain with reidite domains. The high-pressure zircon polymorph reidite is within the center of outer grain margins, which have been recrystallized to granular neoblastic zircon grains each exhibiting their own unique orientation. Special orientation boundaries in zircon shown as coloured lines. (D) A fully granular zircon grain found in close proximity to the three granular, reidite-bearing zircon grains. Orientation relationship data, revealed from EBSD analysis, suggest this granular zircon crystallized from a zircon grain that contained reidite domains. Special orientation boundaries in zircon shown as coloured lines.

The reidite-bearing granular zircon grains exhibit systematic 90° disorientation relationships between $<001>_{zircon}$ and $<110>_{zircon}$ in the neoblasts (Figure 4.6) (see Appendix A1 for the other two reidite-bearing granular zircon grain EBSD data, Figures A1.12 and 13). This disorientation and alignment has previously been interpreted as evidence for the reversion of reidite to zircon (Cavosie et al., 2016; Timms et al., 2017a). Our study is one of few to report this reversion product in a granular zircon grain still containing reidite (cf. Erickson et al., 2017; Timms et al., 2017a). The reversion from reidite to zircon is also supported by the alignment between the $<110>_{reidite}$ and $<001>_{zircon}$ (Figs. 6D-E).

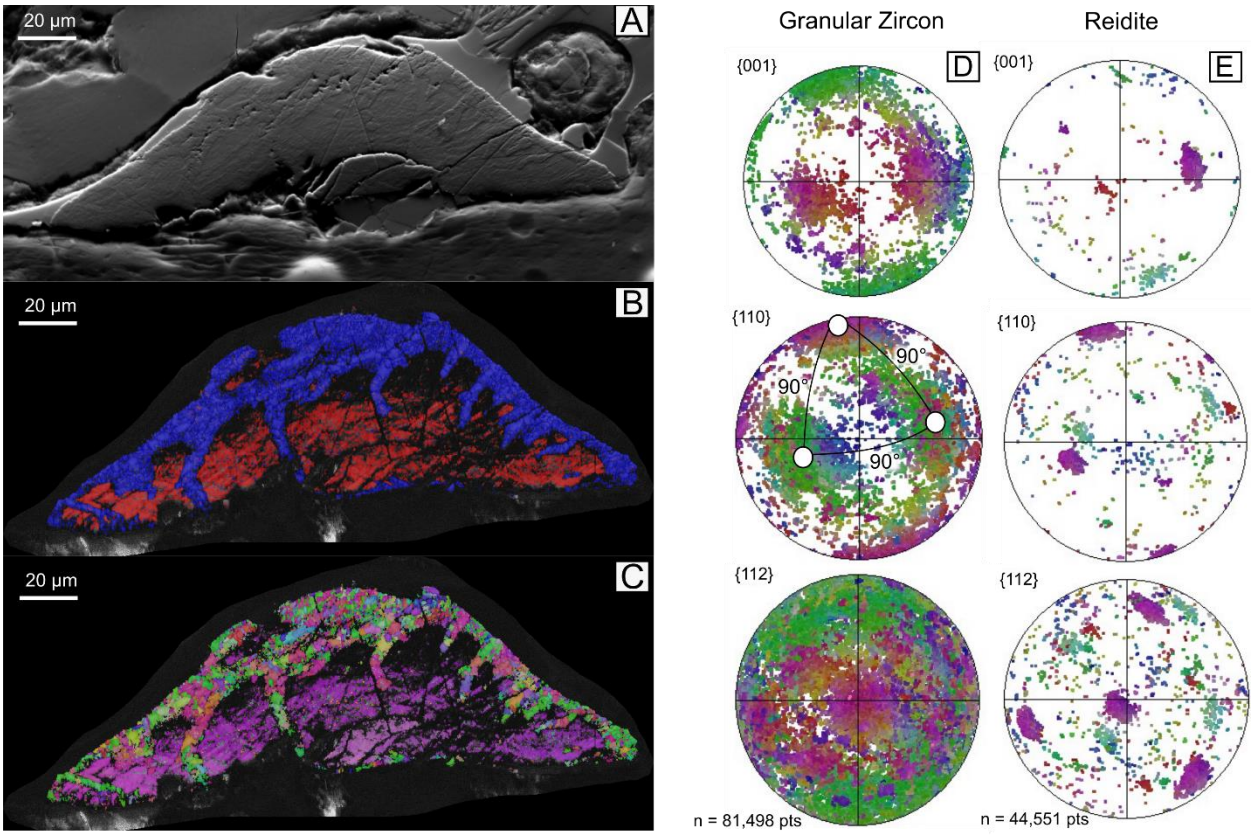

Figure 4.6. Microstructure and crystallographic orientation data of one of the three reidite-bearing granular zircon grains (sample MM09_033A2-21). (A) Forescatter electron (FSE) image of the reidite-bearing granular zircon grain. (B) Electron backscatter diffraction analysis (EBSD) phase map identifying zircon and reidite in the grain. (C) EBSD orientation map of the measured orientations of each zircon neoblast and reidite grain. Zircon and reidite assigned the inverse pole figure (IPF) colour scheme. (D) Pole figures for zircon. Colour scheme as in C. (E) Poles figures for reidite. Colour scheme as in C. Alignment of grouped variants in $<001>_{zircon}$ and $<110>_{reidite}$ (black circles), and the 90° disorientation relations (as annotated in $<110>_{zircon}$ pole figure) in $<110>_{zircon}$ indicate the granular zircon formed from the reversion process of reidite to zircon.

We also observed a fully granular zircon grain in EBSD data (Figure 4.5D). The data from this grain reveals 65° disorientation relationships about the $<110>_{zircon}$ (see Appendix A1, Figure A1.14), which is unique to {112} twinning, similar to the shock twinning observed in the zircon grain in the impact glass sample (Figure 4.3B). We also observe systematic 90° disorientation relationships between $<001>_{zircon}$ and $<110>_{zircon}$, similar to what we observe between the reidite and zircon neoblasts in the reidite-bearing granular zircon grains. These alignments and orientation relations are similar to crystallographic relationships connected to the transformation of zircon to reidite and then reversion of reidite to zircon, where the $<001>_{zircon}$ is parallel to the $<110>_{reidite}$, creating two orthogonal sets containing eight unique orientation variants (Erickson et al., 2017). When reidite reverts to zircon it follows orientation relationship paths that produce three approximately orthogonal orientations of zircon (Erickson et al., 2017;Timms et al., 2017a), showing ~90° disorientations. This confirms that this granular zircon grain is a FRIGN, similar to the FRIGN core identified in the impact glass sample (Figure 4.3D).

4.3.2.2 Crystalline Melt Rock Impactites

4.3.2.2.1 Vesicular Clast-Poor Impact Melt Rock

Only four zircon grains were discovered in the clast-poor vesicular melt, and none had evidence of ZrO_2-SiO_2 dissociation. The grains range in size from 10 μm – 75 μm (Table 4.1). The zircon grains preserve low angle disorientations in their cores, ranging from 0° – 10°. The grains also have voids containing the surrounding silicate melt and fractures that crosscut the

grain core but lack diagnostic high pressure and temperature shock deformation features (Figures. 4.7A-C).

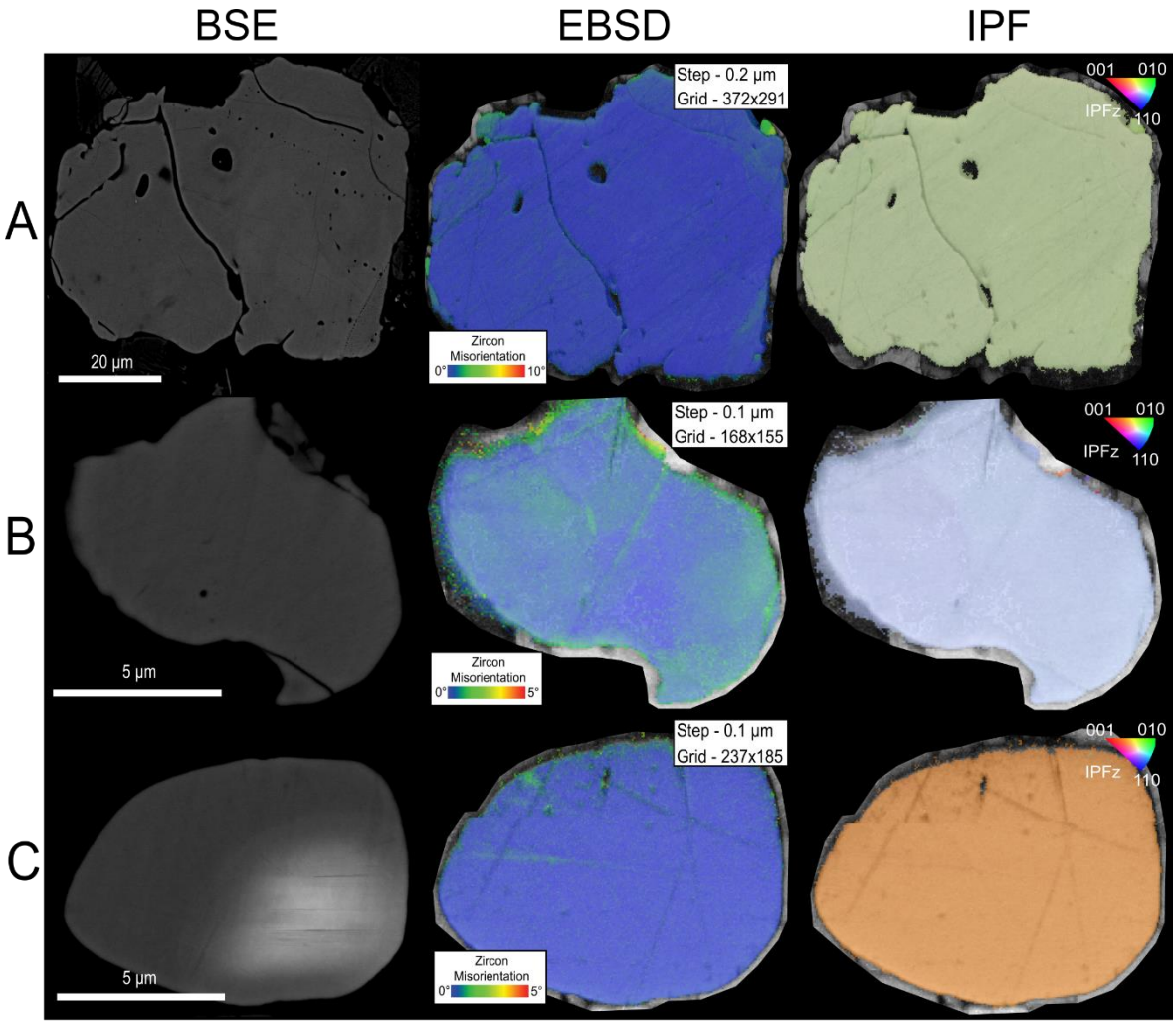

Figure 4.7. Overview of the zircon grain textures identified in the vesicular clast-poor melt rock sample. Left column shows backscatter electron images of the grains, the center column shows EBSD zircon texture component maps, and the right column shows the inverse pole figure (IPF) orientations of the zircon grain acquired from EBSD analysis. (A) Subhedral zircon grain with irregular fractures cross-cutting and several voids, containing the surrounding silicate melt. (B) Anhedral zircon grain with partially scalloped boundaries, and a single void filled with the

surrounding silicate melt. (C) Zircon grain with smoothed margins showing no evidence of fracturing or diagnostic shock metamorphic features. Linear markings shown in the phase and EBSD orientation maps are indentations created from thin section polishing.

4.3.2.2.2 Clast-Rich Impact Melt Rock

Four zircon grains were identified in the clast-rich melt rock, all of which are in direct contact with the melt and range in size from 10 – 90 μm. They exhibit similar morphologies to the grains in the clast-poor vesicular melt rock, showing no evidence of zircon dissociation or diagnostic shock features (Figure 4.8). Only extensive fracturing and undulous extinction is evident. One grain, however, shows evidence of minor melt assimilation (Figure 4.8A) and may have been part of a larger grain that broke apart during the impact event. No evidence of zirconia crystals was found along the boundary of the grain. If zirconia is present then it may have crystallized to a size that is too small to be detected by the electron beam. EBSD analysis revealed no zirconia phases present, only small zircon granules with orientations that differ from the main zircon grain (~20°, 0° – 5°) (Figure 4.8A, see Texture Component column).

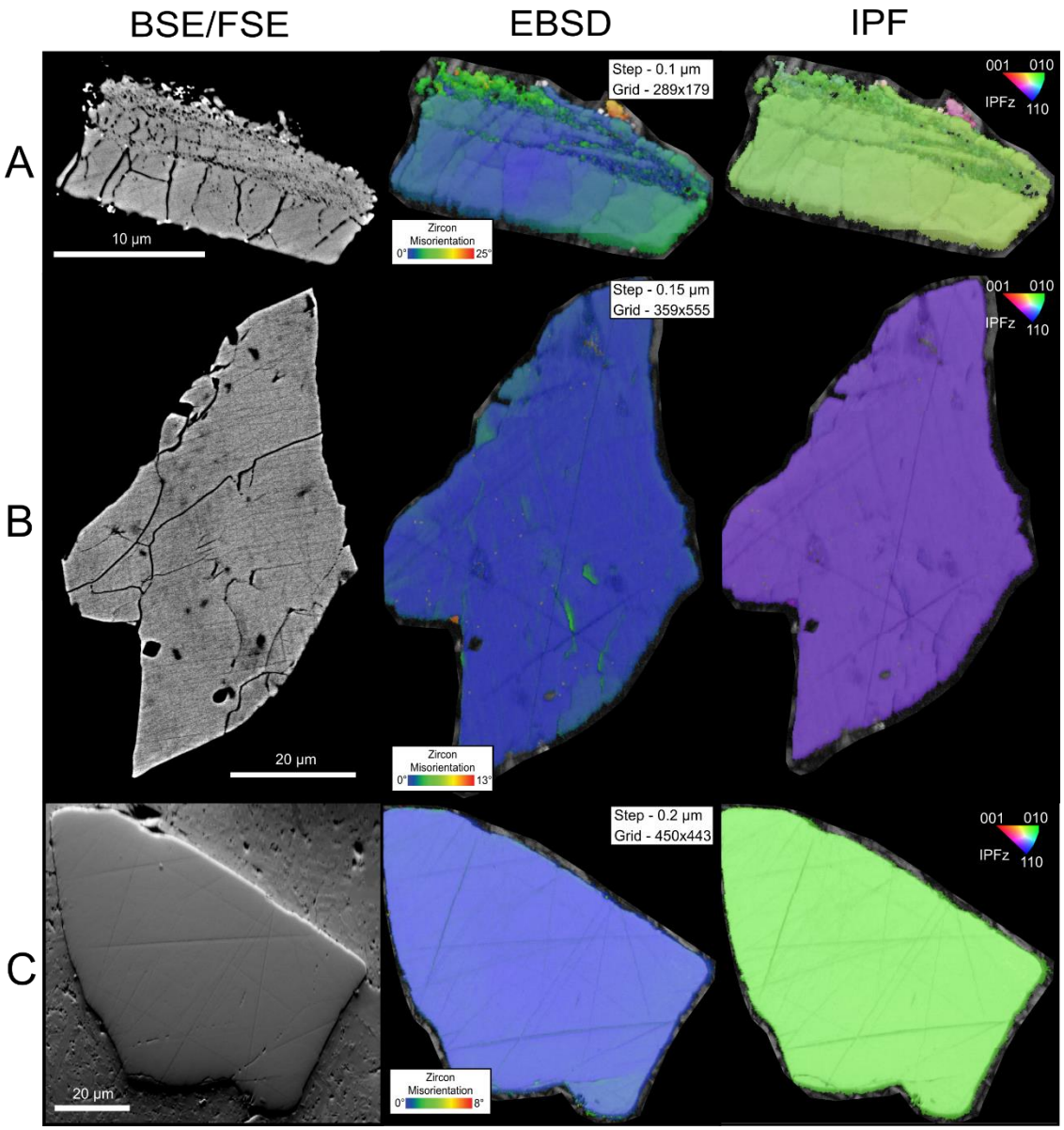

Figure 4.8. Overview of the zircon grain textures identified in the clast-rich melt rock sample. Left column shows backscatter electron (BSE) or forescatter electron (FSE) images of the grains, the center column shows EBSD zircon texture component maps, and the right column shows the inverse pole figure (IPF) orientations of the zircon grain acquired from EBSD analysis. (A) Zircon grain that has experienced extensive fracturing and partial thermal annealing along one margin (top of grain). No zirconia or high-pressure zircon were detected in the grain, and the smaller zircon grain fragments along the top margin exhibit different orientations compared to

the large grain. (B) Anhedral zircon grain with irregular fractures cross-cutting and several voids, containing the surrounding silicate melt. (C) Zircon grain with smoothed margins showing no evidence of fracturing or diagnostic shock metamorphic features. Linear markings shown in the phase and EBSD orientation maps are indentations created from thin section polishing.

4.4 Discussion

4.4.1 Confirming the superheated nature of impact melts

In this work, we identified four zircon grains with coronae of baddeleyite crystals exhibiting systematic orientation relations indicative of cubic to monoclinic zirconia transformation. These results support previous work by Timms et al., (2017b) suggesting that impact melt at Mistastin was superheated at temperatures in excess of 2370°C. However, we only discovered these zircon grains within the impact glass sample, the same type studied by Timms et al., (2017b). The glass was also collected from one location, at the Discovery Hill impact melt deposit, so it remains unclear whether superheating is common in multiple types of impactites. A note to consider is that our sample size was limited to four impactites. A larger sample size may be required to further test our hypothesis.

4.4.2 Zircon diversity in quenched glass

In addition to the confirmation of superheating from zircon grains, we also discovered that the impact glass sample contains a variety of zircon shock features, including shock twinning, granular textures (FRIGN grain), and partial to full dissociation textures. The variety

of zircon shock features record a diverse array of temperature and pressure conditions, revealing more about the P-T history of the Mistastin impact cratering event. The development of shock twinning, indicated by the presence of $\{112\}_{zircon}$ twin lamellae (visible as subvertical fractures in Figure 4.3B), requires shock pressures of ≥20 GPa (Timms et al., 2012), confirmed in static experiments on quenched zircon powder (Morozova, 2015). The lack of evident thermal annealing or ZrO_2-SiO_2 dissociation implies that the grain was entrained into the melt when temperatures were < 1673°C (min. temperature for zircon dissociation (El Goresy, 1965; Timms et al., 2017b; Wittmann et al., 2006)). The zircon grain with twinning would have originated close enough to the point of impact to be within a 20 GPa pressure contour (Melosh, 1989; Morozova, 2015), but far enough from the melting zone to prevent immediate melt entrainment to protect the zircon grain from thermal annealing and dissociation.

The FRIGN grain (Figure 4.3D) in the impact glass would have followed the formation paths for both shock twinning and reidite, prior to being entrained into melt with temperatures >1200°C (Kusaba et al., 1985; Wittmann et al., 2006) to fully revert the reidite to zircon and produce the granular neoblastic texture (Cavosie et al., 2018, 2016; Timms et al., 2017a). Evidence for the former presence of reidite and shock twinning preserved in the zircon neoblasts crystallographic relationships (systematic 90° disorientation alignments in $<110>_{zircon}$, and ~65° disorientations in $<110>_{zircon}$ with alignments of $<110>_{zircon}$ and $<112>_{zircon}$) indicates that a minimum peak pressure condition of >30 GPa was achieved (Kusaba et al., 1985; Morozova, 2015). The presence of baddeleyite along the core boundaries and as inclusions in the grain, but lack of silica polymorphs, indicates that impact melt temperatures had to have exceeded 1687°C (Timms et al., 2017a). No evidence of the cubic to monoclinic transformation is recorded in the baddeleyite crystals, so temperatures could not have exceeded 2370°C. Therefore, the reidite

grain would have been entrained into impact melt with temperatures between 1687°C and <2370 °C.

Our documentation of fully, partially, and non-dissociated zircon grain textures in the impact glass sample is surprising, given the high temperature variations and time exposures to superheated melt needed to produce these textures (El Goresy, 1965; Wittmann et al., 2006; Timms et al., 2017b). It is possible that the fully dissociated grains are 2D slices of baddeleyite corona, which could be an explanation as to why we do not observe any systematic orientations that indicate transformations from high temperature zirconia polymorphs. For the partially dissociated zircon grains, we report two preserved temperature thresholds both recorded in baddeleyite systematic orientation relationships. The discovery of the four grains with coronae of baddeleyite that exhibit evidence of cubic to monoclinic zirconia transformation provides us with a temperature threshold between 2370 °C and 2700 °C (cubic zirconia would have melted at temperatures in excess of 2700°C (Timms et al., 2017b)). For the other 13 partially dissociated zircon grains, the crystallographic orientation relationships imply that tetragonal zirconia was the high temperature polymorph, not cubic zirconia, signifying a melt temperature range of 1687 °C to <2370 °C (the lack of silica polymorphs in coronas indicates that a minimum temperature had to be at least 1687°C; Timms et al., 2017b).

The simplest explanation for the preservation of both partially and non-dissociated zircon grain textures is that the partially dissociated grains were entrained earlier during the opening of the transient cavity, when the impact melt was still superheated. The zircon grains lacking evidence for dissociation were likely entrained closer to the end of the impact crater formation process. At this point, the impact melt temperature was <1673°C and close to quenching, but the viscosity of the melt had not yet reached a critical point when it could no longer entrain clasts

and minerals (Onorato et al., 1978). The quenching of the glass would need to be rapid enough to prevent thermal annealing and erasure of the high temperature zirconia polymorph transformation orientation data, but prolonged enough to allow the melt to mix and acquire zircon grains from different locations in the transient cavity.

4.4.3 Preservation of high P-T indicators

The glass-bearing impact breccia contains the first confirmed identification of the high-pressure zircon polymorph reidite in the Mistastin Lake impact structure. This is one of the few studies to report reidite still preserved in a granular zircon grain (cf. Erickson et al., 2017; Timms et al., 2017a). The presence of three granular neoblastic zircons with reidite domains with no evidence of zircon dissociation indicates that the grains were subjected to a minimum peak pressure >30 GPa and then postimpact temperatures >1200 °C but <1673 °C (Kusaba et al., 1985; Wittmann et al., 2006; Erickson et al., 2017; Stangarone et al., 2019). The melt matrix of the glass-bearing impact breccia was therefore at temperatures sufficient to revert reidite to zircon but rapidly cooled at a rate that allowed some reidite to be retained in the granular zircon grains. This is consistent with the lithology of the glass-bearing impact breccia, which shows evidence for the melt quenching rapidly and fragmenting during transportation, prior to intruding into fractures in the crater floor (Mader and Osinski, 2018).

The presence of a FRIGN grain in close proximity to the reidite-bearing granular zircon grains in the glass-bearing impact breccia sample implies that the quenching time of the melt may have been heterogenous. The melt surrounding the FRIGN grain must have maintained a temperature >1200 °C for a longer period (Cavosie et al., 2016), allowing the complete reversion

of reidite to zircon. The cryptic preservation of both reidite and shock twinning (90° disorientation about $<110>_{zircon}$ and alignment between $<001>_{zircon}$ and $<110>_{zircon}$, 65° disorientation about $<110>_{zircon}$) in the FRIGN grain indicates that the minimum shock pressure would have been ≥ 30 GPa (Kusaba et al. 1985). Unfortunately, we cannot interpret the peak pressure conditions of the FRIGN grain because it is challenging to determine the state of the original zircon grain prior to recrystallization. However, the systematic orientation data of the zircon neoblasts do indicate that the granular zircon was not amorphous prior to recrystallization (Cavosie et al., 2016), and that the grain may have been similar to the original state of the reidite-bearing granular zircon; originally a massive reidite grain. After transformation to reidite, the grains would have mixed with the melt at temperatures between 1200 °C and 1673 °C, and were emplaced as impact breccia dykes (Mader and Osinski, 2018).

4.4.4 High P-T shock zircon indicators in other impact structures

Evidence for superheating at Mistastin suggests that other similarly sized (and larger) terrestrial impact structures with crystalline targets would produce impact melt with similar temperatures. Nearby crystalline impact structures, West Clearwater Lake (36-km diameter) and Manicouagan (65-km diameter) located in Quebec, Canada, are ideal examples of where we might expect to find evidence for superheating. Both impact structures are of similar size and exhibit large quantities of impact melt deposits. It is possible the melt deposits at these craters contain evidence of both high temperature and high-pressure conditions, preserved in baddeleyite crystallographic orientation data, and as reidite-bearing and/or FRIGN grains.

If both high P-T zircon indicators are more common than initially thought in terrestrial impact structures, then impact melt deposits from lunar craters may also contain these zircon grains. Previous work has investigated the microstructures and crystallography of zircon grains identified in Apollo impactites and lunar regolith samples (Liu et al., 2012; Timms et al., 2012; Crow et al., 2017), but to date, no studies have solely focused on searching for zircon grains encased within the impact glass and melt matrices. Recent work by Xing et al., (2020) reported the first evidence of reidite in the regolith portion of the lunar meteorite Sayh al Uhaymir (SaU) 169. The presence of reidite in a lunar meteorite sample has implications for the possible presence of reidite in Apollo samples, which would allow us to better constrain the shock pressure history of lunar impact cratering events (Crow et al., 2017; Xing et al., 2020). In addition to high pressure indicators, we are confident in saying that superheated temperatures can be preserved in lunar samples, as demonstrated by work reported by White et al., (2020). It is now a question of whether high pressure indicators and evidence of superheating is common in other lunar impact melt samples.

4.5 Conclusions

We identified 69 zircon grains from four impactite samples (impact glass, clast-poor impact melt rock, clast-rich impact melt rock, and glass-bearing impact breccia) from the Mistastin Lake impact structure. The grains exhibit a broad range of different microstructures, levels of shock metamorphism, and ZrO_2-SiO_2 dissociation. We discovered four zircon grains with evidence for the transformation of zircon to cubic zirconia in the impact glass sample, supporting work by Timms et al., (2017b) that the Mistastin Lake impact melt was superheated

to temperatures > 2370°C. In the glass-bearing impact breccia sample, we discovered the first evidence of reidite at Mistastin, preserved in three granular zircon grains. The fully granular zircon grain in the glass-bearing impact breccia and the granular zircon core with a corona of baddeleyite in the impact glass had crystallographic orientation relations that recorded the former presence of reidite (i.e., FRIGN zircon). The FRIGN zircon grains are also the first to be discovered at Mistastin.

The lack of diagnostic shock metamorphic features and zircon dissociation in the clast-rich impact melt rock and the clast-poor impact melt rock reveals the heterogeneity of temperature conditions at Mistastin, with evidence for superheating currently only found in glass-bearing impactites. However, we were only able to analyze one thin section from these two impactites, so the analysis of additional samples could lead to the discovery of finding evidence of superheating in crystalline impact melt rocks. The occurrence of reidite-bearing granular zircon grains and FRIGN grains demonstrates that high pressure zircon polymorphs are prevalent in high temperature melt environments, helping us constrain both the high P and high T conditions of impact cratering events. An outstanding question from this study is whether high pressure zircon polymorphs and evidence for cubic to monoclinic zirconia transformation are present in other similarly sized terrestrial impact structures, and in lunar impactites. Impact craters with equivalent or greater size to Mistastin would have been commonly produced in the early history of the Earth-Moon system when the frequency and magnitude of impacts were greater. Therefore, constraining the P-T evolution of impact melts can provide new information about how impacts modified the early Earth-Moon system.

References

Cavosie, A.J., Timms, N.E., Erickson, T.M., Hagerty, J.J., Hörz, F., 2016. Transformations to granular zircon revealed: Twinning, reidite, and ZrO2 in shocked zircon from Meteor Crater (Arizona, USA). Geology 44, 703–706. https://doi.org/10.1130/G38043.1

Cavosie, A.J., Timms, N.E., Ferrière, L., Rochette, P., 2018. FRIGN zircon-The only terrestrial mineral diagnostic of high-pressure and high-temperature shock deformation. Geology 46, 891–894. https://doi.org/10.1130/G45079.1

Cayron, C., 2007. ARPGE: A computer program to automatically reconstruct the parent grains from electron backscatter diffraction data. J. Appl. Crystallogr. 40, 1183–1188. https://doi.org/10.1107/S0021889807048777

Cayron, C., Douillard, T., Sibil, A., Fantozzi, G., Sao-Jao, S., 2010. Reconstruction of the cubic and tetragonal parent grains from electron backscatter diffraction maps of monoclinic zirconia. J. Am. Ceram. Soc. 93, 2541–2544. https://doi.org/10.1111/j.1551-2916.2010.03894.x

Cherniak, D.J., Manchester, J., Watson, E.B., 2007. Zr and Hf diffusion in rutile 261, 267–279. https://doi.org/10.1016/j.epsl.2007.06.027

Chhabra, R.P., 2010. Non-Newtonian fluids: An introduction, in: Rheology of Complex Fluids. Springer, New York, pp. 3–34. https://doi.org/10.1007/978-1-4419-6494-6_1

Crow, C.A., McKeegan, K.D., Moser, D.E., 2017. Coordinated U–Pb geochronology, trace element, Ti-in-zircon thermometry and microstructural analysis of Apollo zircons.

Geochim. Cosmochim. Acta 202, 264–284. https://doi.org/10.1016/j.gca.2016.12.019

Dressler, B.O., Morrison, G.G., Peredery, W. V., Rao, B. V., 1987. Shock Metamorphism features in the Sudbury Structure, Ontario, Canada - A Review, in: In: Pohl J. (Eds) Research in Terrestrial Impact Structures. Earth Evolution Sciences (International Monograph Series on Interdisciplinary Earth Science Research and Applications). Vieweg+Teubner Verlag, Wiesbaden, pp. 39–68. https://doi.org/https://doi.org/10.1007/978-3-663-01889-6_3

El Goresy, A., 1968. The opaque minerals in impactite glasses, in: Shock Metamorphism of Natural Materials. Mono Book Corp, pp. 531–553.

El Goresy, A., 1965. Baddeleyite and its significance in impact glasses. J. Geophys. Res. 70, 3453–3456. https://doi.org/10.1029/jz070i014p03453

Erickson, T.M., Kirkland, C.L., Jourdan, F., Schmieder, M., Hartnady, M.I.H., Cox, M.A., Timms, N.E., 2021. Resolving the age of the Haughton impact structure using coupled 40Ar/39Ar and U-Pb geochronology. Geochim. Cosmochim. Acta 304, 68–82. https://doi.org/10.1016/j.gca.2021.04.008

Erickson, T.M., Pearce, M.A., Reddy, S.M., Timms, N.E., Cavosie, A.J., Bourdet, J., Rickard, W.D.A., Nemchin, A.A., 2017. Microstructural constraints on the mechanisms of the transformation to reidite in naturally shocked zircon. Contrib. to Mineral. Petrol. 172, 1–26. https://doi.org/10.1007/s00410-016-1322-0

Erickson, T.M., Timms, N.E., Pearce, M.A., Cayron, C., Deutsch, A., Keller, L.P., Kring, D.A., 2019. Shock-produced high-pressure (La, Ce, Th)PO4 polymorph revealed by

microstructural phase heritage of monazite. Geology 47, 504–508. https://doi.org/10.1130/G46008.1

Farnan, I., Balan, E., Pickard, C. J., & Mauri, F. 2003. The effect of radiation damage on local structure in the crystalline fraction of ZrSiO4: Investigating the 29Si NMR response to pressure in zircon and reidite. American Mineralogist, 88, 11-12, 1663-1667. https://doi.org/10.2138/am-2003-11-1205

Gomes, R., Levison, H.F., Tsiganis, K., Morbidelli, A., 2005. Origin of the cataclysmic Late Heavy Bombardment period of the terrestrial planets. Nature 435, 466–469. https://doi.org/10.1038/nature03676

Grieve, R.A.F., 2006. Mistastin, in: Impact Structures in Canada. Geological Association of Canada, pp. 115–120.

Grieve, R.A.F., 1975. Petrology and chemistry of the impact melt at Mistastin Lake crater, Labrador. Bull. Geol. Soc. Am. 86, 1617–1629. https://doi.org/10.1130/0016-7606(1975)86<1617:PACOTI>2.0.CO;2

Grieve, R.A.F., Dence, M.R., Robertson, P.B., 1977. Cratering processes: As interpreted from the occurrence of impact melts, in: In Impact and Explosion Cratering: Planetary and Terrestrial Implications. pp. 791–814.

Hart, S.R., Davis, K.E., 1978. Nickel Partitioning between Olivine and Silicate Melt. Earth Planet. Sci. Lett. 40, 203–219. https://doi.org/10.1016/0012-821X(78)90091-2

Hazen, R. M., & Finger, L. W. 1979. Crystal structure and compressibility of zircon at high

pressure. American Mineralogist, 64, 1-2, 196-201.

Howard, C. J., Hill, R. J., & Reichert, B. E. 1988. Structures of ZrO2 polymorphs at room temperature by high-resolution neutron powder diffraction. Acta Cryst. Section B: Structural Science, 44, 2, 116-120. https://doi.org/10.1107/S0108768187010279

Kaiser, A., Lobert, M., Telle, R., 2008. Thermal stability of zircon (ZrSiO4). J. Eur. Cermaic Soc. 28, 2199–2211. https://doi.org/10.1016/j.jeurceramsoc.2007.12.040

Kring, D.A., Cohen, B.A., 2002. Cataclysmic bombardment throughout the inner solar system 3.9-4.0 Ga. J. Geophys. Res. E Planets 107, 4–1. https://doi.org/10.1029/2001je001529

Kusaba, K., Syono, Y., Kikuchi, M., Fukuoka, K., 1985. Shock behavior of zircon: phase transition to scheelite structure and decomposition. Earth Planet. Sci. Lett. 72, 433–439. https://doi.org/10.1016/0012-821X(85)90064-0

Lev, E., Hamilton, C.W., Voigt, J.R.C., Stadermann, A.C., Zhan, Y., Neish, C.D., in press. Emplacement conditions of lunar impact melt flows. Icarus.

Lindsley, D.H., Andersen, D.J., 1983. A Two-Pyroxene Thermometer. J. Geophys. Res. 88, 887–906. https://doi.org/10.1029/JB088iS02p0A887

Liu, D., Jolliff, B.L., Zeigler, R.A., Korotev, R.L., Wan, Y., Xie, H., Zhang, Y., Dong, C., Wang, W., 2012. Comparative zircon U-Pb geochronology of impact melt breccias from Apollo 12 and lunar meteorite SaU 169, and implications for the age of the Imbrium impact. Earth Planet. Sci. Lett. 319–320, 277–286. https://doi.org/10.1016/j.epsl.2011.12.014

Mader, M.M., Osinski, G.R., 2018. Impactites of the Mistastin Lake impact structure: Insights

into impact ejecta emplacement. Meteorit. Planet. Sci. in press. https://doi.org/10.1111/maps.13173

Marchi, S., Bottke, W.F., Bierhaus, M., Wuennemann, K., Morbidelli, A., Kring, D.A., 2014. Widespread mixing and burial of Earth's Hadean crust by asteroid impacts. Nature 511, 578–582. https://doi.org/10.1038/nature13539

Marion, C.L., Sylvester, P.J., 2010. Composition and heterogeneity of anorthositic impact melt at Mistastin Lake crater, Labrador. Planet. Space Sci. 58, 552–573. https://doi.org/10.1016/j.pss.2009.09.018

Melosh, H.J., 1989. Impact Cratering: A Geologic Process. Oxford University Press (Oxford Monographs on Geology and Geophysics, No. 11).

Morbidelli, A., Marchi, S., Bottke, W.F., Kring, D.A., 2012. A sawtooth-like timeline for the first billion years of lunar bombardment. Earth Planet. Sci. Lett. 355–356, 144–151. https://doi.org/10.1016/j.epsl.2012.07.037

Morozova, I., 2015. Strength Study of Zircon Under High Pressure [M.Sc. Thesis]: Western University, 112 p.

Onorato, P.I.K., Uhlmann, D.R., Simonds, C.H., 1978. The Thermal History of the Manicouagan Impact Melt Sheet , Quebec. J. Geophys. Res. 83, 2789–2798. https://doi.org/10.1029/JB083iB06p02789

Osinski, G.R., Grieve, R.A.F., Bleacher, J.E., Neish, C.D., Pilles, E.A., Tornabene, L.L., 2018. Igneous rocks formed by hypervelocity impact. J. Volcanol. Geotherm. Res. 353, 25–54.

https://doi.org/10.1016/j.jvolgeores.2018.01.015

Osinski, G.R., Grieve, R.A.F., Marion, C.L., Chanou, A., 2012. Impact Melting, in: Osinski, G.R., Pierazzo, E. (Eds.), Impact Cratering: Processes and Products. Wiley-Blackwell, pp. 125–145. https://doi.org/10.1002/9781118447307.ch9

Osinski, G.R., Pierazzo, E., 2012. Impact Cratering Processes and Products, 1st ed. Wiley-Blackwell.

Osinski, G.R., Tornabene, L.L., Grieve, R.A.F., 2011. Impact ejecta emplacement on terrestrial planets. Earth Planet. Sci. Lett. 310, 167–181. https://doi.org/http://dx.doi.org/10.1016/j.epsl.2011.08.012

Sack, R.O., Ghiorso, M.S., 1991. Chromian spinels as petrogenetic indicators: thermodynamics and petrological applications. Am. Mineral. 76, 827–847.

Stangarone, C., Angel, R.J., Prencipe, M., Mihailova, B., Alvaro, M., 2019. New insights into the zircon-reidite phase transition. Am. Mineral. 104, 830–837. https://doi.org/10.2138/am-2019-6827

Sylvester, P., Crowley, J., Schmitz, M., 2013. U-Pb zircon age of Mistastin Lake Crater, Labrador, Canada - implications for high-precision dating of small impact melt sheets and the end eocene extinction, in: Goldschmidt. p. 2295.

Timms, N. E., Erickson, T.M., Pearce, M.A., Cavosie, A.J., Schmieder, M., Tohver, E., Reddy, S.M., Zanetti, M.R., Nemchin, A.A., Wittman, A., 2017a. A pressure-temperature phase diagram for zircon at extreme conditions. Earth-Science Rev. 165, 185–202.

https://doi.org/10.1016/j.earscirev.2016.12.008

Timms, Nicholas E., Erickson, T.M., Zanetti, M.R., Pearce, M.A., Cayron, C., Cavosie, A.J., Reddy, S.M., Wittmann, A., Carpenter, P.K., 2017b. Cubic zirconia in >2370◦C impact melt records Earth's hottest crust. Earth Planet. Sci. Lett. 477, 52–58. https://doi.org/10.1016/j.epsl.2017.08.012

Timms, N.E., Reddy, S.M., Healy, D., Nemchin, A.A., Grange, M.L., Pidgeon, R.T., Hart, R., 2012. Resolution of impact-related microstructures in lunar zircon: A shock-deformation mechanism map. Meteorit. Planet. Sci. 47, 120–141. https://doi.org/10.1111/j.1945-5100.2011.01316.x

Wittmann, A., Kenkmann, T., Schmitt, R.T., Stöffler, D., 2006. Shock-metamorphosed zircon in terrestrial impact craters. Meteorit. Planet. Sci. 41, 433–454. https://doi.org/10.1111/j.1945-5100.2006.tb00472.x

White, L.F., Černok, A., Darling, J.R., Whitehouse, M.J., Joy, K.H., Cayron, C., Dunlop, J., Tait, K.T. and Anand, M., 2020. Evidence of extensive lunar crust formation in impact melt sheets 4,330 Myr ago. Nature Astronomy, v. 622, p.1–5. https://doi.org/10.1038/s41550-020-1092-5

Xing, W., Lin, Y., Zhang, C., Zhang, M., Hu, S., Hofmann, B.A., Sekine, T., Xiao, L., Gu, L., 2020. Discovery of Reidite in the Lunar Meteorite Sayh al Uhaymir 169. Geophys. Res. Lett. 47. https://doi.org/10.1029/2020GL089583

Chapter 5: Discussion and Conclusion

5.1 Discussion

This thesis work investigated both the surface roughness of lava flows and pressure and temperature conditions of impact melt deposits to gain greater insight into the emplacement mechanisms of lunar impact melt flows. From Chapters 2 and 3, we investigated the capabilities and limitations of using SAR data to differentiate terrestrial lava flows based off their surface roughness. In Chapter 4, we sought to constrain the pressure and temperature conditions of impact melt deposits at the Mistastin Lake impact structure. Overall, we summarize three points: (1) it is challenging to differentiate transitional, siliceous block-ʻaʻā, and ʻaʻā lava flow types, and lava facies using SAR data, (2) impact melt at the Mistastin Lake impact structure were superheated >2370°C implying they behaved as Newtonian fluids before substantial cooling was achieved, and (3) high-pressure shock zircon indicators can be found within glass and melt matrices in impactites that exhibited high temperatures.

5.1.1 Lava Flows and Impact Melt

We focused on using radar to quantify the surface roughness of terrestrial lava flows because surface roughness can be used to infer the style of flow emplacement (Peterson and Tilling, 1980; Rowland and Walker, 1990; Solana et al., 2004; Guilbaud et al., 2005; Duraiswami et al., 2008b; Harris et al., 2017). Our analyses (see Chapters 2 and 3) demonstrate that there are limitations when using SAR data to differentiate moderately rough lava flows (i.e., ʻaʻā and block-ʻaʻā latite), transitional lava flow types, and lava facies in large lava flow-fields.

As a note, transitional rubbly pāhoehoe lava flows are reported to be the closest analogue in terms of surface roughness to lunar impact melt flows, but their CPR values at the decimetre-scale are not as high as the values acquired from lunar radar data sets (0.5–0.73 vs. >1) (Neish et al., 2017). We emphasized throughout this study that if we are incapable of differentiating these lava flows using radar remote sensing data, then we will have difficulty understanding the emplacement mechanisms of impact melt flows and lava flows on planetary bodies (Greeley and King, 1977; Lancaster et al., 1995; Keszthelyi et al., 2000a, 2006; Rodriguez Sanchez-Vahamonde and Neish, 2021). We also emphasized in this thesis that because lava flows form under different geologic processes (i.e., decompression/flux melting vs instantaneous shock) and exhibit different intrinsic physical properties compared to impact melt, we needed to study a physical property of impact melt that profoundly influences flow emplacement (see Section 1.1 in Chapter 1).

If we want to fully understand the emplacement mechanisms of lunar impact melt flows, we needed to constrain the temperature of impact melt since temperature has a direct influence on the behaviour of melt fluid dynamics and rheology (e.g., Lev et al., in press; Pierazzo et al., 1997; Cashman et al., 1999; Griffiths, 2000; Sehlke et al., 2014). All impact melt forms are interpreted to form at superheated temperatures (Grieve et al., 1977; Osinski et al., 2018) that far exceed the sub-liquidus temperatures of lava flows, which implies their fluid behaviour will be Newtonian (Chhabra, 2010) during their initial formation and emplacement (e.g., Dence, 1971; Grieve et al., 1977; Timms et al., 2017b). Constraining the temperature of impact melt was therefore a vital addition to this study since remote sensing analysis is not sufficient for providing detailed impact melt temperature constraints.

The SAR and crystallographic orientation data presented in this work were not directly compared to remote sensing data sets and measurements of lunar impact melt flows in this study. Despite this however, we were able to establish a better understanding on how we can use SAR to study lava flows on planetary bodies and use zircon grains and zirconia crystals to constrain impact melt P-T conditions more accurately. The derived temperature threshold data confirming the superheated nature of impact melts can be applied to impact bombardment models (e.g., Lev et al., in press; Albarede, 2009; Onorato et al., 1978) used to understand the size and morphology of impact craters and distribution of impact melt deposits, and our conclusions on how different lava flow types can exhibit similar CPR and backscatter results imply that it will be challenging to infer emplacement processes without ground-truth data or the addition of high resolution imagery.

5.1.2 Limitations of SAR Analysis for Lava Flow Roughness Analysis

If we want to understand the current limitations of utilizing SAR applications for lava flow and impact melt flow emplacement studies, we need to revisit the reasons why certain lava flow types and lava facies can and cannot be differentiated. As reported in Chapters 2 and 3, we are capable of analyzing the roughness of numerous lava flow types and lava facies using SAR data. We were able to make clear distinctions between smooth and very rough lava flow types (e.g., smooth pāhoehoe and blocky lava at Craters of the Moon) using CPR data, building on the work of previous authors who have used radar remote sensing analysis to investigate the roughness of terrestrial and planetary lava flows (e.g., Schaber et al., 1980; Campbell and Shepard, 1996; Campbell, 2012; Harmon et al., 2012; Morgan et al., 2016; Neish et al., 2017).

What we have highlighted in this work is the limitation of using SAR to differentiate transitional lava flows (e.g., rubbly pāhoehoe, slabby pāhoehoe, spiny pāhoehoe, shelly pāhoehoe, etc.) from unique siliceous block-ʻaʻā latite lava flows, and the limitation of using SAR to differentiate lava facies that exhibit similar combinations of lava flow type mixtures (i.e., the rubbly and undifferentiated rubbly-spiny facies mapped at Holuhraun (Voigt et al., 2021)).

When analyzing the surface of a lava flow, we must recall that roughness is a scale dependent property. Thus, a surface can appear smooth or rough depending on the wavelength of the remote sensing instrument and the size of the clasts on a disrupted lava surface (Campbell, 2002; Carter et al., 2011; Neish and Carter, 2014). We have also shown from our study that lava flows with different surface textures and emplacement histories can return similar roughness characteristics. We observed this conundrum at COTM where the rubbly pāhoehoe and siliceous block-ʻaʻā returned similar CPR despite both lava flows exhibiting different textures (mechanically fractured pāhoehoe crust vs. sharp, clinker-like viscous-tearing, blocky surface) and forming under different emplacement mechanisms (Tolometti et al., 2020). The volume (i.e., diffuse) scattering of the radar signals on the surface of the rubbly and block-ʻaʻā produce a moderate CPR value (~0.7), as both lack surface features that induce predominantly quasi-specular (single-bounce) or dihedral (double bounce) scattering effects. We can differentiate a smooth lava flow (e.g., smooth pāhoehoe) from a very rough lava flow (e.g., blocky) confidently using SAR, but challenges still stand when we include transitional and moderately rough (CPR, 0.5–0.7) lava flow types.

At Holuhraun, we noticed similar limitations when it came to using quad-polarized UAVSAR and dual-polarized Sentinel-1 radar to differentiate the three dominant lava facies (rubbly, spiny, and undifferentiated rubbly-spiny facies) mapped by Voigt et al., (2021). Through

qualitative and quantitative analyses, we are only able to confidently say that the spiny facies, which only cover 25.96% of the lava flow-field (Voigt et al., 2021), are separable from the rubbly and undifferentiated rubbly-spiny facies. No distinctions could be made using the SAR data between the rubbly and undifferentiated rubbly-spiny facies, even at two different wavelengths. One-Way ANOVA and Tukey-Kramer tests suggested the rubbly and undifferentiated rubbly-spiny facies are statistically separable using the Sentinel-1 radar data, but their VH/VV data distribution overlapped within errors, and their mean values were practically identical. These two facies are difficult to differentiate due to their similarities in their corresponding lava flow types. Rubbly pāhoehoe is the dominant lava flow type in both the rubbly and undifferentiated rubbly-spiny facies, which can exhibit CPR values from 0.5–0.7 (Neish et al., 2017; Tolometti et al., 2020) at the decimetre-scale. Voigt et al., (2021) reports that the surface of the undifferentiated rubbly-spiny facies is dominated by lava flow morphologies and surface textures similar to the rubbly facies so this could explain our challenge in differentiating it in the two SAR data sets.

Despite the limitations of SAR analysis of lava flows presented in this work, we find that radar remote sensing is still an effective tool for analyzing and quantifying the surface roughness of lava flows on planetary bodies. However, further studies should investigate whether transitional lava flow types can be differentiated using new SAR decomposition and filtering techniques (Lee and Pottier, 2009). Transitional lava flows are the most common lava flow types to form during the emplacement of large lava flow-fields (i.e., flood lavas and flood basalts), which cover vast surfaces of terrestrial planetary bodies such as Mars (e.g., Keszthelyi et al., 2004, 2006; Jaeger et al., 2010), Venus (e.g., Lancaster et al., 1995; Zimbelman, 1998), and Jupiter's moon Io (e.g., Keszthelyi et al., 2006). The inclusion of more terrestrial analogue field

sites to ground-truth SAR data will be vital for determining if transitional lava flows can be differentiated from radar data. Examples of alternative terrestrial analogue field sites that exhibit transitional, as well as traditional pāhoehoe, ‘a‘ā, and blocky lava flows, are situated across the SW region of the United States, Peru, and Iceland. Some potential field sites include the Carrizozo lava flow (New Mexico, USA), Sabancaya (Peru), SP Crater (Arizona, USA), and Sunset Crater (Arizona, USA) (Figure 5.1. A-D).

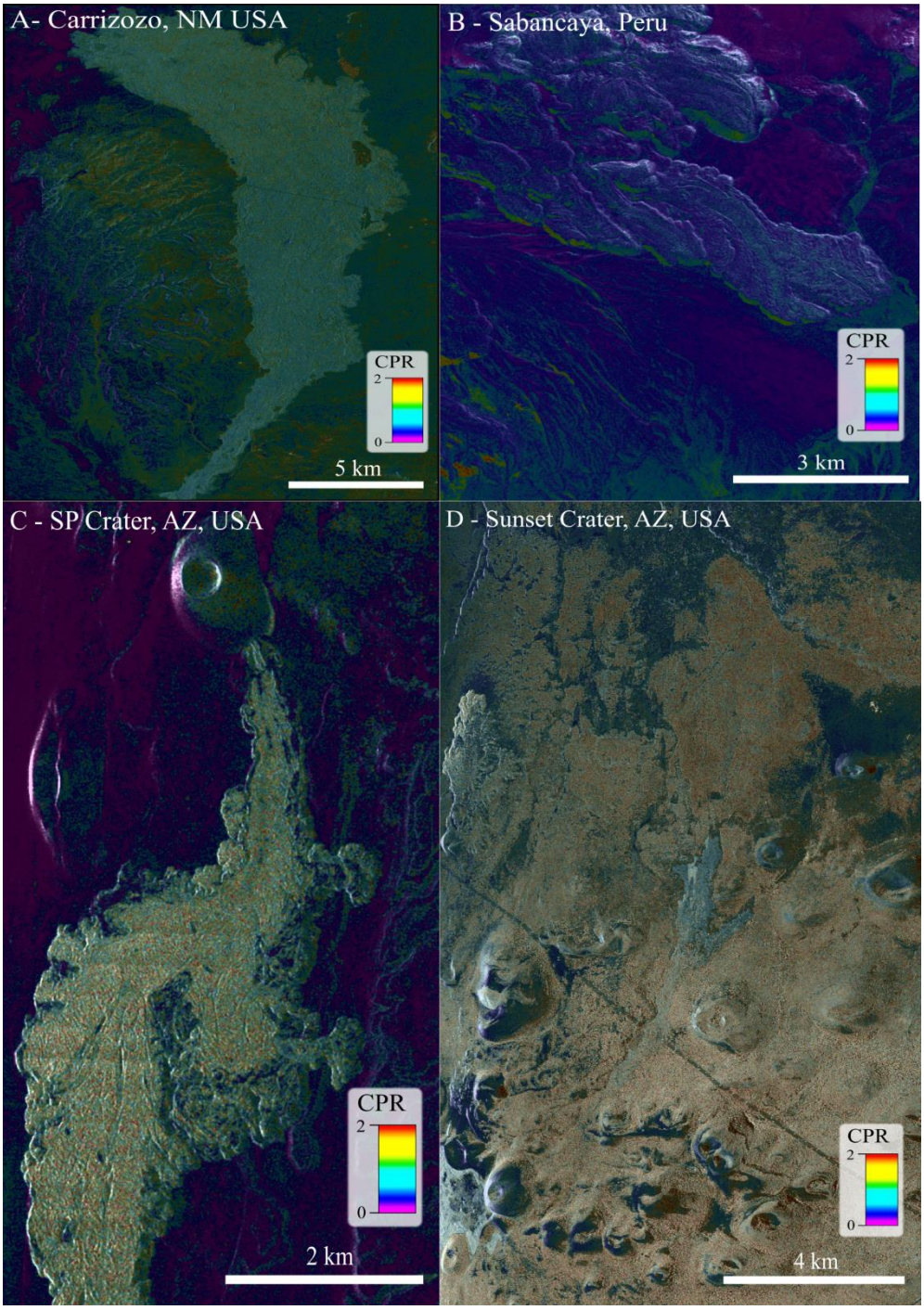

Figure 5.1. L-band synthetic aperture radar data of terrestrial volcanic sites collected by airbourne platforms (AIRSAR and UAVSAR). (A) Carrizozo lava flow, NM, USA. (B) Sabancaya block lava flow, Peru. (C) SP Crater flow, AZ, USA. (D) Sunset Crater National Monument, AZ, USA.

5.1.3 Constraining Impact Melt P-T Conditions from Zircon and Zirconia

Our investigation of impactites from the Mistastin Lake impact structure led to several interesting discoveries regarding impact melt temperature thresholds and the impact event pressure conditions. First, was the discovery of four zircon grains with coronae of baddeleyite crystals in the impact glass sample that exhibit systematic orientation relations indicative of cubic to monoclinic zirconia transformation. This transformation implies the zircon grains were subjected to melt temperature >2370°C to <2700°C, which further supports the consensus that the Mistastin Lake impact melt was initially superheated (Timms et al., 2017b). In addition, the impact glass sample contained zircon grains that experienced dissociation, implying an impact melt temperature >1687°C to <2370°C. Our second discovery were two FRIGN zircon grains – first occurrence at the Mistastin Lake impact structure – in the impact glass and glass-bearing impact breccia samples. These zircon grains are unique for recording both high temperature and high pressure conditions (Cavosie et al., 2018b; Kovaleva et al., 2019; Zhao et al., 2021), as they record the transformation from zircon to reidite (minimum P = >30 GPa, (Kusaba et al., 1985; Wittmann et al., 2006)) and the reversion from reidite to zircon through thermal annealing (>1200 °C, (Cavosie et al., 2016)). The final discovery was reidite – first occurrence of the high-pressure zircon polymorph at the Mistastin Lake impact structure – within granular zircon cores from the glass-bearing impact breccia. Reidite is a rare high-pressure zircon polymorph and has only been found preserved in a few other terrestrial impact structures (e.g., Chen et al., 2013; Cavosie et al., 2015; Reddy et al., 2015; Erickson et al., 2017; Cox et al., 2018) and one lunar meteorite (Xing et al., 2020). From these discoveries, we noticed that evidence for superheating was only found preserved in the quenched impact glass samples. In addition, all of the high-pressure shock indicators (i.e., reidite and FRIGN zircon grains) were found within the melt

matrices and not within clastic matrices or shocked clasts (c.f. Cavosie et al., 2015, 2018; Reddy et al., 2015; Erickson et al., 2017; Kovaleva et al., 2019). It is worth noting, that our sample size was limited to four impactites from only four localities across the entire impact structure. It is therefore possible that sample biasing may have contributed to the lack of evidence for superheating in the crystalline impact melt rocks and glass-bearing impact breccia samples we studied. To resolve this, we would need to perform a more thorough sampling procedure at Mistastin, which would involve collecting samples of melt-bearing impactites along a set stratigraphic traverse at all of the impact melt deposits (see Section 2.21 for more details).

5.2 Future Work

5.2.1 Planetary Analogues: SAR Analysis of Lava Flows

Studying the surface roughness of terrestrial lava flows can help provide us to understand the emplacement of planetary lava flows with analogous surface properties. Planetary volcanism is listed as a high priority science topic for planetary exploration studies, including reports such as the Lunar Exploration Roadmap (Lunar Exploration Analysis Group, 2016). A step towards improving comparative studies between terrestrial and planetary lava flows is to increase the priority of incorporating new SAR instruments onboard future orbiter missions to Mars, Venus, and other planetary bodies with volcanic terrains. The SAR instrument would require a wavelength akin to terrestrial SAR instruments, as this would make comparing the planetary and terrestrial radar data results more intuitive. Terrestrial SAR instruments, as demonstrated in this study, commonly use C-band and L-band wavelengths to analyze the surface roughness of lava

flows and other geologic landforms (e.g., Schaber et al., 1980; Campbell and Shepard, 1996; Khan et al., 2007; Campbell, 2012; Neish et al., 2017; Tolometti et al., 2020) while planetary spacecraft missions – up until the launch of the Indian Space Research Organization (ISRO) Chandrayaan-2 spacecraft (Putrevu et al., 2020) – primarily use S-band (λ = 12.6 cm) (e.g., Spudis et al., 2009; Carter et al., 2011; Cahill et al., 2014; Neish et al., 2014; Patterson et al., 2017). As a result, we currently cannot make true comparisons between terrestrial and planetary features in SAR data. Since surface roughness is a scale dependent property (Campbell and Shepard, 1996; Shepard et al., 2001), even a small difference in wavelength can affect the radar backscattering properties of a surface. A lava flow imaged with S-band radar on the Moon could return CPR values similar to a terrestrial lava flow imaged with an L-band radar, but it is challenging to say whether that means they are analogues or not.

The arrival of ISRO's Chandrayaan-2 spacecraft to the Moon in 2019 brought the first SAR instrument into lunar orbit that includes both S-band and L-band frequencies (Figure 5.2), providing us with SAR data that is comparable to terrestrial SAR platforms (e.g., AIRSAR, UAVSAR, and ALOS PALSAR) (Putrevu et al., 2016, 2020). Although data coverage is not currently as extensive as that from the LRO Mini-RF instrument or the Arecibo Observatory (Carter et al., 2012; Lawrence et al., 2013; Patterson et al., 2017), it is the first steps towards making true SAR comparisons between terrestrial lava flows and lunar impact melt flows and lava flows. In addition, the L-band wavelength provides a penetration depth that is intermediate between the S-band and P-band radar used to study the lunar near-side with Arecibo (e.g., Campbell et al., 2010; Carter et al., 2011; Morgan et al., 2016). Mare lava flows are covered in metre-thick layers of lunar regolith, and S-band and P-band data have been used to penetrate the regolith layer and discern lava flow boundaries (Morgan et al., 2016). The addition of an L-band

data set would be able to provide new information about the roughness, distribution, and extent of mare lava flows, and the thickness and physical properties of the regolith layers (Bhiravarasu et al., 2021).

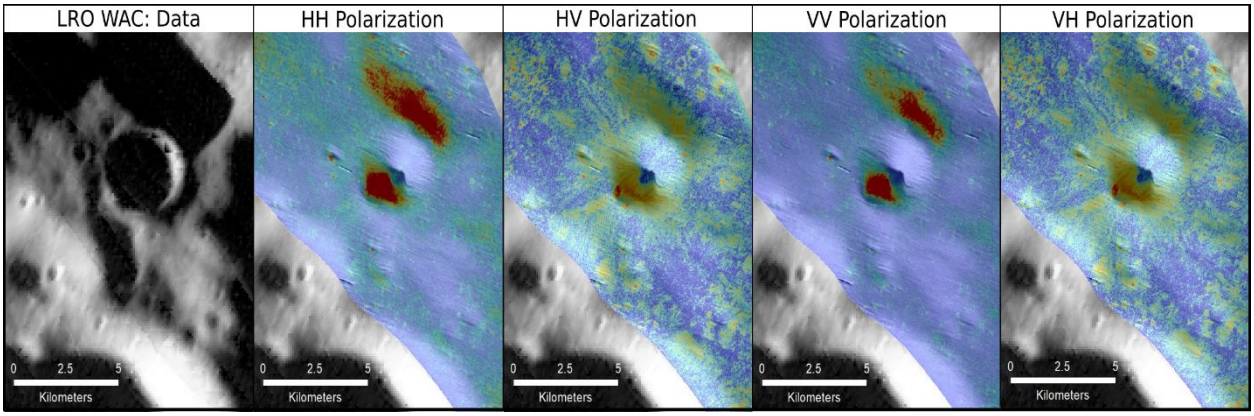

Figure 5.2. Full polarimetric SAR data acquired by the ISRO Chandrayaan-2 spacecraft. Four polarimetric radar signals (HH, HV, VV, and VH) showing impact ejecta deposits surrounding the rims of an ~4-km diameter simple crater north of the Ibn Bajja crater in the lunar south pole (-86.234° N, -68.928° E). Highlighted in the HV and VH polarization data are rays of impact ejecta – volume scattering represented by cross-polarized radar signals.

For Mars, a proposed mission concept with the goal of searching for water and suitable landing sites for humans would include an L-band SAR instrument with a hybrid polarization mode (transmit circular polarization signal and receive two linear polarization (H and V) signals (Campbell, 2002; Lee and Pottier, 2009; Neish and Carter, 2014)). Called the International Mars Ice Mapper (Davis, 2021), it is a mission proposal that is being developed by NASA, the Canadian Space Agency (CSA), the Italian Space Agency (ASI), and the Japan Aerospace

Exploration Agency (JAXA). The proposed mission may have a human exploration and an in-situ resource utilization (ISRU) focused goal, but the L-band SAR instrument could also be used to analyze the geology of the Martian surface, including volcanism and impact cratering. If it goes forward, this mission would provide us with a new set quantitative radar data of the Martian surface, a missing piece of information required to more precisely compare terrestrial lava flows to Martian lava flows (Rodriguez Sanchez-Vahamonde and Neish, 2021).

As mentioned in Chapter 3, the use of SAR to determine whether lava facies at the 2014-2015 Holuhraun lava flow-field could be differentiated from one another can be applied to segmenting lava facies in lava flow-fields on other planetary bodies. Two missions to our sister planet "Venus" have a strong SAR component, including the newly selected NASA Discovery mission Venus Emissivity, Radio Science, Insar, Topography, And Spectroscopy (VERITAS) (Hensley et al., 2012) and the newly selected ESA Cosmic Vision EnVision mission (Ghail et al., 2012). Both of these missions seek to understand the geologic history of Venus, but the EnVision mission science objectives and instrument suite are more in line with the goals and objectives of this research. Some of the science objectives outlined in the EnVision Assessment Study Report (ESA/SCI (2021)) seek to address the following topics: (1) to determine the style of volcanic processes, emplacement styles, magma properties, and relative ages of different lava flows on Venus; and (2) to constrain the nature and occurrence of volcanism on Venus and how its volcanic processes compare to terrestrial and other planetary body volcanism. The EnVision mission is an orbiter that will carry a variety of remote sensing instruments including a dual-polarization S-band SAR that will map the surface of Venus at spatial resolutions of 10 m (high-resolution, local mapping) and 30 m (global coverage) using altimetry, polarimetry, and radiometry. The SAR instrument, known as VenSAR, was designed to reconstruct the surface

stratigraphy of Venus to reveal geological and chronological relations between different units, providing a more refined understanding of the Venusian geologic history. The VenSAR S-band component can be used to compare the morphology and evolution of Venusian volcanism to lunar volcanism, since the LRO Mini-RF and ISRO Chandrayaan-1 and 2 spacecrafts use the same wavelength. Comparisons between Venusian and terrestrial volcanism can be made after the launch of the NASA-ISRO SAR Mission (NISAR) spacecraft in 2022. NISAR will be the first satellite to carry two different SAR frequencies, at S-band and L-band.

5.2.2 Expanding Zircon and Zirconia Studies

5.2.2.1 Preservation of High P-T indicators across Mistastin and other terrestrial impact structures

An outstanding question from our analysis of the impactites from the Mistastin Lake impact structure is whether high pressure and temperature shock metamorphic indicators occur across the entire structure or are constrained to specific localities. Our sample suite was restricted to four different localities, and not all of the samples were collected in-situ or along a traverse line moving up the impactite stratigraphy. Documenting how the zircon grain and zirconia crystal microstructures and crystallographic orientations change moving up the impactite stratigraphy from all melt deposits preserved at Mistastin would provide us with a full picture of the thermal conditions of the impact event. The preservation of the entire impactite stratigraphy is heterogenous across the impact structure however, with the most well-preserved deposits situated at Cote Creek and Discovery Hill (see Figure 4.1 in Chapter 4). An ideal sampling method at these sites would be to collect several impactite samples from each melt-bearing impactite unit (Figure 5.3) to ensure each sample is in-situ and that we increase our chances of

finding a plethora of zircon grains for analysis. At melt deposit localities where preserved impactites are fewer (e.g., Piccadilly Creek, West Point, South Shore, and Steep Creek (Grieve, 1975; Marion and Sylvester, 2010; Mader and Osinski, 2018)), we will have to collect as many different impactite samples in-situ. If we are able to discover evidence of reidite, FRIGN zircon grains, and superheating at other locations at the Mistastin Lake impact structure, then we can state that (1) high-pressure zircon polymorphs are more prevalent in impact events that produce a high abundance of superheated impact melt, and (2) evidence for superheating is not constrained to quenched impact glass samples.

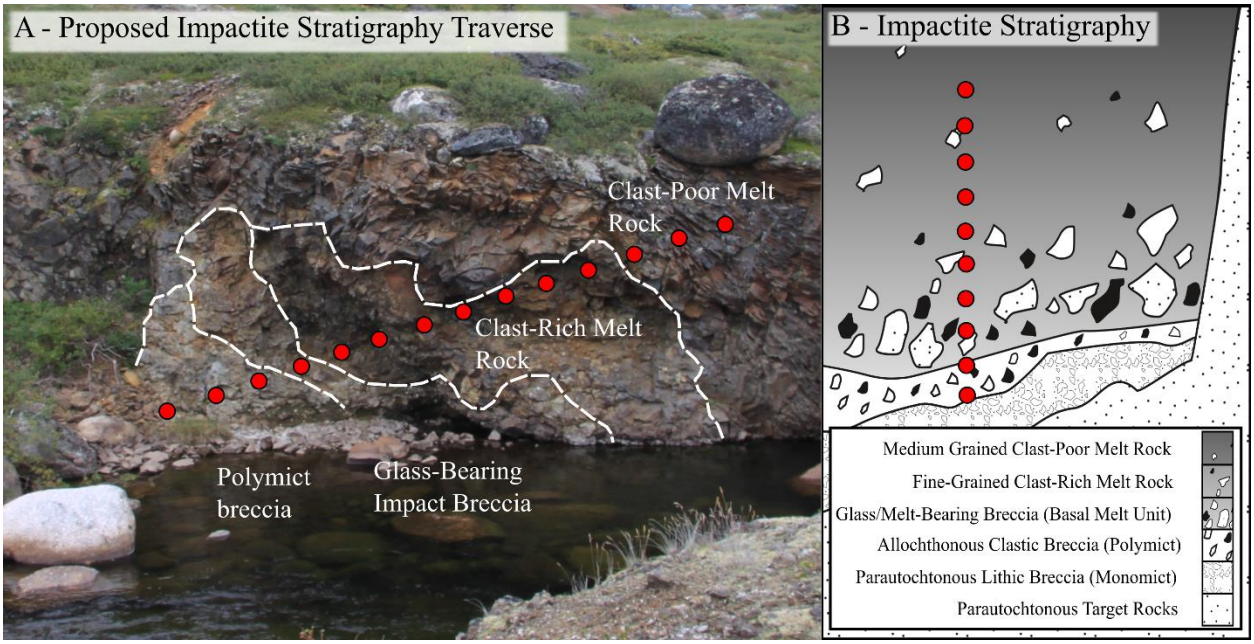

Figure 5.3. Illustration of a proposed sampling method to collect impactites up the Mistastin Lake impactite stratigraphy. (A) Field image of Cote Creek with all melt-bearing impactites exposed in a riverbed outcrop. Red points mark rough locations of where a sample would be collected in the field. (B) Generalized illustration of the Mistastin impactite stratigraphy, modified from Osinski et al., (2008), showing the locations of where the red dots in (A) would be situated.

Studies have shown that reidite (e.g., Reddy et al., 2015; Timms et al., 2017a), granular zircons (e.g., Kamo et al., 1996; Cavosie et al., 2010, 2016, 2018a; Moser et al., 2011; Kenny et al., 2017), FRIGN zircon grains (e.g., Cavosie et al., 2018b; Kovaleva et al., 2019; Zhao et al., 2021), and zirconia crystallized from high-T conditions (Kovaleva et al., 2021; Timms et al., 2017b) can be found in terrestrial impact structures. However, it remains to be seen how prevalent these zircon grain microtextures and polymorphs are between different impact structures. If reidite, FRIGN zircon grains, and evidence for >2370 °C superheating is preserved at the Mistastin Lake impact structure, then it is credible to say that similar shock zircon indicators could be found in other terrestrial impact structures of similar or greater size. The Canadian Shield is an outstanding natural laboratory for studying impact cratering processes, as numerous craters of various sizes and melt abundances have been documented and sampled during past field deployments (summary provided by Grieve (2006)). Examples of some of the impact structures that are situated in the Canadian Shield and have target rocks compositionally analogous to Mistastin are Manicouagan, Quebec (Floran et al., 1978; Simonds et al., 1978a), West Clearwater, Quebec (Phinney et al., 1978; Simonds et al., 1978), East Clearwater, Quebec (Reimold et al., 1981), and La Moinerie, Quebec (Bottomley et al., 1978).

If high pressure zircon shock indicators and zirconia crystals with crystallographic orientation relationships indicative of superheating are present in terrestrial impact structures such as Manicouagan, West Clearwater, East Clearwater, and/or La Moinerie, then we can compare the thermal and shock pressure conditions and histories of the impact structures. Currently, no zircon and zirconia microstructure and crystallography focused studies have been conducted on these terrestrial impact structures, and current studies have only focused on a few other terrestrial impact structures located in other continents (e.g., Meteor Crater (Cavosie et al.,

2016, 2018b), Chicxulub impact structure (Zhao et al., 2021), Vredefort Dome (Erickson et al., 2013; Kenny et al., 2017; Kovaleva et al., 2021), Stac Fada impactite (Reddy et al., 2015), Chesapeake Bay (Glass and Liu, 2001), Xiuyan Crater (Chen et al., 2013), and Woodleigh impact structure (Cox et al., 2018)). This is a major gap in impact cratering research, and until we conduct thorough investigations into constraining the pressure and temperature conditions of multiple impact structures, we will not be able to acquire a full understanding of impact melt formation and peak shock metamorphism in our Solar System.

5.2.2.2 Shock Metamorphism and Impact Melting of Lunar Rocks

As reported in Chapter 4, evidence for granular zircons, cubic zirconia transformation, and reidite have been discovered in Apollo samples (Timms et al., 2012; Crow et al., 2017; White et al., 2020) and lunar meteorite samples (Zhang et al., 2011; Xing et al., 2020). Although few in number, the occurrence of these zircon grain microtextures, zirconia crystals, and domains of reidite are a sign that more grains could be preserved in other lunar impactite samples. The reason few data on the temperature and pressure conditions of lunar impactites has been reported in the literature is because very few studies have focused on searching for zircon grains encased within melt and glass matrices. We would not be able to find as many zircon grains as compared to terrestrial samples, due to the greatly accessibility. However, if we dedicate more studies to searching for zircon grains in Apollo and lunar meteorite samples, we will take a major step forward in understanding how impact cratering has modified and shocked extraterrestrial material.

The Artemis initiative led by NASA has the 2024 deadline of sending the next man and first woman to the far side of the Moon to return new samples. The far side of the Moon has never been explored by humans on the surface. The samples that will be returned from the far side of the Moon from the Artemis program will help address the questions mentioned in this thesis, as well as other high priority science goals published in planetary committee reports, including The Lunar Exploration Roadmap (Lunar Exploration Analysis Group, 2016) and the NASA Advanced Science of the Moon Special Action Team (ASM-SAT) report (Lunar Exploration Analysis Group, 2017). Both reports highlight the importance of understanding how impact cratering has built and modified the lunar stratigraphy, and the evolution of the Earth-Moon system. One of the objectives in the Lunar Exploration Roadmap (Lunar Exploration Analysis Group, 2016), emphasizes that we need to determine how impact events have modified, redistributed, and mixed materials on the surface (Objective-Sci-A-7, Investigation-B). In addition to the distribution of the shock wave emitted from the point of impact, impact melt plays a major role in modifying and mixing material on the lunar surface. Other objectives (Table 5.1) focus on understanding the impact cratering process stages in the lunar environment (Objective-Sci-A-7, Investigation-A), determining the origin and evolution of basin melt sheets (Objective-Sci-A-7, Investigation-C), and understanding the impact history of the Moon (Objective-Sci-A-8, Investigation-A). All of these objectives, and more listed in the Lunar Exploration Roadmap and the NASA ASM-SAT report, can only be properly addressed by studying samples returned from future human and robotic missions to the Moon.

Table 5.1. Summary of the science goals and objectives from the Lunar Exploration Roadmap and ASM-SAT report that can be addressed by constraining temperature and pressure conditions of lunar impactites.

Science Goal	Science Objectives	Source
Understand the impact process (Objective Sci-A-7)	Investigation-A: Determine and understand the stages of formation of simple and complex craters, and multi-ring basins	Lunar Exploration Analysis Group (2016)[1]
Understand the impact process (Objective Sci-A-7)	Investigation-B: Determine how impacts modify, redistribute, and mix materials	Lunar Exploration Analysis Group (2016) [1]
Determine the stratigraphy, structure, and geological history of the Moon (Objective Sci-A-8)	Investigation-A: Understand the impact history of the Moon	Lunar Exploration Analysis Group (2016) [1]
The Moon is an accessible laboratory for studying the impact process on planetary surfaces (Concept 6)	6c: Quantify the effects of planetary characteristics (composition, density, impact velocities) on crater formation and morphology	Lunar Exploration Analysis Group (2017)[2]

[1](Lunar Exploration Analysis Group, 2016), [2](Lunar Exploration Analysis Group, 2017)

5.3 Conclusion

To summarize, this thesis incorporated two complimentary investigations to provide further insight into the emplacement mechanisms of lunar impact melt flows: (1) radar analysis of terrestrial lava flow surface roughness, and (2) crystallographic orientation and

microstructural analysis of zircon grains and zirconia crystals to constrain impact melt temperatures and pressures. We highlight three main take-away points from this thesis: (1) transitional lava flows and moderately rough siliceous lava flows, and lava facies are challenging to differentiate using SAR data without the inclusion of ground-truth information; (2) evidence of superheating may only be preserved in quenched impact glass samples; and (3) high pressure shock indicators such as reidite and FRIGN zircon grains can be found within impact melt matrices and are not only in clastic matrices or shocked clasts.

The limitations of using SAR data to differentiate lava flows is not something to be discouraged by, but a new challenge to address with the addition of more terrestrial analogue ground-truth studies and analysis of current, new, and future planetary radar data sets. The limitations highlighted in this thesis only strengthen the importance of planetary analogue research, and the continued need to ground-truth remote sensing data sets to understand how we can appropriately interpret the geologic history of planetary surfaces. Terrestrial lava flows are an incredible laboratory for understanding how lava flows and impact melt may have been emplaced on terrestrial planetary bodies, and zircon grains and zirconia crystals offer a more detailed view into the superheated nature and high-pressure conditions of impact cratering events. Expanding our analysis of zircon grains and zirconia crystals to other terrestrial impact structures and lunar impactite samples will broaden our understanding of the temperature and pressure conditions of the impact cratering process. By prioritizing more detailed studies on terrestrial impactite samples across multiple impact structures and lunar melt-bearing impactites, we will be able to address high priority science goals established by the Lunar Exploration Analysis Group, which will be beneficial for the Artemis initiative established by NASA.

Reference

Albarède, F., 2009. Volatile accretion history of the terrestrial planets and dynamic implications. Nature 461, 1227–1233. https://doi.org/10.1038/nature08477

Bhiravarasu, S.S., Chakraborty, T., Putrevu, D., Pandey, D.K., Das, A.K., Ramanujam, V.M., Mehra, R., Parasher, P., Agrawal, K.M., Gupta, S., Seth, G.S., Shukla, A., Pandya, N.Y., Trivedi, S., Misra, A., Jyoti, R., Kumar, R., 2021. Chandrayaan-2 Dual-Frequency SAR (DFSAR): Performance Characterization and Initial Results. arXiv Prepr. arXiv:2104.

Bottomley, R.J., York, D., Grieve, R.A.F., 1978. 40Ar-39Ar dating of canadian impact craters: Lac couture and Lac la moinerie. Meteoritics 13, 395.

Cahill, J.T.S., Thomson, B.J., Patterson, G.W., Bussey, D.B.J., Neish, C.D., Lopez, N.R., Turner, F.S., Aldridge, T., McAdam, M., Meyer, H.M., Raney, R.K., Carter, L.M., Spudis, P.D., Hiesinger, H., Pasckert, J.H., 2014. The Miniature Radio Frequency instrument's (Mini-RF) global observations of Earth's Moon. Icarus 243, 173–190. https://doi.org/10.1016/j.icarus.2014.07.018

Campbell, B.A., 2012. High circular polarization ratios in radar scattering from geologic targets. J. Geophys. Res. 117. https://doi.org/10.1029/2012JE004061

Campbell, B.A., 2002. Radar Remote Sensing of Planetary Surfaces. Cambridge University Press.

Campbell, B.A., Carter, L.M., Campbell, D.B., Nolan, M., Chandler, J., Ghent, R.R., Ray Hawke, B., Anderson, R.F., Wells, K., 2010. Earth-based 12.6-cm wavelength radar mapping of the Moon: New views of impact melt distribution and mare physical properties.

Icarus 208, 565–573. https://doi.org/10.1016/j.icarus.2010.03.011

Campbell, B.A., Shepard, M.K., 1996. Lava flow surface roughness and depolarized radar scattering. J. Geophys. Res. 101, 18,941-18,951.

Carter, L.M., Campbell, D.B., Campbell, B.A., 2011. Geologic studies of planetary surfaces using radar polarimetric imaging. Proc. IEEE 99, 770–782. https://doi.org/10.1109/JPROC.2010.2099090

Carter, L.M., Neish, C.D., Bussey, D.B.J., Spudis, P.D., Patterson, G.W., Cahill, J.T., Raney, R.K., 2012. Initial observations of lunar impact melts and ejecta flows with the Mini-RF radar. J. Geophys. Res. 117, 1–13. https://doi.org/10.1029/2011JE003911

Cashman, K. V., Thornber, C., Kauahikaua, J.P., 1999. Cooling and crystallization of lava in open channels, and the transition of Pahoehoe Lava to'A'a. Bull. Volcanol. 61, 306–323.

Cavosie, A.J., Erickson, T.M., Timms, N.E., 2015. Nanoscale records of ancient shock deformation: Reidite (ZrSiO4) in sandstone at the Ordovician Rock Elm impact crater. Geology 43, 315–318. https://doi.org/10.1130/G36489.1

Cavosie, A.J., Quintero, R.R., Radovan, H.A., Moser, D.E., 2010. A record of ancient cataclysm in modern sand: Shock microstructures in detrital minerals from the Vaal river, Vredefort Dome, South Africa. Bull. Geol. Soc. Am. 122, 1968–1980. https://doi.org/10.1130/B30187.1

Cavosie, A.J., Timms, N.E., Erickson, T.M., Hagerty, J.J., Hörz, F., 2016. Transformations to granular zircon revealed: Twinning, reidite, and ZrO2 in shocked zircon from Meteor Crater (Arizona, USA). Geology 44, 703–706. https://doi.org/10.1130/G38043.1

Cavosie, A.J., Timms, N.E., Erickson, T.M., Koeberl, C., 2018a. New clues from Earth's most elusive impact crater: Evidence of reidite in Australasian tektites from Thailand. Geology. https://doi.org/10.1130/G39711.1

Cavosie, A.J., Timms, N.E., Ferrière, L., Rochette, P., 2018b. FRIGN zircon-The only terrestrial mineral diagnostic of high-pressure and high-temperature shock deformation. Geology 46, 891–894. https://doi.org/10.1130/G45079.1

Chen, M., Yin, F., Li, X., Xie, X., Xiao, W., Tan, D., 2013. Natural occurrence of reidite in the Xiuyan crater of China. Meteorit. Planet. Sci. 48, 796–805. https://doi.org/10.1111/maps.12106

Chhabra, R.P., 2010. Non-Newtonian fluids: An introduction, in: Rheology of Complex Fluids. Springer, New York, pp. 3–34. https://doi.org/10.1007/978-1-4419-6494-6_1

Cox, M.A., Cavosie, A.J., Bland, P.A., Milijkovic, K., Wingate, T.D., 2018. Microstructural dynamics of central uplifts: Reidite offset by zircon twins at the Woodleigh impact structure, Australia. Geology 46, 983–986.

Crow, C.A., McKeegan, K.D., Moser, D.E., 2017. Coordinated U–Pb geochronology, trace element, Ti-in-zircon thermometry and microstructural analysis of Apollo zircons. Geochim. Cosmochim. Acta 202, 264–284. https://doi.org/10.1016/j.gca.2016.12.019

Davis, R.D., 2021. International Mars Ice Mapper Mission: The First Human Exploration Reconnaissance Mission to Mars, in: 52nd Lunar and Planetary Science Conference. p. 2614.

Dence, M.R., 1971. Impact Melts. J. Geophys. Res. 76, 5552–5565.

Duraiswami, R.A., Bondre, N.R., Managave, S., 2008. Morphology of rubbly pahoehoe (simple) flows from the Deccan Volcanic Province: Implications for style of emplacement. J. Volcanol. Geotherm. Res. 177, 822–836. https://doi.org/10.1016/j.jvolgeores.2008.01.048

Erickson, T.M., Cavosie, A.J., Moser, D.E., Barker, I.R., Radovan, H.A., 2013. Correlating planar microstructures in shocked zircon from the Vredefort Dome at multiple scales: Crystallographic modeling, external and internal imaging, and EBSD structural analysis. Am. Mineral. 98, 53–65. https://doi.org/10.2138/am.2013.4165

Erickson, T.M., Pearce, M.A., Reddy, S.M., Timms, N.E., Cavosie, A.J., Bourdet, J., Rickard, W.D.A., Nemchin, A.A., 2017. Microstructural constraints on the mechanisms of the transformation to reidite in naturally shocked zircon. Contrib. to Mineral. Petrol. 172, 1–26. https://doi.org/10.1007/s00410-016-1322-0

Floran, R.J., Grieve, R.A.F., Phinney, W.C., Warner, J.L., Simonds, C.H., Blanchard, D.P., Dence, M.R., 1978. Manicouagan Impact Melt, Quebec, 1, Stratigraphy, petrology, and chemistry. J. Geophys. Res. Solid Earth 83, 2737–2759. https://doi.org/10.1029/JB083iB06p02737

Ghail, R., Wilson, C., Galand, M., Hall, D., Cochrane, C., Mason, P., Helbert, J., MontMessin, F., Limaye, S., Patel, M., Stam, D., Wahlund, J.-E., Rocca, F., Mather, T., Waltham, D., Genge, M., Paillou, P., Mitchell, K., Wilson, L., 2012. EnVision: taking the pulse of our twin planet. Exp. Astron. 2–3, 337–363.

Glass, B.P., Liu, S., 2001. Discovery of high-pressure ZrSiO4 polymorph in naturally occurring shock-metamorphosed zircons. Geology 29, 371–373. https://doi.org/10.1130/0091-7613(2001)029<0371:DOHPZP>2.0.CO;2

Greeley, R., King, J.S., 1977. Volcanism of the eastern Snake River Plain, Idaho: A Comparative planetary geology-guidebook. Washington, D.C., NASA CR 154621.

Grieve, R.A.F., 1975. Petrology and chemistry of the impact melt at Mistastin Lake crater, Labrador. Bull. Geol. Soc. Am. 86, 1617–1629. https://doi.org/10.1130/0016-7606(1975)86<1617:PACOTI>2.0.CO;2

Grieve, R.A.F., Dence, M.R., Robertson, P.B., 1977. Cratering processes: As interpreted from the occurrence of impact melts, in: In Impact and Explosion Cratering: Planetary and Terrestrial Implications. pp. 791–814.

Griffiths, R.W., 2000. The Dynamics of Lava Flows. Annu. Rev. Fluid Mech. 32, 477–518. https://doi.org/10.1146/annurev.fluid.32.1.477

Guilbaud, M.-N., Self, S., Thordarson, T., Blake, S., 2005. Morphology, surface structures, and emplacement of lavas produced by Laki, A.D. 1783 – 1784. GSA Spec. Pap. 396, 81–102. https://doi.org/10.1130/2005.2396(07).

Harmon, J.K., Nolan, M.C., Husmann, D.I., Campbell, B. a., 2012. Arecibo radar imagery of Mars: The major volcanic provinces. Icarus 220, 990–1030. https://doi.org/10.1016/j.icarus.2012.06.030

Harris, A.J.L., Rowland, S.K., Villeneuve, N., Thordarson, T., 2017. Pāhoehoe, ʻaʻā, and block lava: an illustrated history of the nomenclature, Bulletin of Volcanology. Bulletin of Volcanology. https://doi.org/10.1007/s00445-016-1075-7

Hensley, S., Smrekar, S.E., Pollard, B., 2012. VERITAS: A Mission Concept for the High Resolution Topographic Mapping and Imaging of Venus, in: American Geophysical Union,

Fall Meeting. pp. P33C-1950.

Jaeger, W.L., Keszthelyi, L.P., Skinner, J.A., Milazzo, M.P., McEwen, A.S., Titus, T.N., Rosiek, M.R., Galuszka, D.M., Howington-Kraus, E., Kirk, R.L., 2010. Emplacement of the youngest flood lava on Mars: A short, turbulent story. Icarus 205, 230–243. https://doi.org/10.1016/j.icarus.2009.09.011

Kamo, S.L., Reimold, W.U., Krogh, T.E., Colliston, W.P., 1996. A 2.023 Ga age for the Vredefort impact event and a first report of shock metamorphosed zircons in pseudotachylitic breccias and Granophyre. Earth Planet. Sci. Lett. 144, 369–387. https://doi.org/10.1016/s0012-821x(96)00180-x

Kenny, G.G., Morales, L.F., Whitehouse, M.J., Petrus, J.A., Kamber, B.S., 2017. The formation of large neoblasts in shocked zircon and their utility in dating impacts. Geology 45, 1003–1006. https://doi.org/10.1130/G39328.1

Keszthelyi, L., Mcewen, A.S., Thordarson, T., 2000. Terrestrial analogs and thermal models for Martian flood lavas. J. Geophys. Res. E Planets 105, 15,027-15,049. https://doi.org/10.1029/1999je001191

Keszthelyi, L., Self, S., Thordarson, T., 2006. Flood lavas on Earth, Io and Mars. J. Geol. Soc. London. 163, 253–264. https://doi.org/10.1144/0016-764904-503

Keszthelyi, L., Thordarson, T., McEwen, A., Haack, H., Guilbaud, M.N., Self, S., Rossi, M.J., 2004. Icelandic analogs to Martian flood lavas. Geochemistry, Geophys. Geosystems 5, 1–32. https://doi.org/10.1029/2004GC000758

Khan, S., Essam, H., Jaime, F., 2007. Mapping exposed and buried lava flows using synthetic

aperture and ground-penetrating radar in craters of the moon lava field. 2007 GSA Denver Annu. Meet. (28–31 Oct. 2007) 72, 123. https://doi.org/10.1190/1.2793298

Kovaleva, E., Kusiak, M.A., Kenny, G.G., Whitehouse, M.J., Habler, G., Schreiber, A., Wirth, R., 2021. Nano-scale investigation of granular neoblastic zircon, Vredefort impact structure, South Africa: Evidence for complete shock melting. Earth Planet. Sci. Lett. 565, 116948. https://doi.org/10.1016/j.epsl.2021.116948

Kovaleva, E., Zamyatin, D.A., Habler, G., 2019. Granular zircon from Vredefort granophyre (South Africa) confirms the deep injection model for impact melt in large impact structures. Geology 47, 691–694.

Kusaba, K., Syono, Y., Kikuchi, M., Fukuoka, K., 1985. Shock behavior of zircon: phase transition to scheelite structure and decomposition. Earth Planet. Sci. Lett. 72, 433–439. https://doi.org/10.1016/0012-821X(85)90064-0

Lancaster, M.G., Guest, J.E., Magee, K.P., 1995. Great Lava Flow Fields on Venus. Icarus. https://doi.org/10.1006/icar.1995.1178

Lawrence, S.J., Stopar, J.D., Hawke, B.R., Greenhagen, B.T., Cahill, J.T.S., Bandfield, J.L., Jolliff, B.L., Denevi, B.W., Robinson, M.S., Glotch, T.D., Bussey, D.B.J., Spudis, P.D., Giguere, T.A., Garry, W.B., 2013. LRO observations of morphology and surface roughness of volcanic cones and lobate lava flows in the Marius Hills. J. Geophys. Res. E Planets 118, 615–634. https://doi.org/10.1002/jgre.20060

Lee, J.-S., Pottier, 2009. Polarimetric Radar Imaging: from basics to applications. CRC Press Taylor & Francis Group, New York.

Lev, E., Hamilton, C.W., Voigt, J.R.C., Stadermann, A.C., Zhan, Y., Neish, C.D., in press. Emplacement conditions of lunar impact melt flows. Icarus.

Lunar Exploration Analysis Group, 2017. Advancing Science of the Moon: Report of the Specific Action Team.

Lunar Exploration Analysis Group, 2016. The Lunar Exploration Roadmap: Exploring the Moon in the 21st Century: Themes, Goals, Objectives, Investigations, and Priorities, 2016.

Mader, M.M., Osinski, G.R., 2018. Impactites of the Mistastin Lake impact structure: Insights into impact ejecta emplacement. Meteorit. Planet. Sci. in press. https://doi.org/10.1111/maps.13173

Marion, C.L., Sylvester, P.J., 2010. Composition and heterogeneity of anorthositic impact melt at Mistastin Lake crater, Labrador. Planet. Space Sci. 58, 552–573. https://doi.org/10.1016/j.pss.2009.09.018

Morgan, G.A., Campbell, B.A., Campbell, D.B., Hawke, B.R., 2016. Investigating the stratigraphy of Mare Imbrium flow emplacement with Earth-based radar. J. Geophys. Res. 121, 1498–1513. https://doi.org/10.1002/2016JE005041.Received

Moser, D.E., Cupelli, C.L., Barker, I.R., Flowers, R.M., Bowman, J.R., Wooden, J., Hart, J.R., 2011. New zircon shock phenomena and their use for dating and reconstruction of large impact structures revealed by electron nanobeam (EBSD, CL, EDS) and isotopic U-Pb and (U-Th)/he analysis of the vredefort dome. Can. J. Earth Sci. 48, 117–139. https://doi.org/10.1139/E11-011

Neish, C.D., Carter, L.M., 2014. Planetary Radar, in: Encyclopedia of the Solar System. pp.

1133–1159.

Neish, C.D., Hamilton, C.W., Hughes, S.S., Nawotniak, S.K., Garry, W.B., Skok, J.R., Elphic, R.C., Schaefer, E., Carter, L.M., Bandfield, J.L., Osinski, G.R., Lim, D., Heldmann, J.L., 2017. Terrestrial analogues for lunar impact melt flows. Icarus 281, 73–89. https://doi.org/10.1016/j.icarus.2016.08.008

Neish, C.D., Madden, J., Carter, L.M., Hawke, B.R., Giguere, T., Bray, V.J., Osinski, G.R., Cahill, J.T.S., 2014. Global distribution of lunar impact melt flows. Icarus 239, 105–117. https://doi.org/10.1016/j.icarus.2014.05.049

Onorato, P.I.K., Uhlmann, D.R., Simonds, C.H., 1978. The Thermal History of the Manicouagan Impact Melt Sheet , Quebec. J. Geophys. Res. 83, 2789–2798. https://doi.org/https://doi.org/10.1029/JB083iB06p02789

Osinski, G.R., Grieve, R.A.F., Bleacher, J.E., Neish, C.D., Pilles, E.A., Tornabene, L.L., 2018. Igneous rocks formed by hypervelocity impact. J. Volcanol. Geotherm. Res. 353, 25–54. https://doi.org/10.1016/j.jvolgeores.2018.01.015

Patterson, G.W., Stickle, A.M., Turner, F.S., Jensen, J.R., Bussey, D.B.J., Spudis, P., Espiritu, R.C., Schulze, R.C., Yocky, D.A., Wahl, D.E., Zimmerman, M., Cahill, J.T.S., Nolan, M., Carter, L., Neish, C.D., Raney, R.K., Thomson, B.J., Kirk, R., Thompson, T.W., Tise, B.L., Erteza, I.A., Jakowatz, C. V., 2017. Bistatic radar observations of the Moon using Mini-RF on LRO and the Arecibo Observatory. Icarus 283, 2–19. https://doi.org/10.1016/j.icarus.2016.05.017

Peterson, D.W., Tilling, R.I., 1980. Transition of Basaltic Lava From Pahoehoe to AA, Kilauea Volcano, Hawaii: Field Observations and Key Factors. Jounral Volcanol. Geotherm.

Researc 7, 271–293.

Phinney, W.C., Simonds, C.H., Cochran, A., McGee, P.E., 1978. West Clearwater, Quebec impact structure, Part II: Petrology. Proc. Lunar Planet. Sci. Conf. 9th 2659–2693.

Pierazzo, E., Vickery, A.M., Melosh, H.J., 1997. A Re-evaluation of Impact Melt Production. Icarus 127, 408–423.

Putrevu, D., Das, A., Vachhani, J.G., Trivedi, S., Misra, T., 2016. Chandrayaan-2 dual-frequency SAR: Further investigation into lunar water and regolith. Adv. Sp. Res. 57, 627–646. https://doi.org/10.1016/j.asr.2015.10.029

Putrevu, D., Trivedi, S., Das, A., Pandey, D., Mehrotra, P., Gard, S.K., Reddy, V., Gangele, S., Patel, H., Sharma, D., Sijwali, R., Pandya, N., Shukla, A., Seth, G., Ramanujam, V.M., Kumar, R., 2020. L- and S-band Polarimetric Synthetic Aperture Radar on Chandrayaan-2 mission. Curr. Sci. 118, 226–233.

Reddy, S.M., Johnson, T.E., Fischer, S., Rickard, W.D.A., Taylor, R.J.M., 2015. Precambrian reidite discovered in shocked zircon from the Stac Fada impactite, Scotland. Geology. https://doi.org/10.1130/G37066.1

Reimold, W.U., Grieve, R.A.F., Palme, H., 1981. Rb-Sr dating of the impact melt from East Clearwater, Quebec. Contrib. to Mineral. Petrol. 76, 73–76. https://doi.org/10.1007/BF00373685

Rodriguez Sanchez-Vahamonde, C., Neish, C., 2021. The Surface Texture of Martian Lava Flows as Inferred from Their Decimeter- and Meter-scale Roughness. Planet. Sci. J. 2. https://doi.org/https://doi.org/10.3847/PSJ/abbfac

Rowland, S.K., Walker, G.P.L., 1990. Pahoehoe and aa in Hawaii: volumetric flow rate controls the lava structure. Bull. Volcanol. 52, 615–628.

Schaber, G.G., Elachi, C., Farr, T.G., 1980. Remote sensing data of SP Mountain and SP Lava flow in North-Central Arizona. Remote Sens. Environ. 9, 149–170. https://doi.org/10.1016/0034-4257(80)90005-X

Sehlke, A., Whittington, A., Robert, B., Harris, A., Gurioli, L., Médard, E., Sehlke, A., 2014. Pahoehoe to áá transition of Hawaiian lavas: An experimental study. Bull. Volcanol. 76. https://doi.org/10.1007/s00445-014-0876-9

Shepard, M.K., Campbell, B.A., Bulmer, M.H., Farr, T.G., Gaddis, L.R., Plaut, J.J., 2001. The roughness of natural terrain: A planetary and remote sensing perspective. J. Geophys. Res. E Planets 106, 32777–32795. https://doi.org/10.1029/2000JE001429

Simonds, C H, Floran, R.J., McGee, P.E., Phinney, W.C., Warner, J.L., 1978. Petrogenesis of melt rocks, Manicouagan impact structure, Quebec. J. Geophys. Res. 83, 2773–2788. https://doi.org/http://dx.doi.org/10.1029/JB083iB06p02773

Simonds, Charles H, Phinney, W.C., McGee, P.E., Cochran, A., 1978. West Clearwater, Quebec impact structure, Part I: Field geology, structure and bulk chemistry. Proc. Lunar Planet. Sci. Conf. 9th 2633–2658. https://doi.org/10.15713/ins.mmj.3

Solana, M.C., Kilburn, C.R.J., Rodriguez Badiola, E., Aparicio, A., 2004. Fast emplacement of extensive pahoehoe flow-fields: The case of the 1736 flows from Monta??a de las Nueces, Lanzarote. J. Volcanol. Geotherm. Res. 132, 189–207. https://doi.org/10.1016/S0377-0273(03)00345-7

Spudis, P., Nozette, S., Bussey, B., Raney, K., Winters, H., Lichtenberg, C.L., Marinelli, W., Crusan, J.C., Gates, M.M., 2009. Mini-SAR: An imaging radar experiment for the Chandrayaan-1 mission to the Moon. Curr. Sci. 96, 533–539.

Timms, N. E., Erickson, T.M., Pearce, M.A., Cavosie, A.J., Schmieder, M., Tohver, E., Reddy, S.M., Zanetti, M.R., Nemchin, A.A., Wittman, A., 2017a. A pressure-temperature phase diagram for zircon at extreme conditions. Earth-Science Rev. 165, 185–202. https://doi.org/10.1016/j.earscirev.2016.12.008

Timms, N. E., Erickson, T.M., Zanetti, M.R., Pearce, M.A., Cayron, C., Cavosie, A.J., Reddy, S.M., Wittmann, A., Carpenter, P.K., 2017b. Cubic zirconia in >2370◦C impact melt records Earth's hottest crust. Earth Planet. Sci. Lett. 477, 52–58. https://doi.org/10.1016/j.epsl.2017.08.012

Timms, N.E., Reddy, S.M., Healy, D., Nemchin, A.A., Grange, M.L., Pidgeon, R.T., Hart, R., 2012. Resolution of impact-related microstructures in lunar zircon: A shock-deformation mechanism map. Meteorit. Planet. Sci. 47, 120–141. https://doi.org/10.1111/j.1945-5100.2011.01316.x

Tolometti, G.D., Neish, C.D., Osinski, G.R., Hughes, S.S., Nawotniak, S.E.K., 2020. Interpretations of lava flow properties from radar remote sensing data. Planet. Space Sci. 190, 104991. https://doi.org/https://doi.org/10.1016/j.pss.2020.104991

Voigt, J.R.C., Hamilton, C.W., Scheidt, S.P., Münzer, U., Höskuldsson, Á., Jónsdottir, I., Thordarson, T., 2021. Geomorphological Characterization of the 2014–2015 Holuhraun Lava Flow-Field in Iceland. J. Volcanol. Geotherm. Res. https://doi.org/https://doi.org/10.1016/ j.jvolgeores.2021.107278

White, L.F., Černok, A., Darling, J.R., Whitehouse, M.J., Joy, K.H., Cayron, C., Dunlop, J., Tait, K.T., Anand, M., 2020. Evidence of extensive lunar crust formation in impact melt sheets 4,330 Myr ago. Nat. Astron. 4, 974–978. https://doi.org/https://doi.org/10.1038/s41550-020-1092-5

Wittmann, A., Kenkmann, T., Schmitt, R.T., Stöffler, D., 2006. Shock-metamorphosed zircon in terrestrial impact craters. Meteorit. Planet. Sci. 41, 433–454. https://doi.org/10.1111/j.1945-5100.2006.tb00472.x

Xing, W., Lin, Y., Zhang, C., Zhang, M., Hu, S., Hofmann, B.A., Sekine, T., Xiao, L., Gu, L., 2020. Discovery of Reidite in the Lunar Meteorite Sayh al Uhaymir 169. Geophys. Res. Lett. 47. https://doi.org/10.1029/2020GL089583

Zhang, A.C., Hsu, W.B., Li, X.H., Ming, H.L., Li, Q.L., Liu, Y., Tang, G.Q., 2011. Impact melting of lunar meteorite Dhofar 458: Evidence from polycrystalline texture and decomposition of zircon. Meteorit. Planet. Sci. 46, 103–115. https://doi.org/10.1111/j.1945-5100.2010.01144.x

Zhao, J., Xiao, L., Xiao, Z., Morgan, J. V., Osinski, G.R., Neal, C.R., Gulick, S.P.S., Riller, U., Claeys, P., Zhao, S., Prieur, N.C., Nemchin, A., Yu, S., IODP 364 Science Party, 2021. Shock-deformed zircon from the Chicxulub impact crater and implications for cratering process. Geology XX, 1–6. https://doi.org/10.1130/g48278.1

Zimbelman, J.R., 1998. Emplacement of long lava flows on planetary surfaces. J. Geophys. Res. 103, 27503–27516. https://doi.org/10.1029/98jb01123

Appendices

A1. Mistastin Impactite Sample Preparation and Parent Zircon and Zirconia Parent Phase Reconstruction

Item 1. Backscatter Electron Images of Zircon Grains from the Four Impactite Samples

Item 1(a). Impact Glass Zircon Grains

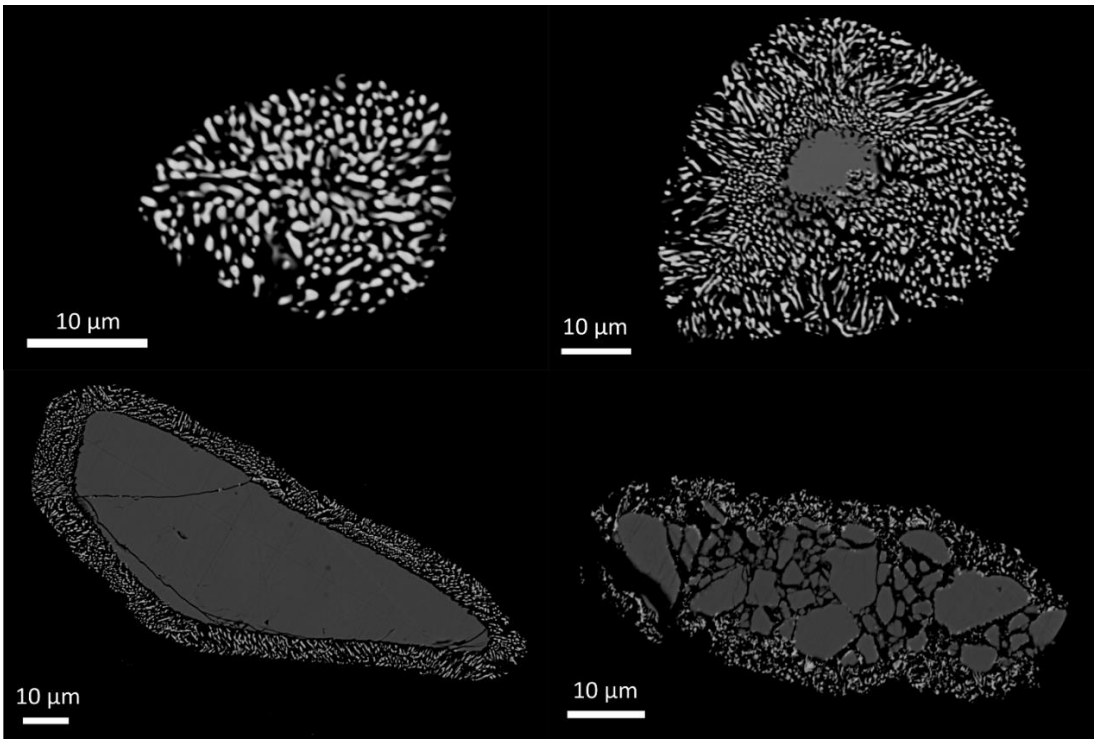

A1.1. Backscatter electron images of a selection of zircon grains discovered in the impact glass sample. Zircon grains show evidence of ZrO_2-SiO_2 dissociation, baddeleyite coronas and brecciated cores. The impact glass sample contained the most zircon grains with ZrO_2-SiO_2 dissociation textures.

Item 1(b). Clast-Poor Vesicular Melt Rock Zircon Grains

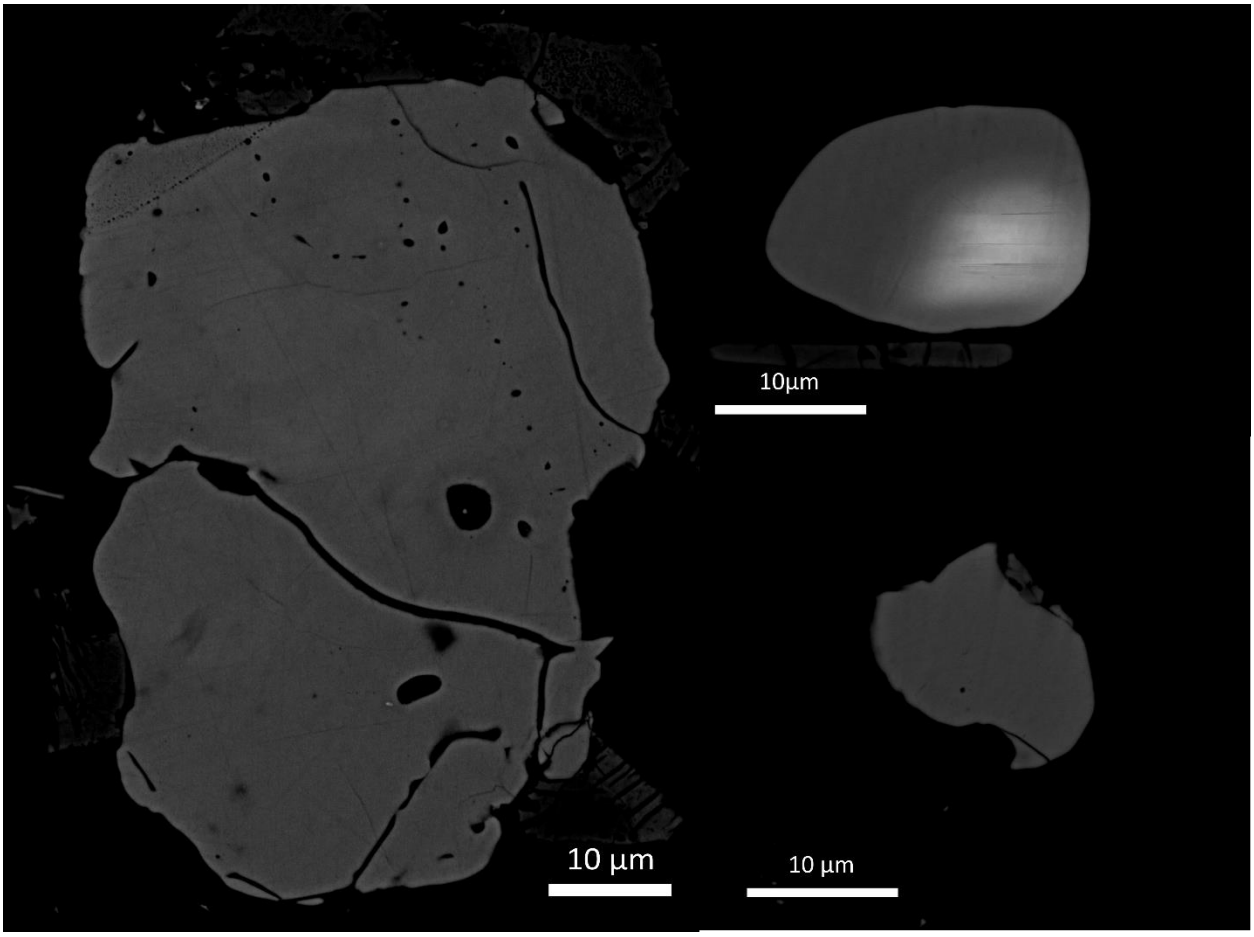

A1.2. Backscatter electron images of a selection of zircon grains discovered in the vesicular melt rock sample. The zircon grains show no evidence of ZrO_2-SiO_2 dissociation. Dissociation textures may have been removed post-shock when the grains were suspended in the impact melt deposits. The grains only exhibit anhedral shapes, some with large fractures and inclusions of silicate impact melt.

Item 1(c). Impact Glass-Bearing Breccia Zircon Grains

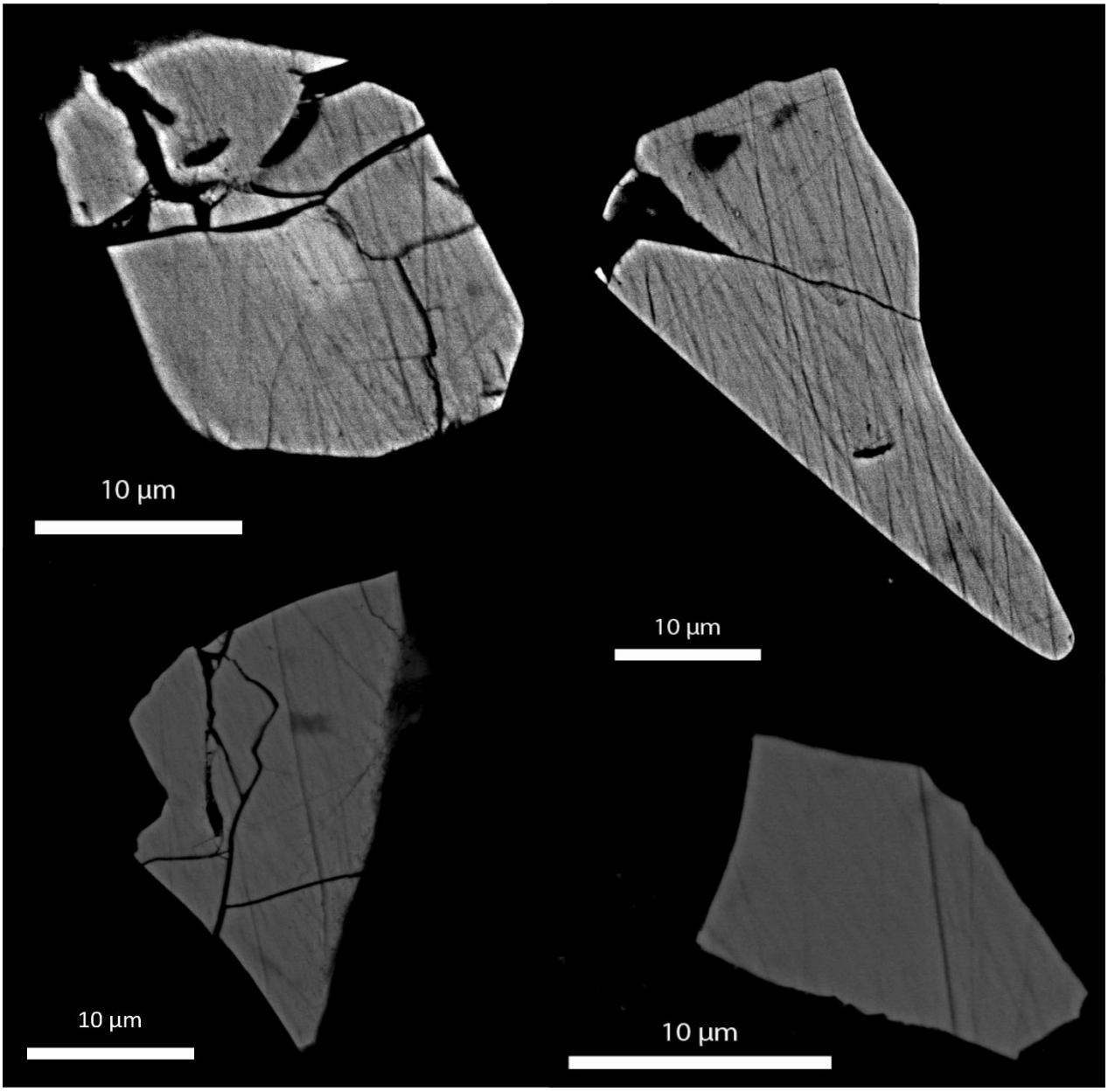

A1.3. Backscatter electron images of a selection of zircon grains discovered in the impact glass-bearing breccia sample. Zircon grains show evidence of ZrO_2-SiO_2 dissociation, baddeleyite coronas, brittle deformation, and anhedral grains. The impact glass-bearing breccia samples contain the most diverse array of zircon grain morphologies and microstructures.

Item 1(d). Clast-Rich Melt Rock Zircon Grains

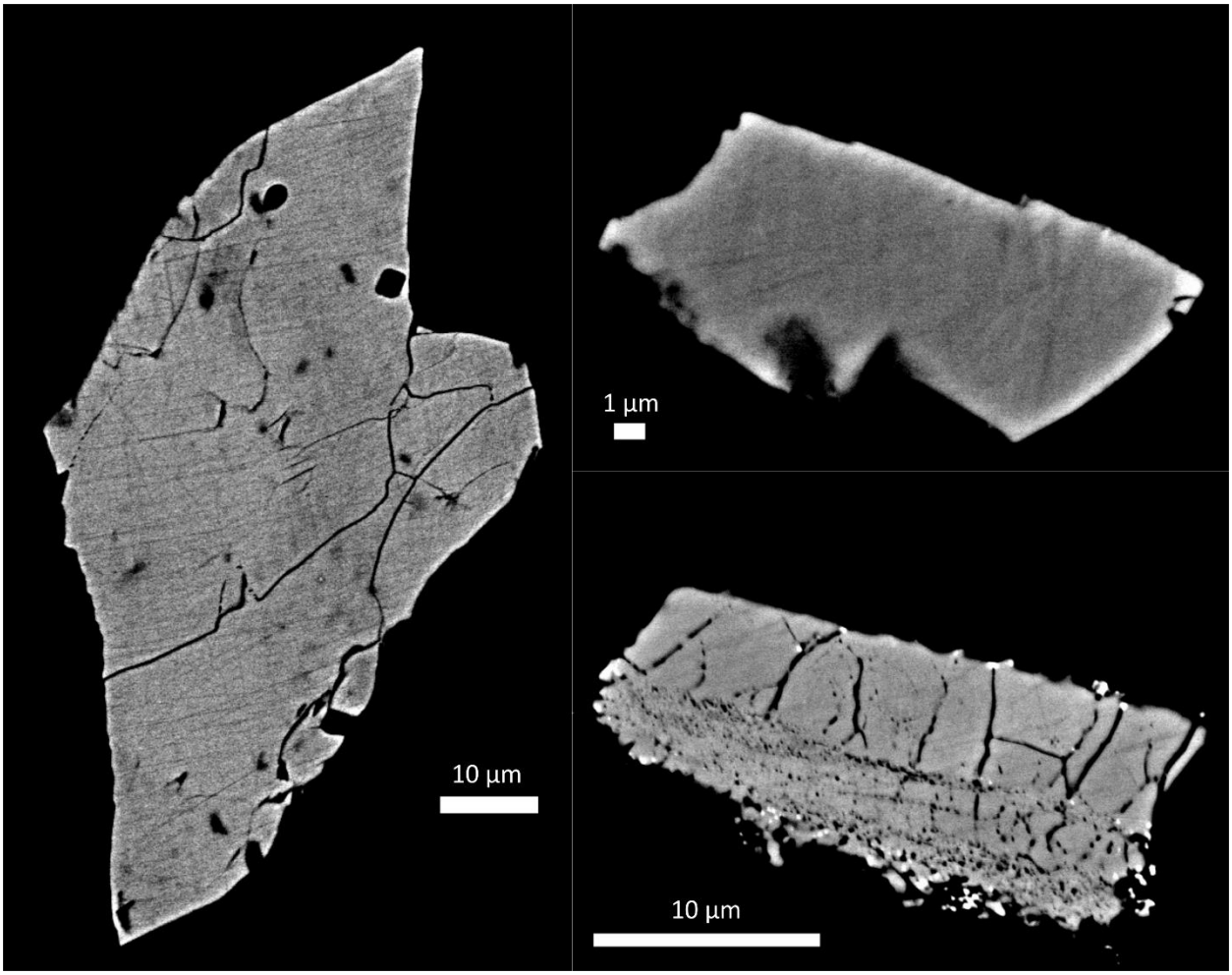

A1.4. Backscatter electron images of a selection of zircon grains discovered in the clast-rich melt rock sample. The zircon grains show no evidence of ZrO_2-SiO_2 dissociation. Dissociation textures may have been removed post-shock when the grains were suspended in the impact melt deposits.

Item 2. EBSD Pole Figures Generated Using the Oxford Channel 5 Program

CM09-05_06 – Impact Glass

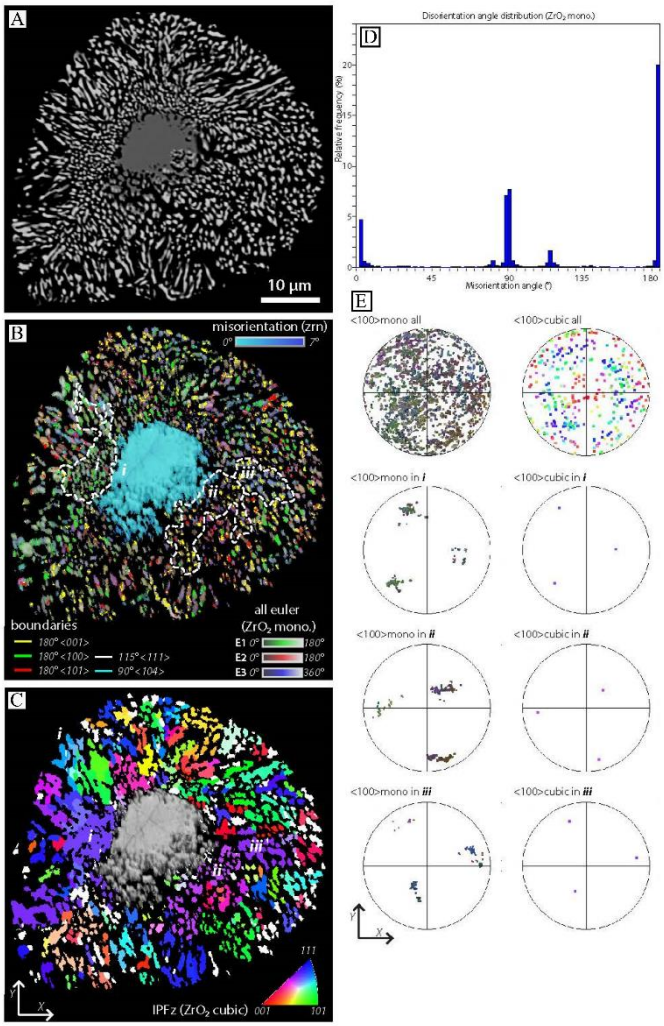

A1.5. A – Backscatter electron image of the zircon grain, showing the vermicular corona containing dendritic baddeleyite crystals. B – EBSD map showing 7° misorientation. No brittle deformation and strain are found within the zircon grain. Baddeleyite in corona is colored for orientation using all Euler scheme. C – Reconstruction of cubic zirconia grains using crystallographic transformation paths in the ARPGE program. D – Histogram of disorientation

angles between the monoclinic zirconia in C. E – Pole figures of principal planes of three baddeleyite clusters and reconstructed cubic zirconia parent grains (*i*, *ii* and *iii*).

CM09-05A_11 – Impact Glass

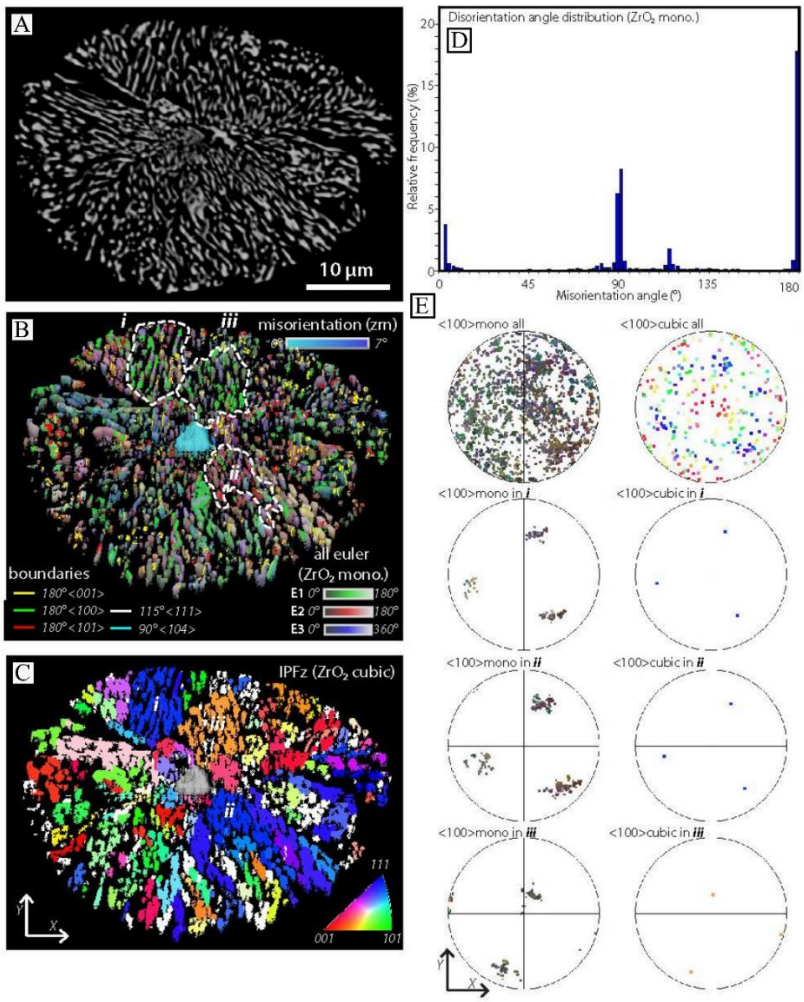

A1.6. A – Backscatter electron image of the zircon grain, showing the vermicular corona containing dendritic baddeleyite crystals. B – EBSD map showing 7° misorientation. No brittle deformation and strain are found within the zircon grain. Baddeleyite in corona is colored for orientation using all Euler scheme. C – Reconstruction of cubic zirconia grains using

crystallographic transformation paths in the ARPGE program. D – Histogram of disorientation angles between the monoclinic zirconia in C. E – Pole figures of principal planes of three baddeleyite clusters and reconstructed cubic zirconia parent grains (*i*, *ii* and *iii*).

CM09-05A_12 – Impact Glass

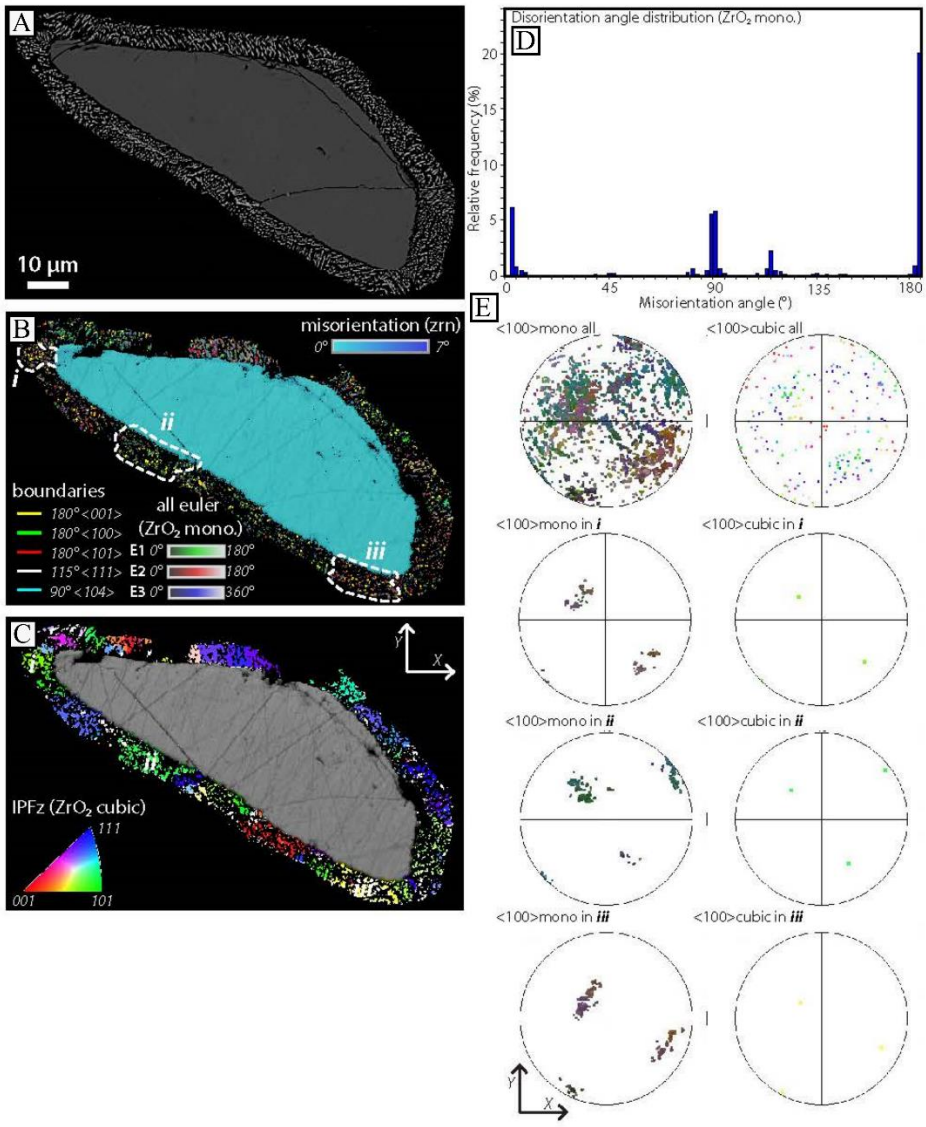

A1.7. A – backscatter electron image of the zircon grain, showing the vermicular corona containing dendritic baddeleyite crystals. B – EBSD map showing 7° misorientation. No brittle deformation and strain are found within the zircon grain. Baddeleyite in corona is colored for orientation using all Euler scheme. C – Reconstruction of cubic zirconia grains using crystallographic transformation paths in the ARPGE program. D – Histogram of disorientation angles between the monoclinic zirconia in C. E – Pole figures of principal planes of three baddeleyite clusters and reconstructed cubic zirconia parent grains (*i, ii* and *iii*).

CM09-05B_06 – Impact Glass

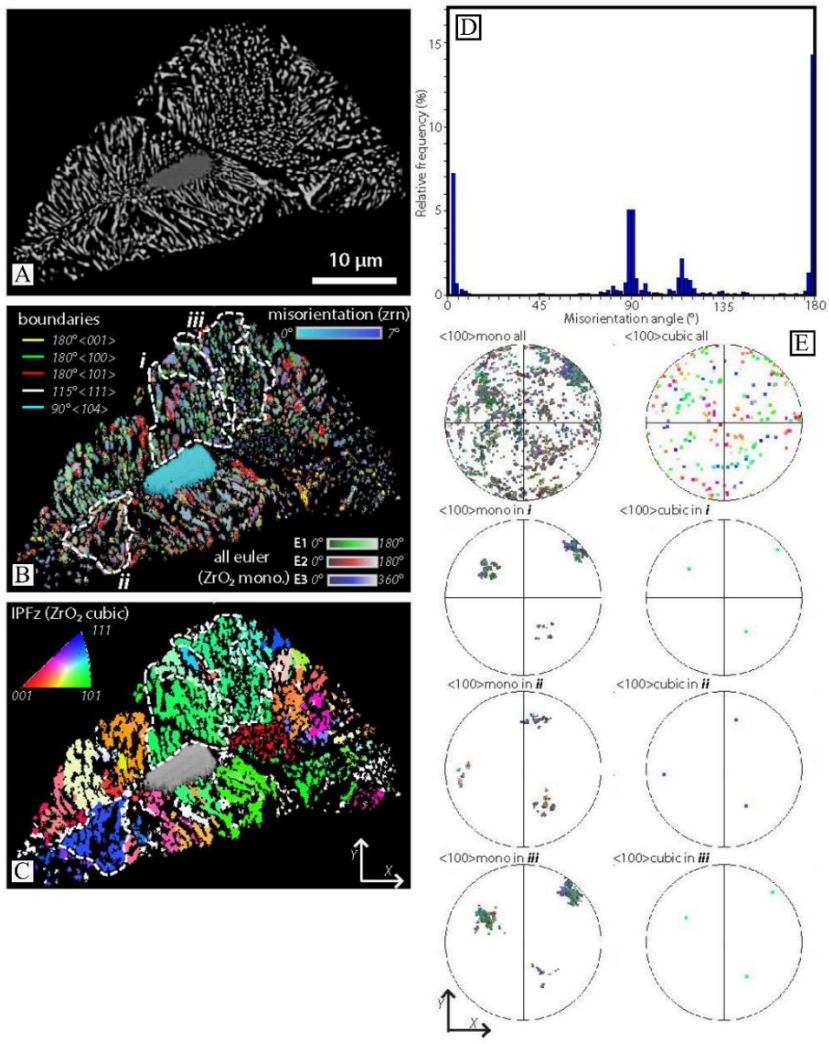

A1.8. A – Backscatter electron image of the zircon grain, showing the vermicular corona containing dendritic baddeleyite crystals. B – EBSD map showing 7° misorientation. No brittle deformation and strain are found within the zircon grain. Baddeleyite in corona is colored for orientation using all Euler scheme. C – Reconstruction of cubic zirconia grains using crystallographic transformation paths in the ARPGE program. D – Histogram of disorientation angles between the monoclinic zirconia in C. E – Pole figures of principal planes of three baddeleyite clusters and reconstructed cubic zirconia parent grains (*i*, *ii* and *iii*).

CM09-05C_11 – Impact Glass

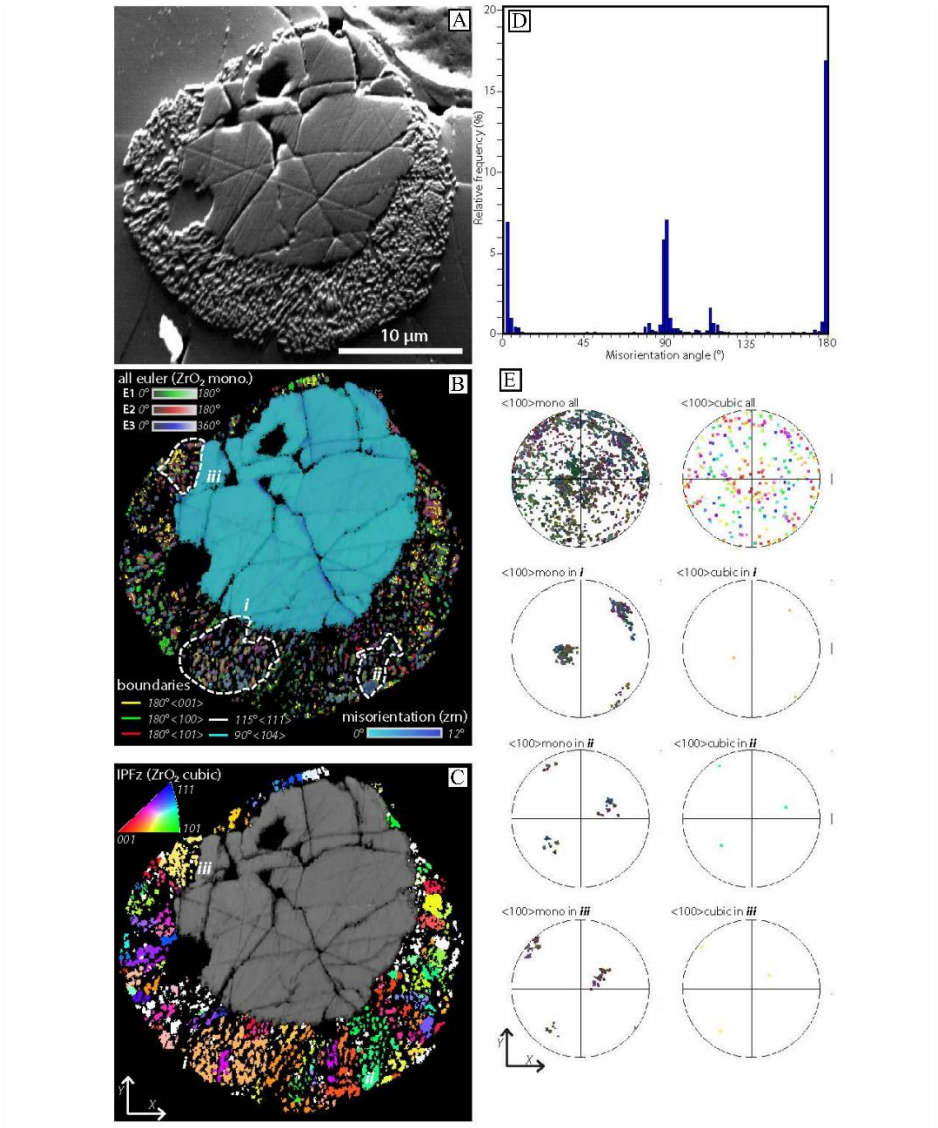

A1.9. A – Backscatter electron image of the zircon grain, showing the vermicular corona containing dendritic baddeleyite crystals. B – EBSD map showing 7° misorientation. No brittle deformation and strain are found within the zircon grain. Baddeleyite in corona is colored for orientation using all Euler scheme. C – Reconstruction of cubic zirconia grains using crystallographic transformation paths in the ARPGE program. D – Histogram of disorientation

angles between the monoclinic zirconia in C. E – Pole figures of principal planes of three baddeleyite clusters and reconstructed cubic zirconia parent grains (*i*, *ii* and *iii*).

CM09_05A-Zr08 – Impact Glass

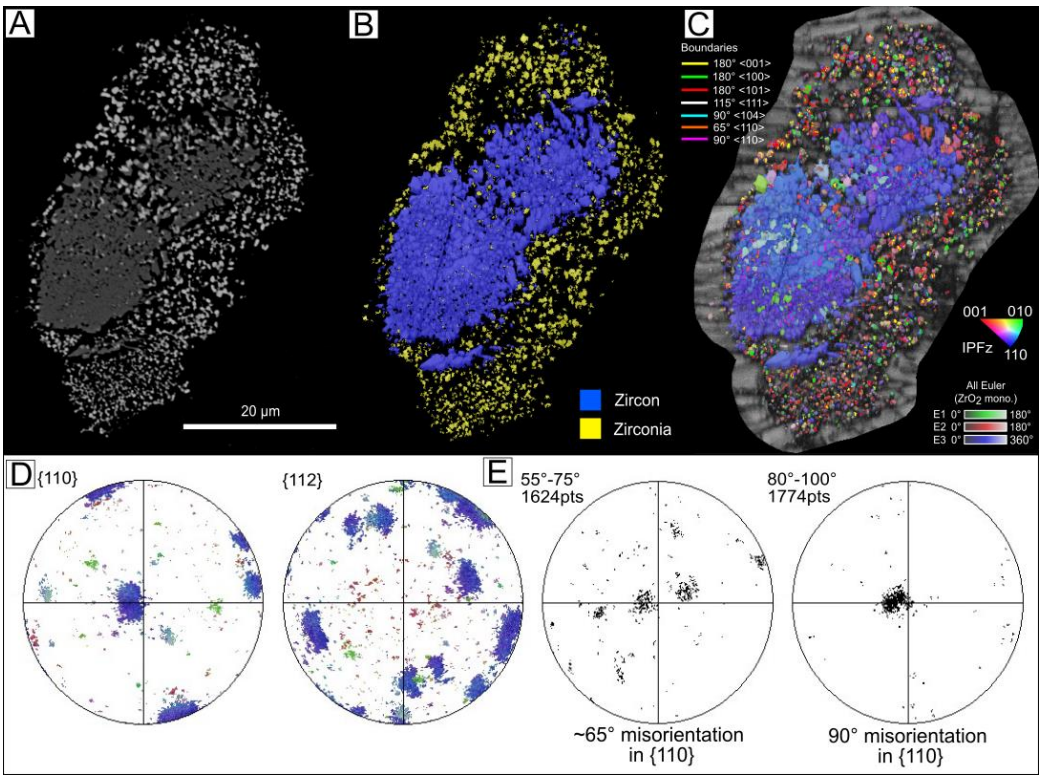

Figure A1.10. Microstructure and crystallographic orientation relationship data of a granular zircon grain with a corona of baddeleyite crystals (Sample ID CM09_05A-Zr08). (A) Backscatter electron (BSE) image of the zircon grain. (B) Zircon phase map distinguishing the granular neoblastic zircons (dark blue) and the baddeleyite crystals (yellow). (C) EBSD orientation map of the measured orientations of each zircon neoblast and reidite grain. Zircon orientations are assigned the inverse pole figure (IPF) colour scheme and the zirconia crystals are assigned all Euler plots. (D) Pole figures for the zircon. (E) Equal area projections of disorientation axes binned by disorientation angles 55°-75° and 80°-100°.

Impact Glass-Bearing Breccia

MM09-033 A2 Zircon 20

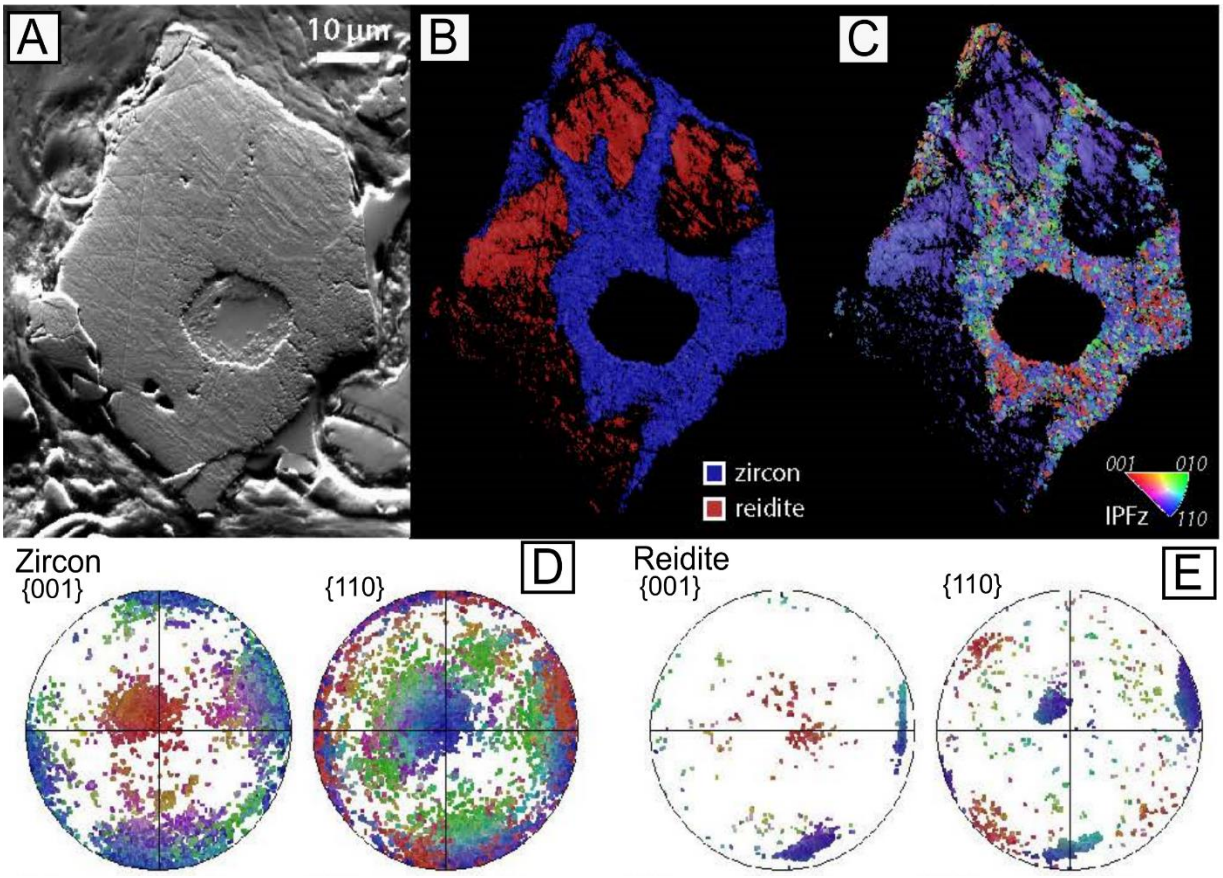

Figure A1.11. A – Forescatter electron image of a zircon grain with granular neoblastic zircon grains and reidite domains. B – Zircon phase map of the zircon grain showing the zircon crystal and reidite phases. C – Inverse Pole Figure (IPF) orientation color scheme. Each neoblastic zircon grain showing an individual orientation, produced during recrystallization. D – Orientation measurement of the zircon granules. E – Orientation measurement of each reidite grain.

MM09-033 A2 Zircon 24

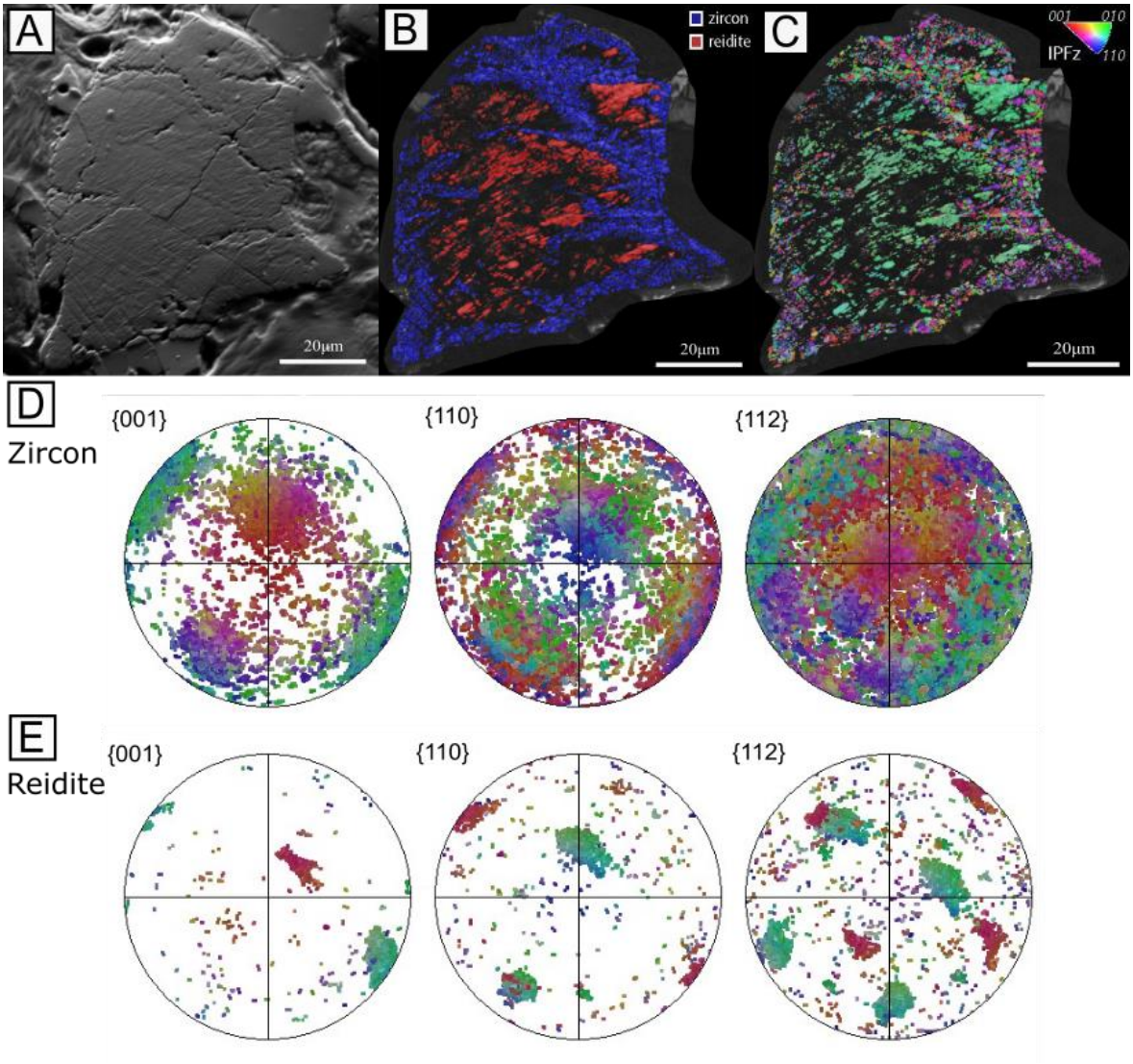

Figure A.1.12. A – Forescatter electron image of a zircon grain with granular neoblastic zircon grains and reidite domains. B – Zircon phase map of the zircon grain showing the zircon crystal and reidite phases. C – Inverse Pole Figure (IPF) orientation color scheme. Each neoblastic zircon grain showing an individual orientation, produced during recrystallization. D – Orientation measurement of the zircon granules. E – Orientation measurement of the reidite.

MM09-033 A2 Zircon 23

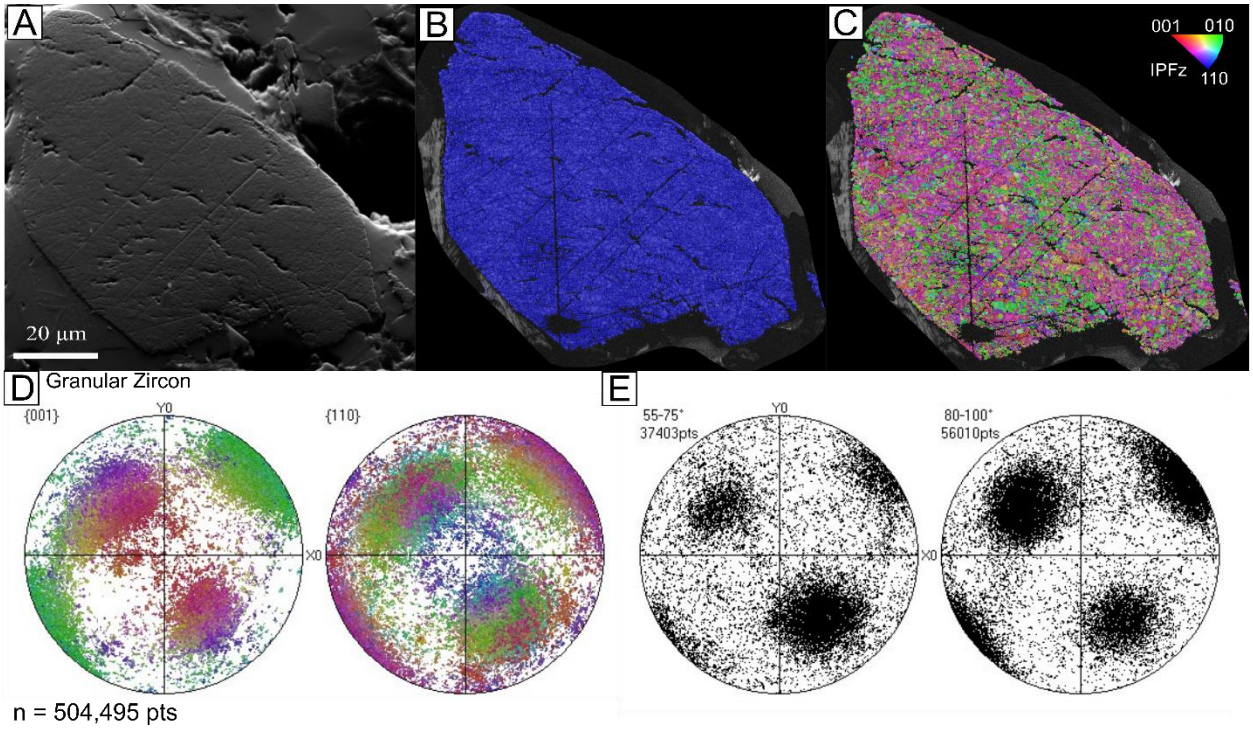

Figure A.1.13. Microstructure and crystallographic orientation data of the fully granular zircon grain, identified as a Former Reidite In Granular Neoblasts (FRIGN) grain (Cavosie et al., 2018b). (A) Forescatter electron (FSE) image of the FRIGN grain. (B) Electron backscatter diffraction analysis (EBSD) phase map identifying only zircon to be present in the grain. (C) EBSD orientation map of the measured orientations of each zircon neoblast in the grain. Zircon assigned the inverse pole figure (IPF) colour scheme. (D) Pole figures for zircon. Coloured scheme as in C. (E) Equal area projections of disorientation axes binned by disorientation angles 55°-75° and 80°-100°.

Item 3. Zircon Grains Reconstructed to Parent Phases Using the Python Program ARPGE

The distinctive twelve variant orientation patterns from clusters of baddeleyite grains in a selection of dissociated zircon grains from the impact glass indicate the pre-existence of cubic zirconia (Cayron et al., 2010). Using crystallographic information from known transformations from cubic → tetragonal → monoclinic and tetragonal → monoclinic tested for ceramic applications (Cayron, 2007; Cayron et al., 2010), the APRGE program can be used to reconstruct 'parent' grains using orientation relationships in daughter phases established from the phase transformations. The initial stage of EBSD map processing involved dilation of the baddeleyite grains in the vermicular coronas using an interactive nearest neighbour extrapolation routine. This step was required to perform neighbour-pair disorientation analysis within ARPGE.

Disorientation analysis shows peaks in the studied zircon grains at 90°, 115°, and 180° (Figure A1.20 shows a high frequency of disorientations at ~0°. This grain had a very low indexation when run through ARPGE, so the results are not as reliable as the other grains). These disorientations are consistent with cubic → monoclinic transformation twinning, confirming the pre-existence of a cubic 'parent' grain. The parent grain transformation can occur via two OR paths (Cayron et al., 2010):

type 1

$\langle a \rangle_{tetragonal}$ or $\langle c \rangle_{tetragonal} \rightarrow \langle b \rangle_{monoclinic}$

$\langle a \rangle_{tetragonal}$ or $\langle c \rangle_{tetragonal} \rightarrow \langle a \rangle_{monoclinic}$

type 2

$\langle a \rangle_{tetragonal}$ or $\langle c \rangle_{tetragonal} \rightarrow \langle c \rangle_{monoclinic}$

The disorientations observed in these grains correspond with OR type 2. With the OR set, we used ARPGE to reconstruct the baddeleyite clusters with the twelve variant patterns to determine whether cubic zirconia was present in the grains. Only seven grains (Figures A1.14–20) contained enough orientation data to use in the ARPGE software. Some grains had few data and high noise in the EBSD maps, making it impossible to rely on the reconstructed data. These grains were ignored in this part of the study.

The pole figures generated using MTEX were compared with the APRGE experimental pole figures. Experimental pole figures containing the cross-shaped, twelve variant patterns were identified as pre-existing cubic zirconia. Poles absent of this pattern, and only containing one to two cross-shape patterns, were identified as mainly tetragonal. Some baddeleyite clusters were described as slightly cubic. These clusters contained few orientation patterns to imply cubic, but not enough to confirm its pre-existence. Therefore, those clusters were considered as tetragonal. Out of the seven grains, only four showed enough evidence to confirm the presence of the parent cubic zirconia phase. The other three grains only supported tetragonal → monoclinic transformation, implying these grains were not exposed to melt temperatures >2370 °C (Timms et al., 2017).

The figures below (Figures A1.14–20) show reconstructed cubic phase maps with disorientation frequency graphs and experimental pole figures at <100>, {100}, <010>, {010}, <001> and {001}. The red point in the pole figures represent the reconstructed cubic zirconia orientations and the blue points represent the measured monoclinic orientations. If the twelve

variant pattern is observed, then the baddeleyite cluster is identified as cubic. If not, the cluster is identified as tetragonal.

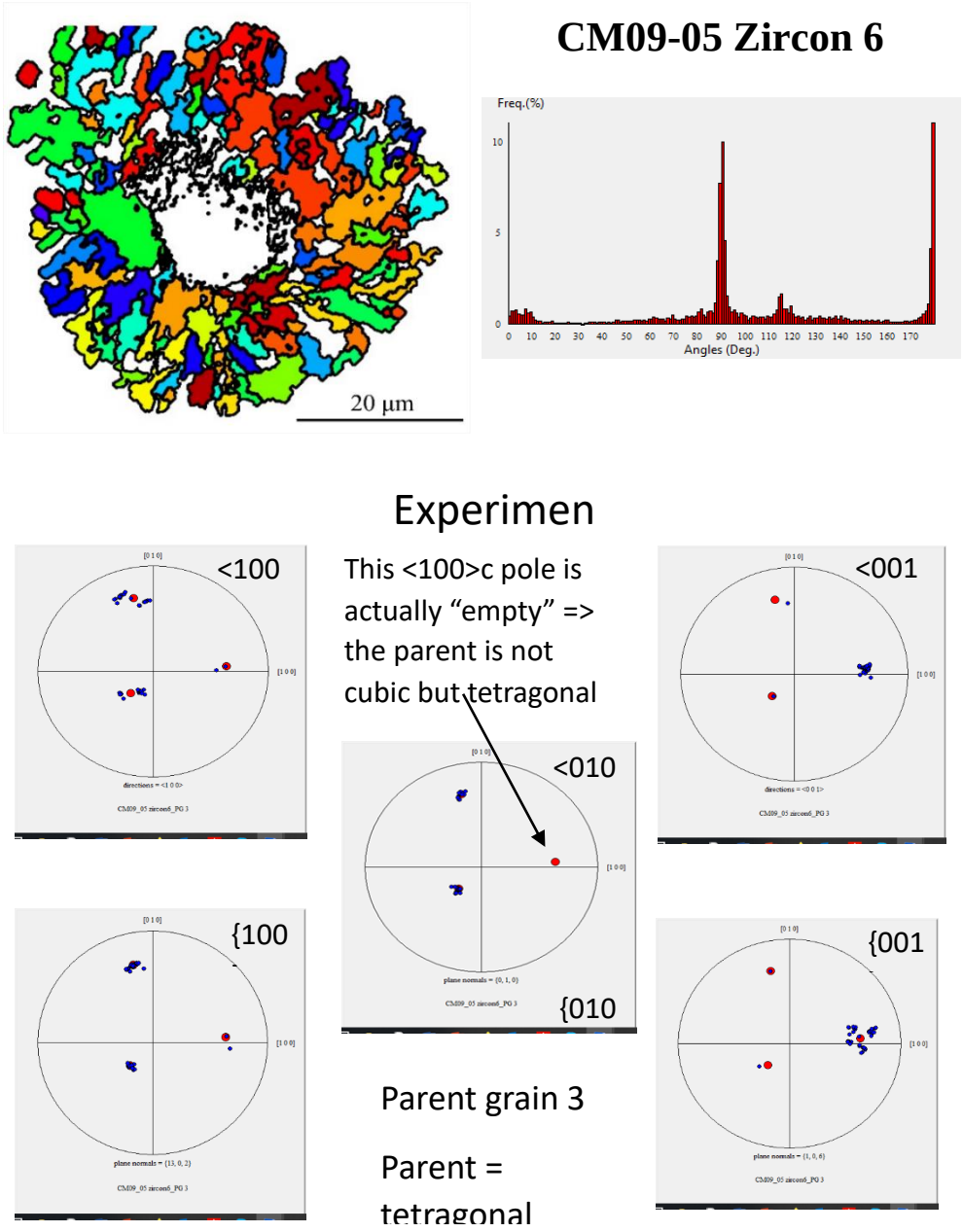

A1.14. Reconstructed zircon grain CM09-05-6 showing the distribution and 'parent' phase orientations. Experimental pole figures show a cubic orientation in the <100> c pole missing measured monoclinic orientations, indicating the parent grain to be tetragonal.

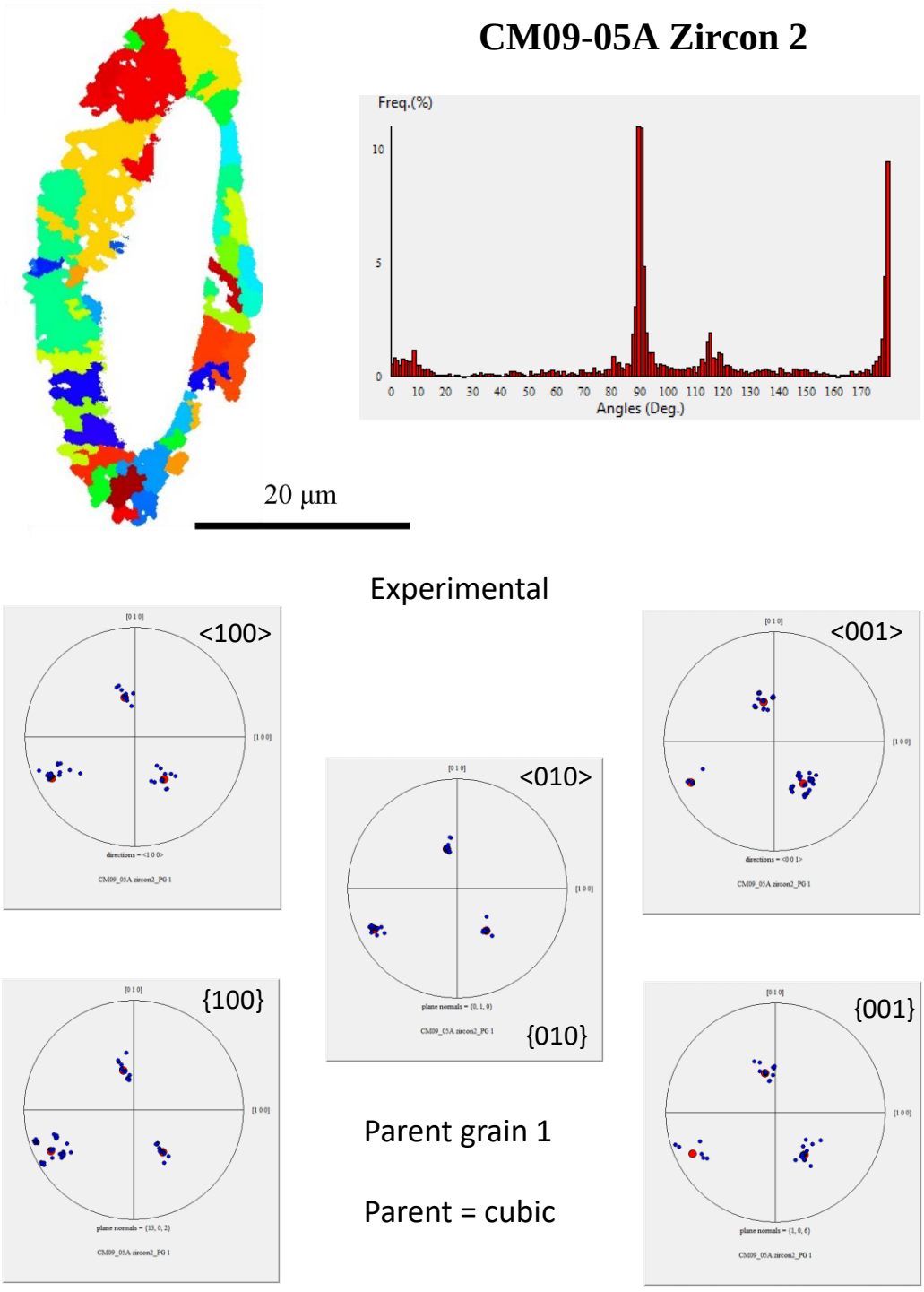

A1.15. Reconstructed zircon grain CM09-05A-2 showing the distribution and 'parent' phase orientations. Experimental pole figures show the twelve variant patterns in the 100, 010 and 001 poles, indicating the parent grain to be cubic.

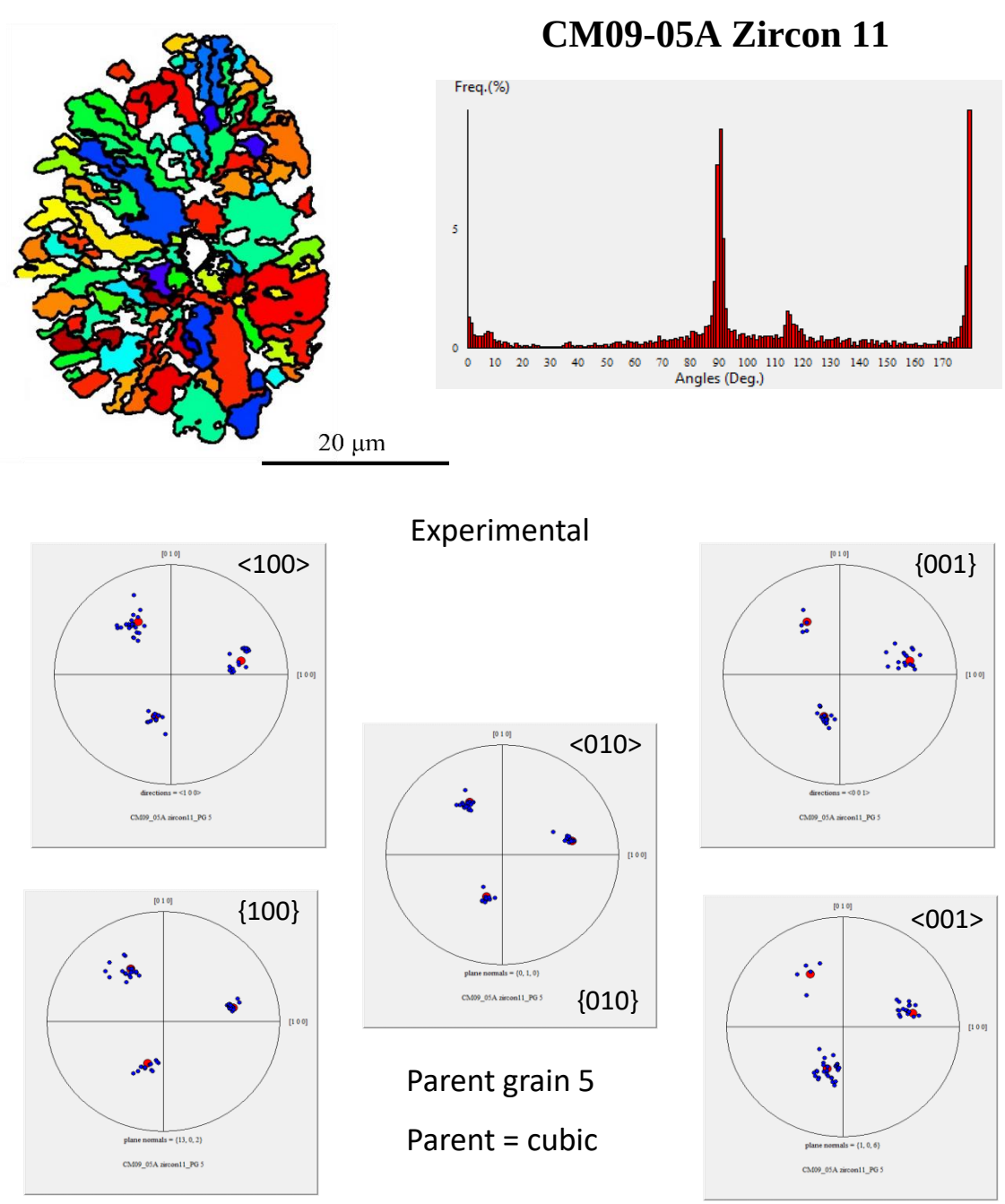

A1.16. Reconstructed zircon grain CM09-05A-11 showing the distribution and 'parent' phase orientations. Experimental pole figures show the twelve variant patterns in the 100, 010 and 001 poles, indicating the parent grain to be cubic.

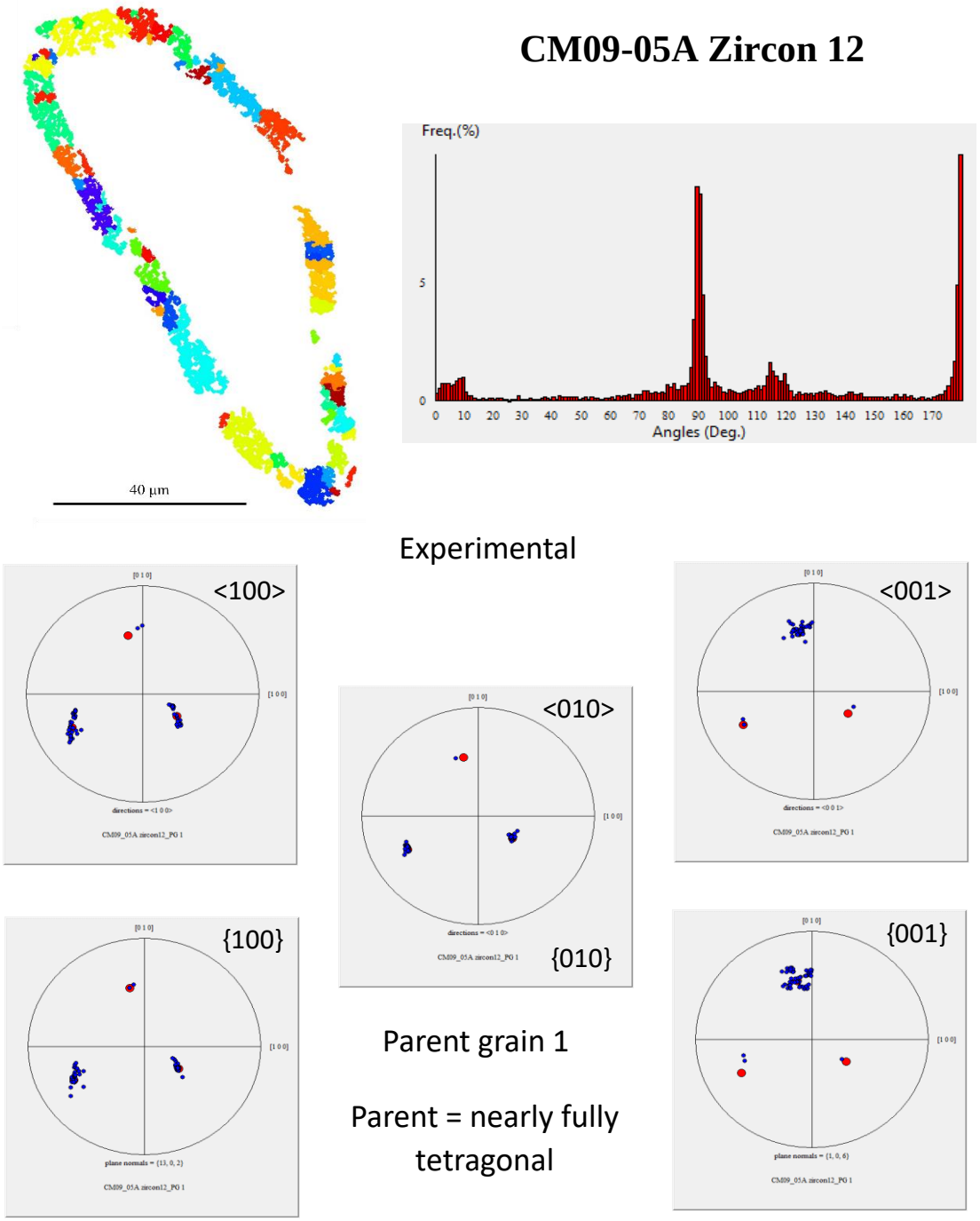

A1.17. Reconstructed zircon grain CM09-05A-12 showing the distribution and 'parent' phase orientations. Experimental pole figures are missing the twelve variant patterns in <010>, {010}. <001> and {001}, indicating the parent grain to be almost completely tetragonal.

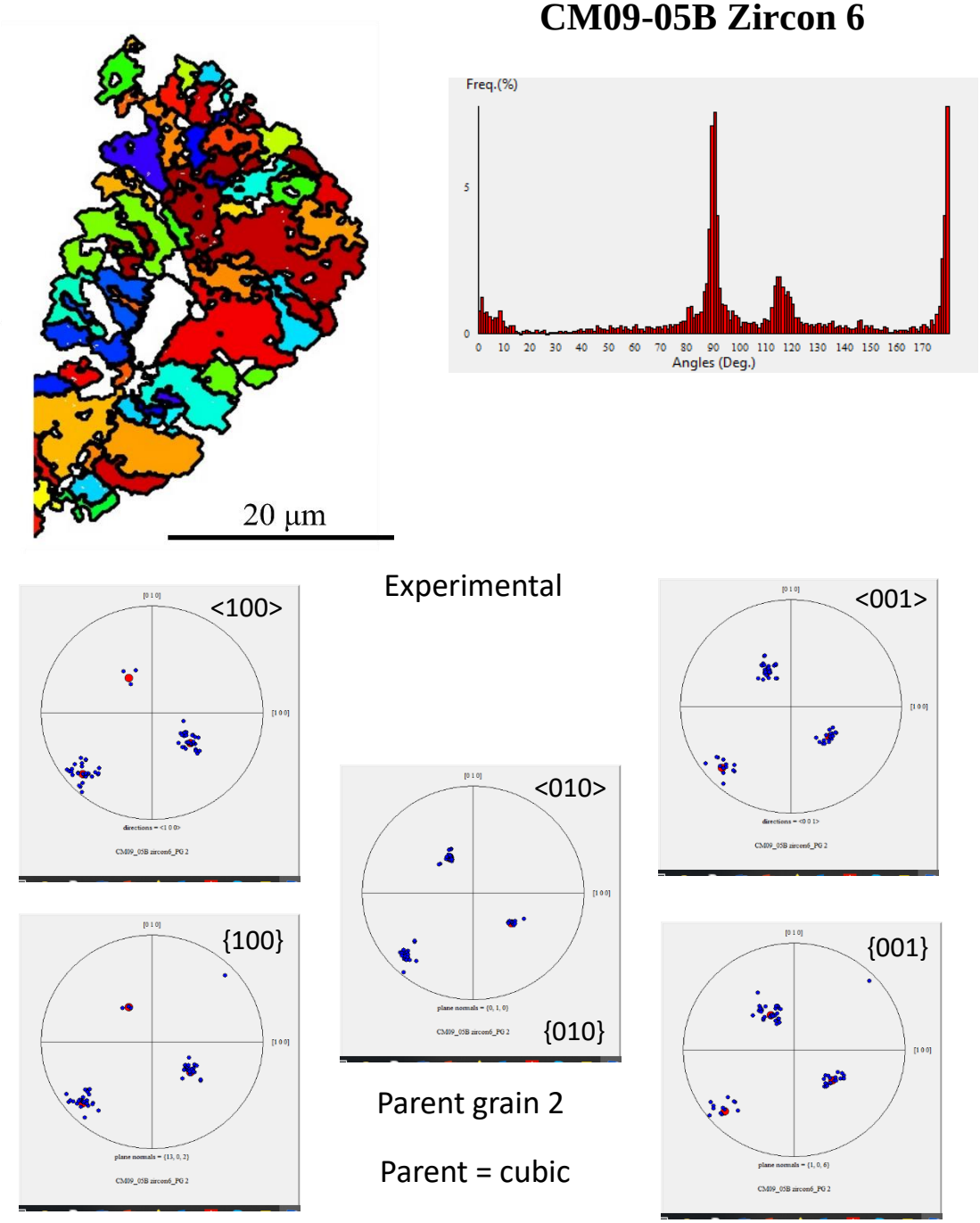

A1.18. Reconstructed zircon grain CM09-05B-6 showing the distribution and 'parent' phase orientations. Experimental pole figures show the twelve variant patterns in the 100, 010 and 001 poles, indicating the parent grain to be cubic.

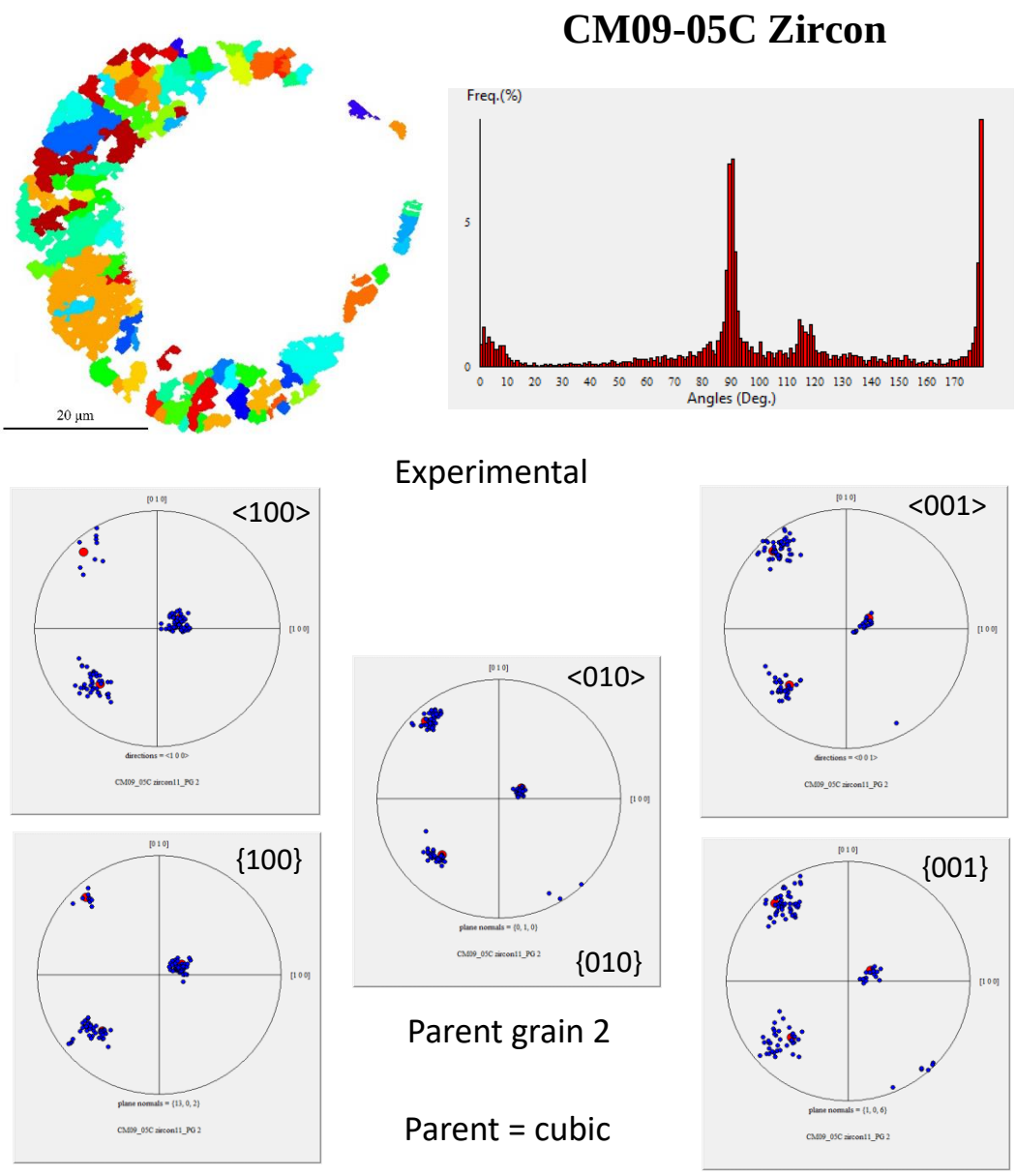

A1.19. Reconstructed zircon grain CM09-05C-11 showing the distribution and 'parent' phase orientations. Experimental pole figures show the twelve variant patterns in the 100, 010 and 001 poles, indicating the parent grain to be cubic.

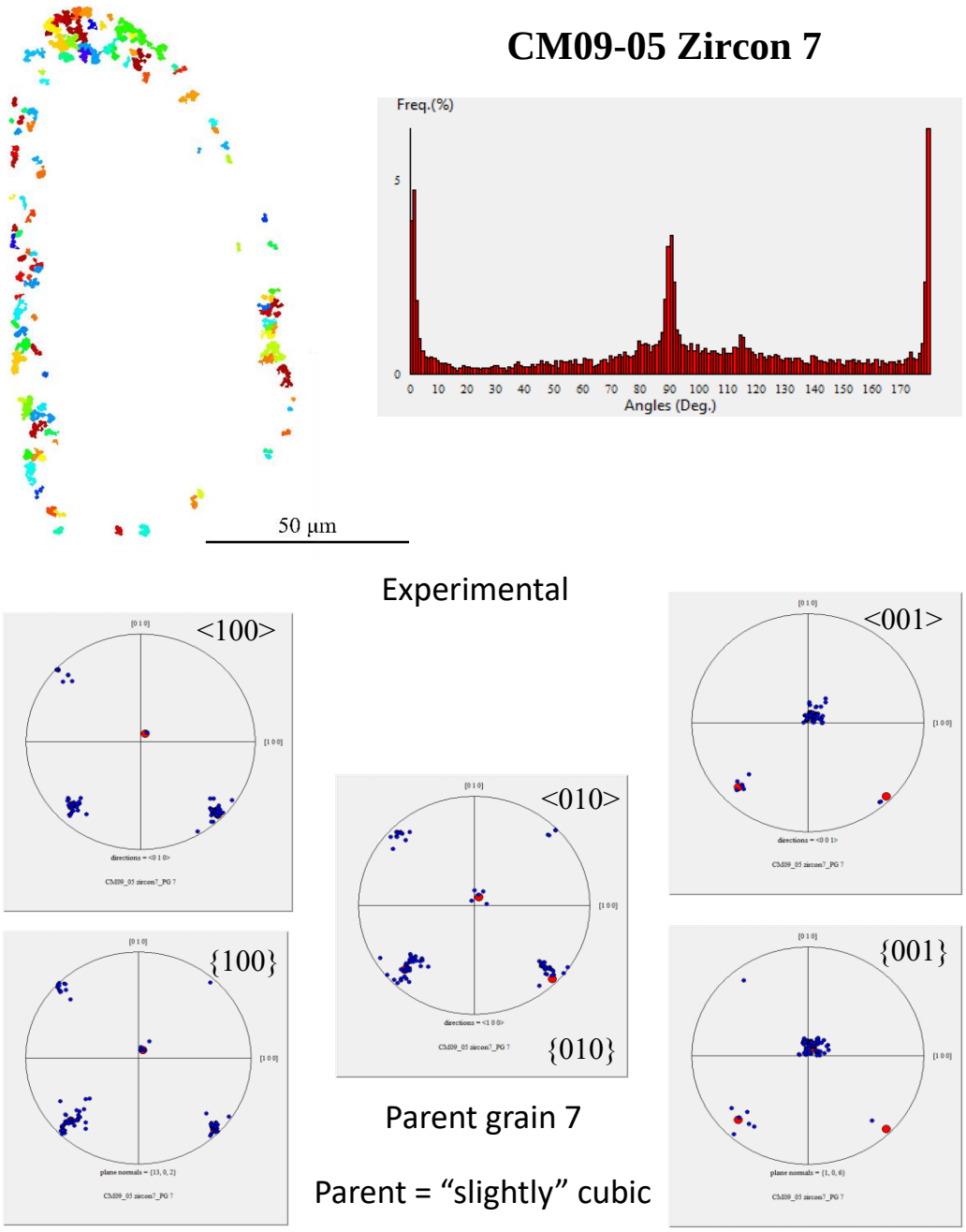

A1.20. Reconstructed zircon grain CM09-05-7 showing the distribution and ‘parent’ phase orientations. Experimental pole figures did not contain enough experimental cubic orientations and measured monoclinic orientations to confirm the pre-existence of parent cubic zirconia. The baddeleyite cluster is labelled as being a slightly cubic parent grain.

Item 4. Impact Glass WDS Analysis

In Table A1.1, we report the average composition of the impact glass. Two impact glass polished thin sections were analyzed using a JEOL JXA-8530F field emission electron microprobe WDS analysis at the University of Western Ontario. The WDS results show the impact glass is locally heterogenous (Table A1.1). Areas where the glass exhibits a white appearance have a lower SiO_2, $Al2O_3$, Na_2O, and K_2O composition.

Table A1.1 IMPACT GLASS GEOCHEMISTRY[1]

	SiO2(%)	Al2O3(%)	Na2O(%)	MgO(%)	CaO(%)	K2O(%)	FeO(%)	MnO(%)	Total (%)
CM09_05A - Grey Matrix	54.54	22.06	4.22	1.20	8.37	1.58	5.55	0.08	97.59
CM09_05A - White Matrix	46.59	15.79	2.69	2.43	9.30	1.25	15.71	0.22	93.97
CM09_05C - Grey Matrix	53.40	21.47	4.14	1.41	8.37	1.47	6.86	0.13	97.25
CM09_05C - White Matrix	40.93	9.89	1.96	2.53	9.85	0.70	23.96	0.48	90.29

[1]Geochemical data acquired using EPMA Wave Dispersive Spectroscopy (WDS)

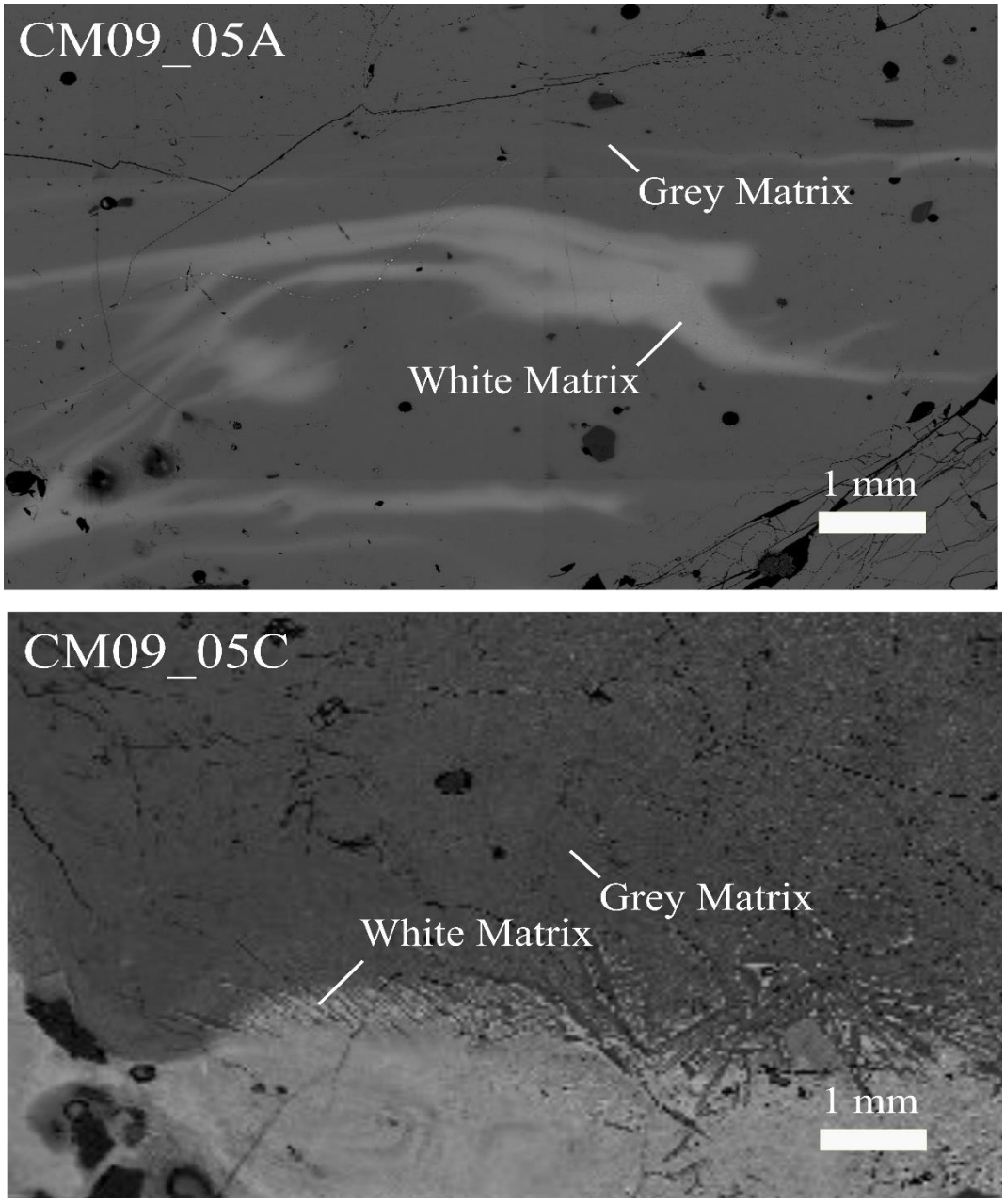

A1.21. Backscatter electron images of the two-impact glass sample thin sections used for WDS analysis. The major element compositions of the glass matrix are reported in Table A1.1.

References

Cayron, C., 2007, ARPGE: A computer program to automatically reconstruct the parent grains from electron backscatter diffraction data: Journal of Applied Crystallography, v. 40, p. 1183–1188, doi:10.1107/S0021889807048777.

Cayron, C., Douillard, T., Sibil, A., Fantozzi, G., and Sao-Jao, S., 2010, Reconstruction of the cubic and tetragonal parent grains from electron backscatter diffraction maps of monoclinic zirconia: Journal of the American Ceramic Society, v. 93, p. 2541–2544, doi:10.1111/j.1551-2916.2010.03894.x.

Timms, N.E., Erickson, T.M., Pearce, M.A., Cavosie, A.J., Schmieder, M., Tohver, E., Reddy, S.M., Zanetti, M.R., Nemchin, A.A., and Wittman, A., 2017, A pressure-temperature phase diagram for zircon at extreme conditions: Earth-Science Reviews, v. 165, p. 185–202, doi:10.1016/j.earscirev.2016.12.008.

Curriculum Vitae

Education

University of Western Ontario — August 2016 – August 2021
Ph.D., Earth and Planetary Sciences

University of St Andrews — September 2012 – June 2016
B.Sc., Geology

Employment History

Graduate Research Assistant — 2016 – Present
Department of Earth Sciences, University of Western Ontario

Graduate Teaching Assistant — 2016 – Present
Department of Earth Sciences, University of Western Ontario

Outreach Assistant — 2018 – Present
Institute for Earth and Space Exploration, University of Western Ontario

Space Explorers Camp Instructor — June – July 2017
Institute for Earth and Space Exploration, University of Western Ontario

Professional Experience

Spacecraft Mission Involvement:

Affiliate of the NASA Lunar Reconnaissance Orbiter Miniature-Radio Frequency Science Team — October 2019 – Present

Science and Operations Mission Planning, Mars Reconnaissance Orbiter, High Resolution Imaging Science Experiment (HiRISE) Mission — March – May 2017

Scientific Collaborations:

PhD Research and Field Work, Volcanic Analogues for the Exploration of Mars. Funded by the Canadian Space Agency (CSA) — September 2018 – Present

PhD Research and Field Work on Radar Interpretations of Lava Flow Surface Roughness, NASA SSERVI FINESSE Node. Funded by the CSA. — August 2016 – August 2017

Internships and Workshops:

6th European Space Agency (ESA) Advanced Course on Radar Polarimetry (Virtual) — May 2021

Geology & Planetary Mapping Winter School (Virtual) — February 2021

- Courses and interactive assessments learning methods and programs used to create 2-D and 3-D images of planetary surfaces. Online course organized by PLANMAP and GMAP.

Lunar and Planetary Institute (LPI) Exploration Science Summer Intern Program — May 2018 – August 2018
Supervisor: Dr David Kring, Lunar and Planetary Institute.

ESA Rosetta Science Operations Scheduling Legacy Workshop — October 2017

Planetary Analogue Mission Experience:

CSA CanMoon Sample Return Mission 2019: Planning Team - Data Manager August 2019

- Undertook the role of Data Manager for a high-fidelity lunar sample return mission funded by the Canadian Space Agency. Role involved organization of data products uploaded by a simulated rover in Lanzarote Spain.

CSA Precursor to Human and Science Rover (PHASR) Lunar Mission September 2017 – August 2018

- Collaborator attending mission planning and science goals meetings, assisting in planning reconnaissance field work, and contributing to science discussions.

CSA CanMars Sample Return Mission 2016 October 2016 – November 2016

- A part of the field team operating portal XRF, LIBS, and Raman to simulate the science analysis of the CSA Mars Exploration Science Rover.

Scholarships and Awards

The Barringer Family Fund for Meteoritic Impact Research June 2021
Total Award: $3600 USD

Lunar and Planetary Institute Career Development Award March 2020
Total Award: $1000 USD

Mary Ann Underwood Small Global Opportunities Award February 2020
Total Award: $2000 CAD

Leverhulme Trust Study Abroad Scholarship September 2017
Total Award: £21,000 GBP

Centre for Planetary Science and Exploration (CPSX) Travel Award July 2017
Total Award: $1000 CAD

Western Graduate Research Scholarship September 2016
Total Award: $10,636.34 CAD

Mineralogical Association of Canada Travel/Research Grant May 2017
Total Award: $600 CAD

IOM3 Travel Bursary – European Geoscience Union (EGU) April 2016
Total Award: £250 GBP

Research Experience

PhD Research, University of Western Ontario August 2016 – Present

- Geochemical, petrographic, and remote sensing research on the physical properties of volcanic and impact melt rocks that alter the surfaces of planetary bodies. Research is funded by the Canadian Space Agency. Supervised by Dr. Catherine Neish and Dr. Gordon Osinski.

Terrestrial Impact Melt Temperature Constrain Research February 2020 – Present

- Part of my PhD thesis involves constraining the temperature of impact melt deposits at the Mistastin Lake impact structure, northern Labrador, Canada, by studying the crystallographic orientations of zircon and zirconia polymorph. I travelled to the Johnson Space Center to perform scanning electron microscopy and electron backscatter diffraction analysis with Dr. Timmons Erickson.

Research Visit at the Applied Physics Laboratory February 2020

- Awarded the Mary Ann Underwood Small Global Opportunities Award to travel to the Applied Physics Laboratory in Baltimore to learn about the technical aspects and data products of the NASA Miniature-Radio Frequency Instrument. Hosted by Dr. Wes Patterson.

High-Altitude Balloon (HAB) Mission – Outreach Lead September 2017 – August 2019

- Head of the CPSX HAB outreach team with the goal to collect bioaerosol species and water moisture in the stratosphere. Recently awarded the Students for the Exploration and Development of Space (SEDS) Stratospheric Balloon Experiment Design Challenge (CAN_SBX) in partnership with the CSA.

X-ray Diffraction (XRD) and Rietveld Refinement May – August 2017

- Continuation of XRD and Rietveld Refinement lab analysis from advance mineralogy course project at the University of Western Ontario taught by Dr Roberta Flemming.

Undergraduate Research Assistant July 2015

- Worked with Dr. Will McCarthy to determine the precise ages of granites located at Galway, Ireland using zircon dating. Prepared samples through a variety of techniques all kept at extremely clean conditions to avoid contamination.

Undergraduate Research Assistant June – August 2014

- Over the summer of 2014 I worked with Dr Harry Oduro at the University of St Andrews Earth Science Department on sulphur isotope geochemistry. Getting hands on experience setting up sulphur lab apparatuses and using UV spectrometers.

Field Experience

CSA, Volcanic Analogues for the Exploration of Mars July 2019 – August 2019

- PhD research funded by the Canadian Space Agency to study the 2014-15 Holuhraun lava field. Research involves quantifying the surface roughness of the Holuhraun lava flows and comparing them to Martian lava flows with analogous morphological features.
- Logistics Lead for 2019 field deployment at the 2014-15 Holuhraun lava field in Iceland. Collaboration with the NASA Goddard Instrument Field Team planning logistics, field gear and health and safety.

CSA PHASR Lunar Mission – Field Reconnaissance Team March 2018

- Field team reconnaissance in Lanzarote, Spain locating potential field sites for the Lunar Exploration Analogue Deployment to start in 2019.

Planetary Surface Processes Field School May 2017

- Studying field locations in Arizona and Utah with geological features applicable to planetary field analogue research. Course offered by the Institute for Earth and Space Exploration.

Undergraduate Field Experience September 2012 – April 2016

- 100+ extensive field workdays in the UK and Europe: Spain, Italy, Ireland, and Switzerland

- June 2015, independent field work in Connemara, Ireland. The aim was to understand the structural controls of Mo-Cu mineralisation in the Murvey Granite (supervisor: Dr Will McCarthy).

Articles in Refereed Journals

- **Tolometti G. D.,** Erickson T. M., Osinski G. R., Cayron, C., Neish C. D. ***under review***. Hot Rocks: Constraining the Thermal Conditions of Impact Melt Deposits Using Zircon and Zirconia Polymorphs. Earth and Planetary Science Letters. No.: EPSL-D-21-00707.
- Czaplenski E.C., Harrington, E. M., Bell, S.K., **Tolometti, G.D.,** Farrant, B.E., Bickel, V.T., Honniball, C.I., Martinez, S.N., Rogaski, A., Sargeant, H.M., Kring, D.A., (2021). Human-Assisted Sample Return Mission at the Schrödinger Basin, Lunar Farside using a New Geologic Map and Rover Traverses. The Planetary Space Journal, 2, 2, 51.
- **Tolometti G.D.,** Neish, C.D., Osinski G.R., Hughes S.S., Nawotniak S.E., 2020. Interpretations of Lava Flow Properties from Radar Remote Sensing Data. *Planetary and Space Science*, 190, No. 104991.
- Sargeant, H.M., Bickel, V.T., Honniball, C.I., Martinez, S.N., Rogaski, A., Bell, S.K., Czaplinski, E.C., Farrant, B.E., Harrington, E.M., **Tolometti, G.D.,** Kring, D.A., 2020. Using Boulder Tracks as a Tool to Understand the Bearing Capacity of Permanently Shadowed Regions of the Moon. *Journal of Geophysical Research: Planets, 125,* e2019JE006157. https://doi.org/10.1029/2019JE006157
- Bickel, V. T., Honniball, C. I., Martinez, S. N., Rogaski, A., Sargeant, H. M., Bell, S.K., Czaplinski, E.C., Farrant, B.E., Harrington, E.M., **Tolometti, G.D.,** Kring, D.A., 2019. Analysis of lunar boulder tracks: Implications for trafficability of pyroclastic deposits. Journal of Geophysical Research: Planets, 124, 1296–1314. https://doi.org/10.1029/2018JE005876
- Caudill, C.M., Osinski, G.R., Pilles, E., Sapers, H.M., Pontefract, A.J., Francis, R., Duff, S., Laughton, J., O'Callaghan, J., Sopoco, R. and **Tolometti, G.**, 2019. Field and laboratory validation of remote rover operations Science Team findings: The CanMars Mars Sample Return analogue mission. *Planetary and Space Science*, 176, No. 104682.
- Osinski, G. R., M. Battler, M. Caudill, Francis, R., Kerrigan, M., Pilles, E., Pontefract, A., Tornabene, L. L., Allard, P., Bakambu, J. N., Balachandran, K., Beaty, D., Bednar, D. J., Bina, A., Bourassa, M., Cao, F., Christoffersen, P., Choe, B-H., Cloutis, E., Cote, K., Cross, M., D'Aoust, B., Draz, O., Dudley, B., Duff, S., Dzamba, T., Fulford, P., Godin, E., Goordial, J., Grau, A., Haid, T., Haltigin, T., Harrington, E., Harrison, T., Hawkswell, J., Hickson, D., Hill, P., Hipkin, V., Innis, L., King, D., Kissi, J., Laughton, J., Li, Y., Lymer, B., Maggiori, C., Maloney, M., Marion, C. L., Maris, J., McFadden, S., McLennan, S. M., Mittelholz, A., Morse, Z., Newman, J., O'Callaghan, J., Pascual, A., Patel, P., Picard, M., Pritchard, I., Poitras, J., Ryan, C., Sapers, H., Silber, E. A., Simpson, S., Sopoco, R., Svensson, M., **Tolometti, G.,** Uribe, D., Wilks, R., Williford, K., Xie, T., and Zylberman, W. 2019. The CanMars Mars sample return analogue mission. *Planetary and Space Science*, *166*, pp.110-130.

Selected Conference Publications[3]

- **Tolometti G. D**.; Neish C. D.; Osinski G. R.; Kukko A.; Voigt J. R. C.; Hamilton C. W. Roughness Analysis of the Holuhraun Lava Flow-Field for Lunar and Martian Volcanic Analogues. Geological Society of America Meeting. October 2020.
- **Tolometti G. D**.; Erickson T. M.; Osinski G. R.; Cayron C.; Neish C. D. Temperature Constraint of the Mistastin Lake Impact Structure Impact Melt Rocks. Geological Society of America Meeting. October 2020.
- **Tolometti G. D**.; Neish C. D.; Osinski G. R.; Kukko A.; Voigt J. R. C.; Hamilton C. W. Studying Lunar Lava Flow Emplacement by Quantifying the Surface Roughness of the Holuhraun Lava Flow-Field. NASA Exploration and Science Forum. July 2020.

[3] Total of 25 conference abstracts

- **Tolometti G. D**.; Bickel V. T.; Czaplinski E. C.; Sargeant H. M., Kring D. A. Using Temperature Constraints to Identify Potentially Traversable Permanently Shadowed Regions at the Lunar South Pole. NASA Exploration and Science Forum. July 2020
- **Tolometti G. D**.; Neish C. D.; Osinski G. R.; Kukko A.; Voigt J. R. C.; Hamilton C. W. Quantifying the Surface Roughness of the 2014-15 Holuhraun Lava Flow Using Radar and LiDAR Remote Sensing. *51st Lunar and Planetary Science Conference*. The Woodlands, Texas. March 2020 (Conference canceled)
- **Tolometti G. D**.; Osinski G. R.; Neish C. D.; Grieve R. A. F.; Erickson T. M. Constraining the Temperature of Impact Melt from the Mistastin Lake Impact Structure Using Zircon Crystal Structures. *51st Lunar and Planetary Science Conference*. The Woodlands, Texas. March 2020 (Conference canceled)
- **Tolometti G. D**.; Roberta F. L.; Neish C. D.; Osinski G. R. Redox Conditions and Surface Roughness of Lava Flows. *49th Lunar and Planetary Science Conference*. The Woodlands, Texas. March 2018
- **Tolometti G. D**.; Osinski G. R.; Neish C. D. The Impact Melt Sheet at West Clearwater Lake Impact Structure: A Petrographic and Geochemical Analysis. *49th Lunar and Planetary Science Conference*. The Woodlands, Texas. March 2018
- **Tolometti G. D**.; Neish C. D.; Osinski G. R.; Zanetti M.; Maj R.; S. S. Hughes, S. E. Kobs Nawotniak: Basaltic lava flow field analog at Craters of the Moon National Monument and Preserve. *GAC-MAC 2017*. Kingston, Ontario. May 2017.
- **Tolometti G. D**.; Neish C. D.; Osinski G. R.; Zanetti M.; Maj R.; S. S. Hughes, S. E. Kobs Nawotniak: Variation in Petrography of Basaltic Lava Flows with Similar Surface Roughness. *48th Lunar and Planetary Science Conference*. The Woodlands, Texas. March 2017.
- **Tolometti G**.; McCarthy W.: Hydrothermal modification of host rock geochemistry within Mo-Cu porphyry deposits in the Galway Granite, western Ireland. *European Geoscience Union*. Vienna, Austria. April 2016.